FZR - 218
May 1998

Annual Report 1997

Institute of Radiochemistry

Editor: Prof. Dr. H. Nitsche

Editorial staff: Dr. H.-J. Engelmann
PD Dr. G. Bernhard

Foreword

The overall goal of the institute is to contribute through basic and applied research to the better understanding of radionuclide transport in the environment. The main focus is the description of radionuclide behavior in ground and surface waters. This includes the interactions on surface boundaries between the aqueous phase and rock, minerals, and soil, the formation and distribution of colloids, and mobilization and retardation processes. The goal will be reached by closely combining laboratory and field experiments.

We have made further progress with our synthetic humic acid model substances by preparing humic acids with varying concentrations of functional groups and even blocked phenolic groups. This should help in further elucidating the binding mechanisms to uranium and other metal ions. We studied humic acid colloids by combining photon auto-correlation spectroscopy with scanning force microscopy. In a collaboration with the Institute of Materials Research of the Technische Universität Dresden, we were able to visualize for the first time the size and shape of humic acid colloids at different pH values.

We installed a laser-induced photoacoustic spectrometer and studied the complex formation of uranyl ions with carbonate. By directly measuring waters from a uranium mill tailing pond, we could show that the uranium exists as uranyl triscarbonato complex in these waters. Furthermore, uranyl arsenate complexation was studied for the first time by laser-induced fluorescence spectroscopy. The results were integrated in the international thermodynamic data base and now allow for calculating an improved uranium speciation in arsenic-containing uranium mining-related flood and seepage waters.

We established a permanent link to the Technische Universität Dresden by delegating one researcher to the radiochemistry laboratories at the university. He coordinates the radiochemistry laboratory teaching and is responsible for the day-to-day laboratory operation. His research on metal organic compounds will soon expand to transuranium elements.

Within the international EU-project RESTRAT, we implemented surface complexation modeling into risk and performance assessment models. These codes are currently being used to assess the radiation risk for radioactive contaminated areas in Belgium, Sweden and Great Britain.

Our newly-founded microbiology laboratory is now fully established. Microbiological and genetic studies on soil samples from a uranium mine tailing pile showed that certain bacteria adapt to uranium. Several of the isolated pure *desulfovibrio* cultures displayed a much higher ability to reduce uranium(VI) to uranium(IV) than all known *desulfovibrio* reference cultures. We verified the bacterial uranium reduction by XANES measurements at the Stanford Synchrotron Radiation Laboratory (SSRL).

The construction of our Rossendorf Beam Line (ROBL) at the European Synchrotron Radiation Facility (ESRF) in Grenoble, France, continues to move forward according to the projected time plan and budget. First monochromatic light is available since the end of 1997 and recent EXAFS experiments showed the excellent quality of the optics. The measured energy resolution ( ) $E/E = 1.8 \times 10^{-4}$) is very close to the theoretical value.

I am happy to report that we were finally granted the operating license for our new radiochemistry building in March 1998. This ends the long struggle of legal and construction problems which prevented the granting of this license, and we are devoted to minimizing the impact that this delay of over two years has caused to our research.

We proudly report that three of the institute's graduate students, Dr. S. Pompe, Dr. H. Moll, and Dr. A. Brachmann, obtained their degrees from the Technische Universität Dresden in 1997. One graduated with *summa cum laude*, two with *magna cum laude*. Dr. A. Vahle was awarded the Georg-Helm-Preis of the Technische Universität Dresden and the Doktorandenpreis 1997 of the Wissenschaftsgemeinschaft “Blaue Liste” (now Gottfried-Wilhelm-Leibniz Gesellschaft). Dr.

Pompe won a recognition award given by the Forschungszentrum Rossendorf e.V.

We would like to thank the many visitors, German and international, for their interest in our research and for their participation in the institute's seminars. We would like to also thank our scientific collaborators and the visiting scientists for coming to Rossendorf during 1997 to share their knowledge and experience with us. We continue to strongly encourage the collaborations and visits by scientists in the future.

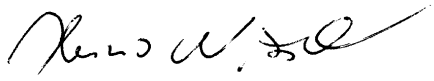

Rossendorf, April 1998 Prof. Dr. Heino Nitsche

CONTENTS

I. SCIENTIFIC CONTRIBUTIONS

Speciation and Migration of Radionuclides

CHARACTERIZATION OF PHYLLITE WITH SEM/EDS, PIXE, AND THIN SECTION MICROSCOPY

T. Arnold, T. Zorn, G. Bernhard, H. Nitsche
Forschungszentrum Rossendorf e.V., Institute of Radiochemistry

A detailed characterization of the light-colored phyllite with thin section-microscopy, SEM/EDS, and PIXE was conducted to identify the mineralogical constituents of the phyllite. It was found that the phyllite is composed of 48 vol.% quartz, 25 vol.% chlorite, and 20 vol.% muscovite. Furthermore, albite porphyroblasts (- 5 vol.%) and opaqueous minerals (< 2 vol.%) were observed.

Results and Discussion

Light colored phyllite, collected 540 m below ground, was obtained from the uranium mine Schlema-Alberoda in Western “Erzgebirge” in Saxony/Germany. Thin section microscopy showed that the light colored phyllite is mainly composed of the minerals quartz, muscovite, chlorite, and albite feldspar. Muscovite occurs in its variety sericite. Biotite was not observed in the phyllite samples indicating that the phyllite, following the BARROW Model, is assigned to the lowest grade metamorphic zone in the greenschist facies, the subzone chlorite zone (Matthes, 1983). This zone is characterized by the minerals quartz + muscovite + chlorite + albite. The phyllite itself shows tectonic foliation in which layers of melanocrate phyllosilicates of sericite and chlorite, intimately intergrown with each other, are segregated by leucocrate quartz layers. This texture is denoted as slaty cleavage. The quartz layers show mortar texture indicating tectonic stress. Furthermore, some albite porphyroblasts are observed within the phyllosilicates. These albite porphyroblasts are overgrown over the texture of the phyllite indicating that the albite porphyroblasts are posttectonic in nature. Also, there is a small amount of brownish opaqueous material present in the phyllite. Based on the observations made under the polarization microscope, the phyllite is composed of 48 vol.% of quartz, 25 vol.% of chlorite, 20 vol.% of muscovite, 5 vol.% of albite, and < 2 vol.% of opaqueous minerals.

The phyllite was further characterized by detailed SEM/EDS (Scanning Electron Microscopy / Energy Dispersive Spectrometry) investigations of phyllite powder and solid phyllite. The SEM/EDS specimens were prepared by embedding some of the 63-200 µm fraction of the phyllite sample and two phyllite rock specimens in epoxide resin (ARALDITE from Ciba-Geigy), surface polishing of the resin and carbon-coating of the surface. SEM revealed that the 63-200 µm phyllite fraction contained grains of the expected grain size, but additionally many smaller grains. These grains, often much smaller than 63 µm, appeared as fine needle-like platy and lamilliferous aggregates and were identified by EDS as muscovite ($KAl_2[(OH,F)_2|AlSi_3O_{10}]$ / phengite ($K(Mg,Fe)_{0.5}Al_{1.5}[(OH)_2|Al_{0.5}Si_{3.5}O_{10}]$ / paragonite ($NaAl_2[(OH,F)_2|AlSi_3O_{10}]$ and chlorite $(Mg, Fe^{2+})_{5-4}(Al, Fe^{3+})_{1-2}[(OH)_8|AlSi_3O_8]$. The large grains consisted almost exclusively of quartz SiO_2 and albite $NaAlSi_3O_8$. Small inclusions of apatite $Ca_5[F, OH, Cl)|(PO_4)_3]$, titanium oxide TiO_2, zirkon $Zr[SiO_4]$, and monazite (Ce, La, Nd, Th) $[PO_4]$ were also detected within the albite grains. Two characteristic EDS spectra of muscovite and chlorite are shown in Fig. 1.

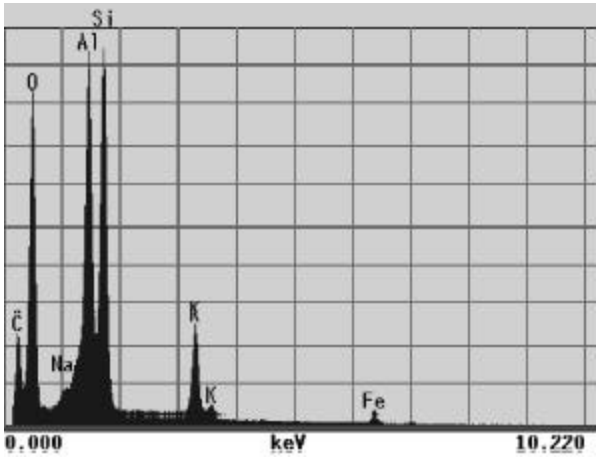

Fig. 1A

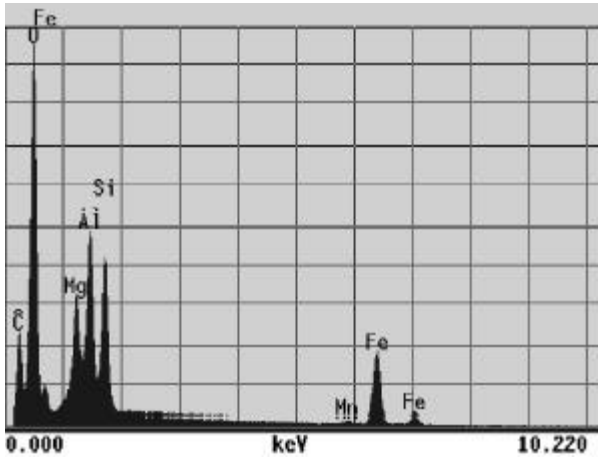

Fig. 1B

Fig. 1A shows a EDS spectrum of muscovite with small amounts of Fe and Na indicating the presence of phengite and paragonite. An EDS spectrum of chlorite is shown in Fig. 1B.

Manganese among other cations is reported to occur as part of the chlorite structure as well /2/. Phengite and paragonite are typical minerals of the greenschist facies, subfacies chlorite zone. In addition to the above named minerals and related to the presence of brownish-opaqueous material, titanium oxide, probably rutile, and tiny small scales with diameters of less than 1 µm were identified as Fe-oxide minerals.

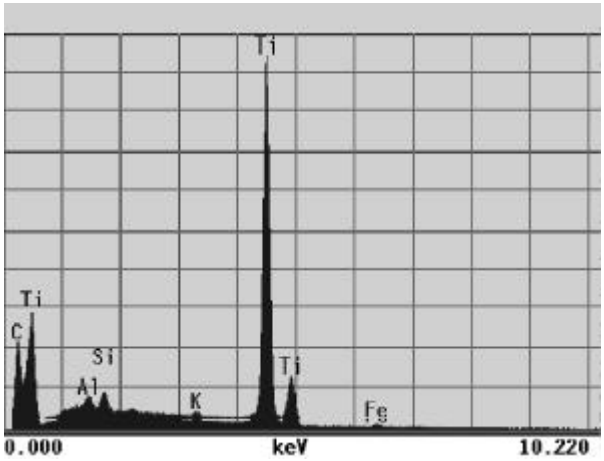

Fig. 1C

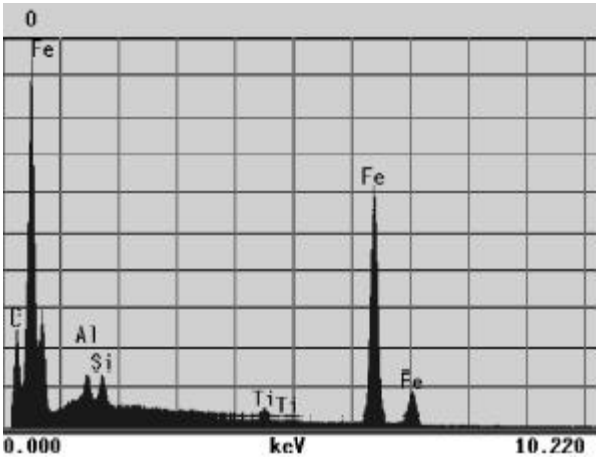

Fig. 1D

Fig. 1: EDS Spectra of mineralogical constituents of phyllite. A. muscovite, B. chlorite, C. titanium oxide, D. iron oxide.

Fig. 1C shows a spectrum of titanium oxide and Fig. 1D represents an Fe-oxide spectrum. The peaks for Al and Si in Fig. 1C and 1D are attributed to the surrounding of the Ti-oxide and Fe-oxide particle. SEM/EDS investigations of the rock specimens confirmed the observations made with thin section microscopy and confirmed the results of the SEM/EDS studies on the 63 to 200 µm powder fractions. It further verified the mineralogical composition of the phyllite and confirmed that the phyllite powder was representative of the rock phyllite.

Additionally, a polished sample of a phyllite rock specimens was studied by PIXE (Photon Induced X - ray Emission) by conducting a line scan across the surface, about 12 mm in length and two elemental mappings. The elements Si, K, Fe, Ti, and Ca were detected to be the dominant elements with an atomic number higher than 13 (Al). Based on the elemental distribution and in accordance with thin section microscopy it was possible to distinguish various mineral layers in the phyllite. It is composed of phyllosilicate layers, consisting of the intimately intergrown minerals muscovite and chlorite, and quartz layers. Layers enriched in Si and without K, Fe, or Ti were attributed to quartz layers. K-enriched layers indicated the presence of muscovite. Iron was distributed in the phyllosilicate layers which is indicative for chlorite. In higher concentrations, however, it was identified as iron oxide mineral, typically following cracks and fissures or as locally enriched spots. Titanium was also enriched in the phyllosilicate layers, but in lower concentrations. Higher concentrations of titanium were found as locally enriched spots. They were identified as titanium oxide, very likely rutile (TiO_2). Hence, iron oxide minerals, together with titanium oxide minerals, were identified as the opaqueous minerals observed with thin section microscopy. Moreover, the accessory minerals monazite, apatite and zircon were detected. Especially monazite was in particular identified because of its ion-luminescence behavior.

Acknowledgments

We would like to thank D. Grambole and F. Herrmann from the Institute for Ion-Beam Physics and Materials Research, FZR for conducting PIXE measurements. We also thank R. Müller and E. Cristalle from the Zentralabteilung Analytik, FZR, and R. Opitz, Zentralabteilung Analytik for preparing SEM/EDS specimens.

References

/1/ Matthes, S.: *Mineralogie.* Springer Verlag, Berlin, Heidelberg, p.340 (1983)

/2/ Barnhisel, R.I., Bertsch, P.M.: Chlorites and Hydroxy-interlayered Vermiculites and Smectites. In: *Minerals in Soil Environments.* Dixon, J.B., Weed, S.B. (eds.), Soil Science Society of America, Madison, Wisconsin, USA, p.729-788 (1989)

SORPTION OF URANIUM (VI) ONTO PHYLLITE AND ITS MINERALOGICAL CONSTITUENTS

T. Zorn, T. Arnold, G. Bernhard, H. Nitsche
Forschungszentrum Rossendorf e.V., Institute of Radiochemistry

The sorption of U(VI) on phyllite and on the main mineral constituents of phyllite was studied in individual batch experiments under ambient pressure. The study showed that the maximum amount of uranium sorbed onto each individual mineral was different and ranged from 48 % of initially added uranium for quartz, to 58 % for albite, to 70 % for muscovite and chlorite, and to 97 % for phyllite. From this, we conclude that none of the main mineral constituents of phyllite dominates the sorption behavior of uranium onto phyllite. Mössbauer spectroscopy on the phyllite before and after sorption experiments showed that the Fe(III) concentration had increased by three percent. This initiates that a secondarily formed iron mineral, very likely ferrihydrite, dominates the sorption behavior of U(VI) onto phyllite.

Experimental

Phyllite was obtained from the uranium mine site “Schlema-Alberoda” near Aue in Western Saxony. It was collected 540 m underground and represents /1/ a typical light-colored phyllite of this mining site. Based on visual impression gained from thin section microscopy, the mineralogical constituents of the phyllite are quartz (48 vol.%), muscovite (20 vol.%), chlorite (25 vol.%), albite (5 vol.%), and brownish opaqueous material (2 vol.%). Half a gram of phyllite and the mineral samples of the 63-200 µm fraction (for chlorite the fraction < 40 µm) were added to 20 mL of 0.1 M $NaClO_4$ solution in 50 mL polypropylene centrifuge tubes. Then the mineral samples were altered for 24 hours. After this period additional 20 mL of 0.1 M $NaClO_4$ solution were added to reach a final volume of 40 mL. The pH was adjusted to the desired pH value using the appropriate amounts of HNO_3 and NaOH. In samples adjusted to pH values higher than 7, a certain amount of $NaHCO_3$ was added to speed up the equilibration process with atmospheric CO_2. The next day the pH was checked and if necessary readjusted. This was repeated until the pH was stable. Then about 80 µL of a $5 \cdot 10^{-4}$ M uranylperchlorate solution was added to the pH-adjusted samples to set the final U(VI) concentration in the slurries to $1 \cdot 10^{-6}$ M. Immediately after the addition of the uranium, the pH was readjusted to the values measured just prior to the U(VI) addition. Then the samples were rotated end-over-end at 1 - 5 rpm for about 60 hours to avoid abrasion and to keep the geomaterial in suspension. At the end of the 60 hours period, the final pH values were taken. The aqueous phase and the solid phase were separated by centrifugation at 3000 rpm for 7 minutes. Subsequently, the supernatant was filtered. Centrisart C 30 membranes with a pore size of 5 nm were used for the filtrations. The filtrate was acidified to a pH of about 1.5, and the sample was analyzed for uranium by ICP-MS (Inductive Coupled Plasma-Mass Spectrometry).
The difference between the concentration in the supernatant solution and the total uranium concentration ($1 \cdot 10^{-6}$ M) was attributed to sorption onto the minerals.

Results and Discussion

The results of the batch sorption experiments for phyllite and the mineral constituents of phyllite and ferrihydrite are depicted in Fig. 1.

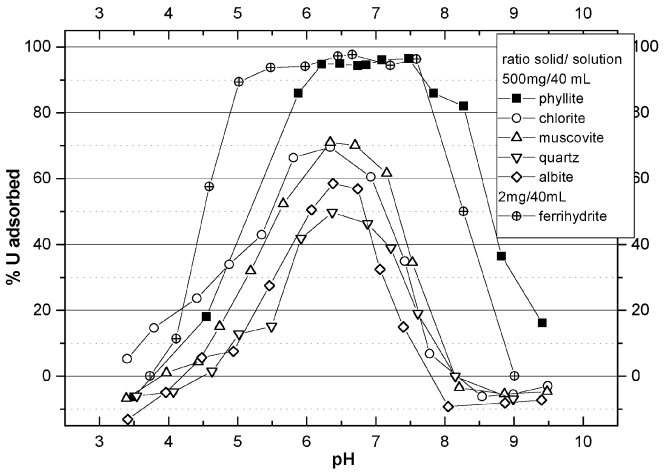

Fig. 1: Sorption of U (VI) (10^{-6} M) onto phyllite, its mineral constituents, and ferrihydrite.

The results show that the sorption maxima of uranium on phyllite and on the investigated pure mineral phases takes place in the near neutral pH range. However, there is a big difference in the sorption intensity and the adsorption edge of phyllite compared to each of its individual mineralogical constituents. The pure mineral phases had its sorption maximum between pH 6.0 and 7.0, whereas phyllite reached its sorption maximum in a wider pH range of 5.8 to 8.3. Quartz sorbs less uranium (approximately 50 %) compared to albite 58 %, muscovite and chlorite which sorb up to 70 %. Uranium sorption onto phyllite was very high and reached a maximum of 97 %, which is distinctively more uranium than any of

the pure mineral phases, that predominantly comprise the phyllite. Conclusively, there must be an additional component responsible for sorbing uranium. This is further supported by considering the BET specific surface areas of the pure minerals and of the phyllite. Phyllite with 4.0 m^2/g has by far the highest value followed by chlorite (1.6 m^2/g), muscovite (1.4 m^2/g), albite (0.2 m^2/g), and quartz (0.1 m^2/g). The additional component which is predominantly responsible for U (VI) sorption onto phyllite may be an alteration product or a newly formed secondary iron mineral, very likely ferrihydrite. This explanation is supported by the observation of a very thin film with reddish-brown color which formed in the course of the batch experiments. The main evidence for this conclusion was obtained by Mössbauer spectroscopy (MS) analysis of phyllite samples before and after the batch sorption experiments. According to this technique, 79.7 % ± 2.0 % of the iron in the fresh phyllite 63 to 200 µm fraction is Fe(II) and 20.3 % ± 1.0 % is Fe(III). In the fraction 63 to 200 µm fraction with the reddish-brown color, i.e., the sample after the batch sorption experiment, Fe(III) increased and Fe(II) decreased. In this sample 76.9 % ± 2.4 % is found as Fe (II) and 23.1 % ± 1.9 % is detected as Fe(III). Even considering the analytical error, there is a distinct increase in ferric iron which is present in an amorphous iron phase. This ferric iron increase may be attributed to alteration reactions at the chlorite surface. Numerous observations described in the literature point to this fact. Makumbi and Herbilon /2/ and Ross /3/ report that the amount of structural Fe (II), and its subsequent oxidation, plays a significant role in the weathering of chlorite to vermiculite.

Acknowledgment
The authors would like to thank G. Wildner from the WISMUT GmbH for the phyllite samples, W. Wiesner, Zentralabteilung Analytik, Forschungszentrum Rossendorf, for ICP-MS measurements, G. Schuster, Institute of Radiochemistry, for determining the BET specific surface area of geomaterials, H. Reuter, Institute for Ion-Beam Physics and Materials Research, for Mössbauer spectroscopy measurements. We also thank H.R. von Gunten, Paul Scherrer Institut, Labor für Radio- und Umweltchemie, Villigen, for providing the chlorite sample.

References
/1/ Wildner, G., WISMUT GmbH, personal communication, 1996
/2/ Makumbi, L., Herbilon, A.J.: Vermiculitisation expementale d`une chlorite. Bulletin du Groupe Francaise des. Argiles **24**, 153-164 (1972)
/3/ Ross, G.J.: Experimental alteration of chlorites into vermiculates by chemical oxidation. Nature **255**, 133-134 (1975)

OXIDATION OF STRUCTURAL IRON IN CHLORITE DETECTED BY MÖSSBAUER SPECTROSCOPY

T. Arnold, T. Zorn, H. Reuther [1], G. Bernhard, H. Nitsche
Forschungszentrum Rossendorf e.V., Institute of Radiochemistry
[1] Institute of Ion Beam Physics and Material Research

Phyllite powders of the fraction 63-200 µm, predominantly composed of quartz, chlorite, muscovite, and albite, were measured with transmission mössbauer spectroscopy (TMS) before and after conducting batch sorption experiments. The TMS spectra revealed that the amount of ferric iron increased in the course of the batch experiments by approximately 3 %. This increase in ferric iron, together with a concomitant color change from grayish green to grayish-reddish brown, was related to structural oxidation of ferrous iron within and at the surface of chlorite, one of the mineralogical constituents of phyllite, leading eventually to the formation of the iron oxyhydroxide mineral ferrihydrite.

Results and discussion
Sorption experiments with phyllite and its mineralogical constituents, quartz, chlorite, muscovite and albite, revealed that these minerals are not exclusively responsible for the U(VI) sorption capacity of the rock phyllite. Hence, an additional component minor in volume and mass must be present which significantly increases the uranium sorption capacity. Based on the observation of a very thin film with reddish-brownish color which formed in the course of the batch experiments, it was assumed that the formation of Fe-alteration products may be related to this additional component. Iron oxides and hydroxides are strong pigments, and small amounts of these minerals account for most of the brown and red color of soils (Schulze, 1989). For this

reason, the phyllite powder of the fraction 63-200 µm was measured with transmission Mössbauer spectroscopy (TMS) analysis before and after the sorption experiments. TMS measurements were carried out at room temperature. It is a conventional spectrometry in the constant acceleration regime and had nominally 3.7 Gbq. The source used was ^{57}Co in Rh matrix. A quadrupole splitting of > 2 mm/s is characteristic for Fe(II), while a quadrupole splitting of 0.5 to 0.8 mm/s is indicative for Fe(III). The spectrum shown in Fig. 1 may be interpreted in terms of the super-position of two large quadrupole split absorptions attributable to Fe(II) ions in two inequivalent sites and two narrow doublets centered at about 0.43 and 0.71 mm/s which are characteristic of Fe(III) ions.

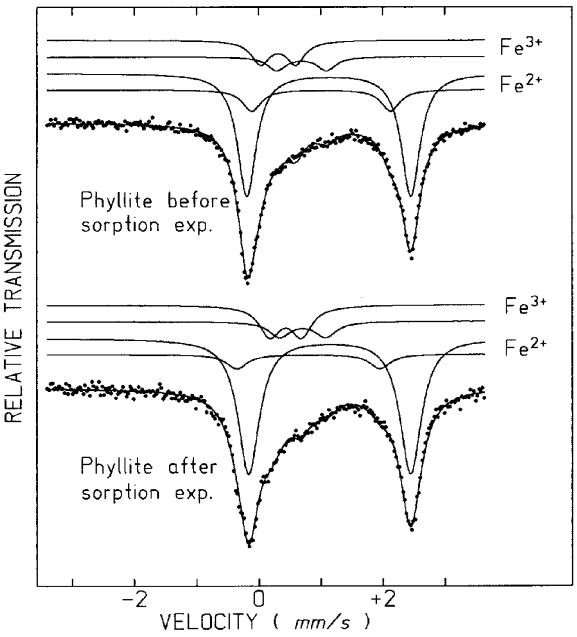

Fig. 1: Transmission Mössbauer spectra (TMS) of phyllite measured before conducting sorption experiments and of phyllite measured after finishing the sorption experiments.

The spectra were computer fitted with two Fe(II) quadrupole doublets and two Fe(III) quadrupole doublets. The line widths and the line intensities of the two lines in each doublet were made equal. The results, including the mössbauer parameters, i.e., chemical isomer shift, the quadrupole splitting, and the line width, are given in Tab. 1. The relative area of the Fe(II) and Fe(III) components can be considered to be equal to the fraction of iron in the respective oxidation state.

			site 1				site 2			
	oxidation state	ARE	ISO	QUA	WID	ARE	ISO	QUA	WID	ARE
Phyllite before sorption exp.	Fe^{2+}	79.7 (2.0)	1.133	2.64	0.362	67.8	1.011	2.23	0.362	12.0
	Fe^{3+}	20.3 (1.0)	0.694	0.801	0.362	7.5	0.317	0.562	0.362	12.8
Phyllite at the end of sorption exp.	Fe^{2+}	76.9 (2.4)	1.142	2.61	0.412	69.6	0.799	2.30	0.412	7.3
	Fe^{3+}	23.1 (1.9)	0.706	0.740	0.412	7.9	0.433	0.509	0.412	15.2

ARE = relative area in %, ISO = isomer shift relative to "-Fe in mm/s, QUA = quadrupole splitting in mm/s, WID = line width in mm/s

Tab. 1: Result of the TMS analyses.

The results from TMS showed that 79.7 ± 2.0 % of the iron in the fresh phyllite, 63 to 200 µm fraction, before the sorption experiment is Fe(II) and 20.3 ± 1.0 % is Fe(III). In the sample with the reddish-brown color, also 63 to 200 µm fraction, i.e. the sample obtained at the end of the batch sorption experiment, there is an increase in Fe(III) and a decrease in Fe(II). In this sample 76.9 ± 2.4 % is found for Fe (II) and 23.1 ± 1.9 % is detected for Fe(III). The TMS analysis revealed that the amount of Fe(III) within the analytical error significantly increased by 2.8 ± 2.1 % in the phyllite in the course of the batch experiments. This leads to the conclusion that some of the Fe(II) within or at the chlorite mineral surface, one of the mineralogical constituents of the phyllite, was oxidized and that a poorly ordered iron oxyhydroxide mineral, very likely ferrihydrite, has formed. Ferrihydrite is well known for its high uranium sorption capacity /2/ and may be the mineral minor in mass and volume which is responsible for increasing the U(VI) sorption capacity of the rock phyllite relative to the sorption capacity of the main mineralogical constituents of the phyllite /3/. Moreover, despite a similar chemical composition there is a clear difference between the uranium(VI) sorption behaviour of the pure mineral phase chlorite obtained from Grimsel in Switzerland and the chlorite as mineralogical constituent of the phyllite. Consequently, it was assumed that the chlorite from Grimsel has to be attributed to a pedogenic clay whereas the chlorite as mineralogical constituents of the phyllite was identified as a primary chlorite. Pedogenic chlorites are well known for the reduced susceptibility for weathering

whereas primary chlorite are not very resistant to weathering and may weather much faster than pedogenic chlorite /4/. This seems to be the reason why there is a difference between the sorption behaviour of phyllite and the sorption behaviour of its mineralogical constituents.

References

/1/ Schulze, D.G.: An introduction to Soil Mineralogy. In: *Minerals in Soil Environments.* Dixon, J.B., Weed, S.B. (eds.), Soil Science Society of America, Madison, Wisconsin, USA, p.1-34 (1989)

/2/ Waite, T.D., Davis, J.A., Payne, T.E., Waychunas, G.A., Xu, N.: Uranium(VI) adsorption to ferrihydrite: Application of a surface complexation model. Geochimica et Cosmochimica Acta **58**, 5465-5478 (1994)

/3/ Zorn, T., Arnold, T., Bernhard, G., Nitsche, H.: Sorption of uranium (VI) onto phyllite and its mineralogical constituents. In: This report, Institute of Radiochemistry, Annual report 1997, p.3 (1998)

/4/ Barnhisel, R.I., Bertsch, P.M.: Chlorites and Hydroxy-interlayered Vermiculites and Smectites. In: *Minerals in Soil Environments.* Dixon, J.B., Weed, S.B. (eds.), Soil Science Society of America, Madison, Wisconsin, USA, p.729-788 (1989).

URANIUM SORPTION ON METAMORPHIC ROCKS AND SEDIMENTS UNDER THE INFLUENCE OF HYDROTHERMAL WOOD DEGRADATION PRODUCTS

L. Baraniak, G. Bernhard, H. Nitsche
Forschungszentrum Rossendorf e.V., Institute of Radiochemistry

Uranium adsorption on rocks and sediments that are typical for the Saxon mining areas was studied in the presence of wood degradation products, pine wood lignin, vanillic and gluconic acid by batch experiments using ^{234}U tracer and LSC.

A central task in the restoration of the decommissioned uranium mining areas in Saxony and Thuringia (Germany) is the flooding of the large and deep underground mines /1/. In this process the interaction of water with the mine wood leads to the introduction of dissolved organic substances (DOC) into the water. This DOC plays an important role in the water chemistry, especially its ability to complex radionuclides and heavy metals /2,3/.

For over 30 years pine wood was used to reinforce the shafts and galleries in the Schema uranium mine. It was strongly attacked by brown rot fungi. The cell matrix of more than two-thirds of the trunks' cross-sections were destroyed and much of the wood's cellulose fibers and polyoses were decomposed. In this process, the lignin content of the mine wood increased from usually 33% to about 76%. The hydrothermal leaching process that is currently taking place in the flooded mine was simulated by boiling wood shavings in water under reflux for five hours (wood to water ratio: 0.025) /4/. In this treatment about 10 wt % of the wood was dissolved. The leachate contains 300 mg/L DOC with about 50% phenolic and 42% saccharic compounds with wide molecular weight distribution. The phenols are in the upper molecular weight range ($\$10^4$) and most of the saccharides are below $3 \cdot 10^3$ u. The leached compounds are highly functionalized: 7.8 mmol/g strongly acidic groups ($pK_{Diss.}$= 4.4) and 6.3 mmol/g weak acidic groups ($pK_{Diss.}$= 8.5) /3/.

The following rocks and minerals that are characteristic for the western ore mountains mining area were investigated: (1) *phyllite* (uranium mining rock pile no. 372, Schema), a fine slate-like metamorphic rock that mainly consists of muscovite, chlorite and quartz; (2) *granite* (Demitz-Thumitz/Lusatia) containing potash feldspar, plagioclase, quartz, biotite and muscovite; (3) *gneiss* (rock pile "Reiche Zeche", Freiberg/ Saxony), a metamorphic rock of magmatic origin with bright-streaky feldspar and quartz and dark bands of biotite and muscovite; (4) *basalt* (magmatic rock from northern Bohemia), an anorthite-rich plagioclase; (5) *diabase*, a green varistic volcanic rock, rich in plagioclase with augite, hornblende and chlorite; (6) *calcite* (Nueva Leon/Mexico) as pure mineral (colorless and transparent fission rhombohedrons).

	phyllite	diabase	calcite	gneiss	granite	basalt
surface [1)]	3.3	1.9	0.2	0.5	0.6	4.6
density [2)]	1.24	1.42	1.49	1.33	1.31	1.60

1) specific surface [m^2/g];
2) density of the crushed rock [g/cm^3], particle size: 63-630 µm.

Tab. 1: Specific surface and density of the crushed rocks and minerals.

The sediments come from the different strata of the Königstein mine body and the northern downstream near field. They were deposited in the limestone time about 80 million years ago in the following sequence: cenomanian sandstone Y claystone Y lime marl Y turonian sandstone.

They are characterized by relatively high surface and porosity (Tab. 2). The clayey sediments are able to neutralize acid and to exchange cations.

	quartz [vol %]	surface [m^2/g]	porosity [vol %]	ANC [1] [meq/kg]	CAC [2] [meq/kg]
sandstone [3]	78 - 88	# 1	18 - 24	10 - 28	0.5 - 6
claystone	10 - 20	10 - 12	18 - 20	104 - 170	20
lime marl	70 - 72	10 - 13	6 - 7	2200-3800	60 - 90
lime marl, altered	44 - 65	7 - 9	20 - 24	300 - 650	18 - 2

1) acid neutralization capacity; 2) cation exchange capacity; 3) cenomanian and turonian sandstone.

Tab. 2: Sediment characterization.

Due to the pyrite oxidation and the dissolution of calcite and dolomite, the water of the Schema mine is rich in sulfate (2 g/L) and carbonate (1 g/L). Uranium and organic substances are present to 4-5 and 10-15 mg/L, respectively. The groundwater that inflows into the Königstein mine has a low mineral content. It is estimated that in the final stage of flooding the acidic leaching residues will be neutralized and diluted by a factor of 2.2. Uranium is assumed to be higher than at the Schema site (now 25 mg/L).

The adsorption experiments were carried out by equilibrating 1 g geomaterial with 5 mL aqueous phase containing the U(VI) and the DOC for 4-6 weeks under aerobic condition. The uranium concentrations ranged from $3.2 \cdot 10^{-6}$ to $3.2 \cdot 10^{5}$ mol/L (0.76-7.62 mg/L) and the DOC from 8.3 to 166 mg/L. After steady-state conditions were reached and the solid and liquid phases were carefully separated, the distribution ratios (R_s [mL/g], shown in brackets in the following text) were determined by measuring the added ^{234}U tracer (10-40 Bq/sample) in a liquid scintillation counter.

Uranium adsorption on ore mountains rocks and minerals (Fig. 1):

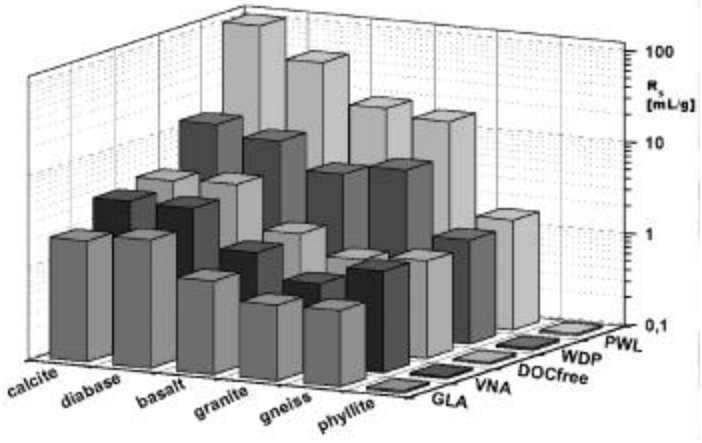

Fig. 1: Influence of wood degradation products on the U(VI) adsorption on metamorphic rocks and minerals.

The adsorption from a DOC-free synthetic mine water takes mainly place on *diabase* (4.8) and *calcite* (4.5); about 80% of the uranium is bound on these minerals. The adsorption under the influence of the wood degradation products (WDP) and pine wood lignin (PWL) increases to 90-95% (calcite: from 13 to 108; diabase: from 9.9 to 59 mL/g). Gluconic acid (GLA) as one of the monomeric cellulose breakdown compounds decreases the uranium adsorption to 15 and 10% for calcite (2.0) and diabase (2.4), respectively. Vanillic acid (VNA), the intermediate of the lignin destruction, reduces the adsorption only little (3.8 for both minerals). *Granite* and *basalt* adsorb from DOC-free mine water 50-60% of the uranium (0.97/1.6). In the presence of the wood leachate and lignin, the adsorption increases to about 80% (granite: 6.5/15.5; basalt: 5.9/18.5). The monomers diminish the adsorption (GLA: 0.64/0.66; VNA: 0.76/1.42). For *gneiss*, the influence of lignin and vanillic acid is insignificant (1.1-1.5); only gluconic acid strongly reduces the adsorption (0.2). The uranium adsorption on *phyllite* is the least. From all solutions, practically no uranium is bound (# 0.1), i.e., the uranium adsorption is smaller than 2%.

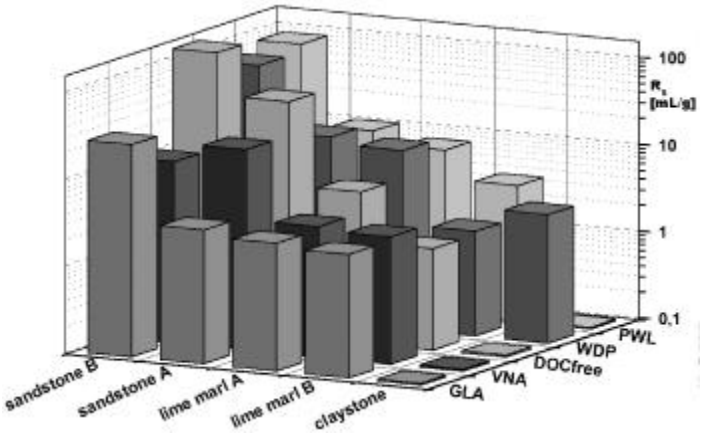

Fig. 2: Uranium adsorption on sandy and clayey sediments in the presence of wood degradation products.

Uranium adsorption on Königstein sediments (Fig. 2):

Uranium is preferentially bound to *sandstone* (91-97%); especially to the limonite-rich turonian sandstone /B/ with a high distribution ratio (142). Even under the influence of the organic compounds, the sorption ranges

from 68 to 93% (10-70). Sorption is decreased by the wood leachate and lignin (2-4%) as well as by vanillic and gluconic acid (10-20%). The level of adsorption on *lime marl* is much lower (22-68%, 1.4-11). In both cases the wood leachate and the lignin enhances the adsorption by 10-20% and the adsorption from vanillic and gluconic acid solution is nearly the same (35%, 2.5-3.0). The studied *claystone* did not bind any uranium. Only in the presence of the wood leachate about one third of the uranium is adsorbed (2.9). The reason may be that this sediment acidifies the aqueous phase (from pH 7.3 to 3.5) and some of the DOC precipitates with part of the uranium on the sediment.

The results show two general tendencies: (1) the highly polymeric wood breakdown substances increase the uranium(VI) adsorption and (2) the phenolic and saccharic monomers decrease the adsorption. The reasons may be that the colloidal polymers strengthen the adsorption by coagulating and precipitating on the geomaterials and the monomers stabilize uranium(VI) in the aqueous phase by complexation.

Acknowledgments
This study was supported by the Sächsisches Ministerium für Wissenschaft und Kunst under contract no. 4.7541.88-FZR/402.

References
/1/ Gatzweiler, R., Jakubick, A.T., Pelz, F.: WISMUT-Sanierung: Konzepte und Technologien. Geowissenschaften **14**, 448 (1996)
/2/ Baraniak, L., Schmidt, M., Bernhard, G., Nitsche, H.: Complex Formation of Hexavalent Uranium with Lignin Degradation Products. In: Report FZR-180, Institute of Radiochemistry, Annual Report 1996, p.28 (1997)
/3/ Schmidt, M., Baraniak, L., Bernhard, G., Nitsche, H.: Interaction of U(VI) with Wood Degradation Products: A Potentiometric Study. In: Report FZR-180, Institute of Radiochemistry, Annual Report 1996, p.30 (1997)
/4/ Jelen, K., Schiene, R., Fischer, K., Baraniak, L., Nitsche, H.: Investigation on the Hydrothermal Degradation of Wood in Flooded Mines. In: Report FZR-123, Institute of Radiochemistry, Annual Report 1995, p.69 (1996)

ASSESSMENT AND MODIFICATION TO THE UNSATCHEM-2D SOFTWARE FOR REACTIVE TRANSPORT MODELING IN UNSATURATED ZONES

V. Brendler, S. Krahl
Forschungszentrum Rossendorf e.V., Institute of Radiochemistry

The UNSATCHEM-2D Software Code /1/ was assessed for its suitability to reactive transport modeling in rock piles originating from the former uranium mining in Saxony and Thuringia. There, unsaturated zones dominate, which exclude the application of most of the available coupled transport codes. Advantages and disadvantages of the software were determined, suggestions for code modification were made to achieve a more reliable and stable computation and to extend the code´s application toward chemical systems typical for uranium mining.

Methodology
We analyzed the soil-chemistry based UNSATCHEM-2D program to evaluate its applicability for former uranium mining and milling sites. The code uses the method of finite elements to solve the differential transport equations for water, gas, dissolved components and heat. For each node, the chemistry is computed by solving a specific system of mass balance equations. There, the program does not utilize a rigorous non-linear minimization algorithm but relies on a stepwise heuristic approach. It is based on various approximations. The most relevant of them had to be identified. Then, the code was prepared to accommodate the planned extension of the chemical system. This included re-arrangements of the code to remove obsolete parts, simplify some routines and separate each function into its own subroutine, together with a thorough commentary as internal documentation. This allows for the identification of all the code lines that would be affected by any changes in the chemical system. Then the introduction of new components with their related species and formation reaction followed. Finally the internal code integrity and the correctness of the modeling was confirmed.

Results
A detailed report /2/ about the analysis and assessment of the UNSATCHEM-2D code was generated. It serves as a documentation as well as a manual for further additions of chemical

components or reaction species. Fig. 1 shows the relationships between the various subroutines contributing to the chemical speciation part. They were analyzed in detail and subsequently modified, if necessary. Comments were inserted to indicate all parts of the code that require modification when adding new components or species (aqueous and solids). Also, the input organization was unified and streamlined, switching from milliequivalents to molarity as default concentration unit.

Uranium was introduced into the chemical system as a new component together with the species UO_2OH^+, $UO_2(OH)_{2(aq)}$, $UO_2(CO_3)_2^{2-}$ and $UO_2(CO_3)_3^{4-}$ as aqueous complexes that are important in uranium mining rock piles. To keep these first extensions manageable with regard to code verification, only a subset of all possible species in the $UO_2^{2+}/OH^-/CO_3^{2-}$ system was selected, also ignoring solid phases like schoepite and rutherfordine.

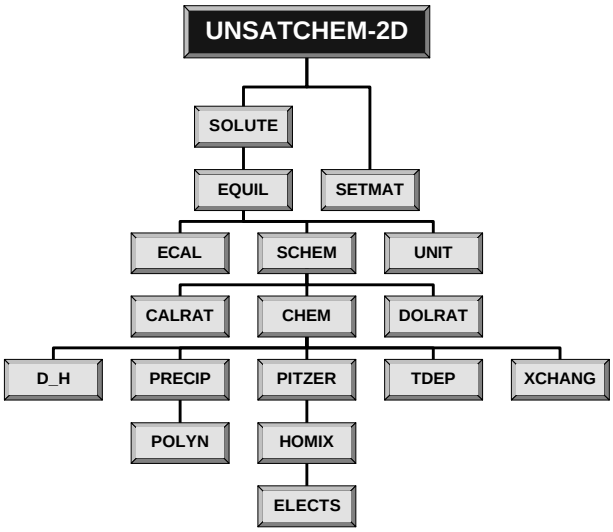

Fig. 1: Subroutines and their internal relationships in the chemical speciation part of UNSATCHEM-2D.

To check whether the code modifications introduced errors, all mass balances were re-calculated using the output from a first computation of UNSATCHEM-2D. This did not show any significant deviations. Then UNSATCHEM-2D and EQ3/6 /3/ were run with chemically identical input files (derived from the composition of seepage waters from uranium mining rock piles), which allowed for a direct comparison of the results from both programs. Despite of the many approximations used in UNSATCHEM-2D and its peculiar solving algorithm, the results for all major complexes did not differ by more than 14%, which can be regarded as satisfactory.

Part of the assessment was a screening of many other reactive transport and chemical speciation codes. A comprehensive data base (in MS Access 2.0) was generated, storing information about 31 software packages so far. It contains also a short description and a listing of the relevant publications for each code.

Discussion and Conclusions

The UNSATCHEM-2D code is one of the very few programs capable of modeling transport and speciation in unsaturated zones, conditions which are most likely being encountered in uranium mining rock piles. The code is robust and very fast, freely accessible and fully documented. Also its comprehensive handling of carbon dioxide transport must be mentioned. Its solving algorithm is rather empirically, relying on several approximations in the chemical speciation code. This makes the routines for computing the chemical equilibrium state fast but difficult to maintain. As a result of this work, reliability, transparency, and documentation of the code was improved. All code segments related to a proposed extension of the chemical system were identified and appropriately labeled.

Further additional changes of the chemical system are now straightforward and their implementation will certainly require less effort than writing a completely new module for the chemical speciation part or adapting chemical speciation codes to the transport modules of UNSATCHEM-2D or other transport modeling software.

A first set of new species was added and the resulting speciation was successfully verified. Further modifications should include a more generic formulation of the chemical speciation part, moving from implicit reaction coding to matrix calculations, especially for the precipitation reactions. Also steps should be taken to include redox reactions and surface complexation.

References

/1/ Simunek, J., Suarez, D.L.: *UNSATCHEM-2D Code for simulating two-dimensional variably saturated water flow, heat transport, carbon dioxide production and transport, and multicomponent solute transport with major ion equilibrium and kinetic chemistry, version 1.1 manual.* Res. Report 128, U.S. Dept. Agriculture, Riverside, 1993

/2/ Krahl, S., Brendler, V.: *Analyse und Bewertung von Software zur Modellierung des reaktiven Transports.* Project report (in German), FZR, Institute of Radiochemistry, Dec. 1997
/3/ Wolery, T.J.: *EQ3/6, A software package for the geochemical modeling of aqueous systems.* Report UCRL-MA-110662 Part I, Lawrence Livermore National Laboratory, Livermore, 1992

DEVELOPMENT OF A META DATA BASE FOR RADIOLOGICAL INFORMATION FROM THE FSU COUNTRIES

V. Brendler, J. van´t Kloosters [1], E.G. Nikonov [2]
Forschungszentrum Rossendorf e.V., Institute of Radiochemistry
[1] Joint Research Centre Ispra (Italy), Environmental Institute
[2] Joint Institute for Nuclear Research Dubna (Russia), Laboratory of Computing Technique and Automation

To better utilize the vast amount of primary radiological data and also the scientific expertise from the countries of the former soviet union (FSU), an EC project was launched to collect such information in a meta data base. This data base will be accessed over the World Wide Web. Its internal structure (tables, relationships, contents and key words) was defined and an input interface to fill the data base developed.

Methodology

The data base discussed here is a meta data base, i.e. it stores information about information. It will not contain the primary radiological data collected in data bases, but rather the information necessary to find such data bases, and to get access to them. This includes bibliographic and organizational information, data history, internal storage formats, documentation, access-ability, or price policy. All the information about one data base is equal to a single entry into the meta data base, which is realized under MS Access 95 /1/, a relational data base management system (RDBMS). This means all information is grouped into smaller tables to avoid redundant storage of information. These tables are connected through relationships. Information will be collected about four areas:

1. Dynamics of deposited radionuclides in the environment, and radioactive waste management;
2. Counter measures for the mitigation of consequences of nuclear accidents and other nuclear contaminations;
3. Health effects arising from exposure in contaminated territories;
4. Techniques for emergency management.

Each area is indexed by its own set of keywords, accompanied by a fifth category of more general keywords. These keywords can be used in queries by external users over the Internet. After defining the data base set-up, a user interface had to be designed to allow data input into the meta data base. The input itself is done by three separate teams from Russia, Belarus and Ukraine. They need an uniform and easy-to-handle input interface, already aimed on data integrity and consistency.

Results

The resulting structure of the meta data base, with all tables, their definition of fields and mutual relations is shown in Fig. 1, and called an Entity-Relationship-Diagram. It follows a short description of the content of the most important tables. The *Main* table contains all the information (such as name, scope, size, quality criteria) to uniquely identify a data base entry. It contains references to most other tables, like *Organization*, *Person* and *Country*, which specify the contact for potential users. *Price* gives information about the charging policy of a data base. *Keyword* delivers all terms for indexing. *Manual* describes how a data base is documented, whereas *Publication* informs about external papers concerning the data base or its application. *TransferProtocol* lists various access ways to the data base. *Medium* informs about the distribution media of a data base or its documentation. If there are multiple references between two tables, called an N:M relationship, auxiliary tables are introduced. An example is the relation between *Main* and *Keyword*: a data base can have many keywords, and simultaneously a keyword can be used in many data bases. Therefore the extra table *IndexTerm* is created to store each such relation between a data base and a keyword. The design shown here can cover both numerical and descriptive data bases, also collections of software or publications/reviews. On the other way the meta data base itself is kept as simple as possible to allow

for later adaptions and improvements without too much effort.

The input interface for the meta data base has the following features:

- One can choose between the input of new data or the update of existing data;
- Access is restricted to qualified users (authentification at login);
- Logging information is generated to track down any data additions or changes;
- The set of input masks can only be worked through in a fixed order;
- Internal check for data validity and integrity (range, type etc.) is integrated;
- Besides pre-defined keywords own (new) keywords can be created;
- The input masks are a one-to-one representation of the printed questionnaire;
- Extensive documentation (both inside the data base and as separate papers) are available and supplemented by a tutorial.

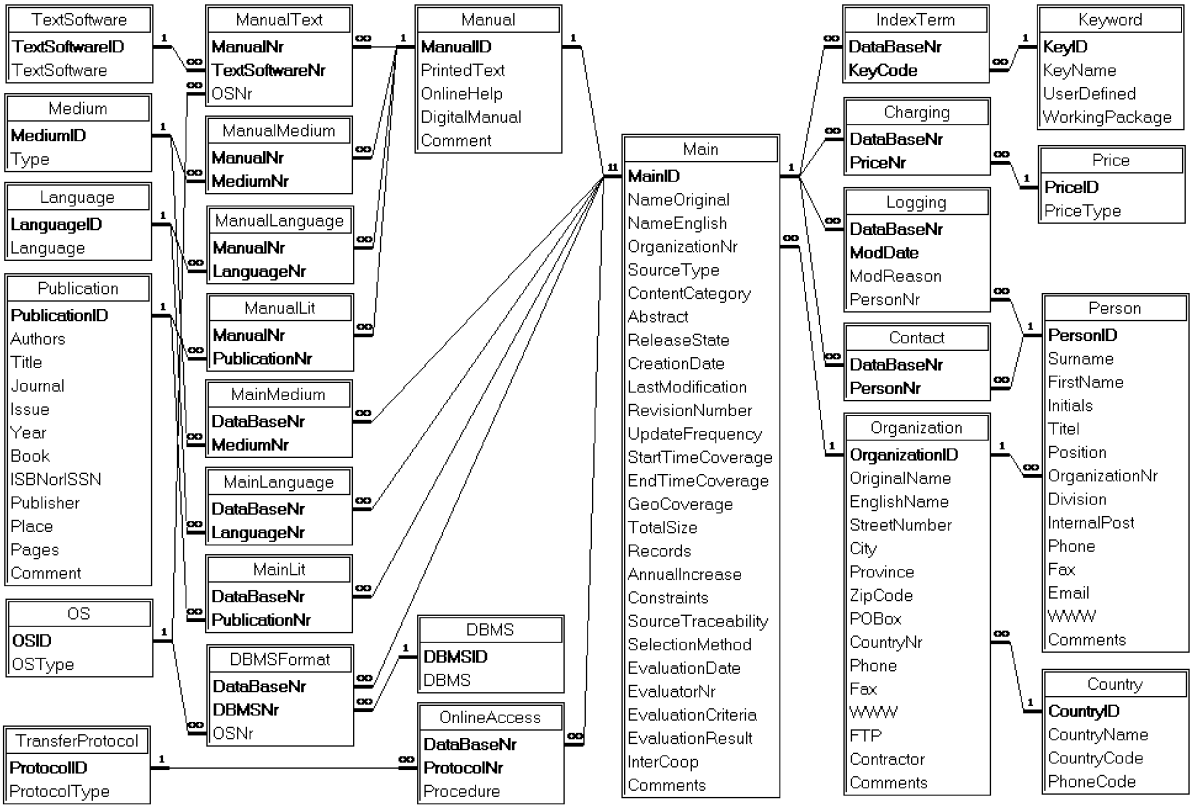

Fig. 1: Entity-relationship diagram for the radiological meta data base.

Discussion and Conclusions

The developed software allows for a distributed data collection, it is user-friendly and aids a correct data input. The data sets will later be transferred to an Oracle data base, hosted in parallel by servers at the FZ Rossendorf and ISPRA. This transfer also includes the merging of the data set collections from each of the three FSU partners into one and the checking for duplicates and inconsistencies. Based on the Oracle version, an Internet gateway is now designed, which allows world-wide access to the content of the meta data base with web browsers, using the Java technology.

The establishing of such a meta data base of radiological information will certainly help to extend scientific collaboration with FSU institutions, to distribute their data bases and use their experience.

References

/1/ *MS Access 2.0 Manual.* Microsoft Corporation, 1994

STUDIES OF THE COMPLEX FORMATION BETWEEN URANYL AND ARSENATE BY TIME-RESOLVED LASER-INDUCED FLUORESCENCE SPECTROSCOPY (TRLFS)

M. Rutsch, G. Geipel, V. Brendler, G. Bernhard, H. Nitsche
Forschungzentrum Rossendorf e.V., Institute of Radiochemistry

The complex formation between uranyl and arsenate ions was studied in 0.1 M $NaClO_4$ solution over a pH-range from 1.5 to 5 using Time-Resolved Laser-Induced Fluorescence Spectroscopy (TRLFS). Three different uranyl arsenate complexes were found. The complex formation constants, the fluorescence lifetimes and the fluorescence emission bands were determined.

Experimental and Results

The TRLFS spectra were measured at an excitation wavelength of 266 nm. The equipment for TRLFS is detailed described in /1/. The arsenic acid concentration was varied from $5*10^{-5}$ M to $5*10^{-3}$ M at a constant uranyl concentration of $5*10^{-6}$ M.

Fig. 1 shows the uranyl fluorescence spectra as a function of the arsenic acid concentration at pH 2.5. Between pH 1.5 and 3, the fluorescence intensity of uranyl increases with increasing arsenic acid concentration and the maxima of the fluorescence emission bands are shifted to higher wavelength.

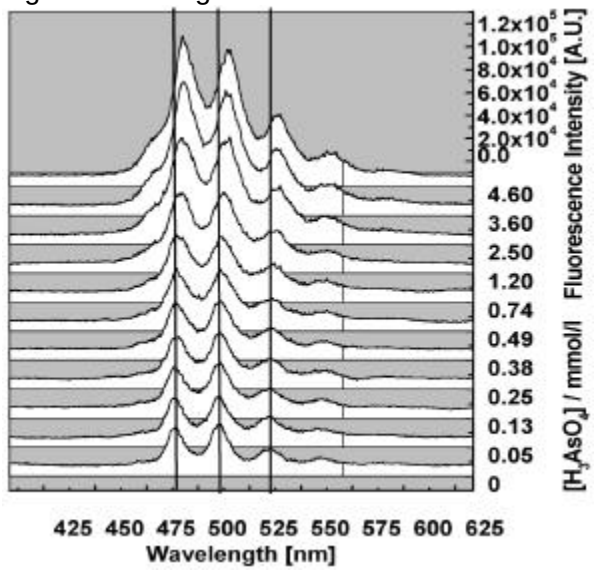

Fig. 1: TRLFS spectra as a function of arsenic acid concentration at pH 2.5.

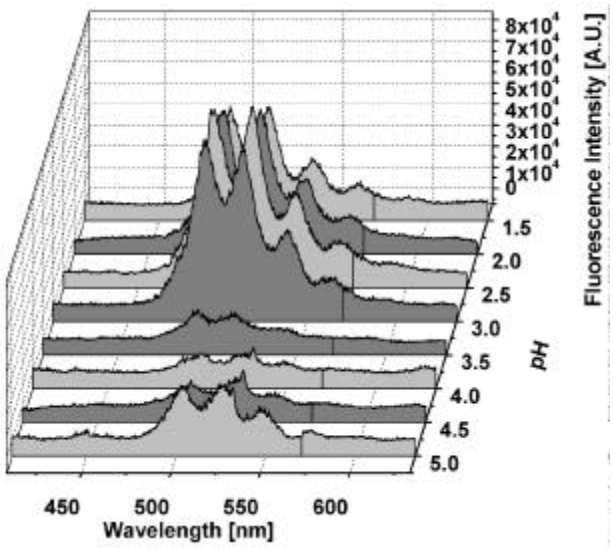

Fig. 2: TRLFS spectra as a function of pH. $[H_3AsO_4]$ = $1.20*10^{-3}$ mol/L

Above pH 3.0 the fluorescence intensity decreases drastically (Fig. 2) and shows no systematic dependence on the arsenic acid concentration. The maxima of fluorescence emissions bands, however, continue to shift to higher wavelength with increasing arsenic acid concentration and pH.

Presently, no data on the complexation behavior of uranyl with arsenate are available in the literature. Assuming that arsenate complexation is a similar to the phosphate complexation, three main uranyl arsenate solution species are possible in the investigated pH range /2/:

$$UO_2^{2+} + 2\ H^+ + AsO_4^{3-} \quad \text{W} \quad UO_2H_2AsO_4^+ \qquad (1)$$

$$UO_2^{2+} + H^+ + AsO_4^{3-} \quad \text{W} \quad UO_2(HAsO_4)(aq) \qquad (2)$$

$$UO_2^{2+} + 4\ H^+ + 2\ AsO_4^{3-} \quad \text{W} \quad UO_2(H_2AsO_4)_2\ (aq) \qquad (3)$$

Furthermore, we assumed that the species distribution in the uranyl arsenate system is similar to the uranyl phosphate system, because the arsenic acid protonation constants are similar to phosphoric acid /3/.

The spectra at pH 1.5, 2.5 and 4.0 were analysed with the programm POLYLIFE /1/, giving the lifetime and the fluorescence yields for each wavelength of the assumed three uranyl arsenate complexes and for free uranyl ion. The lifetime for the free uranyl ion was determined to be 1.70

± 0.50 µs. This value is typical for free uranyl ion in aqueous solution /1/. The fluorescence lifetimes and fluorescence emissions bands of the uranyl arsenate solution species are shown in Tab. 1.

species	lifetime J (I=0.1) [µs]	fluorescence emission band [nm]
$UO_2H_2AsO_4^+$	12.25 ± 1.20	478, 494, 514, 539, 563
$UO_2(HAsO_4)(aq)$	0.1<J<1	504, 525, 547
$UO_2(H_2AsO_4)_2$ (aq)	38.30 ± 3.50	481, 497, 518, 541, 571

Tab. 1: Fluorescence lifetimes and fluorescence emissions bands of uranyl arsenate solution species

The yields of the involved species at different arsenic acid concentration were determined from the deconvoluted spectra between 470 nm and 570 nm by the method described in /1/.
The complex formation constants were calculated according to the above listed reaction equations. The stoichiometry between uranyl and arsenate was confirmed by slope analysis of the linear regression of a plot of uranyl arsenate complex concentration divided by free uranyl concentration versus free arsenate concentration. The different quantity of protons of the uranyl arsenate complexes were taken in this consideration. The following slopes were determined: for the UO_2HAsO_4 (aq) complex 0.95 ± 0.11, for the $UO_2H_2AsO_4^+$ complex 0.96 ± 0.04 and for the $UO_2(H_2AsO_4)_2$ (aq) complex 2.12 ± 0.09. The determined constants were extrapolated to infinite dilution using the Davies-Equation /3/.

Species	log ß $_{I=0.1}$	log ß $_{I=0}$
$UO_2H_2AsO_4^+$	20.39 ± 0.24 (2F)	21.96 ± 0.24 (2F)
$UO_2(HAsO_4)$ (aq)	17.19 ± 0.31 (2F)	18.76 ± 0.31 (2F)
$UO_2(H_2AsO_4)_2$ (aq)	38.61 ± 0.20 (2F)	41.53 ± 0.20 (2F)

Tab. 2: Complex formation constants between uranyl and arsenate ions

The results are shown in Tab. 2. The complex formation constants of the uranyl arsenate species are smaller than the complex formation constants of the analogous uranyl phosphate species /2/. Fig. 3 shows the uranyl species distribution in the arsenate system using the determined complex formation constants. This calculation confirms the assumption that uranyl ions form similar complexes with arsenate and phosphate ions.
The rapid decrease of fluorescence intensity at pH above 3.0 is due to a strong increase of the concentration of the UO_2HAsO_4 (aq) complex and can be explained that this complex interacts stronger with the water molecules. According to the species distribution in Fig. 3, the concentration of the $UO_2(H_2AsO4)_2$ (aq) complex is smaller than 1 %. In spite of this low concentration, a quantitative determination of the complex $UO_2(H_2AsO4)_2$ (aq) was possible due to the strong fluorescence intensity of this complex.

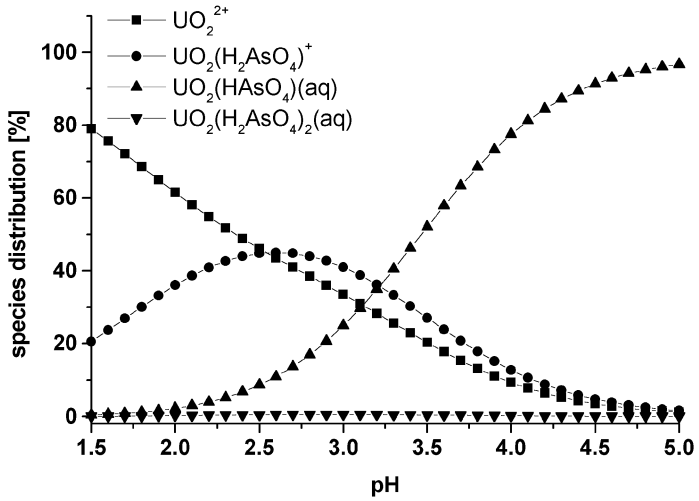

Fig. 3: Species distribution of $5*10^{-6}$ M uranyl in $1.25*10^{-3}$ M arsenic acid as a function of pH

Acknowledgment
The authors would like to thank Dr. W. Wiesner and U. Schäfer, Department of Analytics, Forschungszentrum Rossendorf e.V. for the ICP-MS and AAS measurements.

References

/1/ Brachmann, A.: *Zeitaufgelöste laserinduzierte Fluoreszenzspektroskopie zur Charakterisierung der Wechselwirkung des Uranylions mit Huminsäuren und Carboxylatliganden*. Dissertation, TU Dresden (1997)
/2/ Brendler, V., Geipel, G., Bernhard, G., Nitsche, H.: Complexation in the system $UO_2^{2+}/PO_4^{3-}/OH^-$ (aq): Potentiometric and Spectroscopic Investigations at very low Ionic Strength. Radiochim. Acta **74**, 75-80 (1996)
/3/ Grenthe, I., Fuger, J., Konings, R.J.M., Lemire, R.J., Muller, A.B., Nguyuen-Trung Cregu, Ch., Wanner, H.: *Chemical Thermodynamics of Uranium*, NEA OECD, 1992, p. 683

SYNTHESIS AND CHARACTERIZATION OF CALCIUM URANYL CARBONATE: $Ca_2[UO_2(CO_3)_3] \cdot 10H_2O$ (LIEBIGITE)

S. Amayri, G. Geipel, W. Matz [1], G. Schuster, L. Baraniak, G. Bernhard, H. Nitsche
Forschungszentrum Rossendorf e.V., Institute of Radiochemistry
[1] Institute of Ion Beam Physics and Material Research

A preparation procedure for calcium uranyl carbonate is described according to Meyrowitz /1/. ICP-MS analysis, fine-structure analysis, thermal degradation, and laser-fluorescence analysis were used to identify the substance and to determine its purity.

Liebigite is a secondary mineral of uranium. The solubility is not yet systematically described. The aim of this study was to develop a procedure for the preparation of calcium uranyl carbonate with the composition $Ca_2[UO_2(CO_3)_3] \cdot 10H_2O$ and to characterize the final product for its composition and purity. Such well characterized material can be used as model substance for solubility and speciation investigations studying the environmental behavior of uranium in laboratory experiments.

Preparation of $Ca_2[UO_2(CO_3)_3] \cdot 10H_2O$

The preparation was carried out as proposed by Meyrowitz /1/. The compound was prepared in 0.1 mmol batches by slowly adding aqueous sodium carbonate solution (0.03 mol/L) in a tenfold excess to uranyl nitrate solution (0.01 mol/L) followed with a stoichiometric admixing of calcium nitrate (0.02 mol/L). After the pH was adjusted to 8 by sodium carbonate solution, the final product precipitated in the form of fine greenish-yellow crystals. The precipitate was filtered, three times washed with deionized water, air dried for 24 h. The yield was about 60%.

Characterization

Chemical analysis by ICP-MS and AAS

The U content was determined using an inductively coupled plasma (Ar-plasma) mass spectrometer (Elan-5000, Perkin Elmer, Überlingen, Germany) and Ca content was determined using a flame-atomic absorption spectrometer (AAS 4100, Perkin Elmer, Überlingen, Germany). Calcium uranyl carbonate with the composition $Ca_2[UO_2(CO_3)_3] \cdot 10H_2O$ contains 33.51% uranium, 11.28% calcium, 5.07% carbon and 2.84% crystal water and has a uranium to calcium ratio of 0.5. ICP-MS analysis showed that the synthesized samples contain 33.46 ± 0.95% U and 11.27 ± 0.72% Ca, i.e., exact the theoretical stoichiometry.

X-ray analysis

XRD measurements were carried out using the diffractometer URD-6 (Freiberger Präzisionsmechanik) in Bragg-Brentano geometry with Cu-K$_\alpha$ radiation (0,1542 nm). The diffractograms

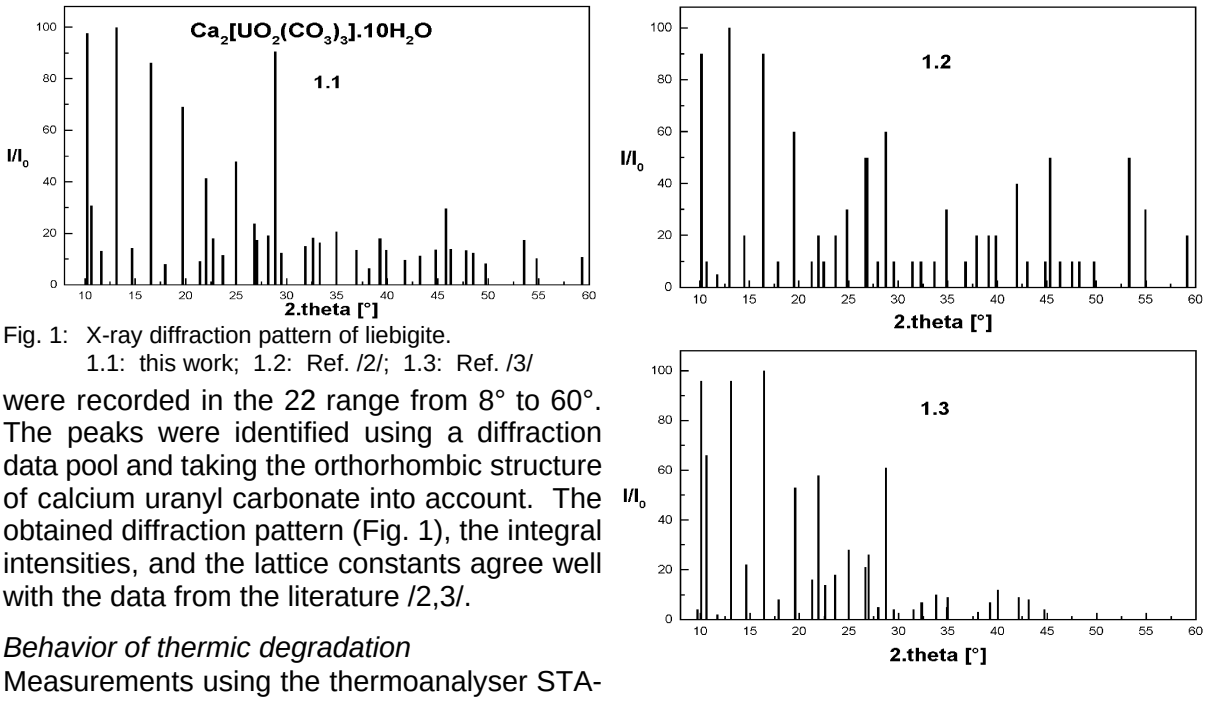

Fig. 1: X-ray diffraction pattern of liebigite.
1.1: this work; 1.2: Ref. /2/; 1.3: Ref. /3/

were recorded in the 22 range from 8° to 60°. The peaks were identified using a diffraction data pool and taking the orthorhombic structure of calcium uranyl carbonate into account. The obtained diffraction pattern (Fig. 1), the integral intensities, and the lattice constants agree well with the data from the literature /2,3/.

Behavior of thermic degradation

Measurements using the thermoanalyser STA-92 (Setaram, France) were carried out in the range 20 - 800 °C with a heating rate of 10 °C/min under oxygen.

$Ca_2[UO_2(CO_3)_3]$ @ $10H_2O$	a [nm]	b [nm]	c [nm]	V [nm^3]
Liebigite	1.668 ± 0.002	1.750 ± 0.004	1.369 ± 0.003	3.998 ± 0.01
Ref. /2/	1.670	1.751	1.374	4.019
Ref. /3/	1.670	1.756	1.370	4.016

Tab. 1: Lattice constants of the prepared liebigite compared with Refs. /2,3/

The thermographimetric (TG) and differential-thermoanalytical (DTA) diagram (Fig. 2) can be explained by the following processes: (1) the endothermal release of structural water from 103.2 - 301.3 °C (first sharp peak of the DTA curve) and (2) the endothermal release of carbon dioxide from 301.3 - 800.3 °C (second sharp and third peak). The decomposition occurs according to: $Ca_2[UO_2(CO_3)_3]@10H_2O \div Ca_2UO_5 + 3CO_2 + 10H_2O$.

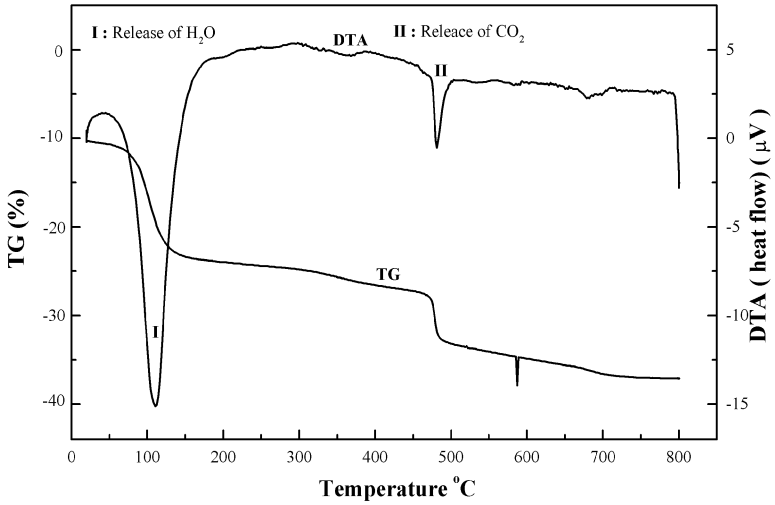

Fig. 2: Thermal gravimetry (TG) and differential thermoanalysis (DTA) of the synthesized liebigite (10 °C/min, oxygen).

The release of crystal water starts already at very low temperature, reaches its maximum at 103.3 °C, and is completed at 301.3 °C. The carbon dioxide release occurs in three steps in the temperature ranges: (1) 301.3 - 430.5 °C, (2) 430.5 - 650.6 °C (main reaction) and (3) 650.6 - 800 °C. The formation of Ca_2UO_5 begins above 900 °C. The structural water was found to be 2.75 ± 0.01% corresponding to a formula index of 9.76 ± 0.05 and the carbon dioxide amounts to 4.97 ± 0.24% equivalent to the index 2.94 ± 0.14.

Time-resolved laser-induced fluorescence spectroscopic measurements

This method was applied to compare the prepared liebigite with the pure mineral. The characteristic fluorescence was induced by exciting the sample with a 266 nm laser beam (Nd-YAG-laser system: Spectra Physics, Mountain View, CA, USA). The fluorescence signals were recorded in the range 450 - 600 nm with delay times from 0.1 µs to 156 µs after the excitation with each laser pulse. The main fluorescence lines found for the synthetic and natural liebigite are the same (Tab. 2). From the chemical composition, the determined fine structure, the oxidative thermal degradation and the fluorescence spectrum, we conclude that the calcium uranyl carbonate prepared according to our procedure has the same composition and purity as the mineral liebigite. This synthetic liebigite will be used for solubility experiments.

Sample (solid)	Main emission maxima [nm]					Lifetime [µs]
	I	II	III	IV	V	
Liebigite (synthesized)	465.4	482.9	502.7	524.5	547.8	146 ± 5
Liebigite, nat. Ref. /4/	465.7	482.4	502.8	523.7	545.8	270 ± 30

Tab. 2: Fluorescence signals of solid calcium uranyl.

Acknowledgment

The authors thank Dr W. Wiesner and Ms. U. Schäfer for the ICP-MS and AAS measurements and Ms. A. Scholz for the X-ray diffraction measurements.

References

/1/ Meyrowiz, R., Ross, D.R., Weeks, A.D.: Synthese of Liebigite. Survey Prof. Paper **475-B**, B 162-163 (1963)

/2/ *Powder Diffraction File.* International Center of Diffraction Data, New town Square, Pennsylvania, USA , Diffraction Data Card No. 70 (1991)

/3/ Mereiter, K.: The Crystal Structure of Liebigite $Ca_2UO_2(CO_3)_3.\sim 11H_2O$. Tschermaks Min. Petr. Mitt. **30**, 227 (1982)

/4/ Bernhard, G., Geipel, G., Brendler, V., Nitsche, H.: Speciation of Uranium in Seepage Waters of a Mine Tailing Pile Studied by Time-Resolved Laser-Induced Fluorescence Spectroscopy (TRLFS). Radiochim. Acta **74**, 87 (1996)

VALIDATION OF COMPLEX FORMATION OF Ca^{2+} , UO_2^{2+} AND CO_3^{2-}

G. Bernhard, G. Geipel, V. Brendler, T. Reich, H. Nitsche
Forschungszentrum Rossendorf e.V., Institute of Radiochemistry

The complex formation constant of $Ca_2UO_2(CO_3)_3 aq.$ was determined as log β_{213} = 25.7 ± 0.7. Slope analysis of the log([$Ca_bUO_2(CO_3)_3^{(4-2b)-}{}_{(aq.)}$]/[$UO_2(CO_3)_3^{4-}$]) versus log ([$Ca^{2+}$]) gave a value of 1.80 ± 0.20, confirming the stoichiometry. Furthermore, we measured the absorption spectra of this complex in comparison to the free uranyl carbonate complex by LIPAS and UV-vis spectroscopy. We also investigated the formation of the dissolved calcium uranyl carbonate complex as a first step toward the formation of the secondary mineral liebigite.

Experimental and Discussion

In an earlier study of mining related waters we have found a uranium species containing Ca^{2+}, UO_2^{2+} and CO_3^{2-} /1/. This calcium uranyl carbonate species was not listed in the NEA data base /2/. Therefore the goal of this study was the validation of the complex formation and the brutto stability constant of this $Ca_2UO_2(CO_3)_3 aq.$ - complex by TRLFS. To validate the stoichiometry and formation constant, we measured different series of synthetic solutions containing Ca^{2+}, UO_2^{2+} and CO_3^{2-} by Time -Resolved Laser-Induced Fluorescence Spectroscopy.

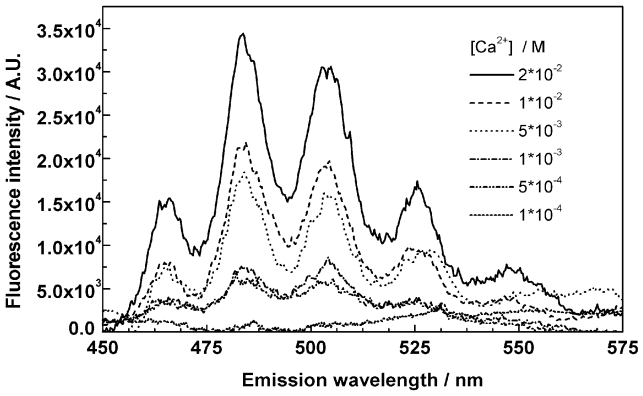

Fig.1.: Fluorescence spectra of $Ca_2UO_2(CO_3)_3(aq.)$. Fluorescence intensity as function of Ca^{2+} -concentration (2 x10^{-5} M UO_2^{2+}, 8x10^{-3} M HCO_3^-/CO_3^{2-}, pH 8.0)

The setup for TRLFS experiments is given in /3/ and for LIPAS in /4/, respectively.
Fig. 1 depicts a set of time-resolved fluorescence spectra with $2 \cdot 10^{-5}$ M UO_2^{2+}, $8 \cdot 10^{-3}$ M HCO_3^-/CO_3^{2-} at pH 8.0 at different calcium concentration, varying from $1 \cdot 10^{-4}$ to $5 \cdot 10^{-3}$ M. The interaction of $UO_2(CO_3)_3^{4-}$ with Ca^{2+} was clearly detectable by increasing of the fluorescence intensity with the calcium content. The free uranyl carbonate complex does not show any uranium fluorescence. The integrated fluorescence signal from 450 nm to 570 nm is proportional to different calcium concentrations.

The ratio of Ca-complexed/Ca-uncomplexed uranium (R) is calculated by

$$R = \frac{[Ca_bUO_2(CO_3)_3]}{[U_{(total)}] - [Ca_bUO_2(CO_3)_3]} \qquad (1)$$

considering that no other uranyl species is present in the solution.
Furthermore the calcium concentration is calculated considering that the equilibrium between Ca^{2+} and CO_3^{2-} to form of calcite and/or aragonite in the solution is well established. This means that the concentration of free Ca^{2+} ions in the solutions is smaller that the total calcium concentration.
The equilibrium constant of the investigated complex is based on the reaction:

$$b\ Ca^{2+} + UO_2(CO_3)_3^{4-} \leftrightarrow Ca_bUO_2(CO_3)_3^{(4-2b)-}{}_{(aq.)} \qquad (2)$$

The following equations are used for the validation of the calcium uranylcarbonate complex:

$$Ca^{2+} + CO_3^{2-} \leftrightarrow CaCO_3{}_{(aq.)} \qquad (3) \qquad\qquad b\ Ca^{2+} + UO_2(CO_3)_3^{4-} \leftrightarrow Ca_bUO_2(CO_3)_3^{(4-2b)-}{}_{(aq.)} \qquad (4)$$

$$K_1 = \frac{[Ca_bUO_2(CO_3)_3^{(2x-4)}{}_{(aq.)}]}{[Ca^{2+}]^b \times [UO_2(CO_3)_3^{4-}]} \qquad (5)$$

The equation (6) must be also fulfilled:

$$[UO_2(CO_3)_3^{4-}] + [Ca_bUO_2(CO_3)_3^{(4-2b)-}{}_{(aq.)}] = [U_{(total)}] \qquad (6)$$

The linear equation can be derived by rearranging equations (5) and (6).

$$\log \frac{[Ca_bUO_2(CO_3)_3^{(4-2b)-}{}_{(aq.)}]}{[U_{(total)}] - [Ca_bUO_2(CO_3)_3^{(4-2b)-}{}_{(aq.)}]} = \log(R) = b \times \log[Ca^{2+}] + \log K \qquad (7)$$

The stability constant of reaction (1) was calculated with equation (7) using linear regression

(Fig.2). The resulting slope of 1.80 ± 0.20 shows a predominant 2 : 1 complex formation between calcium and uranylcarbonate. The stability constant at I = 0.1 M is found to log K (0.1M) = 6.8 ± 0.7. At infinite solution, we calculate a value of 4.1 using the Davies-Equation. Using the NEA data base /4/ constant of log $ = 21.6 ± 0.05 for the reaction

$$UO_2^{2+} + 3\,CO_3^{2-} \circ UO_2(CO_3)_3^{4-} \qquad (8)$$

we calculate a overall constant at infinite dilution for the reaction

$$UO_2^{2+} + 3\,CO_3^{2-} + 2\,Ca^{2+} \circ Ca_2UO_2(CO_3)_3\,(aq.) \qquad (9)$$

of log $\$_{213}$ = 25.7 ± 0.7.

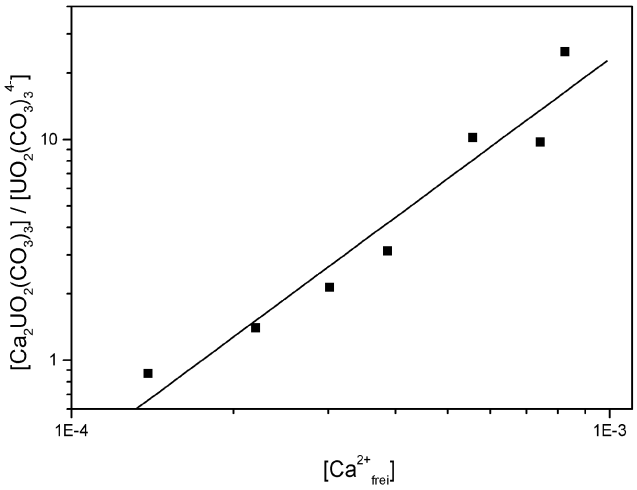

Fig.2.: Validation of the complex formation reaction. (5x10^{-5} M UO_2^{2+} ; pH 8)

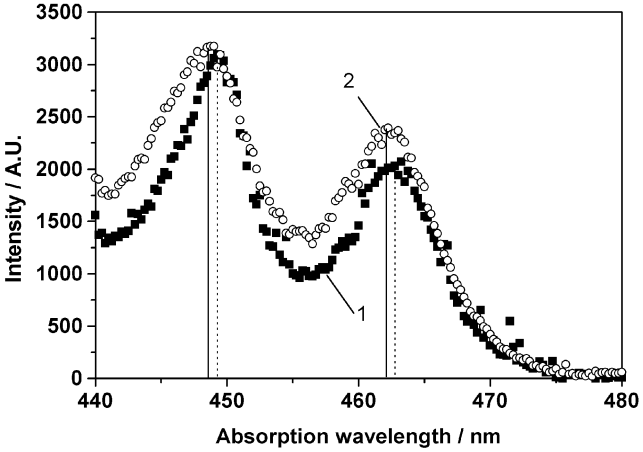

Fig.3.: LIPAS- spectra
1 free uranyl carbonate complex (*5x10^{-4} M UO_2^{2+}, 2x10^{-2} M CO_3^{2-}/HCO_3^-, pH: 8.0)*
2 calcium uranyl carbonate complex *(2x10^{-3} M Ca^{2+}, 5x10^{-4} M UO_2^{2+} , 2x10^{-2} M CO_3^{2-}/HCO_3^-, pH: 8.0)*

This value differs from the earlier given constant /1/. We are now taking into account the formation of undissociated $CaCO_3$. By this way the straight line in Fig. 2 is shifted to lower calcium concentrations causing a higher intersection, which is synonymous with a stronger formation constant.

The absorption spectra were recorded by a Carry 5 G spectrometer (Varian, Canberra, Australia). The uranium concentrations of both calcium uranyl carbonate complex and in uranyl carbonate complex were 0.005 M. The wavelength sensitivity is 0.04 nm. The detection limit for the uranyl carbonate complex is about 5•10^{-4} M. The spectra were recorded with a step width of 0.1 nm. Fig. 3 shows the LIPAS spectra of free uranyl carbonate complex and the calcium uranyl carbonate complex. The interaction of Ca^{2+} with the free uranyl carbonate complex is detectable by a slight red shift of about 0.35 nm in the spectra (Ca^{2+} from 0 to 1•10^{-2}M) which can be detected especially at the two absorption bands in the longer wavelength region (462 nm and 448 nm). The differences between the spectra are 0.36 nm in the region 462 nm and 0.33 nm in the region 448 nm respectively. The sum of the calculated errors are 0.057 nm and 0.081 nm respectively, and thus the wavelength shift lies outside the measuring errors. This is an additional indicate for the existence of the $Ca_2UO_2(CO_3)_3$(aq.) -species.

References

/1/ Bernhard, G., Geipel, G., Brendler, V., Nitsche, H.: Speciation of Uranium in Seepage Waters of a Mine Tailing Pile Studied by Time-Resolved Laser-Induced Fluorescence Spectroscopy (TRLFS). Radiochim. Acta **74**, 87 (1996).

/2/ Grenthe, I., Fuger, J., Lemire, R.J., Muller, A.B., Nguyen-Trung, C., Wanner, H.: *Chemical Thermodynamics of Uranium.* 1st ed. , Elsevier Science Publishers, Amsterdam, 1992.

/3/ Geipel, G., Brachmann, A., Brendler, V., Bernhard, G., Nitsche, H.: Uranium(VI) Sulfate Complexation Studied by Time-Resolved Laser-Induced Fluorescence Spectroscopy (TRLFS). Radiochim. Acta **75**, 199 (1996).

/4/ Geipel, G., Bernhard, G., Brendler, V., Nitsche, H.: Complex Formation between UO_2^{2+} and CO_3^{2-} Studied by Laser-Induced Photoacoustic Spectroscopy. Radiochim. Acta, accepted

URANIUM SPECIATION IN WATERS OF DIFFERENT URANIUM MINING AREAS

G. Bernhard, G. Geipel, V. Brendler, H. Nitsche
Forschungszentrum Rossendorf e.V., Institute of Radiochemistry

The uranium speciation in four uranium mining-related waters from Saxony/Germany was experimentally determined by laser spectroscopy. Depending on the chemical constituents of the individual water, the following three different solution complexes characterize the uranium speciation in the investigated waters: (1) in carbonate- and calcium-containing mine and seepage water from Schlema at pH 7.8 and 7.1, respectively, $Ca_2UO_2(CO_3)_3$ (aq.); (2) in carbonate-containing and calcium-poor tailing water from Helmsdorf at pH 9.8, $UO_2(CO_3)_3^{4-}$; (3) in sulfate-rich mine water from Königstein at pH 2.6, UO_2SO_4 (aq.).

Introduction

The knowledge of uranium speciation in waters from uranium mining and milling areas is essential for predicting radionuclide migration and for installing effective water purification technology. Furthermore, comprehensive and accurate knowledge of the speciation of uranium and its decay products is required to aid decisions for restoration strategies of the contaminated sites.

The Organization of Economic Development/Nuclear Energy Agency (OECD/NEA) has published a comprehensive and peer-reviewed data base/1/. However, due to a lack of experimental data, it still contains some thermodynamic data with rather large uncertainties. Moreover, most of the recommended stability constants for uranium complexes were derived by measurements of simple solutions with compositions that consider only binary or, at the most, some ternary solution complexes. Even some of the proposed species are derived as a result of data fitting with no other independent experimental verification such as spectroscopy. Natural waters can often contain many more constituents such as anions, cations, and natural and anthropogenic organic materials that may significantly influence the metal ion speciation. The much simpler laboratory systems often contain significantly less constituents than environmental aqueous systems and may therefore not completely represent the speciation in natural systems. Such unknown species can only be identified if thermodynamic information is obtained from real systems. In an earlier study, we have identified a calcium uranyl carbonate species in a mine tailing seepage water that was not listed in the NEA data base because of the above-given reasons /2/.

Therefore, it was the goal of this study to experimentally determine uranium speciation in different mining-related waters and compare the findings with modeling results to detect possible discrepancies and missing data in the uranium data base.

Results and Discussion

We used time-resolved laser-induced fluorescence spectroscopy (TRLFS) and laser-induced photoacoustic spectroscopy (LIPAS) to measure the uranium speciation. These methods are non-intrusive and therefore do not change the chemical composition of the investigated waters. This is very important, because any change of the system under study may also change the speciation. We also compared the measured uranium speciation in the water samples with thermodynamic speciation calculations. A detailed description of the equipment for laser induced spectroscopy to determine the speciation in these waters is given elsewhere [3,4].

Component	Concentration [mmol/L]			
	Seepage water Schlema	Mine water Schlema	Mine water Königstein	Tailingwater Helmsdorf
Ca	7.8	6.9	5.9	0.3
Mg	17.1	11.6	0.7	0.9
Na	0.5	20.6	6.1	166.3
K	0.3	1.0	0.04	0.9
U	0.009	0.021	0.073	0.025
SO_4^{2-}	25.6	20.7	23.9	35.6
HCO_3^-/CO_3^{2-}	0.45	3.9	<0.02	10.3
PO_4^{3-}	<0.02	<0.02	<0.02	0.29
AsO_4^{3-}	0.01	0.03	0.01	0.52
Cl^-	0.1	3.3	3.8	25.8
TOC(mg/L)	1.0	62.0	3.5	132.0
pH	7.82	7.13	2.6	9.76

Tab. 1: Chemical Analysis of different mining related waters.

Water samples from different mining areas were analyzed for elemental content by inductively

coupled plasma mass-spectrometry (ICP-MS) and atom absorption spectroscopy (AAS). The samples were collected under oxidizing conditions. The anions were determined by ion chromatography. All water samples were filtered before measurement. Tab. 1 summarizes the concentrations of major ions of four mining related waters in Saxony in Germany.

The waters are from uranium mines in Schlema and Königstein, one seepage water from the mine tailing pile No. 66 in Schlema, and one mill tailing water from Helmsdorf. To validate thermodynamic calculations /5/, the different mining related waters were measured by TRLFS and LIPAS.

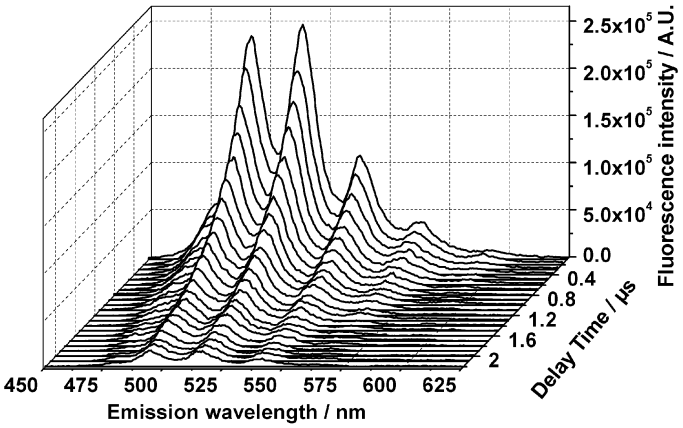

Fig. 1: TRLFS spectrum of mine water from Königstein. Excitation wavelength 410 nm

The TRLFS spectrum of the mine water and the seepage water from Schlema show a very short lifetime component which indicates the possible presence of organic material. Additionally, by comparing the fluorescence bands and their lifetimes of the seepage and mine water from Schlema with the data for the calcium uranyl carbonate complex, $Ca_2UO_2(CO_3)_3$ (aq.), we conclude that this is also the main species in these waters /2/.

The spectra, shown in Fig. 1, and the fluorescence lifetime of the Königstein mine water are different from the Schlema waters. The emission band wavelengths are characteristic for uranium sulfate complexes. The lifetimes of the sulfate complexes found in the original water are substantially smaller than in a system containing only sulfate and uranyl ions /3/. This is due to chloride fluorescence quenching. This is also the reason that the free uranyl ion is not detectable in this water.

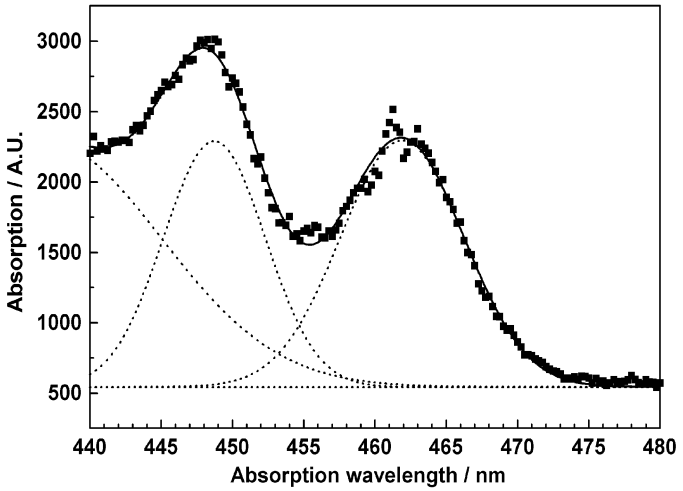

Fig. 2: LIPAS spectrum of tailing water from Helmsdorf.

The tailing water sample showed no uranium fluorescence. The photoacoustic spectrum of the tailing water in the wavelength region from 440 to 480 nm is shown in Fig. 2. The absorption bands are characteristic for the $UO_2(CO_3)_3^{4-}$ complex. Based on this information we assign the uranyl species in the tailing water as uranyl carbonate complexes /4/.

Acknowledgments

The authors would like to thank Dr. K. Krogner and Dr. W. Wiesener, Department of Analytics, Forschungszentrum Rossendorf e.V., for the AAS and ICP-MS measurements.

References

/1/ Grenthe, I., Fuger, J., Lemire, R.J., Muller, A.B., Nguyen-Trung, C., Wanner, H.: *Chemical Thermodynamics of Uranium.* 1st ed. , Elsevier Science Publishers, Amsterdam, 1992.

/2/ Bernhard, G., Geipel, G., Brendler, V., Nitsche, H.: Radiochim. Acta **74**, 87 (1996).

/3/ Geipel, G., Brachmann, A., Brendler, V., Bernhard, G., Nitsche, H.: Radiochim. Acta **75**, 199 (1996).

/4/ Geipel, G., Bernhard, G., Brendler, V., Nitsche, H.: Complex formation between UO_2^{2+} and CO_3^{2-} studied by laser-induced photoacoustic spectroscopy. Radiochim. Acta, accepted.

/5/ Bernhard, G., Geipel, G., Brendler, V., Nitsche, H.: Uranium Speciation in Waters of Different Uranium Mining Areas. Actinides `97. Symposium T4A Environmental Remediation, Waste management and Actinide Mitigation.

PREPARATION AND CHARACTERIZATION OF URANYL CARBONATE

D. Vulpius [2], R. Nicolai, G. Geipel, W. Matz [1], G. Bernhard, H. Nitsche
Forschungszentrum Rossendorf e.V., Institute of Radiochemistry
[1] Institute of Ion Beam Physics and Material Research
[2] Fachhochschule Magdeburg, Department of Chemistry and Pharmaceutical Technology

Uranyl carbonate, UO_2CO_3, was prepared by passing CO_2 /1/ pressurized to 5 bar through a solution of uranyl nitrate at pH = 5.00 /2/. A pale yellow-greenish precipitate was formed. After an aging period of four weeks, the vacuum-dried precipitate was characterized by elemental analysis, X-ray powder diffraction (XRD), scanning electron microscopy (SEM), and FTIR spectroscopy. The described analytical methods demonstrate that we obtained a very pure uranyl carbonate using pressurized CO_2 and maturing the precipitate under a CO_2 atmosphere.

Introduction

To study the chemical behavior of uranium in natural systems, such as exist in the environment of the former uranium mining in the southeast of Germany (Saxony, Thuringia), it is necessary to prepare and to characterize different model compounds of the uranium in a high chemical purity. In this work, uranyl carbonate which occurs in the nature as the mineral rutherfordine, was prepared and identified.

Experimental

5.00 g of $UO_2(NO_3)_2 \cdot 6\ H_2O$ (Merck p. a.) were dissolved in 100.0 mL deionized water. The pH of this solution was adjusted to 5.00 with 1 M NaOH under stirring with a magnetic stirrer. While doing so, a yellow microcrystalline precipitate of uranyl hydroxide, $UO_2(OH)_2 \cdot H_2O$, chemically equivalent to $UO_3 \cdot 2\ H_2O$, was formed. This solution was filled into a PTFE-beaker which was put into an autoclave. CO_2 pressurized to 5 bar was bubbled through the solution for 24 hours. After turning off the CO_2 stream, the precipitate showed a pale yellow-greenish color. The reaction solution was treated subsequently in the autoclave for four weeks under a 5 bar CO_2 atmosphere.

After the aging process, the precipitate was separated from its mother liquor by ultrafiltration through a cellulose nitrate filter of 0.45 µm pore size. The solid was washed with CO_2-saturated deionized water for three times and finally dried over anhydrous $CaCl_2$ in an exsiccator for one day. The yield was 3.09 g (94 % of the theory).

Results

Uranyl carbonate with the formula UO_2CO_3 contains 72.12 wt% uranium and 3.64 wt% carbon and has a stoichiometric ratio n(U) : n(C) = 1 mol : 1 mol. Our synthetic sample contains 72.88 ± 0.22 wt% U and 3.46 ± 0.02 wt% C (related to anhydrous substance) and has a stoichiometric ratio n(U) : n(C) = 1 mol : 0.94 mol. The amount of adsorbed water is 1.49 ± 0.01 wt%. The elemental analysis demonstrates that our sample has the molar composition of uranyl carbonate.

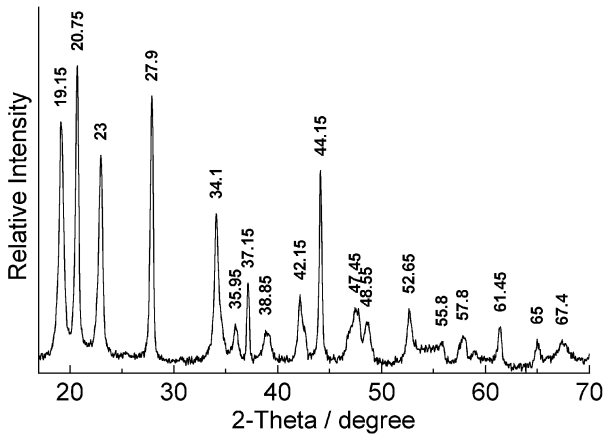

Fig. 1: X-ray diffraction pattern of synthetic uranyl carbonate.

Lattice constants	Synthetic UO_2CO_3	Rutherfordine /4/
a / Å	4.837 ± 0.006	4.848
b / Å	9.233 ± 0.012	9.236
c / Å	4.287 ± 0.006	4.327
V / Å^3	191.45 ± 0.35	193.75

Tab. 1: Comparison of the calculated lattice constants of synthetic uranyl carbonate with the literature data of natural rutherfordine (orthorhombic crystal system).

The X-ray diffraction pattern of synthetic uranyl carbonate is given in Fig. 1. The pattern was recorded with Cu K_α - radiation. The lattice constants are calculated in Tab. 1. In a first approach, our X-ray diffraction data are in agreement with the literature data known for rutherfordine /4/. The existing divergences are due to the incompletely formed crystal structure of the synthetic uranyl carbonate.

Fig. 2 shows the SEM micrograph of our synthetic uranyl carbonate. The average particle size is 1.2 µm. Initial crystal structures are discernible. We have observed that the particle size and

the crystallinity increase mainly by preparing uranyl carbonate with pressurized CO_2 in an autoclave.

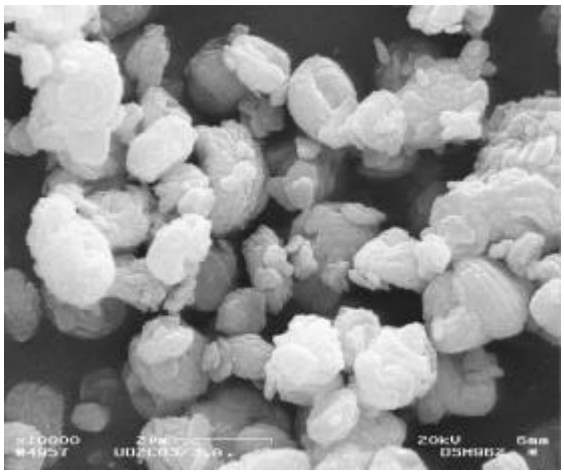

Fig. 2: SEM micrograph of synthetic uranyl carbonate. (magnification x 10000).

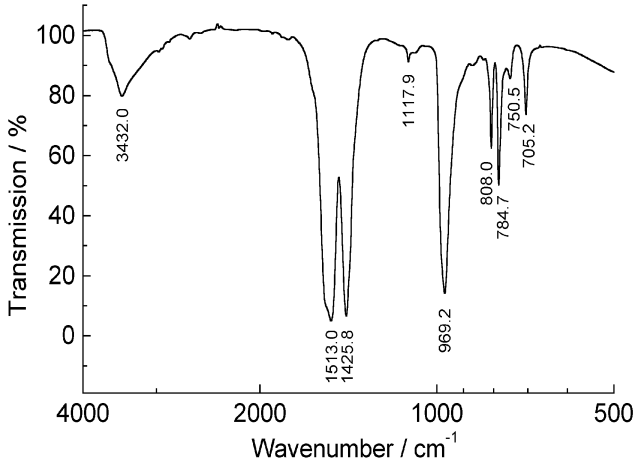

Fig. 3: FTIR spectrum of synthetic uranyl carbonate.

The FTIR spectrum of synthetic uranyl carbonate is shown in Fig. 3. The sample was prepared as KBr pellet and the spectrum was recorded with a photometric detector (photomultiplier). Tab. 2 gives an interpretation of the obtained spectral data. These data are compared with those from the literature which were recorded with a photoacoustic detector /3/. Differences between both detection methods can occur in the relative band intensities. The bands position of both methods is identical.

Wavenumber / cm^{-1}		Assignment
This work	Reference /3/	
705.2 m	706 m	CO_3 bending
784.7 m	783 m	CO_3 bending
808.0 m	864 w*	UO_2 symmetric stretching
969.2 s	970 s	UO_2 asymmetric stretching
1117.9 w	1170 w	combination of UO_2 asymmetric stretching and UO_2 bending
1425.8 s	1437 s	combination of CO_3 symmetric stretching and COH bending (hydrogen bonds)
1513.0 s	1532 s	CO_3 asymmetric stretching
3432.0 m	3600 m	OH_2 symmetric stretching (hydrogen bonds)

* The corresponding absorption band to 808.0 cm^{-1} in the FTIR spectrum of Ref. /3/ is discernible but not well resolved, so that an assignment error could be happened in this case.

Tab. 2: Interpretation of the FTIR spectrum of synthetic uranyl carbonate and comparison with the literature data (band intensity: s = strong; m = medium; w = weak).

The lower wave numbers of the absorption bands at 1425.8 and 3432.0 cm^{-1} compared with /3/ can be explained by hydrogen bonds coming from adsorbed water. This explains the decrease of the absorption bands at 1117.9 cm^{-1} and 1513.0 cm^{-1}. Obviously, the water is bound by chemisorption on the surface of the uranyl carbonate particles and not bound by physical adsorption. That explains also why the compound can not be dried completely by desication.

Conclusion

The results of the analysis demonstrate that pure uranyl carbonate was synthesized. It is important to carry out the synthesis at pH 5. To increase the purity and the crystallinity of uranyl carbonate, it is necessary to prepare the compound with pressurized CO_2 in an autoclave and to mature the precipitate under a pressurized CO_2 atmosphere.

Acknowledgments

The authors would like to thank Dr. W. Wiesener for the ICP-MS measurements, D. Birnstein for the elemental analysis, E. Christalle for the SEM micrographs, and A. Scholz for the X-ray diffraction patterns.

References

/1/ Pashalidis, I., Runde, W., Kim, J.I.: A Study of Solid-Liquid Phase Equilibria of Pu(VI) and U(VI) in Aqueous Carbonate Systems. Radiochimica Acta **61**, 141 (1993).

/2/ Meinrath, G., Klenze, R., Kim, J.I.: Direct Spectroscopic Speciation of Uranium(VI) in Carbonate Solutions. Radiochimica Acta **74**, 81 (1996).

/3/ Meinrath, G., Kimura, T.: Behavior of U(VI) Solids under Conditions of Natural Aquatic Systems. Inorganica Chimica Acta **204**, 79 (1993).

/4/ *JCPDS Powder Diffraction File*. Table 11-263.

COMPLEX FORMATION BETWEEN UO_2^{2+} AND CO_3^{2-} : STUDIED BY LASER-INDUCED PHOTOACOUSTIC SPECTROSCOPY (LIPAS)

G. Geipel, G. Bernhard, V. Brendler, H. Nitsche
Forschungszentrum Rossendorf e.V., Institute of Radiochemistry

The formation constant log ß^0 = 21.57 ± 0.70 of the uranyl triscarbonato complex, $UO_2(CO_3)_3^{4-}$, was determined for the first time by laser-induced photoacoustic spectroscopy at uranium concentrations from 5 x 10^{-4} to 10^{-5} M. The photoacoustic absorption spectra from pH 5 to 10 were recorded in the UV-vis range using a continuous scan mode from 380 nm to 480 nm. Furthermore, a mill tailing water from Helmsdorf in Saxony, Germany, with a uranium concentration of 2.5 x 10^{-5} M was measured by LIPAS. By comparing this spectrum with the spectrum of pure uranyl triscarbonate, the main species in the mill tailing water was identified as the uranyl triscarbonato complex. This finding agrees with speciation calculations.

Experimental

A novel tunable laser system with an optical parametric oscillator was used to study the spectroscopic properties of the uranyl carbonate system. The schematic of the experimental setup is described elsewhere /2/. Because dye lasers do not cover wavelengths below 410 nm, we employed a novel solid state laser system with ß-barium borate crystals as tuning elements. Through frequency doubling, the system can cover a range from 220 nm to 690 nm which enables us to study the essential parts of the absorption spectrum of uranium(VI). Three series with uranium solution concentrations of 5 x 10^{-5}; 1 x 10^{-4} and 5 x 10^{-4} M were measured. The measurements were carried out in two steps because it is not possible to scan over the whole wavelength range without changing the prism. The first measurement was from 380 nm to 440 nm, and the second measurement was from 440 nm to 480 nm after removing the FDO input prism. For the second wavelength range the power attenuator was used to decrease the laser energy.

Results

Fig. 1 and Fig. 2 show measured spectra from 380 nm to 440 nm and 440 nm to 480 nm, respectively. From the absorption data of these spectra, we calculated the concentration of the uranyl carbonate complex and the residual hydroxy complex.

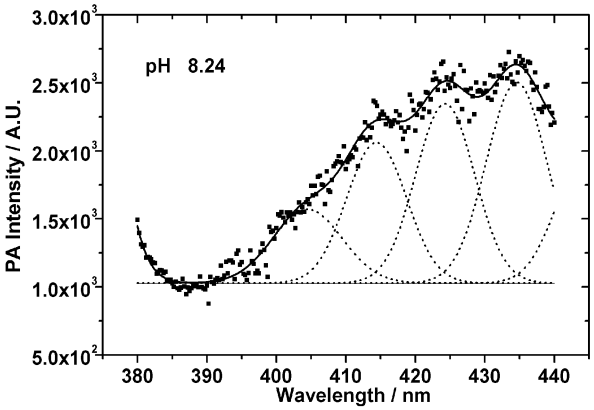

Fig. 1: Absorption spectra from 380 nm to 440 nm for 5 x 10^{-5} M UO_2^{2+} under atmospheric conditions.

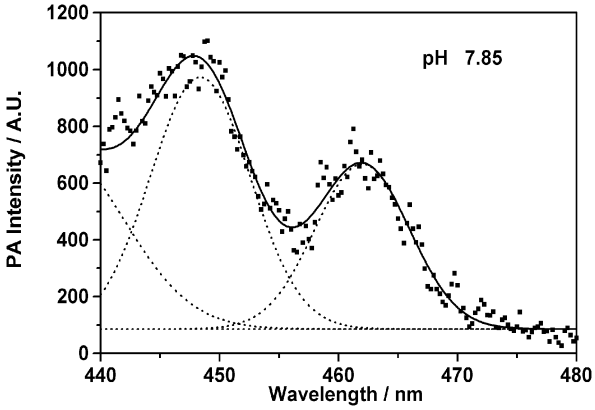

Fig. 2: Absorption spectra from 440 nm to 480 nm for 1 x 10^{-5} M UO_2^{2+} under atmospheric conditions.

From a plot of log $[UO_2(CO_3)_x^{(2x-2)-}/\{U_{tot.}-UO_2(CO_3)_x^{(2x-2)-}\}]$ vs. log $[HCO_3^-]$, we obtain for pH greater than 7 a straight line with a slope of 2.9 ± 0.3 (Fig. 3). This slope indicates the formation of the triscarbonato complex from pH 7.5 to about 10 with the following formation reaction:

$$UO_2(OH)_3^- + 3\ HCO_3^- \ \circ\ UO_2(CO_3)_3^{4-} + 3\ H_2O \qquad (1)$$

The slope in Fig. 3 validates that three HCO_3^- ions are involved in the equilibrium. From the intercept, the formation constant log K(0.1 M) = 8.5 ± 0.7 was determined. Using the Davies equation, log $\$^0$ = 9.78 ± 0.7 was calculated.

To calculate the overall formation constant, log $\$^0$ = 21.57 ± 0.7 for the reaction

$$UO_2^{2+} + 3\ CO_3^{2-} \ \circ\ UO_2(CO_3)_3^{4-} \qquad (2)$$

we used the reactions

$$UO_2^{2+} + 3\ H_2O \ \circ\ UO_2(OH)_3^- + 3\ H^+ \qquad (3)$$

with log $\$^0$ = 19.2 ± 0.4 and

$$CO_3^{2-} + H^+ \quad \circ \quad HCO_3^- \qquad (4)$$

with log $\$^0$ = 10.33 /3/.

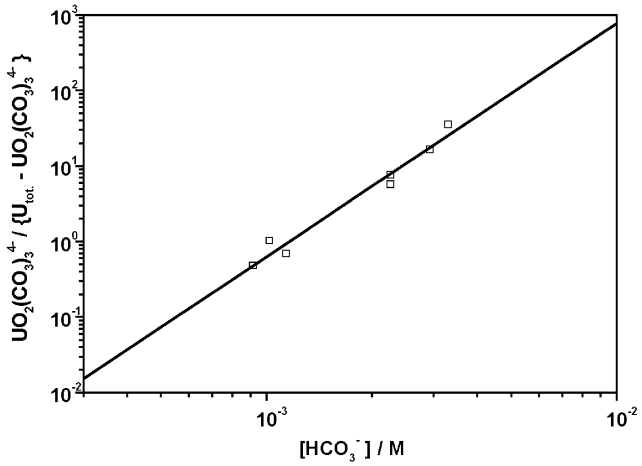

Fig. 3: Validation of the complex formation constant: Ratio $[UO_2(CO_3)_x^{(2x-2)-}/\{U_{tot.} - UO_2(CO_3)_x^{(2x-2)-}\}]$ as function of HCO_3^- concentration

The calculated value is in a very good agreement with log $\$^0$ = 21.60 ± 0.05 given in the NEA data base /4/.

We published earlier /1/ that the tailing water does not show any uranium fluorescence properties. The LIPAS spectrum, recorded without any pre-conditioning, shows a strong increase of the signal with decreasing wavelength. This is caused by the organic components (TOC) in the tailing water. After peak fitting and spectrum deconvolution, a residual spectrum is obtained in the region 440 to 480 nm with two maxima that are located at 448.1 and 461.9 nm. By comparing these spectra with the above discussed uranyl carbonate standard solutions, the absorption maxima can be assigned to the uranyl triscarbonato complex.

Acknowledgment

The authors thank Dr. U. Wiesener for ICP-MS measurements and Mr. W. Birnstein for the ion chromatographic determination of the carbonate concentrations.

References

/1/ Bernhard, G., Geipel, G., Brendler, V., Nitsche, H.: Uranium Speciation in Waters of Different Uranium Mining Areas. Lecture, Actinides '97, Baden-Baden, September 21-26, 1997

/2/ Geipel, G., Bernhard, G., Brendler, V., Nitsche, H.: Complex Formation between UO_2^{2+} and CO_3^{2-}. Studied by Laser-Induced Photoacoustic Spectroscopy (LIPAS). Radiochim. Acta, accepted

/3/ Sigg, L., Stumm, W.: *Aquatische Chemie*. B.G. Teubner, Stuttgart, 1994, 129.

/4/ Grenthe, I., Fuger, J., Konings, R.J.M., Lemire, R.J., Muller, A.B., Nguyen-Trung Cregu, Ch., Wanner, H.: *Chemical Thermodynamics of Uranium*. North-Holland, Amsterdam-London-New York-Tokyo, 1992; pp. 107 , 313.

URANYL HYDROXO CARBONATE COMPLEXES STUDIED BY LASER-INDUCED SPECTROSCOPY

G. Geipel, G. Bernhard, V. Brendler, H. Nitsche
Forschungszentrum Rossendorf e.V., Institute of Radiochemistry

We studied the influence of increasing amounts of HCO_3^-/CO_3^{2-} ions on the fluorescence of the uranyl at pH 7, 8 and 9. From the decrease of the signal intensity, we calculated the stability constant of the $(UO_2)_2CO_3(OH)_3^-$ complex as log K = - 18.9 ± 1.0. This value agrees with the one given in the NEA data base /9/. An additional species was identified with a fluorescence lifetime of about 48 ns, which we assigned to $UO_2(OH)_4^{2-}$.

Results

Carbonate complexes of uranium are the most important species in natural transport processes. Several previous studies /1-4/ were reported on the complexation of uranium(VI) with carbonate. In these studies the concentration of uranium was relatively high when compared to the concentrations in natural systems. As a first step to reach lower concentration ranges than with UV-vis and potentiometric methods, we studied the complex formation of the mixed uranylhydroxocarbonate complex, $(UO_2)_2CO_3(OH)_3^-$. This complex does not have fluorescence properties. Nevertheless, we used time-resolved laser-induced fluorescence spectroscopy (TRLFS) for our study by measuring the uranyl hydroxo complexes that form the non-fluorescent uranyl hydroxo carbonate complex when carbonate is added to the solution. We measured the decrease of the fluorescence intensity of the hydroxo complexes. The approach is only feasible when only one non-fluorescent species exists in the solution. We selected the experimental

conditions accordingly. Fig. 1 gives the calculated speciation diagram.

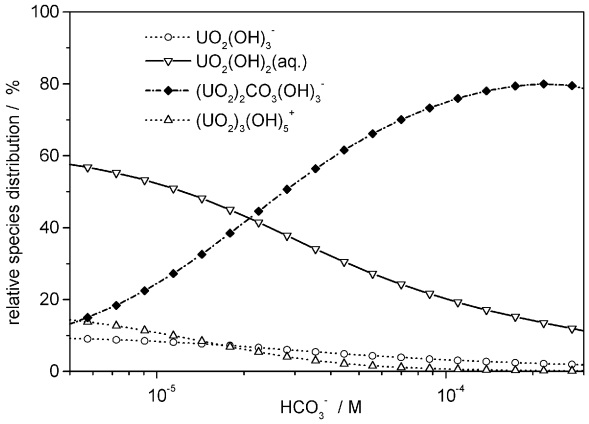

Fig. 1: Calculated species distribution of UO_2^{2+} at pH 8 as a function of HCO_3^- concentration

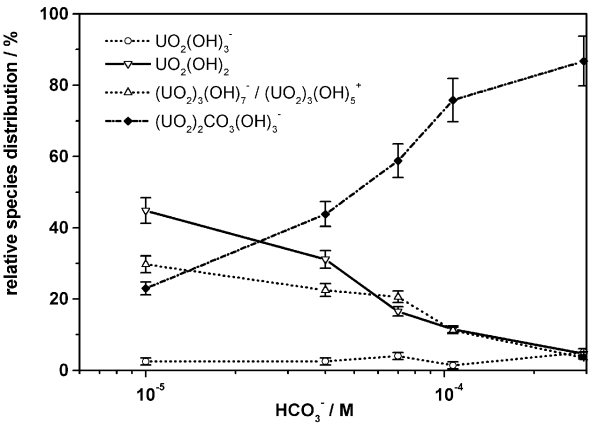

Fig. 3: Measured species distribution as function of HCO_3^- concentration at pH 8; $[UO_2^{2+}]_{total}$ =5x10^{-5} M

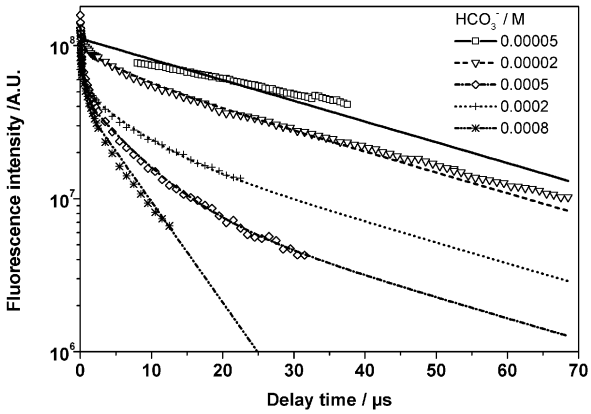

Fig. 2: Fluorescence decay and lifetime fit for measurements at pH 7

TRLFS measurements were carried out with the spectrometer described elsewhere /5/.
Three different experimental series were studied at pH values of 7, 8 and 9. The uranium concentration of all solutions was 5 x 10^{-5} M. The measurements were carried out using 1 x 10^{-5} M and 5 x 10^{-4} M HCO_3^-.
As an example, Fig. 2 shows measured fluorescence decay curves for pH 9. The decay depends on the hydrogen carbonate concentration. From the fluorescence intensities at t=0 for the different fitted lifetime curves, the species concentrations in the solution were calculated. The calculation was described previously /5-7/. The most important condition for the lifetime fit of all measurements was, that the sum of the relative amounts calculated for the species with fluorescence properties was smaller than one. The difference between this sum and one was assigned to the non-fluorescent $(UO_2)_2CO_3(OH)_3^-$-species. Following this procedure, we constructed from our measurements a species distribution diagram as function of bicarbonate concentration.
The species distribution calculated with the results of the TRLFS measurement for pH 8 is shown in Fig. 3. The calculated species distributions at pH 7 and 9 are analogous. The determined species concentrations for the $UO_2(OH)_2$ and the $UO_2(OH)_3^-$ species agree with EQ3/6 /8,9/ calculations. The measured $(UO_2)_2CO_3(OH)_3^-$ species showed its relative maximum at lower pH than the EQ3/6 calculations predicted. From the lifetime fit we found an additional species with a fluorescence lifetime of 45 ± 10 ns. This species caused that the concentration of the other species was found lower than calculated. We assign at this lifetime to the $UO_2(OH)_4^{2-}$ species.
We calculated the complex formation constant using the $(UO_2)_2CO_3(OH)_3^-$ concentrations and the actual pH. From the determined HCO_3^- concentrations we calculated the CO_3^{2-} concentration using the HCO_3^-/CO_3^{2-} equilibrium under atmospheric conditions /10/.
The values represent the equilibrium of the mixed hydroxo-carbonate complex with the main species in the solution at the actual pH. These reactions are for:

pH 7; 8: $UO_2(OH)_2$aq. + CO_3^{2-} + OH^-] $(UO_2)_2CO_3(OH)_3^-$ (1)
pH 9: $UO_2(OH)_3^-$ + CO_3^{2-}] $(UO_2)_2CO_3(OH)_3^-$ (2)

The overall formation constant for the reaction

$$2\ UO_2^{2+} + CO_2 + 3\ H_2O \quad] \quad (UO_2)_2CO_3(OH)_3^- + 3OH^- \qquad (3)$$

can be derived from the formation constants of the different hydroxo complexes /9/ and the carbonate equilibrium /15/.

Accordingly, we calculated the equilibrium constants for the reaction (1)

$$\log K(1) = 4.97 \pm 0.39 \text{ (pH 7)} ; \quad 5.54 \pm 0.57 \text{ (pH 8)}$$

and for the reaction (2)

$$\log K(2) = -3.39 \pm 0.21.$$

The formation constant of $(UO_2)_2CO_3(OH)_3^-$ according to reaction (3) was calculated to

$$\log K(3) = -18.9 \pm 1.0.$$

Acknowledgments
The authors thank Mr. D. Birnstein, analytical department, for ion-chromatographic determination of the concentration of hydrogen carbonate.

References

/1/ Meinrath, G., Klenze, R., Kim, J.I.: Direct Spectroscopic Speciation of Uranium(VI) in Carbonate Solutions. Radiochimica Acta **74**, 81-86 (1996)
/2/ Kato, Y., Meinrath, G., Kimura, T., Yoshida, Z.: A Study of U(VI) Hydrolysis and Carbonate Complexation by Time-Resolved Laser-Induced Fluorescence Spectroscopy. Radiochimica Acta **64**, 107-111 (1994)
/3/ Meinrath, G., Kimura, T.: Carbonate complexation of the uranyl(VI) ion. Journal of Alloys and Compounds **202**, 89-93 (1993)
/4/ Kimura, T., Serrano, G.J., Nakayama, S., Takahashi, K., Takeishi, H.: Speciation of Uranium in Aqueous Solutions and in Precipitates by Photoacoustic Spectroscopy. Radiochimica Acta **58/59**, 172-178 (1992)
/5/ Geipel, G., Brachmann, A., Brendler, V., Bernhard, G., Nitsche, H.: Uranium(VI) Sulfate Complexation Studied by Time-Resolved Laser-Induced Fluorescence Spectroscopy. Radiochimica Acta **75**, 199-204 (1996)
/6/ Moll, H., Geipel, G., Matz, W., Bernhard, G., Nitsche, H.: Solubility and Speciation of $(UO_2)_2SiO_2{\cdot}2H_2O$ in Aqueous Systems. Radiochimica Acta **74**, 3-7 (1996)
/7/ Moll, H., Geipel, G., Brendler, V., Bernhard, G., Nitsche, H.: Interaction of Uranium(VI) with Silicic Acid in Aqueous Solutions Studied by Time-resolved Laser-Induced Fluorescence Spectroscopy. submitted to Actinides'97
/8/ Wolery, T.J.: *EQ3/6, A software package for the geochemical modeling of aqueous systems.* Report URCL-MA-110662 Part I, Lawrence Livermore National Laboratory (1992)
/9/ Grenthe, I., Fuger, J., Konings, R.J.M., Lemire, R.J., Muller, A.B., Nguyen-Trung Cregu, Wanner H.: *Chemical Thermodynamics of Uranium*. NEA OECD, p308-329 (1992)
/10/ Sigg, L., Stumm, W.: *Aquatische Chemie*. B.G.Teubner Verlag Stuttgart (1994), 2. Aufl., 85-126

DETERMINATION OF ACTINIDES AT CONCRETE SURFACES

C. Nebelung, H. Nitsche
Forschungszentrum Rossendorf e.V. , Institute of Radiochemistry

During the dismantling of nuclear installations much building material must be disposed of. The material may be contaminated by low-levels of alpha-radiation-emitting radionuclides. Because the contamination levels are often near the legal activity levels, an accurate and quick method is essential to determine whether or not this material can be treated as non-radioactive waste. We use direct alpha spectrometry after only mechanical preparation of the concrete samples. For the detection of small contamination spots at the concrete surface we also measure the surface activity of selected pieces of concrete.

Direct alpha-radiation measurements of concrete in buildings are impossible without sampling because the alpha-particles are absorbed by concrete, painting and air. Chemical analysis of the alpha-contaminants requires many time-consuming analytical steps and is therefore rather unsuitable. We use direct alpha spectrometry on samples that are prepared by a relatively simple mechanical procedure. The concrete is crushed, wet milled and the sources are prepared by pouring or spraying the wet suspension onto the sample plates and subsequently drying them /1/, /2/. Extremely thin (up to 0.6 µm) sources are necessary to directly measure the alpha radiation in concrete, because it is absorbed in the concrete layers due to the short range of the alpha radiation. Our method works without concentration of the actinides but requires a large sample area (diameter of 200 mm). The alpha-spectra of the sources were measured using a large grid ionization chamber.

We determined the peak shape and the self absorption of the alpha radiation as a function of the sample layer's thickness using standard concretes that were spiked with actinides. Fig. 1 shows a comparison of standard concrete samples with different mass and layer thickness. The spectral resolution of the 0.6 µm-source is comparable to ideal "massless" spectra.

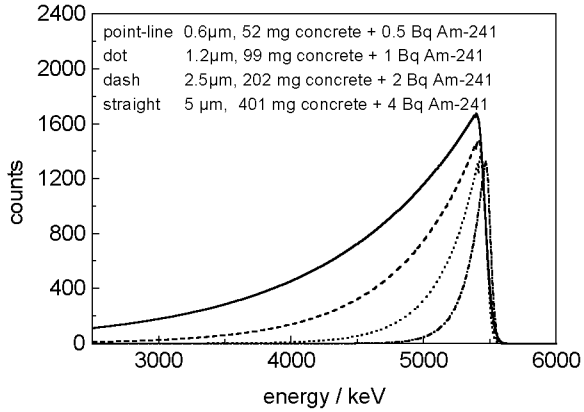

Fig. 1: Fitted peak shape of a concrete with 10 Bq/g Am-241 at various source thicknesses

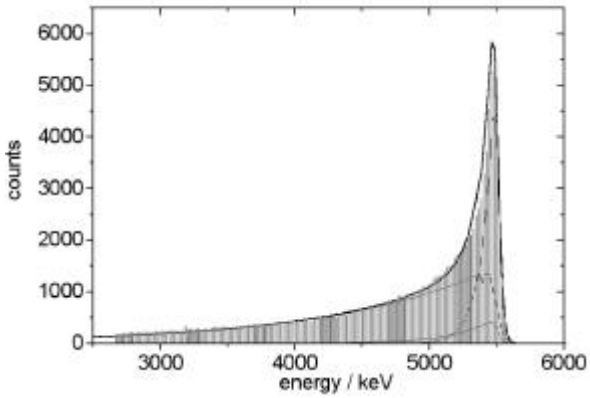

Fig. 2: Direct alpha-spectrum of a 25 g piece of concrete with 5 Bq Am-241 at the surface

During sample preparation the concrete is homogenized by milling. Small spots of surface activity will be diluted in the whole bulk. The specific activity of samples with such spots after homogenization can be below the detection limit. Nevertheless, the detection of such small activities at the surface of concrete pieces before crushing is possible by hand selecting the contaminated pieces. Fig. 2 shows the spectrum of a 25.1 gram piece of concrete to which 5 Bq Am-241 were added at the surface.

The overall peak shape of this spectrum is different from the shapes of homogenized concrete (shown in Fig. 1). The sharp thin peak at high energy determines the activity at the outer surface. The low-energy tailing shows that a part of activity has seeped into the bulk. The activity in Fig. 2 is calculated by splitting the peak into three parts: (1) At high energies, the spectrum is comparable to a "massless" standard sample; (2) the layer's thickness of the second peak lies between the two others; and (3) the tailing of the third peak at lower energies is comparable to a source with a thickness of about 5 µm. The sum of the three peak fitting curves agrees well with the real spectrum:

1.	"massless" sample about 0 µm thickness	(0.90 ± 0.15) Bq
2.	100 mg - sample about 1,2 µm thickness	(0.42 ± 0.13) Bq
3.	400 mg - sample about 5 µm thickness	(3.32 ± 0.15) Bq

The sum of fitted activity is (4.65 ± 0.11) Bq which again shows a good agreement with the 5 Bq that we added.

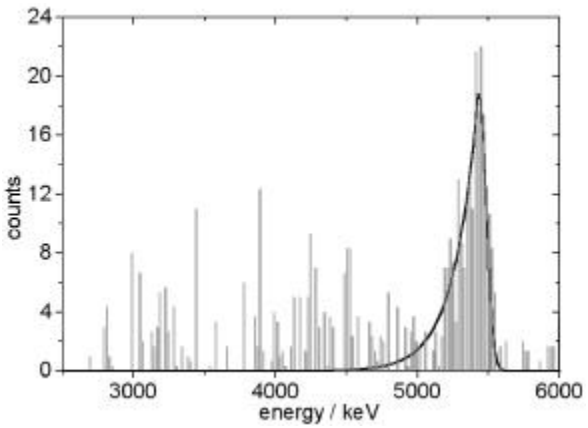

Fig. 3: Alpha-spectrum of the 25 g concrete piece with 5 Bq Am-241 after homogenisation. Sample thickness 0.6 µm, spectrum of "inactive" concrete substracted.

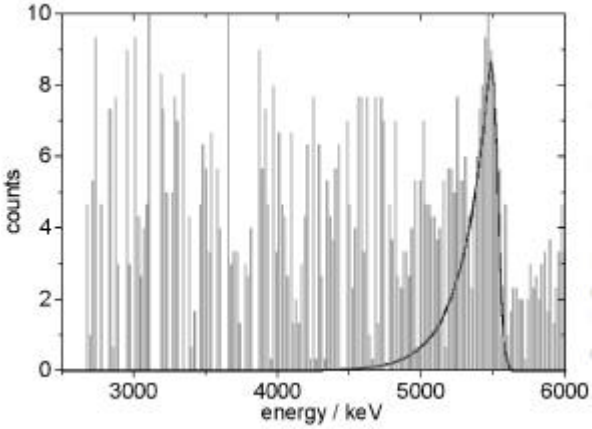

Fig. 4: Direct alpha-spectrum of a piece of concrete with 0.002 Bq Am-241 at the surface

The same sample was mechanical treated according to /2/ and thus the surface activity was evenly distributed in the whole concrete mass. After homogenisation we expect a specific

activity of 0.199 Bq/g (5 Bq / 25.1 g). The spectrum of a 0.6 µm-source of this homogenized sample (after correction by the concrete activity without contamination) is depicted in Fig. 3. The measured specific activity is (0.204 + 0.012 Bq/g).
The detection limit of the specific activity of actinides in large homogenized thin samples is 0.01 Bq/g per nuclide /2/. The detection limit of the activity at the surface is 0.002 Bq (Fig. 4) according 0.00008 Bq/g in a 25.1 g concrete piece.
Direct alpha-spectrometry of homogenized samples is a good additional method to quantitatively determine small spots of actinides at the surface of concrete pieces.

Acknowledgment
This work was supported by the Bundesministerium für Bildung, Wissenschaft, Forschung und Technologie of the Federal Republic of Germany under the contract number 02 S 7655A8.

References
/1/ Nebelung, C., Hübener, S., Bernhard, G.: *Methodenentwicklung zur Freimessung von Bauschutt auf alpha-aktive Nuklide (Th, U, Np, Pu, Am)*. Schlußbericht zum Fördervorhaben BMBF 02 S 7442 2, 1995
/2/ Nebelung, C., Nitsche, H., Bernhard, G.: Methode zur schnellen Bestimmung von Actiniden in Bauschutt zur Freigabeentscheidung. V. Stillegungskolloquium Hannover und IV. Statusbericht Stillegung und Rückbau kerntechnischer Anlagen. 24.-25.06.1997 Hannover, Tagungsband S. 293-301

CALCULATION OF THE ALPHA-SPECTRA OF THIN CONCRETE SOURCES CONTAINING ACTINIDES

J. Henniger [1], G. Mann [1], C. Nebelung, H. Nitsche
Forschungszentrum Rossendorf e.V. , Institute of Radiochemistry
[1] Technische Universität Dresden, Institute of Physics of Radiation Protection

During the decommissioning of nuclear power plants the measurement of alpha-radiation is essential. The direct alpha-spectrometry of extremely thin and large area concrete sources is a fast method to determine whether these building materials can be treated as radioactive or non-radioactive waste. The calculation of the concrete layer structure and the resulting absorption of alpha-radiation in these sources is of interest for the interpretation of alpha-spectra.

The conventional method for determining low levels of actinides in concrete is a very time-consuming process with thermal and chemical treatment, chemical separation and, finally, electrochemical deposition. The direct alpha-spectrometry of extremely thin concrete sources is easier and faster. The sources require only mechanical preparation of the concrete samples by breaking and wet milling them and then pouring or spraying the milled suspension onto the counting plate which is subsequently dried /1/. The absorption of the alpha-radiation in the concrete layers must be considered. The measuring efficiency and the peak shape of the resulting spectra of such sources differ from those of “massless” sources. It depends on the spectrometer, the actinide energy, the layer’s thickness, the packing density, the specific density and the particle size distribution.

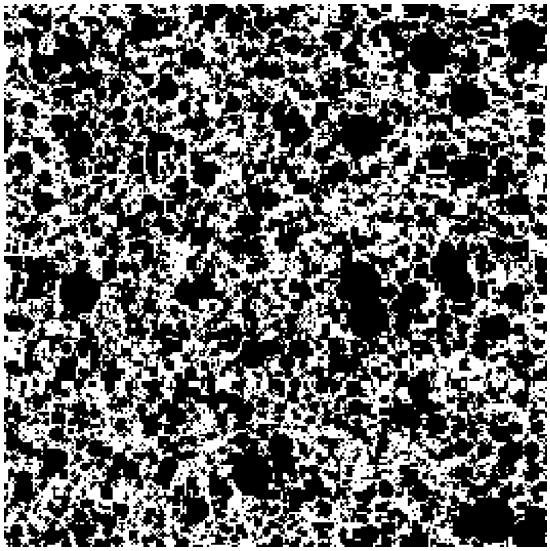

Fig. 1: Calculated layer, filling density 0.5

Calculations that consider these effects were performed with the multi-purpose radiation transport code system AMOS /2/. The code is based on a fast rigorous numerical method for the solution of radiation transport problems by using multi-group double-differential cross sections (DDX) for neutral particles and continuous slow down approximations (CSDA) for ions /3,4/.
For an accurate calculation a geometrical model is proposed. It is based on measured particle size distribution in the mill suspension and the particle size and packing density in the dried

layer. These parameters were determined by scanning electron microscopy. The relevant source-volume is divided in elements of 0.1 µm³. The growth of the layer up to the required density is calculated using the volume elements. Fig. 1 shows a calculated layer with a filling density of 0.5, i.e. 50% concrete and 50% gas. Fig. 2 and Fig. 3 are side views of two different thicknesses of concrete layers.

Fig. 2: Calculated layer, 5 µm thickness, side view

Fig. 3: Calculated layer, 0.6 µm thickness, side view

The first approximation is that consistent layers produce an equal energy distribution between E_{max} and E_{min} determined by the layer thickness. This is not corresponding to the real sample geometry. It is only the 0th approximation. The second approximation assumes that a mono layer is formed by packing of spheres. The energy distribution begins at high energies with a sharp shoulder and has an exponential decay to lower energies. The third approximation calculates layers which consist of spheres with a diameter smaller than the layer thickness. In this case, the energy decreases linearly corresponding to the layer's thickness between E_{max} and then the exponential decay begins. Fig. 4 shows the calculated energies of samples with 5 µm and 0.6 µm thicknesses, the same thickness as shown in Fig. 2 and Fig. 3.

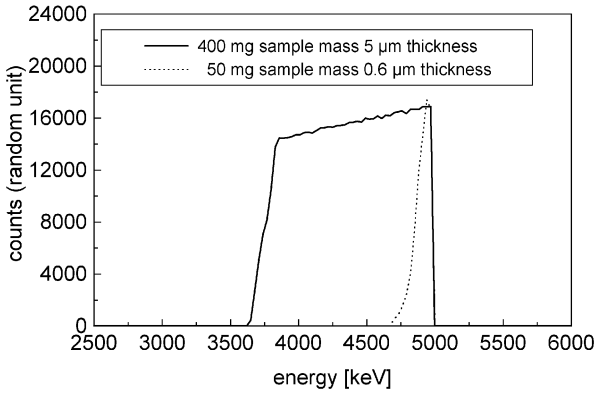

Fig. 4: Simulated alpha-spectra at 5000 keV at various layer thickness

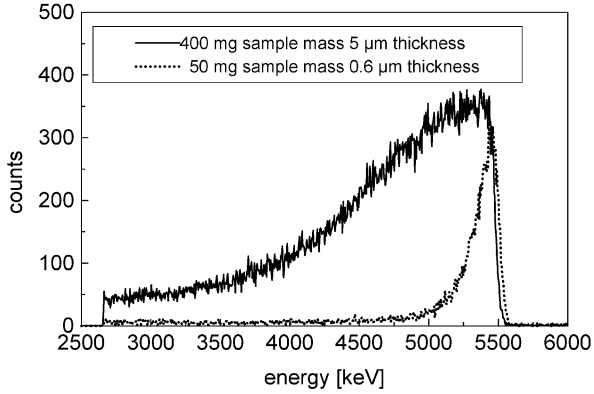

Fig. 5: Measured alpha-spectra of concrete with 10 Bq/g Am-241 (at 5499 keV) at various layer thickness

The measured spectra of the 5 µm and 0.6 µm sources are shown in Fig. 5. The measured spectra tail at lower energies, whereas the simulated spectra decrease steeply. This tailing is not caused by the particle size distribution but by heterogeneities of about 10 µm, which are probably caused by the topographic unevenness of the sources' metal support.
There are still differences between the simulated and the measured alpha spectra. Further calculations are being carried out to reduce the differences.

Acknowledgment
This work was supported by the Bundesministerium für Bildung, Wissenschaft, Forschung und Technologie of the Federal Republic of Germany under the contract number 02 S 7655A8.

References

/1/ Nebelung, C., Nitsche, H., Bernhard, G.: Methode zur schnellen Bestimmung von Actiniden in Bauschutt zur Freigabeentscheidung. V. Stillegungskolloquium Hannover und IV. Statusbericht Stillegung und Rückbau kerntechnischer Anlagen. 24.-25.06.1997 Hannover, Tagungsband S. 293-301

/2/ Henniger, J.: Amos - ein multivalent nutzbares Programmsystem zur Berechnung von Strahlungstransportproblemen. In: *Strahlenschutz, Physik und Meßtechnik*. Bd.1, S. 145-150, 26. Jahrestagung des Fachverbandes für Strahlenschutz e.V., Karlsruhe, 24.-26.05. 1994

/3/ Ziegler, J.F., Biersack, J.P., Littmark, U.: The Stopping and Ranges of Ions in Solids. In: J.F. Ziegler (ed.) *The Stopping and Ranges of Ions in Matter.* Pergamon, New York 1985 Vol. 1

/4/ Henniger, J.: *StopPow2000 - a program for fast ion stopping in continuous slowing down approximation*. TU Dresden

Organic Matter and its Interaction with Radionuclides

DEFINED MODEL SUBSTANCES FOR HUMIC ACIDS
I. SYNTHESIS AND CHARACTERIZATION OF NITROGEN-FREE HUMIC ACIDS

S. Pompe, M. Bubner, M. Meyer, K.H. Heise, R. Nicolai [1], H. Nitsche
Forschungszentrum Rossendorf e.V., Institute of Radiochemistry
[1] Institute of Bioinorganic and Radiopharmaceutical Chemistry

A nitrogen-free humic acid (HA) model substance was synthesized from an aqueous glucose solution and Na_2CO_3. Characterization of the synthetic product showed functional and structural properties that are comparable to natural HA. The material can be used to investigate the role of nitrogen in the metal ion complexation of HA.

The ability of humic acids (HA) to complex metal ions is mainly due to their high concentration of oxygen-containing functional groups, especially carboxylic and phenolic OH groups. However, also other functional groups, such as nitrogen-containing groups, may contribute as electron-donors to the complexation. Defined synthetic HA model substances, which do or do not contain nitrogen may help to elucidate the influence of the nitrogen-containing functional groups on the overall complex formation capability. Therefore, we synthesized a non-nitrogenous HA according to our melanoidin concept /1/. Melanoidins are condensation products of reducing sugars and "-amino acids formed in the “Maillard reaction”. However, reducing sugars, such as glucose and galactose, can undergo the “Maillard reaction” in hot alkaline solution in absence of amino acids and form the so-called nitrogen-free “pseudo melanoidins” /2/.

Experimental and results

A mixture of 12 g D(+)-glucose (Fluka), 0.2 g Na_2CO_3 (p.a., Merck) and 18 mL water was refluxed for 15 days under nitrogen. The starting pH was 8.9. In the initial synthesis, the pH decreased to about 5 after 24 hours for about one week. Therefore, we adjusted the pH of the reaction mixture to 8 by addition of Na_2CO_3 once a day for the first 6 days of the synthesis. The humic acid-like fraction of the reaction product was extracted with 2 M NaOH and then precipitated with 2 M HCl. The resulting precipitate was washed, dialyzed and freeze dried. The synthesis yielded 996 mg of non-nitrogenous synthetic HA.

Elemental analysis		
Element	Synthetic HA	Natural HA /3/
C [%]	57.55 ± 0.03	54 - 59
H [%]	5.26 ± 0.01	3 - 6
O [%]	37.14 ± 0.03	33 - 38

Functional groups			
Functional groups [meq/g]	Synthetic HA		Natural HA /3/
	Calcium acetate exchange /4/	Radiometric determination /1/	
COOH + phenolic OH	-	7.23 ± 0.81	5.6 - 8.9
COOH	2.64 ± 0.12	2.38 ± 0.14	1.5 - 5.7
phenolic OH	-	4.86 ± 0.83	2.1 - 5.7

Tab. 1: Elemental composition and functional group content of the synthesized non-nitrogenous HA and comparison with natural HA /3/.

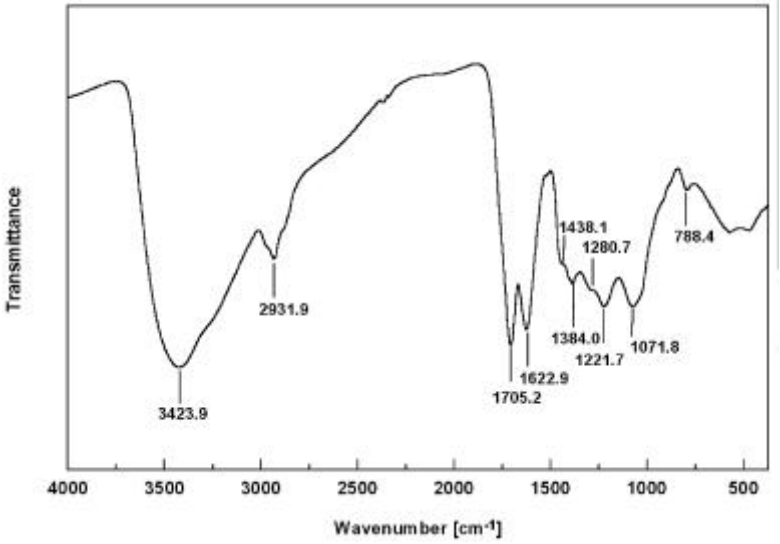

Fig. 1: FTIR spectrum of the non-nitrogenous synthetic HA.

Tab. 1 shows the elemental composition and the functional group content of the non-nitrogenous synthetic HA and a comparison to literature values for natural HA /3/. The synthetic product compares well with natural HA. It is notable that the non-nitrogenous synthetic HA prepared from glucose shows a higher carboxylic group content than other synthetic HA prepared from reducing sugars and "-amino acids. For instance, the synthetic HA from type M1 that were prepared earlier /1/ shows only a concentration of 1.0 meq/g carboxylic groups. We conclude from the radiometric determination of the functional groups that our product contains both phenolic hydroxyl and carboxylic groups.

Fig. 1 shows characteristic absorption bands for HA in the

FTIR spectrum of the non-nitrogenous synthetic HA /3/. The absorption bands and their assignments are summarized in Tab. 2. Additionally, the fact that this HA contains phenolic hydroxyl groups was confirmed by pyrolysis-gas chromatography/mass spectrometry. With this method we detected phenol and phenolic substitution products as thermolysis fragments.

Wavenumber [cm^{-1}]	Assignment
3423.9	O-H stretching vibrations
2931.9	asymmetric and symmetric stretching vibrations of aliphatic C-H bonds, especially CH_2
1705.2	C=O stretching vibrations due to COOH groups
1622.9	aromatic C=C and H-bonded C=O
1438.1	C-H deformation vibrations of aliphatic C-H bonds
1384.0	C-H deformation vibrations of aliphatic C-H bonds
1280.7	O-H deformation vibrations of phenolic OH
1221.7	C-O stretching and O-H deformation vibrations due to COOH groups
1071.8	C-O stretching vibrations of alcoholic OH attributed to the precursor glucose
788.4	olefinic C-H, substituted aromatics

Tab. 2: Assignment of FTIR absorption bands for the non-nitrogenous synthetic HA.

Capillary zone electrophoresis showed that the non-nitrogenous HA has a homogenous charge-to-size ratio distribution that is comparable to other synthetic HA /1/.
The results of the different characterization methods show that it is possible to synthesize non-nitrogenous HA model substances from glucose. The synthetic material will be used to study the metal ion complexation of HA and to compare the results with the complexation behavior of nitrogen-containing HA model substances. This will clarify the role of aliphatic amines and N-heterocyclic groups in the complexation process of HA with metal ions.

Acknowledgments
This work was supported by the Bundesministerium für Bildung und Forschung (BMBF) under contract number 02 E88150.
We thank R. Ruske, R. Jander and H. Görner for their help with the product characterization.

References
/1/ Pompe, S.: *Entwicklung huminsäureähnlicher Melanoidine als Funktionalitätsmodelle für Huminsäuren und ihr Vergleich mit Fluka-Huminsäure hinsichtlich ihres Komplexbildungsverhaltens gegenüber Uran(VI).* Dissertation, TU Dresden 1997.
/2/ Ishiwatari, R., Morinaga, S., Yamamoto, S., Machihara, T., Rubinsztain, Y., Ioselis, P., Aizenshtat, Y., Ikan, R.: A study of formation mechanism of sedimentary humic substances-I. Characterization of synthetic humic substances (melanoidins) by alkaline potassium permanganate oxidation. Org. Geochem. **9**, 11 (1986).
/3/ Stevenson, F.J.: *Humus chemistry, genesis, composition, reactions*. John Wiley & Sons, Inc., New York 1994.
/4/ Schnitzer, M., Khan, S.U.: *Humic substances in the environment.* (A.D. McLaren, ed.). Marcel Dekker, Inc., New York 1972.

DEFINED MODEL SUBSTANCES FOR HUMIC ACIDS
II. SYNTHESIS AND CHARACTERIZATION OF A SYNTHETIC HUMIC ACID WITH BLOCKED PHENOLIC HYDROXYL GROUPS

S. Pompe, M. Bubner, R. Jander, K.H. Heise, R. Nicolai [1], H. Nitsche
Forschungszentrum Rossendorf e.V., Institute of Radiochemistry
[1] Institute of Bioinorganic and Radiopharmaceutical Chemistry

In this work we present the possibility to synthesize a modified synthetic humic acid (HA) of type M1 with blocked phenolic hydroxyl groups for the investigation of the influence of phenolic OH groups on the complexation behavior of HA.

Experimental and Results
Starting from synthetic humic acid (HA) of type M1 /1/ which contains 2.28±0.09 meq/g phenolic OH groups, we synthesized by etherification a HA with blocked phenolic OH groups. Fig. 1 shows a scheme of the synthesis procedure and the derivatization reactions.

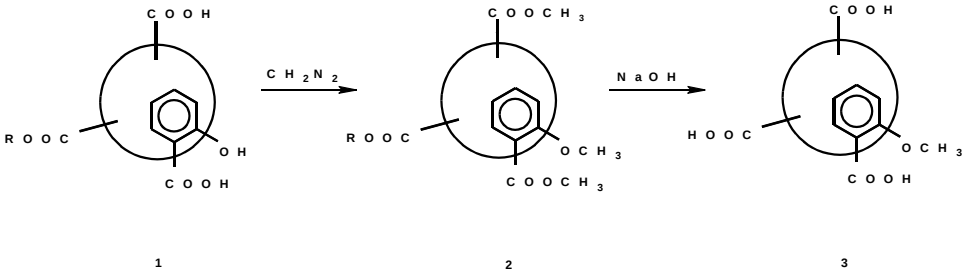

Fig. 1: Reaction scheme of the synthesis of humic acids with blocked phenolic OH groups.

First, 1.5 g of the original HA (1) were suspended in methanol and methylated two times with 5.5 mmol of diazomethane (Sigma-Aldrich) under stirring for 3 hours at -5 to 5°C. The permethylated sample (2) was lyophilized. Then the product was refluxed under stirring for 8 hours with an excess of methanolic NaOH solution to hydrolyze the methyl esters formed during the permethylation process. Following the methanol was removed by distillation. The distillation residue was taken up in water, the non-soluble components were separated by centrifugation and the modified synthetic HA (3) was precipitated from the aqueous solution by adding 1 M HCl. The HA was washed, centrifuged and dialyzed. The methylation procedure and the subsequent saponification of the ester groups were performed for a second time to assure a complete derivatization.

Tab. 1 lists the HA functional groups of the modified (type M1-B) and non-modified (type M1) synthetic HA determined with three different methods. It is surprising that we found 1.06±0.19 meq/g H-acidic functional groups by the radiometric method, for the HA with blocked phenolic OH groups. But it is still not confirmed if these functional groups are non-modified phenolic OH groups or functional groups which may be produced during the derivatization of the HA, and thus are methylated. Nevertheless, at least 54 % of the primary phenolic hydroxyl groups are blocked. Furthermore, the modified synthetic HA (M1-B) shows a higher amount of carboxylic groups than the synthetic HA of type M1. This is due to the hydrolysis of ester groups of the original HA (see Fig. 1). Also hydrolysis of amide groups may occur which results in the formation of carboxylic groups.

Functional group [meq/g]	Calcium acetate exchange /2/			Radiometric determination /3/			Direct titration		
	M1	M1-B	M1-V	M1	M1-B	M1-V	M1	M1-B	M1-V
COOH + phenolic OH	-	-	-	3.53 ±0.10	3.12 ±0.02	4.10 ±0.20	-	-	-
COOH	1.02 ±0.06	1.91 ±0.07	2.03 ±0.02	1.24 ±0.11	2.06 ±0.18	2.40 ±0.15	-	-	-
phenolic OH	-	-	-	2.28 ±0.09	1.06 ±0.19	1.70 ±0.10	-	-	-
PEC[a]	-	-	-	-	-	-	1.36 ±0.08	1.80 ±0.25	2.12 ±0.06

a) PEC = Proton exchange capacity determined by direct titration

Tab. 1: Functional groups of the original synthetic HA (type M1), the synthetic HA with blocked phenolic OH groups (type M1-B) and the alkaline saponified synthetic HA (type M1-V).

The blocking of phenolic hydroxyl groups was further confirmed by FTIR spectroscopy.

Fig. 2 shows the spectra of the modified and non-modified synthetic HA. A def-inite indication for the modification of phenolic hydroxyl groups is the absence of the absorption band at 1292.8 cm^{-1} in the spectrum of HA M1-B, which is due to phenolic OH groups. The spectrum of the unmodified HA M1 shows this band. The ether group absorption bands (1023.9 cm^{-1}, 1097.4 cm^{-1} and 1246.8 cm^{-1}) in the spectrum of the modified HA also confirm that phenolic hydroxyl groups are blocked. Additionally, the increase of the absorption band at 2862.8 cm^{-1} indicates the for-mation of methyl ethers. The increase of the intensity of the absorption band at 1453.5 cm^{-1} (C-H deformation vibrations) comes from the incorporation of CH_3-groups into the HA molecule as a result of the methyl ether formation (see Fig. 1). Furthermore, the synthetic HA of type M1-B has a significantly higher amount of carboxylic groups (1712.2 cm^{-1}) than the original HA.

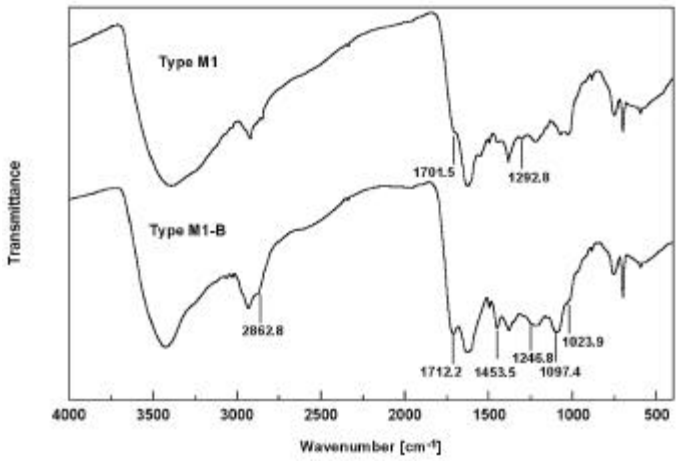

Fig. 2: FTIR spectra of the non-modified synthetic HA of type M1 and the synthetic HA with blocked phenolic OH groups (type M1-B).

For the investigation of the influence of phenolic OH groups on the complexation behavior of HA it is required that both HA, the phenolic OH modified and non-modified HA, have a similar composition and a comparable carboxylic group content. For this reason, we performed an alkaline saponification of the synthetic HA of type M1 in the same manner than the saponification of the permethylated synthetic HA of type M1. The resulting synthetic HA of type M1-V has an amount of carboxylic groups that is comparable with HA from type M1-B, but has a higher content of phenolic OH groups (see Tab. 1). The amount of phenolic OH groups is somewhat lower than in the original HA. This may be caused by condensation reactions during refluxing with methanolic NaOH.

We have successfully synthesized two HA model substances (M1-B, M1-V) to study the influence of phenolic OH groups on the metal ion complexation behavior of HA.

Acknowledgments

This work was supported by the Bundesministerium für Bildung und Forschung (BMBF) under contract number 02 E88150. The authors thank M. Meyer and R. Ruske for their assistance with the characterization of the HA.

References

/1/ Pompe, S., Bubner, M., Denecke, M.A., Reich, T., Brachmann, A., Geipel, G., Nicolai, R., Heise, K.H., Nitsche, H.: A comparison of natural HA with synthetic HA model substances: characterization and interaction with uranium(VI). Radiochim. Acta **74**, 135 (1996)

/2/ Schnitzer, M., Khan, S.U.: *Humic substances in the environment.* (A.D. McLaren, ed.). Marcel Dekker, Inc., New York 1972

/3/ Bubner, M., Heise, K.H.: Characterization of humic acids. II. Characterization by radioreagent-derivatization with [^{14}C]diazomethane. In: Report FZR-43, Institute of Radiochemistry, Annual Report 1993, p.22 (1994)

REDOX SITUATION IN THE SAXON HIGHLAND BOG "KRANICHSEE"

L. Baraniak, A. Abraham [1], D. Vulpius [2], H. Nitsche
Forschungszentrum Rossendorf e.V., Institute of Radiochemistry
[1] Technische Universität Dresden, Institute of Analytical Chemistry, Radiochemical Group
[2] Fachhochschule Magdeburg, Chemical Section

The transition from aerobic to anaerobic conditions was studied in the "Kranichsee" bog ground by measuring the redox potential and the oxygen content of the moor water at the surface and in the roots in different depths.

Weathering processes lead to the decomposition of crystalline geomaterials accompanied with the dissolution of parts of the material. Especially the weathering of pyrite with the generation of sulfuric acid and trivalent iron leads to conditions under these ores and minerals can be oxidized and dissolved. Uraninite and pitchblende are representative for such materials. Uranium mines in Saxony and Thuringia are currently being decommissioned by controlled flooding with ground and surface water. The transition from surface-near aerobic to anearobic conditions in the mine water plays an important role because uranium(VI) can be reductively immobilized. To assess the natural change from oxidizing to reducing conditions, we studied the moor ground *"Kleiner Kranichsee"* near the town Johanngeorgenstadt (Saxony) and measured the redox potential and the oxygen content as a function of the depth.

Description of the highland moor

The moor is situated on the crest of the Erzgebirge at 900 m. Its formation dates back to the later glacial, about 13,000 years ago /1/. The water-impermeable underground like a small

basin was formed by weathering of granite, gneiss, porphyry, and micaslate, the typical acidic rocks of that mountain site (Fig. 1).

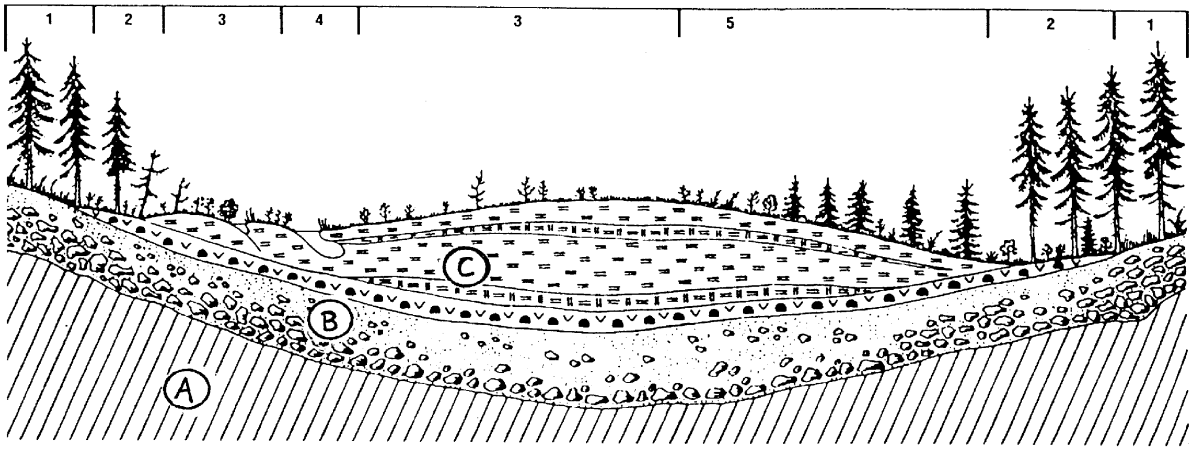

Fig. 1: Schematic of the highland moor *"Kranichsee"*. [1] pine forest on mineral soil; [2] moor pines at the borderline; [3] peat moss population; [4] cotton grass and moss at puddles; [5] dwarf bushes and moor pines. A: acidic crystalline rock basement; B: rock weathering rubble; C: moor-peat body.

The mountain crest has a high rainfall ($1,000 mm/a) and a cold climate (4-5°C average temperature) and only few nutrients. Metabolisms, therefore, proceed slowly and plant growth is very limited (stagnant biotope). Few plants and animals are present under these conditions. The main plants are mosses, cotton grasses, rushes, cranberry, sundew and marsh calla. The moor pines grow to a height of 2 m. The moor bottom consists of dense roots. Dead plants sink to the moor's bottom and decompose under oxygen consumption and create thus anaerobic and reducing conditions /2/.

Measurements and results

The test site was in the eastern moor part about 200 m from the edge. The measurements were carried out in surface water and in five boreholes to a depth of one meter. The moor water is acidic (pH 3.7) and characterized by a very low mineral concentration (salt content# 25 mg/L).

Component	Na	Mg	Al	Si	K	Ca	Mn	Fe	Zn	Ba	Pb	U	HM[1)]
[mg/L]	0.577	0.258	0.305	0.825	0.459	3.590	0.027	0.567	0.050	0.012	0.015	0.002	0.013
Component	chloride			sulfate			carbonate			DOC			
[mg/L]	1.4			6.7			8.8			38.8			

Tab. 1: Chemical composition of the moor surface water. [1)] sum of heavy metals: Co, Cr, Ni, Cu, Cd, As

The main constituents are Ca^{2+}, Na^{+}, Fe^{3+}, K^{+}, Al^{3+}, Mg^{2+}, in the form of carbonates, sulfates, chlorides and silicates (Tab. 1). The water is rich on humic substances (up to 80 mg/L).

Depht [cm]	Oxygen content [mg/L]	Redox potential [mV] vs. SHE
0	11.06 ± 0.19	624.5 ± 5.0
30	0.89 ± 0.03	460.5 ± 11.5
33	2.26 ± 0.49	382.3 ± 6.0
55	0.36 ± 0.05	468.8 ± 3.8
58	3.15 ± 0.20	413.0 ± 21.3
80	1.26 ± 0.09	377.3 ± 8.6

Tab. 2: Oxygen content and redox potential as a function of the moor's soil depth at five different measuring points

The oxygen concentration and the redox potentials were determined by commercial instruments: WTW oximeter, type Oxi 325, sensor: CellOx 325 and potentiometer, type pH 325, sensor: SenTix ORP on the basis of a cell with liquid junction: Pt (sample)//KCl(3 M), $AgCl_s$, Ag. The surface water contains up to 11 mg/L oxygen, corresponding to a redox potential of 625 mV vs. NHE (Tab. 2). Already in a depth of 0.3 m the oxygen concentration and the redox potential is considerably reduced. The values are between 0.4 and 3.2 mg/L oxygen and between 160 and 240 mV vs. NHE and continue to decrease with depth: 377 mV vs. NHE were measured at 0.8 m.

If we compare these results with the redox potentials measured by Baas Becking et al. /3/ in marshy grounds, we find that at the given acidity (pH 3.7) our results lie in the range of 300-650 mV vs. NHE the most frequently occurring values of natural peat fields (Fig. 2).

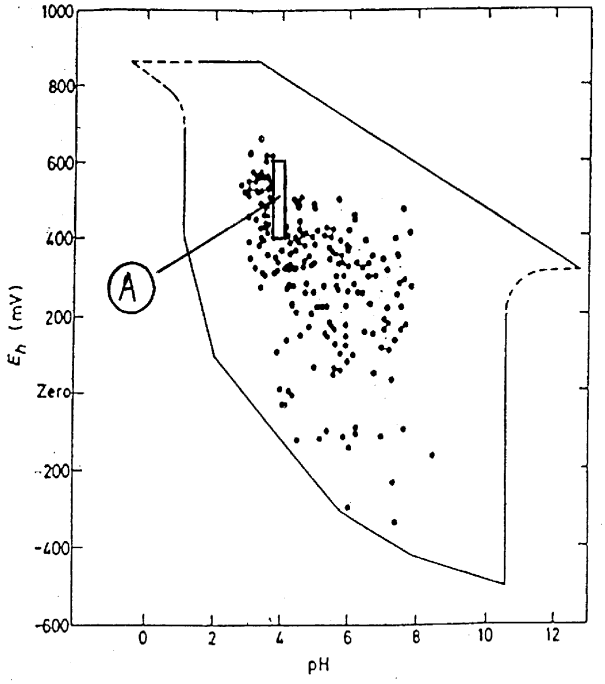

Fig. 2: Eh-pH characteristics of peat fields /2/. (A: range of redox potentials measured at *Kranichsee*)

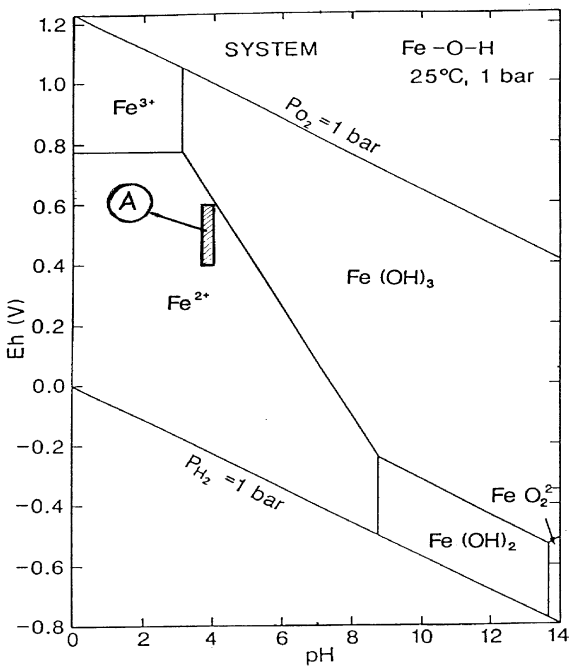

Fig. 3: Eh-pH diagram for the system Fe-O-H at 10^{-6} mol/L dissolved Fe /4/. (A: range of redox potentials measured at *Kranichsee*)

Conclusions

If we arrange our redox potentials in the Eh-pH diagram of the Fe-O-H system (Fig. 3), we find that our sub-surface results lie in the stability field of iron(II), i.e., under such anaerobic conditions iron(III) would be completely reduced to the divalent state /4/. This was confirmed by the iron(II) signal in the voltammetric analysis of the moor water (-1.35 V vs. SE). The reduction of uranium(VI) at this pH requires a potential below 220 mV vs. NHE that is not reached in our case.

References

/1/ Ulbricht, H., Büttner, R., Funke, H., Gutte, P., Hempel, W., Müller, G., Schretzenmayer, M., Weise, G.: Berichte der Arbeitsgemeinschaft sächsischer Botaniker, Neue Folge V/VI, (1963/64), Heft 2
/2/ Szilagyi, M.: Valency changes of metal ions in the interaction with humic acid. FUEL **53**, 26 (1974)
/3/ Baas Becking, L.G.M., Kaplan, I.R., Moore, D.; J. Geol. **68**, 243 (1960)
/4/ Brookins, D.G.: *Eh-pH Diagrams for Geochemistry*. Spinger-Verlag Berlin, 1988, S. 73

ISOLATION AND CHARACTERIZATION OF AQUATIC HUMIC SUBSTANCES FROM BOG WATER

K. Schmeide, S. Pompe, K.H. Heise, R. Nicolai[1], H. Nitsche
Forschungszentrum Rossendorf e.V., Institute of Radiochemistry
[1] Institute of Bioinorganic and Radiopharmaceutical Chemistry

Humic substances were isolated from water of the mountain bog 'Kleiner Kranichsee'. The bog is in the vicinity of the uranium mining sites Johanngeorgenstadt (Saxony). The humic material was separated into humic and fulvic acid fractions and characterized for its elemental composition, functional properties, charge/size distribution ratios and spectroscopic characteristics. The results were compared with data of a commercial humic acid from Aldrich.

Humic and fulvic acids (K-HA and K-FA) were collected by an isolation procedure (described in /1/) utilizing Supelite™ DAX-8 (Supelco) from surface water of the mountain bog 'Kleiner Kranichsee'. The humic material was characterized for its elemental composition, functional properties, charge/size distribution ratios and spectroscopic characteristics.

Results

The elemental composition of the humic substances (corrected for ash and moisture content) is given in Tab. 1. The Kranichsee humic substances have a similar carbon and sulfur content. The hydrogen and especially the nitrogen content of the K-FA are lower than those of K-HA.

Element [%]	Kranichsee HA	Aldrich HA	Literature [c] HA	Kranichsee FA	Literature [c] FA
C	49.9 ± 0.3	58.7 ± 0.6	50 - 60	48.8 ± 0.06	40 - 50
H [a]	3.5 ± 0.4	3.3 ± 0.1	4 - 6	2.6 ± 0.1	4 - 6
N	1.8 ± 0.1	0.8 ± 0.1	2 - 6	0.6 ± 0.005	1 - 3
S	0.5 ± 0.01	4.1 ± 0.03	0 - 2	0.5 ± 0.02	0 - 2
O [b]	33.4 ± 0.3	24.8 ± 0.6	30 - 35	39.1 ± 0.1	44 - 50
O/C	0.50	0.32	0.50 ± 0.03	0.60	0.51 ± 0.10

Tab. 1: Elemental composition of K-HA and K-FA in comparison with A-HA and with literature data. [a] Corrected for water content of samples. [b] Calculated as difference to 100 %. [c] according to /2/.

The K-FA has a higher oxygen content than the K-HA and thus, a higher O/C atomic ratio. These values are typical of those compiled in the literature /2,3/. The Aldrich HA (A-HA) has a different elemental composition than the Kranichsee humic substances which can be attributed to its different origin. Tab. 1 also shows that the elemental compositions of the analyzed humic substances are similar to the average elemental compositions of humic substances given in the literature.

Functional group [meq/g]		COOH + Phenolic OH	COOH	Phenolic OH
Calcium acetate method	Kranichsee HA		4.20 ± 0.17	
	Kranichsee FA		6.05 ± 0.31	
	Aldrich HA		4.41 ± 0.11	
Radiometric method	Kranichsee HA	7.75 ± 0.35	3.88 ± 0.41	3.87 ± 0.52
	Kranichsee FA	8.82 ± 0.48	3.98 ± 0.25	4.84 ± 0.65
	Aldrich HA	7.4 ± 0.4	3.9 ± 0.1	3.4 ± 0.4

Tab. 2: Functional groups of Kranichsee HA and FA in comparison with Aldrich HA

The functional groups of the humics were determined radiometrically and by the calcium acetate method. The results are given in Tab. 2. According to the radiometric analysis, the total acidity and the carboxylic group content of the K-FA are only slightly higher than those of the K-HA. However, the carboxylic group content of the K-FA determined by Ca-exchange (6.05 meq/g) is much higher than the carboxylic group content determined radiometrically (3.98 meq/g). Furthermore, it is even higher than the proton exchange capacity determined by direct titration (5.6 meq/g). We assume that the carboxylic group content of the FA determined by Ca-exchange is too high. One reason could be its content of acidic OH groups /2/ or other acidic protons that could influence the titration result. The A-HA contains more COOH and fewer phenolic OH groups than the K-HA.

The charge-to-size ratio of the humics was determined by capillary zone electrophoresis. Fig. 1 presents the electropherograms of the humic substances. The peak shapes of the humic substances are similar. The larger migration time of the K-FA compared to that of K-HA is caused by its smaller molecular size and its somewhat higher number of dissociated functional groups. This confirms the results of the functional group determination. A-HA exhibits both a higher migration time and a higher UV absorption intensity than the K-HA. This can also be attributed to a higher charge-to-size ratio. Presuming that both HA's have comparable molecular masses, a different amount of charge carriers must exist. According to the calcium acetate and the radiometric method, the COOH-content of A-HA is higher than that of K-HA. The higher UV absorption intensity could be caused by a greater number of UV-active groups.

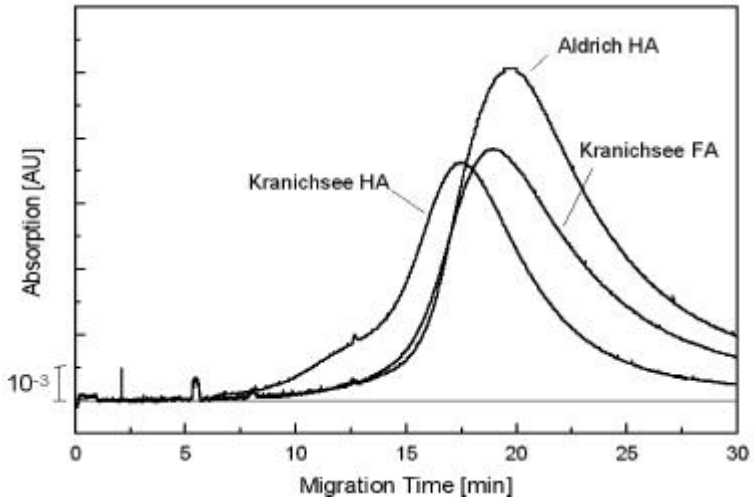

Fig. 1: Electropherograms of Kranichsee HA and FA compared to Aldrich HA. Separation conditions: buffer 40 mM Na_2HPO_4, 20 mM H_3BO_3, pH 7.86; 30E C; 15 kV, I: 84 µA; 214 nm; 15 s injection; fused silica capillary, 75 µm i.d. x 50 cm; P/ACE 2050 Beckman Instruments

The IR spectra of the humics are shown in Fig. 2. These spectra are similar to typical IR spectra of humic and fulvic acids published in the literature /4/. In addition to characteristic absorption bands that are common to all three spectra, differences in the intensity of some bands exist. The intensity of the band centered at about 3415 cm^{-1} region (O-H stretch) is

stronger for the K-HA and K-FA than for the A-HA. This is due to the higher phenolic content of the Kranichsee humic substances and confirms the result of the radiometric functional group determination. The higher intensity of the absorption bands in the 2960-2850 cm^{-1} region indicates a higher content of aliphatic C-H bonds (A-HA > K-HA $ K-FA). All three IR spectra show two sharp absorption bands near 1720 cm^{-1} (C=O stretching of COOH and ketones) and 1620 cm^{-1} (aromatic C=C and H bonded C=O). There are minor differences between the intensities of the 1720 cm^{-1} band and the 1620 cm^{-1} band. The 1720 cm^{-1} band has a slightly higher relative intensity compared to the 1620 cm^{-1} band for the K-FA than for the K-HA, indicating a somewhat higher COOH content for the FA. The small band at 1510 cm^{-1}, present in the spectra of the K-HA and even smaller in the spectra of the K-FA, can be assigned to aromatic C=C double bonds. The very broad band in the 1280-1200 cm^{-1} region (C-O stretch and OH deformation of COOH) decreases in the following sequence: A-HA > K-FA ~ K-HA. This can again be attributed to the content of carboxylic groups.

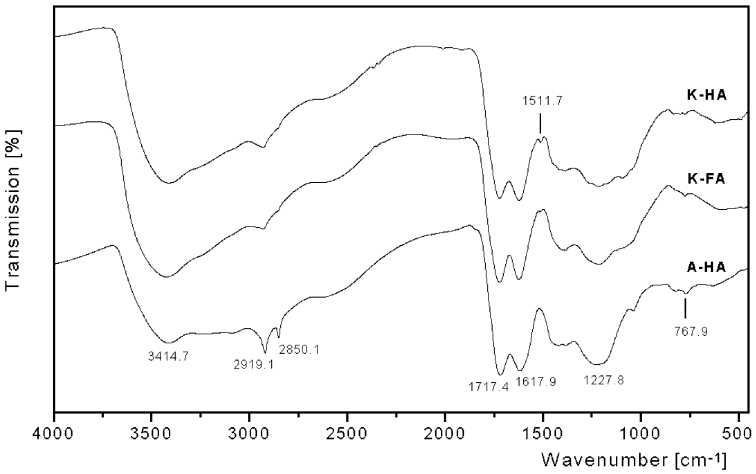

Fig. 2: IR spectra of Kranichsee HA and FA (K-HA, K-FA) compared to Aldrich HA (A-HA)

These isolated site-specific humic substances from the Kranichsee site will be used for complexation studies with uranyl ions.

Acknowledgment

This work was supported by Commission of the European Communities under contract no. F14W-CT96-0027. The authors thank R. Ruske and M. Meyer for determining the functional groups and H. Görner for elemental analyses.

References

/1/ Schmeide, K., Zänker, H., Heise, K.H., Nitsche, H.: Isolation and characterization of aquatic humic substances from the bog ''Kleiner Kranichsee''. In: 1st Technical Progress Report of the EC Project FI4W-CT96-0027 (1998).

/2/ Stevenson, F.J.: *Humus chemistry, genesis, composition, reactions*. John Wiley & Sons, New York 1994.

/3/ Pettersson, C., et al.: On the composition and properties of humic substances isolated from deep groundwater and surface waters. Org. Geochem. **21(5)**, 443-451 (1994).

/4/ Schnitzer, M., Khan, S.U.: *Humic substances in the environment*. (A.D. McLaren, ed.), Marcel Dekker, Inc., New York 1972.

TESTING OF DIFFERENT RESINS FOR ISOLATING AQUATIC HUMIC SUBSTANCES

K. Schmeide, K.H. Heise, H. Nitsche
Forschungszentrum Rossendorf e.V., Institute of Radiochemistry

The suitability of different macroporous resins for isolating aquatic humic substances was investigated. The adsorption capacity and the elution efficiency of EP 61, Lewatit 1062, Lewatit 1064, Lewatit 1066 and Supelite™ DAX-8 in comparison to a sample of Amberlite XAD-8 were determined. DAX-8 is an excellent sorbent for humic acid and can highly be recommended for the isolation of aquatic humic acids.

The adsorption of humic substances onto non-ionic macroporous resins is a practicable method for isolating humic substances from water. Amberlite XAD-8 was widely used to separate aquatic humic substances /1/. This resin is no longer commercially available. Therefore, the following six potential replacement resins that vary in physical properties like pore size and volume as well as specific surface area were investigated with regard to their sorptive properties: EP 61 (ethylvinylbenzene-divinylbenzene copolymer, Chemiekombinat Bitterfeld), Lewatit

1062, Lewatit 1064, Lewatit 1066 (all styrene-divinylbenzene copolymere, Bayer AG, Leverkusen), Supelite™ DAX-8 (acrylic ester polymer, Supelco, Bellefonte, PA), and Amberlite XAD-8 (acrylic ester polymer, Merck, Darmstadt).

Experimental

Commercial humic acid (HA) from Aldrich was used to test the resins. Test solutions containing 4.5 mg HA/L at pH 2 were passed through glass columns that were filled with equal volumes (10 mL) of the resins. The average flow rate was 0.28 mL/min. The column eluate was collected as small-volume fractions (. 20 mL) and the ultraviolet absorption of all fractions was monitored at 360 nm. The loading of the resin was stopped after the HA had broken through and the light absorption of the fractions became nearly constant. The resin was washed with 0.1 M HCl to displace the residual HA solution. Then the HA was eluted with 0.1 M NaOH. This elution solution desorbed the HA and thus, the HA concentration in the column eluate increased rapidly. The small-volume middle fraction that contained the highly concentrated HA solution is termed 'center cut'. After the 'center cut', the HA concentration in the column eluate gradually decreased.

In order to determine the amount of adsorbed HA and its recovery, the ultraviolet absorption of all fractions at 360 nm was compared with the absorption of the HA standard solution at the same wavelength and pH.

As examples, the combination of the breakthrough curve (loading process) and the elution (unloading process) are shown in Fig. 1 and Fig. 2 for DAX-8 and Lewatit 1066, respectively.

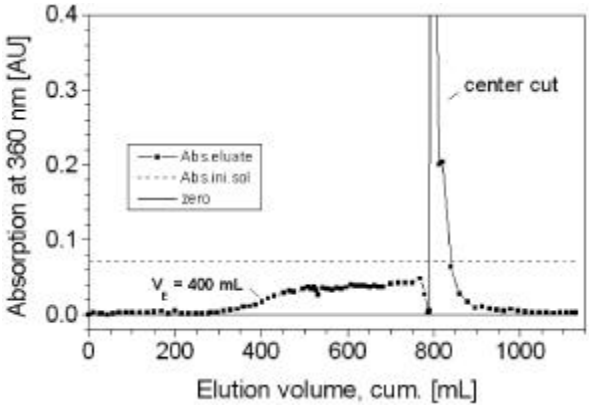

Fig. 1: Elution curve of DAX-8

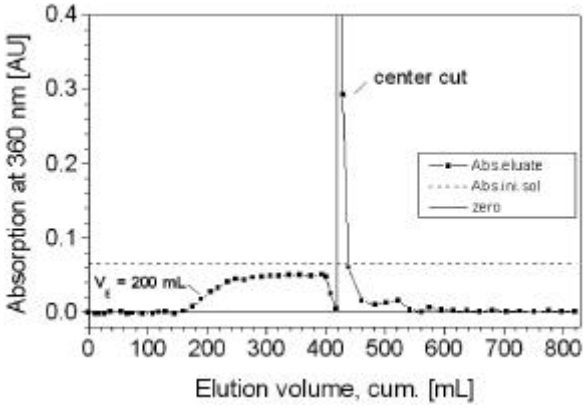

Fig. 2: Elution curve of Lewatit 1066

In order to determine the resins' adsorption capacity, the breakthrough curves were analyzed until the breakthrough point V_E (V_E corresponds to the inflection point of the curves). At V_E the column is near saturation so that large particles break through while smaller ones are further adsorbed. This is indicated by the fact that the light absorption of the HA standard solution is not yet reached even after adding much more HA solution (equilibrium state). This causes an undesired fractionation of HA particles. For the different resins the following characteristic data were determined: i) the breakthrough volume V_E, ii) the part of the added HA that was adsorbed until V_E, and iii) the part of the added HA that could not be adsorbed until V_E.

Furthermore, the elution efficiency of the resins was determined by means of the elution curves. The recovery of the HA was analyzed in relation to the amount of HA that was totally adsorbed during the entire loading process. Moreover, the HA concentration in the first 25 mL of column effluent during the elution (~center cut) was calculated. This is a measure of the resin's ability to concentrate diluted HA solutions.

Results

The results are listed in Tab. 1 and are discussed below.

EP 61: The HA particles are almost completely adsorbed before the breakthrough point V_E, but both V_E and the adsorption capacity are very low (62 mL and 0.25 mg, respectively). Furthermore, the resin shows the lowest ability to concentrate HA (c_{HA}=0.37 mg HA/25 mL).

Lewatit 1062: The adsorption capacity is only slightly higher (until V_E only 0.4 mg of the HA are adsorbed).

Lewatit 1066: The resin adsorbs a higher amount of HA (1.1 mg) and its fractionation tendency until V_E is very low. That means, the HA added to the resin is completely adsorbed.

XAD-8: This resin shows a high adsorption capacity; until V_E 1.5 mg of HA are adsorbed (twice

as much as for Lewatit 1064). The adsorbed HA is completely recovered by eluting the column with NaOH. The concentration in the 'center cut' is 1.84 mg HA/25 mL.

Resin	Average flow rate [mL/min]	Break-through volume V_E [mL]	HA not adsorbed until V_E [mg]	HA ad-sorbed until V_E [mg]	HA ad-sorbed until V_E [%]	Elution of the HA adsorbed (in relation to total loading process) [mg]	Elution of the HA adsorbed (in relation to total loading process) [%]	c_{HA} in first 25 mL during the unload-ing process [mg/25mL]
EP 61	0.27	62	0.02	0.25	92.3	0.4	82	0.37
Lewatit 1062	0.29	100	0.03	0.4	92.1	1.05	72.2	0.87
Lewatit 1064	0.25	177	0.06	0.72	91.8	0.84	76.3	0.71
Lewatit 1064	0.30	174	0.03	0.73	94.5	0.84	76.3	0.83
Lewatit 1066	0.30	200	0.006	1.08	100.7	0.69	54.3	0.65
Amberlite XAD-8	0.27/0.39	354	0.09	1.5	94.4	1.96	104.3	1.84
Supelite™ DAX-8	0.26	400	0.02	1.76	99.0	2.19	80.6	1.97

Tab. 1: Results of the adsorption experiments.

DAX-8: DAX-8 is the most efficient resin of all tested resins for the removal of HA from water. It adsorbs 1.8 mg of HA until V_E which means that 99 % of the added HA's are adsorbed. The recovery, being 81 %, is somewhat lower than the recovery with XAD-8. In contrast to XAD-8, the sorbent DAX-8 was a new and unused resin. We assume that a certain fraction of the HA particles is retained in the pores of the resin. Furthermore, DAX-8 enables one to collect a highly concentrated 'center cut' - a concentration of 1.97 mg HA/25 mL is achieved.

Conclusion

The sequence of resin adsorption capacity was determined as:
DAX-8 > XAD-8 > Lewatit 1066 > Lewatit 1064 > Lewatit 1062 > EP 61. This demonstrates that high specific surface areas, as shown by the Lewatit resins and EP 61 (500-700 m^2/g compared to 140-160 m^2/g of XAD-8 and DAX-8), do not necessarily result in high sorption.
Furthermore, XAD-8 and DAX-8 (resins of aliphatic polymer matrices) can be more efficiently eluted than resins of aromatic polymer matrices (Lewatit resins and EP 61).
EP 61 and Lewatit 1062 are inefficient for isolating HA. Lewatit 1064 and 1066 can possibly be used as sorbents for HA because of their somewhat higher adsorption capacities.
DAX-8 was shown to be an excellent sorbent for HA. The adsorption efficiency of Supelite™ DAX-8 (Supelco) is nearly identical to that of Amberlite XAD-8.

References

/1/ Aiken, G.R., McKnight, D.M., Wershaw, R.L.: *Humic Substances in Soil, Sediment, and Water - Geochemistry, Isolation, and Characterization*. John Wiley & Sons, New York 1985

SPECIATION OF HEXAVALENT URANIUM IN THE PRESENCE OF LIGNIN DEGRADATION PRODUCTS

L. Baraniak, G. Bernhard, H. Nitsche
Forschungszentrum Rossendorf e.V., Institute of Radiochemistry

To quantify the influence of wood decomposition on the uranium(VI) migration via aquatic path speciations in the presence of protocatechuic acid, vanillic acid and vanillin were carried out for carbonate-free and calcite-rich water.

Phenolic compounds, such as protocatechuic acid, vanillic acid and vanillin represent relatively stable intermediates of the hydrothermal lignin decomposition process /1/. These compounds are able to complex uranium(VI) /2/. The influence of these compounds on the uranium speciation was estimated for carbonate-free and calcite-rich solution. The background is the restoration of underground mines in sediments and crystalline rock.

Complex formation in carbonate-free solution

Complex formation with the organic complexants starts with the strong decrease of the $[UO_2^{2+}]$ in the pH range 4.5 to 5.5 and is accompanied by the formation of the typical hydroxo species:

$[UO_2(OH)]^+$, $[(UO_2)_2(OH)_2]^{2+}$, $[(UO_2)_3(OH)_4]^{2+}$, $[(UO_2)_3(OH)_5]^+$, $[(UO_2)_4(OH)_7]^+$ and $[UO_2(OH)_2]$ /3/.

If *protocatechuic acid* (3,4-dihydroxybenzoic acid) /PCA/ is present, the 1:1 complex $[UO_2(PCA)]^-$ occurs between pH 5 and pH 8, and the 1:2 complex $[UO_2(PCA)_2]^{4-}$ lies between pH 7 and pH 11 (Fig. 1).The so far unconfirmed 1:3 complex appears at pH$8.5. Hydrolysis is predominant between pH 5 and pH 7. At higher pH-values, hydrolysis is suppressed by the formation of the strong 1:2 complex.

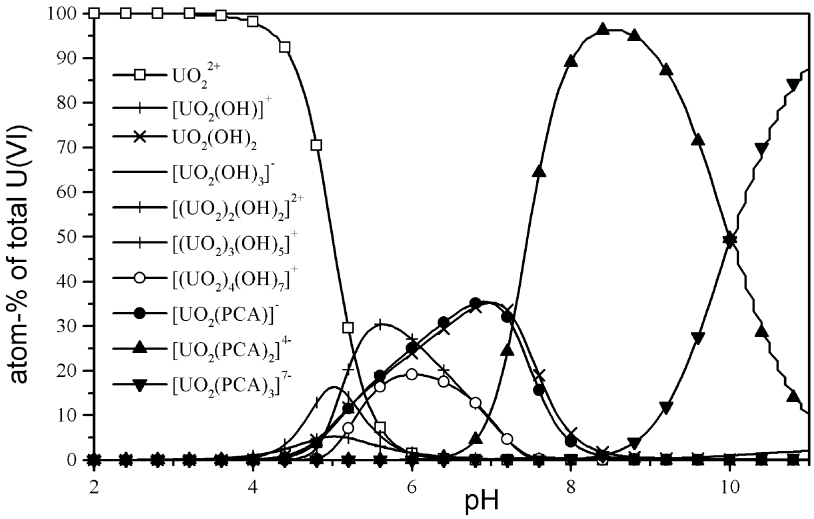

Fig. 1: Speciation of uranium(VI) in the presence of protocatechuic acid (U(VI): 5 ppm; PCA: 25 ppm)

If 5 ppm uranium(VI) are complexed by 25 ppm PCA (a typical concentration of organic matter in mine water), the maximum of $[UO_2(PCA)]^-$ is at pH 7 with 24.5 atom% of the initial uranium(VI) complexed, and the highest content of $[UO_2(PCA)_2]^{4-}$ amounts to 95.6% at pH 8.5 (Tab. 1). A decrease of the [PCA] by one order of magnitude (2.5 ppm) causes a significant decrease of the complex species: $[UO_2(PCA)]^-$ is reduced to 2-3% (pH 6-8) and $[UO_2(PCA)_2]^{4-}$ to about 20% at pH 9.

complex	stability	species distribution [atom-%]	
		acidic (pH 5-6)	neutral (pH 7-8)
$[UO_2(PCA)]^-$	14.5	4.7 - 16.4	24.5
$[UO_2(PCA)_2]^{3-}$	25.6	3.5	9.9 - 88
$[UO_2(VNA)]$	7.37	15.0 - 6.2	0.8
$[UO_2(VNA)_2]^{2-}$	13.5	0.9 - 4.4	8.0
$[UO_2(VAN)]^+$	4.47	1.5 - 0.8	# 0.1
$[UO_2(VAN)_2(OH)_2]^{2-}$	-3.95	0.15	1.8 - 9.3

Tab. 1: Species distribution in weakly acidic and neutral carbonate-free solution

The less stable complexes with *vanillic acid* (4-hydroxy-3-methoxybenzoic acid) /VNA/ were found at VNA contents higher than 3 ppm. In the case of complexation of 5 ppm uranium(VI) with 25 ppm VNA, $[UO_2(VNA)]$ appears in the pH range 4-6 with a maximum content of 15% at pH 5.2 and the $[UO_2(VNA)_2]^{2-}$ lies between pH 5 and pH 9 with 8.1% near pH 8 (Tab. 1). Compared with PCA, hydrolysis in the vanillic acid system is nearly the same under weakly acidic conditions. But in alkaline solution the formation of $[UO_2(VNA)_2]^{2-}$ is much more suppressed by hydrolysis as for $[UO_2(PCA)_2]^{4-}$.

Vanillin (4-hydroxy-3-methoxybenzaldehyde) /VAN/ forms the 1:1 complex $[UO_2(VAN)]^+$ and the partially hydrolyzed species $[UO_2(VAN)_2(OH)_2]^{2-}$ (Tab. 1). The first appears at pH 5.2 and changes to the second at pH 6.5 with its maximum at pH 8.2. At 5 ppm uranium(VI) and 25 ppm organic ligand, about 1.5% of the UO_2^{2+} is bound to $[UO_2(VAN)]^+$ and 10% is complexed to $[UO_2(VAN)_2(OH)_2]^{2-}$.

Complex formation in the presence of carbonate

Carbonate ions form very stable complexes with uranium(VI): $[UO_2CO_3]$ (log ß = 9.68, pH 5-6), $[UO_2(CO_3)_2]^{2-}$ (16.9, pH 6.5-8), $[UO_2(CO_3)_3]^{4-}$ (21.6, pH$8) and $[(UO_2)_2CO_3(OH)_3]^-$ (-19.0, pH 5-7) /4/.

complex	stability	species distribution [atom-%]	
		acidic (pH 5-6)	neutral (pH 7-8)
$[UO_2(PCA)]^-$	14.5	4.4 - 9.1	3.7 - 0.8
$[UO_2(PCA)_2]^{3-}$	25.6	# 0.1	1.0 - 26
$[UO_2(VNA)]$	7.37	15.5 - 3.2	# 0.1
$[UO_2(VNA)_2]^{2-}$	13.5	1.1 - 3.2	1.2 - 0.3
$[UO_2(VAN)]^+$	4.47	1.5 - 0.7	# 0.1
$[UO_2(VAN)_2(OH)_2]^{2-}$	-3.95	# 0.1	0.1 - 0.3

Tab. 2: Species distribution in weakly acidic and neutral carbonate-rich solution

The strongest is $[(UO_2)_2CO_3(OH)_3]^-$ which appears at the given $[UO_2^{2+}]$ already at µmolar $[CO_3^{2-}]$ (#0.1 ppm), whereas the mono-nuclear species $[UO_2(CO_3)_n]^{(2-2n)}$ with n#3 become exists at $[CO_3^{2-}]$ $ 10^{-4} M ($6 ppm). Compared to a carbon-

ate-free solution, the U(VI) speciation in the presence of carbonate is dominated by carbonato complexes at pH$5.5.

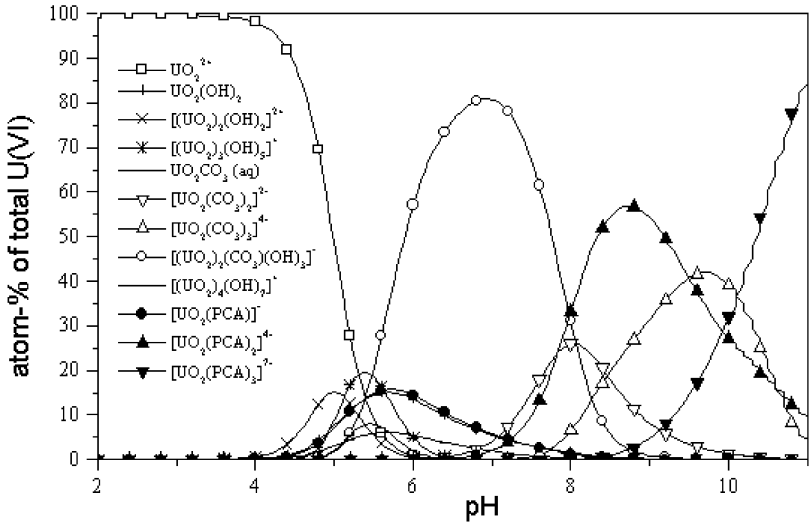

Fig. 2: Speciation of uranium(VI) in the presence of protocatechuic acid and carbonate (U(VI): 5 ppm; PCA: 25 ppm; CO_3^{2-}: 120 ppm)

In the case of complexation with *protocatechuic acid* (5 ppm U, 25 ppm PCA) in the presence of 120 ppm CO_3^{2-}, the 1:1 and 1:2 complexes are formed to 9.6% (pH 5.7) and 47% (pH 8.7), respectively (Fig. 2; Tab. 2). That means the complexation with PCA is decreased by a factor more than two compared with the carbonate-free solution. In the same way hydrolysis is limited, especially at pH$6.3. In calcite-saturated water (1200 ppm CO_3^{2-}) the formation of PCA complexes is negligible.

In the case of *vanillic acid* nearly the same amount uranium(VI) is bound in $[UO_2(VNA)]$ as in the carbonate-free solution (about 15%), whereas the uranium(VI) in $[UO_2(VNA)_2]^{2-}$ is decreased from 9 to 3.2% (Tab. 2).
Complexation with *vanillin* is rather low: $[UO_2(VAN)]^+$ is met to 1.5% and $[UO_2(VNA)_2(OH)_2]^{2-}$, the dominant species in carbo-nate-free solution, disappeared completely (Tab.2).
The following *conclusions* can be drawn: (1) the interaction of uranium(VI) with protocatechuic and vanillic acid in weakly acidic waters leads to stable complexes which occurs in concentrations comparable with the hydroxo species and (2) the interaction with the organic ligands is strongly suppressed in the presence of high carbonate concentrations (neutral calcite-rich waters).

Acknowledgments
This study was supported by the Sächsisches Ministerium für Wissenschaft und Kunst under contract no. 4.7541.88-FZR/402.

References
/1/ Masselter, S., Zemann, A., Bobleter, O.: Analysis of Lignin Degradation Products by Capillary Electrophoresis. Chromatographia **40**, 51-56 (1995)
/2/ Baraniak, L., Schmidt, M., Bernhard, G., Nitsche, H.: Complex Formation of Hexavalent Uranium with Lignin Degradation Products. In: Report FZR-180, Institute of Radiochemistry, Annual Report 1996, p. 28 (1997)
/3/ Baes, Jr., C.F., Mesmer, R.E.: *The Hydrolysis of Cations*. Krieger Publ. Comp., Malabar, Florida 1986, pp. 176.
/4/ Grenthe, I., Fuger, J., Konings, R.J.M., Lemire, R.J., Muller, A.B., Nguyen-Trung Cregu, Wanner, H.: *Chemical Thermodynamics of Uranium*, NEA OECD, 1992, p.308

KINETICS OF IRON(III) REDUCTION BY SPRUCE WOOD LIGNIN

B. Mack, L. Baraniak, G. Bernhard, H. Nitsche
Forschungszentrum Rossendorf e.V., Institute of Radiochemistry

The reduction of Fe(III) by lignin was studied from pH 2 to 4. The reduction decreased with increasing pH and occurs in a two-step process with different reaction rates.

In the process of uranium mine flooding in Saxony and Thuringia, Germany, spruce wood degrades and lignin is released. We investigated how lignin may change the redox potential of mine water by possible reducing Fe(III) to Fe(II).
The lignin was isolated from spruce wood by methanol extraction /1/. The kinetics of Fe(III) reduction by lignin was determined with 55 data points between pH 2 and 4 and at Fe(III)

concentrations from 0.2 to 5 mmol/L. The lignin concentration was 0.15 g/L and the ionic strength 0.1 M (KCl). The samples were equilibrated under nitrogen for 10 weeks in the dark. Subsamples were taken as a function of time and analyzed for Fe(II) concentrations. Lignin was separated by precipitation with sulfuric acid, and Fe(II) was determined spectrophotometrically with 1,10-phenanthroline /2/.

Results

Half of the initial amount of Fe(III) of a 3 mmol/L solution was reduced at pH 2.5 after 10 weeks. The reduced Fe(III) concentrations decreased with increasing pH: from about 50 mol % at pH 2 to 10 mol % at pH 4 (Fig. 1). The time dependence of the reaction shows that the process can be divided into two parts: a starting process with a fast reaction rate which is followed by a slow long-term process.

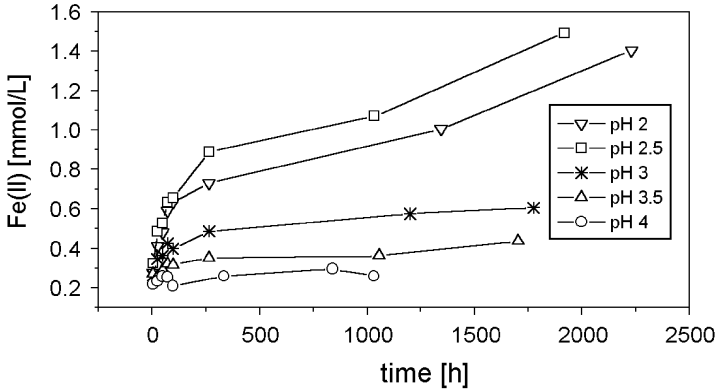

Fig. 1: Time dependence of Fe(III) reduction as $[Fe^{2+}]$; initial Fe(III) concentration 3 mmol/L.

The kinetic analysis, according to

$$Fe^{3+} + n\,H^{+} + m\,Lig_{red} \rightarrow Fe^{2+} + m\,Lig_{ox} \qquad (1)$$

$$\frac{d[Fe^{2+}]}{dt} = -\frac{d[Fe^{3+}]}{dt} = k \cdot [Lig_{red}]^{m} \cdot [H^{+}]^{n} \cdot [Fe^{3+}] \qquad (2)$$

$$\left(\ln \frac{[Fe^{3+}]_0 - [Fe^{2+}]}{[Fe^{3+}]_0}\right)_{t_2} - \left(\ln \frac{[Fe^{3+}]_0 - [Fe^{2+}]}{[Fe^{3+}]_0}\right)_{t_1} = -k^{*} \cdot (t_2 - t_1) \qquad (3)$$

$$\text{with} \quad k^{*} = [Lig_{red}]^{m} \cdot [H^{+}]^{n}; \qquad k^{*} = k' \cdot \ln 10 \qquad (4)$$

leads to k_1^* for the initial process (t < 48 h) and to k_2^* for the long-term reaction (t > 250 h).

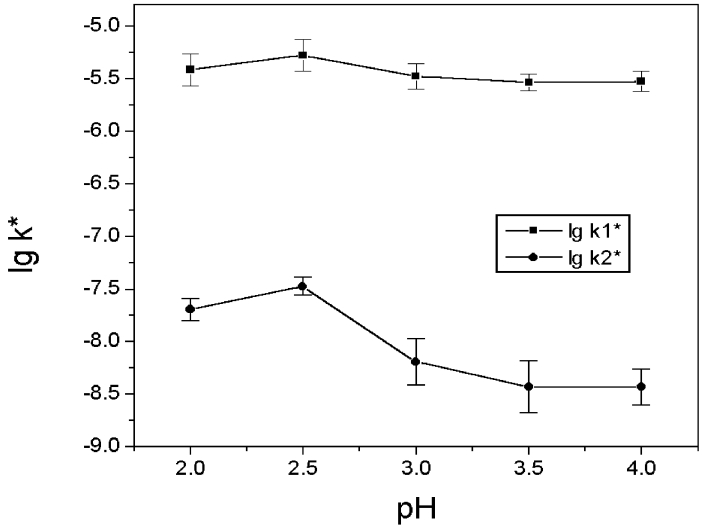

Fig. 2: The pH dependence of the rate constants k_1^* and k_2^*.

The k*-value at each pH in Tab. 1 was determined from five to nine different iron concentrations. The results show a distinct dependence on the pH. For k_1^* at pH 2.5, we find $(5.24 \pm 1.77)\cdot 10^{-6}\ s^{-1}$. Between pH 3 and 4, the average is $(3.1 \pm 0.7)\cdot 10^{-6}\ s^{-1}$. For k_2^* at pH 2.5, we find $(3.35 \pm 0.66)\cdot 10^{-6}\ s^{-1}$. k_2^* decreases with increasing pH to $(0.5 \pm 0.2)\cdot 10^{-8}\ s^{-1}$ which is the average between pH 3 and 4.

These results show that at constant pH and lignin concentration both processes can be described by the first-order equation (3).

The pH dependence of the rate constants (Fig. 2) according to

$$k' = k'' \cdot [H^{+}]^{n} \qquad (5)$$

and

$$\lg k' = \lg k'' - n \cdot pH \qquad (6)$$

shows that indeed the rate constants decrease above pH 2.5. However a linear relationship was not found for k*.

pH	k_1^* [s^{-1}]	k_2^* [s^{-1}]
2	(3.85 ± 1.29)•10^{-6}, (n=5)[1)]	(2.02 ± 0.48)•10^{-8}, (n=8)
2.5	(5.24 ± 1.77)•10^{-6}, (n=5)	(3.35 ± 0.66)•10^{-8}, (n=6)
3	(3.33 ± 0.92)•10^{-6}, (n=7)	(0.64 ± 0.30)•10^{-8}, (n=6)
3.5	(2.93 ± 0.55)•10^{-6}, (n=8)	(0.37 ± 0.19)•10^{-8}, (n=6)
4	(3.00 ± 0.65)•10^{-6}, (n=9)	(0.37 ± 0.14)•10^{-8}, (n=7)

Tab. 1: Specific rates for the Fe(III) reduction at different pH-values. [1)] n represents the number determinations that were recorded in the range 0.2 to 5 mmol/L of total iron

Acknowledgments
This study was supported by the Sächsisches Ministerium für Wissenschaft und Kunst under contract no. 4.7541.88-FZR/512. We thank N. Zier and R. Schiene, Technische Universität Dresden, Institute of Plant and Wood Chemistry, Tharandt, for supplying the lignin samples.

References

/1/ Zier, N.: *Strukturelle Merkmale eines Organosolv-Lignins bei Variation der Aufschlußparameter*. Dissertation, TU Dresden 1996

/2/ Tamura, H., Goto, K., Nagayama, M.: Spectrophotometric determination of iron(II) with 1,10-phenanthroline in the presence of large amounts of iron(III). Talanta **21**, 314 (1974)

VOLTAMMETRIC INVESTIGATION OF THE IRON(III) INTERACTION WITH SPRUCE LIGNIN

A. Abraham[1], L. Baraniak, H. Nitsche
Forschungszentrum Rossendorf e.V., Institute of Radiochemistry
[1]Technische Universität Dresden, Institute of Analytical Chemistry, Radiochemistry Group

The voltammetric determination of iron(III) and iron(II) was studied under non-complexing conditions and in the presence of lignin. Using these results, the iron(III) reduction by lignin was investigated in weakly acidic solution at pH$4 with the result that the reducing capacity of the lignin is 0.142 mmol/g.

The iron redox system (Fe(III)/Fe(II)) and lignin may play a major role in the uranium chemistry of flood waters from defunct mines in Saxony and Thuringia. Therefore, we investigated the reduction of the iron(III) by lignin. The voltammetric behaviour of iron(III) and iron(II) on a dropping mercury electrode was studied in 0.1 M sodium perchlorate solution and in the presence of lignin from a decomposed spruce wood. Using the voltammetric iron(II) signal, the iron(III) reduction by the lignin was measured after an equilibration of a 10^{-4} M $Fe_2(SO_4)_3$ solution with lignin (0,2 g/L) in the pH range from 3.0 to 5.5. Because the reaction is very slow, the samples were gently agitated for at least four weeks /1/.

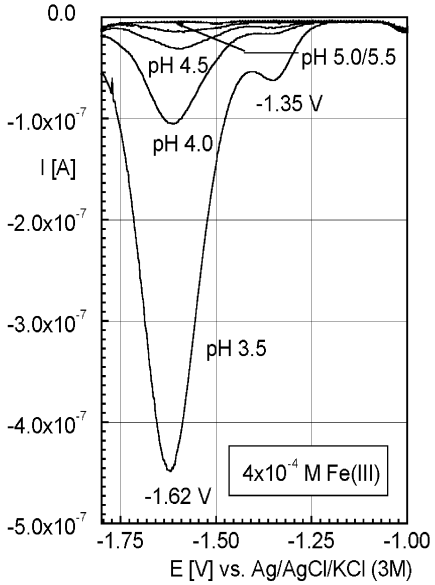

Fig. 1a

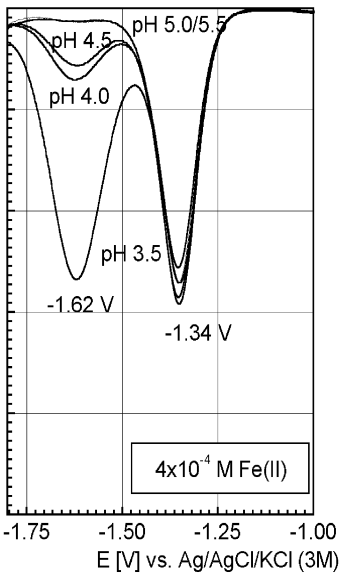

Fig. 1b

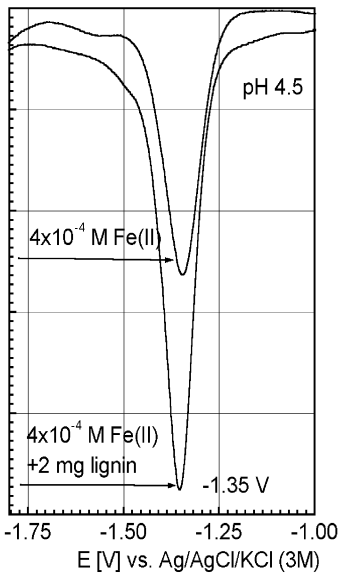

Fig. 1c

Fig. 1: Square-wave voltammograms of iron(III) and iron(II) in 0.1 M $NaClO_4$ and in the presence of lignin.

We investigated the voltammetric behaviour of individual Fe(III) and Fe(II) solution without and with lignin. The results are as follows:

Fe(III) in non-complexing solution (Fig. 1a): We find two reduction waves. A small one at about -1.35 V *vs.* Ag/AgCl and a larger one that is due to the hydrogen discharge at -1.62 V *vs.* Ag/AgCl coming from the decreased hydrogen overvoltage due to the reduced iron on the surface of the mercury /2/. This wave increases with decreasing pH.

Fe(II) in non-complexing solution (Fig. 1b): The iron(II) peak appears at -1.35 V *vs.* Ag/AgCl and represents the reduction of iron(II) to iron. This also causes the hydrogen discharge.

Fe(II) in the presence of lignin (Fig. 1c): The reduction potential is the same as for Fe(II) without lignin, but the voltammetric current is increased by about factor two. This effect can be explained by the adsorption of the lignin on the electrode and the accumulation of iron in this layer /3/. The peak height depends strongly on the iron(II) concentration (Fig. 2). This linear dependency was used to determine the iron(II) in the following iron(III) reduction experiments.

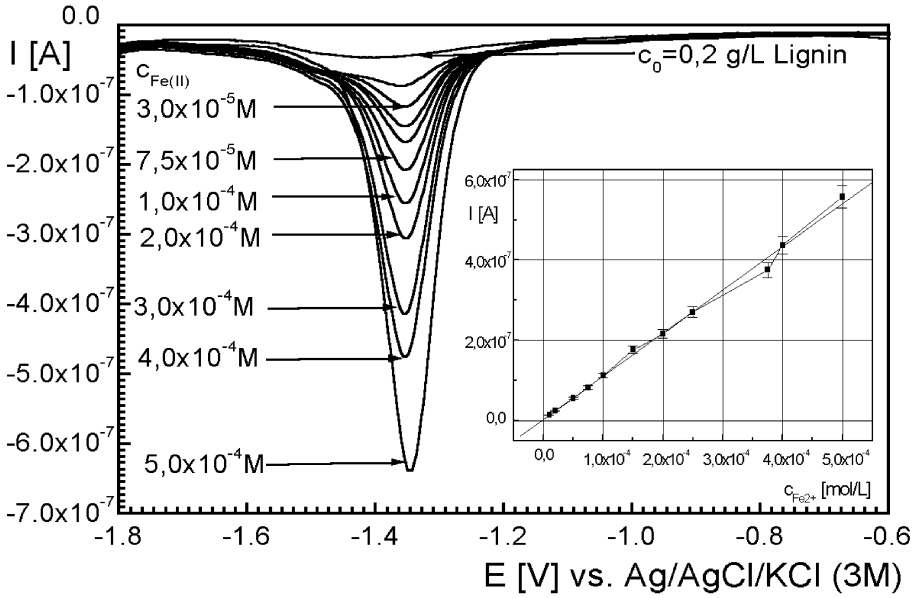

Fig. 2: Calibration curve of the voltammetric peak current in dependence of the iron(II) concentration.

Fe(III) in the presence of lignin (Fig. 3): The main feature is that the reduction peak is at the same potential as that of iron(II) and that no evident hydrogen ion discharge takes place. From this, we conclude that the iron(III) is reduced to iron(II) by the lignin. We deconvoluted the voltammograms to obtain the current for the Fe(II) signal which was used to evaluate the reduction experiments.

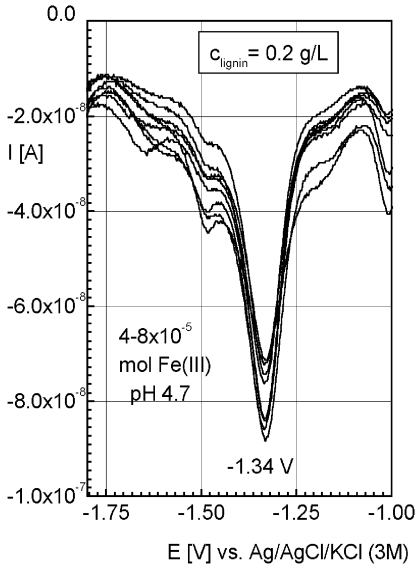

Fig. 3: Square-wave voltammograms of iron(II) formed by the lignin-mediated reduction of iron(III).

$[Fe(III)]_0$ [1] [mol]	$I-I_0$ [2] [A]	[Fe(II)] [3] [mol]
$2.00\ 10^{-6}$	$-2.51\ 10^{-8}$	$2.01\ 10^{-7}$
$2.00\ 10^{-6}$	$-2.58\ 10^{-8}$	$2.13\ 10^{-7}$
$4.00\ 10^{-6}$	$-3.20\ 10^{-8}$	$2.69\ 10^{-7}$
$4.00\ 10^{-6}$	$-2.90\ 10^{-8}$	$2.42\ 10^{-7}$
$4.00\ 10^{-6}$	$-4.02\ 10^{-8}$	$3.45\ 10^{-7}$
$4.00\ 10^{-6}$	$-3.72\ 10^{-8}$	$3.13\ 10^{-7}$
$4.00\ 10^{-6}$	$-3.96\ 10^{-8}$	$3.31\ 10^{-7}$
$4.00\ 10^{-6}$	$-4.12\ 10^{-8}$	$3.56\ 10^{-7}$
$8.00\ 10^{-6}$	$-3.64\ 10^{-8}$	$3.07\ 10^{-7}$
$8.00\ 10^{-6}$	$-3.38\ 10^{-8}$	$2.81\ 10^{-7}$
$1.60\ 10^{-5}$	$-3.50\ 10^{-8}$	$2.97\ 10^{-7}$
$1.60\ 10^{-5}$	$-3.02\ 10^{-8}$	$2.53\ 10^{-7}$

1) initial iron(III) = total iron amount. 2) voltammetric peak current. 3) formed by the reduction with 2 mg lignin.

Tab. 1: Voltammetrically determined amount of iron(II) as a function of the initial iron(III) quantity in the presence of 2 mg lignin

We then determined the amount of iron(III) that can be reduced by a given quantity of lignin at pH 4.5 ± 0.2. The main result is that in the range of $2.0 \cdot 10^{-6}$ to $1.6 \cdot 10^{-5}$ mol iron(III) a constant amount of $(2.84 \pm 0.46) \cdot 10^{-8}$ mol iron(III) was reduced by 2 mg lignin (Tab. 1). An excess of the iron(III) was present in all experiments. The reducing capacity of lignin at pH 4.5 was determined as 0.142 ± 0.023 mmol/g.

Acknowledgements
This study is supported by the Sächsisches Ministerium für Wissenschaft und Kunst under contract No. 4-7541.83-FZR/512.

References

/1/ Mack, B., Baraniak, L., Bernard, G., Nitsche, H.: Kinetics of Iron(III) Reduction by Spruce Wood Lignin. This Report, Institute of Radiochemistry, Annual Report 1997, p.40 (1998)
/2/ Henze, G., Neeb, R.: *Elektrochemische Analytik*. Springer-Verlag Berlin, Heidelberg, New York; 190 (1986)
/3/ Mlakar, M.: Square-wave Voltammetry of the Uranyl-Humate Complex. Analytica Chimica Acta **276**, 367 (1993)

SYNTHESIS OF SOLID IRON AND URANYL COMPLEXES WITH NATURAL AND SYNTHETIC HUMIC ACIDS

M. Bubner, S. Pompe, R. Jander, G. Schuster, K.H. Heise, H. Nitsche
Forschungszentrum Rossendorf e. V., Institute of Radiochemistry

We investigated the complexation of a purified humic acid from Aldrich (A2) and a synthetic humic acid (M1) with UO_2^{2+} and Fe^{3+} ions. Using ^{14}C-tracer technique we showed that both humic acids form in addition to the 1:2 uranyl:humic acid complex also a substantial amount of the 1:1 complex at higher uranyl loading. The humic acid A2 has a higher affinity for Fe^{3+} than for UO_2^{2+}. This is reversed for the humic acid M1.

Experiments and results

Solid Uranyl(VI) and Fe(III) humic acid complexes were prepared by reacting aqueous suspensions of humic acids A2 /1/ and M1 /2/ with 0.01 to 0.1 M solutions of uranyl or iron perchlorate and uranyl acetate, respectively. Depending on the carboxyl group content of the humic acid /3/, different stoichiometric amounts of the reagents were used for the complex formation. To examine the difference in affinity of UO_2^{2+} and Fe^{3+} ions toward the humic acids, the humic acids were reacted with defined mixtures of uranyl and iron perchlorate having metal ratios (meq:meq) of 1:1, 1:3 and 3:1. By using ^{14}C-labeled uranyl acetate, we quantified the acetate ligand in the complex and calculated the amount of uranyl humic acid complex with 1:1 stoichiometry. The acetate ligand can be exchanged with hydroxyl ion by dialysis.

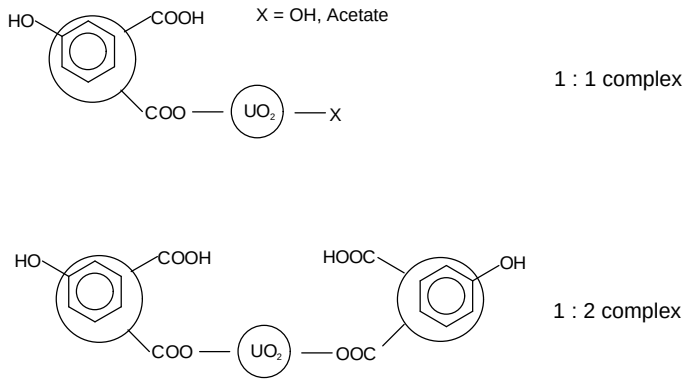

Fig. 1: Possibilities for humic acid uranyl complexation

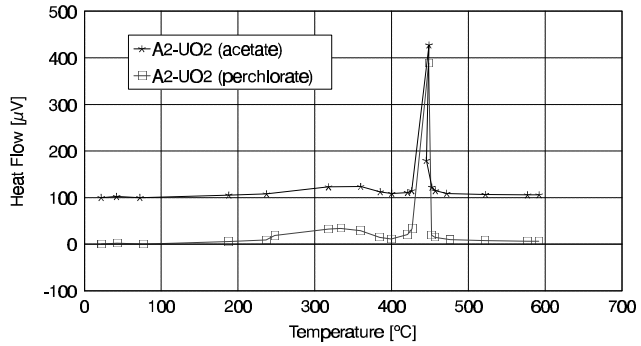

Fig. 2: DTA curves of uranyl humic acid complexes, prepared by reaction of humic acid A2 with uranyl acetate (--**%**--) and with uranyl perchlorate (--**9**--).
Y axis is shifted by 100 µV for A2-UO_2(acetate).

Fig. 1 shows the two possibilities of uranyl humic acid complex formation. The products were isolated by centrifugation, washed with water, dialyzed against purified water and lyophilized. The products in the tracer experiments were not dialyzed, but washed with methanol. The products were characterized by determining the elemental composition with elemental analysis

and ICP-MS after digestion with HNO_3 in a microwave oven. The complex formation was ensured by thermogravimetry and differential thermal analysis (TG/DTA) /4/. The amount of bond metal was determined thermogravimetrically. The concentration of the acetate ligand in the tracer experiments with uranyl [^{14}C]acetate was determined by LSC after the sample was oxidized. The amount of 1:1 uranyl humic acid complex in the product is equivalent to the molar acetate content in the non dialyzed product.

We concluded from our investigation that the reaction of humic acid A2 with equal proportions of uranyl acetate or uranyl perchlorate gives products with the same thermoanalytical behavior, as shown in Fig. 2, and with identical chemical composition. The analogous reactions of humic acid M1, however, gives products with different uranyl loading. This is due to the much lower solubility of the humic acid M1 at pH < 3, as shown in Tab. 1.

Reagent	COOH : UO_2^{2+} [meq : meq]	A2 complex		M1 complex	
		% loading	pH	% loading	pH
$UO_2(CH_3COO)_2$	1 : 0.1	10	1.6	10	4.2
	1 : 1	60	3.2	75	3.9
	1 : 3	112	3.7	120	4.0
$UO_2(ClO_4)_2$	1 : 0.1	10	1.4	10	4.2
	1 : 1	53	2.7	40	2.5
	1 : 3	110	3.3	80	2.0

Tab. 1: UO_2^{2+} loading of humic acids A2 and M1 from uranyl acetate and perchlorate reaction

The amount of 1:1 complex in the product is a function of uranyl to carboxylate ratio and carboxylate content of the humic acids. Statistics favor the formation of the 1:1 complex at lower carboxylate content. This is shown in Tab. 2, where the humic acid A2 (4,8 meq COOH/g) is compared with the humic acid M1 (1meq COOH /g).

Uranyl complex	A2	M1
% Uranyl loading	115	120
1:1 complex [%U]	22	33
1:2 complex [%U]	77	66

Tab. 2: Distribution of 1:1 and 1:2 uranyl humate complexes with humic acids A2 and M1, calculated from ^{14}C-tracer experiments

Complexation studies of the humic acids A2 and M1 with iron(III) perchlorate show a much higher loading of humic acid A2 with iron(III) ions than humic acid M1 under equal conditions.

Reaction mixture COOH : Fe^{3+} [meq : meq]	A2 complex		M1 complex	
	% loading	pH	% loading	pH
1 : 0.1	10	1.3	10	4.2
1 : 1	57	1.3	20	2.5
1 : 3	81	1.4	60	1.9

Tab. 3: Fe^{3+} loading of humic acids A2 and M1 from iron perchlorate reaction

Complexation of the humic acids A2 and M1 with mixtures of iron(III) and uranyl(VI) perchlorate shows that the humic acid A2 has a greater affinity for Fe^{3+} ions than for UO_2^{2+} ions. This is reversed for the humic acid M1. This phenomenon could not yet be interpreted from the molecular structure and the functionality of both humic acids.

Reagent composition	A2 complex		M1 complex	
meq Fe^{3+} : meq UO_2^{2+}	meq Fe^{3+} : meq UO_2^{2+}	pH	meq Fe^{3+} : meq UO_2^{2+}	pH
1 : 1	6 : 1	1.2	0.4 : 1	1.5
3 : 1	16 : 1	1.2	0.5 : 1	1.5
1 : 3	4 : 1	1.5	0.04 : 1	1.5

Tab. 4: Fe^{3+} to UO_2^{2+} ratios in solid complexes of humic acids A2 and M1 from reactions with mixtures of iron and uranyl perchlorate

As it is demonstrated in Fig. 3 for humic acid M1 and its Fe^{3+} and UO_2^{2+} complexes, the shape of the DTA curve of the pure humic acid is strongly changed by the binding of the metal ions.

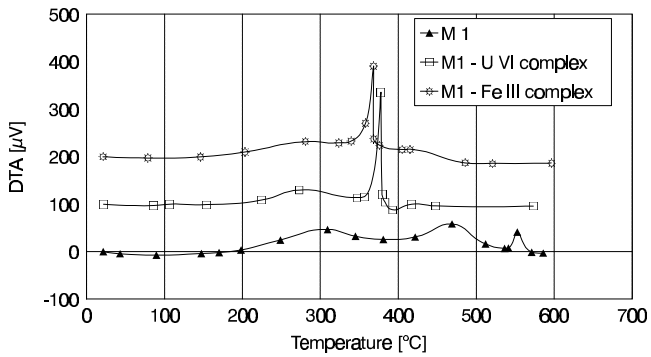

Fig. 3: DTA curves of the synthetic humic acid M 1, and the complexes M1-U(VI) and M1-Fe(III). Y axis is shifted by 100 µV for M1-U(VI) and by 200 µV for M1- Fe(III).

The peaks are closer to each other. The second peak arose above the first and the reaction temperature was decreased. For humic acid A2 and its analogous complexes there is not such an essential change in the shape of the curve, but the decrease of the thermal stability is also evident. We conclude, that the binding of the polyvalent cations with several carboxylic groups of the humic acids causes strains in the macromolecule and this makes it more sensitive for oxidation.

The solid U(VI) and Fe(III) complexes with humic acids A2 and M1 will be used for further investigations by thermal analysis, EXAFS, ESCA, FTIR and solubility studies.

Acknowledgments
The authors thank R. Jander, R. Ruske, K. Heidel, H. Görner and W. Wiesener for their help in preparation and characterization of the humic acid complexes.

References
/1/ Kim, J. I., Buckau, G.: *Characterization of reference and site specific humic acids.* Report RCM 02188, Institut für Radiochemie, TU München (1988)
/2/ Pompe, S., Bubner, M., Denecke, M.A., Reich, T., Brachmann, A., Geipel, G., Nicolai, R., Heise, K.H., Nitsche, H.: A comparison of natural humic acids with synthetic humic acid model substances: Characterization and interaction with uranium(VI). Radiochim. Acta **74**, 135-140 (1996)
/3/ Bubner, M., Pompe, S., Meyer, M., Jander, R., Schuster, G., Heise, K.H.: Synthesis of uranium(VI) and calcium complexes with carboxylic and humic acids. Report FZR-180, Institute of Radiochemistry, Annual Report 1996, 22-23 (1997)
/4/ Schuster, G., Bubner, M., Pompe, S., Heise, K.H., Nitsche, H.: Thermoanalysis of a synthetic and a natural humic acid and their calcium- and uranyl compounds. Report FZR-180, Institute of Radiochemistry, Annual Report 1996, 24-25 (1997)

EXPERIMENTS FOR THE DISPOSAL OF CARBON-14 LABELED ORGANIC MATERIAL: 3. ANODIC OXIDATION OF THE ORGANIC WASTE /1/

E. Förster, S. Heller, K.H. Heise, H. Nitsche
Forschungszentrum Rossendorf e.V., Institute of Radiochemistry,

We have developed a method for the mineralization of organics by anodic oxidation in a silver-sulfate-containing sulfuric-chromic acid. This process can also be used for complete oxidation of "difficult" organic wastes, such as hydrophobic substances like hydrocarbons, plastics, activated carbon, etc.

Introduction
The electrochemical oxidation converts organic compounds to CO_2. Ag(II) /2/ or Co(III) /3/ in nitric acid are used as mediators for this process. We have developed a new method for mediated electrochemical treatment of carbon-14-labeled organic waste using strong sulfuric acid containing Cr(VI) and Ag(I) /4/. Most organic substances are soluble or partially soluble in sulfuric acid. In this process chromium-containing hazardous wastes are avoided by electrolytical regeneration of chromium(III) to chromium(VI). Ideally, this process requires only electrical energy and water. Fig. 1 shows the scheme of the chromium-mediated electrochemical mineralization for organic compounds.

Experimental
The organic substances are oxidized in a small H-cell with stationary platinum electrodes (2 × 3 cm^2) that are separated by a Nafion® 350 cation exchange membrane (Du Pont). The electrochemical cell is charged with an anolyte of 65% sulfuric-acid-containing 0.16 M chromium trioxide, 0.016 M silver sulfate and 30 - 40% sulfuric acid as catholyte. The anodic compartment has a heating jacket and is equipped with a reflux condenser. The condenser is connected to an air filtration unit (Midisart® 2000, Sartorius A.G.) followed by a cupric oxide filled quartz tube (catalyst), a safety bottle, and two gas traps each containing 50 mL of 0.5 M sodium hydroxide. The catalyst in the quartz tube is treated at about 650°C. To measure the radioactivity of $^{14}CO_2$ on-line, a gas flow cuvette is positioned between the quartz tube and the safety bottle. This cuvette is connected to a commercial proportional counter tube (type LB 6280). An equivalent of 12 millimoles of carbon as organic compounds is transferred to the anodic compartment. The experiments are performed with a 1.5 A current. The anodic compartment is kept at 135°C for 6 hours. Then the temperature in the anodic compartment is reduced to 55°C for about 10 hours to regenerate the Cr(III) to hexavalent chromium. The evolving carbon dioxide is transferred by the oxygen stream which is generated at the anode. The inactive carbon dioxide is absorbed in the gas traps and then determined by titration.

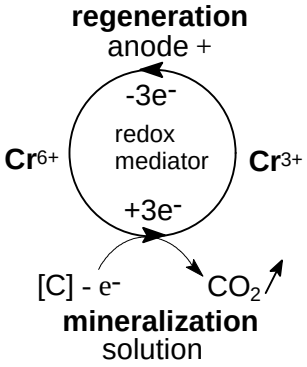

Fig. 1: Reaction scheme for the mediated electro-oxidation of organic compounds

Some low-level experiments were conducted using the following radioactive organic compounds: acetic acid [2-^{14}C] sodium salt, palmitic acid [1-^{14}C], and 4-hydroxy benzoic acid [ring UL-^{14}C]. The recovery of activity in the mineralization of C-14-labeled compounds was

determinated by L.S.-measuring of the initial products and the $^{14}CO_2$ absorbed in the sodium hydroxide solution.

Results and Discussion

The procedure described here is an useful tool for the mineralization of hazardous, C-14-labeled organic wastes. Only halogen compounds may interfere with this reaction by forming chromyl chloride, free halogens or silver halides precipitate. Tab. 1 lists the yields for several inactive organic compounds that were oxidized by the anodic oxidation procedure.

The kinetics of the degradation of C-14-labeled organic substances was monitored by measuring on-line the ß-decay of the produced $^{14}CO_2$. Fig. 2 shows the results.

Acknowledgment

This study was supported by the Sächsisches Ministerium für Wissenschaft und Kunst under contract No. 4-7581. 312/20.

substance name	% CO_2-yield	substance name	% CO_2-yield
Acetic acid, sodium salt	97-100	Palmitic acid (C_{16})	87-92
Acetone	97	Paraffin wax	95
Acetophenone	101	Phenol	95
Activated carbon	53-68	Propionic acid	99
Chloro acetic acid	92	Succinic acid	99
4-Hydroxy benzoic acid	70-95	Thiourea	90
Methyl alcohol	102	2-Toluic acid	101
2-Nitrophenol	90	Trapidil®*	94
Nonanoic acid	99	Xylene (isomers)	73-88

Tab. 1: Mineralization yield of several inactive organic substances.
* pharmaceutical agent (subst. Triazolo pyrimidine)

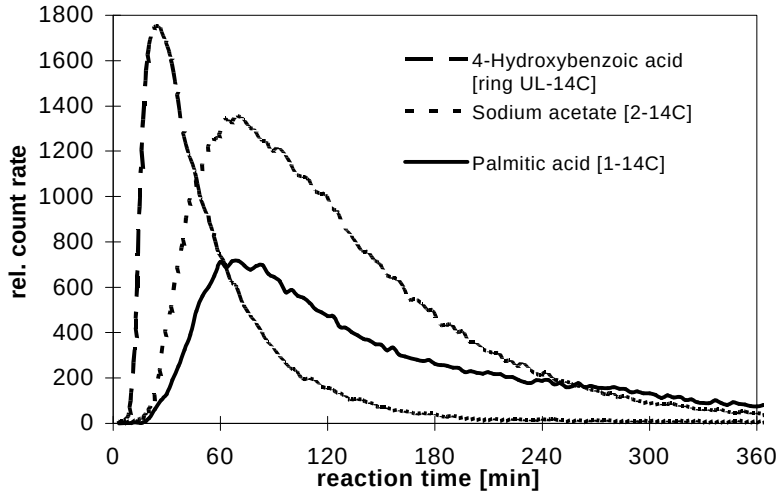

Fig. 2: Kinetics of anodic mineralization for three carbon-14-labeled organic compounds

References

/1/ Förster, E., Petzold, H., Rösseler, M., Heise, K.H., Nitsche, H.: Report FZR-180, Institute of Radiochemistry, Annual Report 1996, p.36 (1997)

/2/ Cellos, R.J.: The Silver II Process for the Destruction of CW Munitions. In: F.W. Holms (ed.): *Scientific Advances in Alternative Demilitarization Technologies*. Kluver Academic Publishers 1996 (Netherlands) pp. 141 -150

/3/ Dziewinski, J., Marczak, S., Smith, W.: Chemtech **26**, 30 - 33 (1996)

/4/ Förster, E., Heise, K.H., Nitsche, H.: *Verfahren zur elektrochemischen Mineralisierung von insbesondere C-14 markierten organischen Abfallstoffen*. Patentanmeldung AZ 196 46 049.2

REACTIONS OF DICHLORO[2-(DIMETHYLAMINOMETHYL)PHENYL-C^1,N] GOLD (III), [AU(DAMP-C^1,N)CL_2], WITH HETEROCYCLIC THIOLS. EVIDENCE FOR AU-N BOND CLEAVAGE AND PROTONATION OF THE DIMETHYLAMINO GROUP

U. Abram, J. Mack[1], K. Ortner[1]
Forschungszentrum Rossendorf e.V., Institute of Radiochemistry
[1]University of Tübingen, Institute of Inorganic Chemistry

[Au(damp-C^1,N)Cl_2] reacts with various heterocyclic thiols under cleavage of the Au-N bond and protonation of the dimethylamino groups in the resulting cationic or neutral Au(III) complexes.

Square-planar gold(III) complexes with the 2-[(dimethylamino)methyl]phenyl-C^1,N ligand, (damp-C^1,N)$^-$, are isostructural and isoelectronic to the well-established cancer drug *cis-platinum*.

Key compounds of this class are the dichloro and diacetato complexes [Au(damp-C^1,N)Cl_2] (1a) and [Au(damp-C^1,N)$(CH_3CO_2)_2$] (1b) which recently have been studied by structural analysis /1/ showing distorted square-planar co-ordination spheres for the gold atoms **(1)**. During ligand

exchange reactions preferably the chloro or acetato ligands are replaced /2/. Only a few examples are reported where the Au-N bond is cleaved.

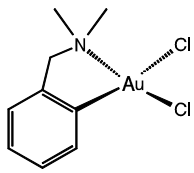

1a

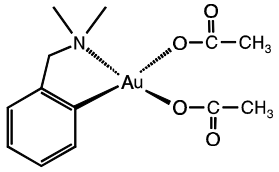

1b

Here, we present the synthesis and structural characterization of complexes which are obtained by the reaction of [Au(damp-C^1,N)Cl_2] with the heterocyclic thiols of Fig. 1. For almost all heterocycles used, tautomeric forms can be formulated involving thiol, thione or zwitter ionic forms. Thus, different co-ordination modes may be expected for the ligands which are applied in their protonated form. All ligands summarized in Fig. 1 react with [Au(damp-C^1,N)Cl_2] under exchange of chloro ligands, cleavage of the Au-N bonds and protonation of the -N$(CH_3)_2$ groups.

This is a new reaction pattern for gold complexes which gives access to novel cationic or neutral gold(III) complexes with promising biological properties. The products have been studied extensively by infrared and NMR spectroscopy, mass spectrometry and X-ray crystallography. The structures of the products are summarized in Fig. 1. The charges of the complex molecules are controlled by the net charge of the heterocyclic ligand and their donor properties.

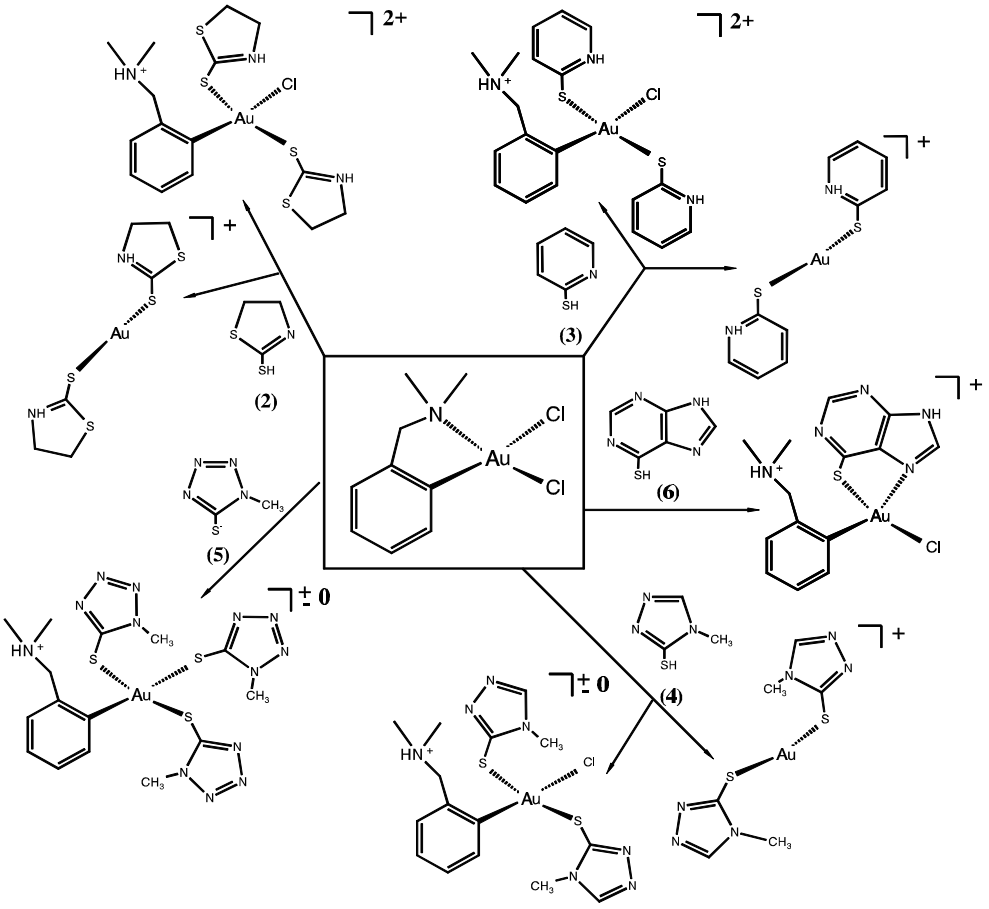

Fig. 1: Summary of the ligands, the studied reactions starting from [Au(damp-C^1,N) Cl_2] and the structures of the isolated products.

2-Mercaptothiazoline **(2)** and 2-mercaptopyridine **(3)** coordinate zwitter-ionic as neutral ligands with protonated ring nitrogen atoms and form complexes of the composition [Au(Hdamp-C^1)Cl$(L)_2$]Cl_2. Whereas the formation of gold(I) cations of the type $[Au(L)_2]^+$ are only formed as side-products with the ligands **(2)** and **(3)** they play a considerable role during the reaction of [Au(damp-C^1,N)Cl_2] with 2-methylmercaptotriazole (HSmetriaz, **(4)**). [Au^I (Hsmetriaz)$_2$]Cl was isolated as the major products of this reaction and the gold(III) complex [Au(Hdamp-C^1)Cl$(Smetriaz)_2$] was only obtained in yields of about 10 per cent.

A clear reaction was observed when the sodium salt of a heterocyclic thiol was used instead of the protonated compound. From sodium 2-methylmercaptotetrazolate (NaSmetetraz, **(5)**) and [Au(damp-C^1,N)Cl_2] the neutral [Au(Hdamp-C^1)$(Smetetraz)_3$] is obtained in good yields.

Spectroscopic studies give evidence for monodentately co-ordinated, protonated Hdamp-C^1 ligands with an IR frequency of 2720 cm^{-1} for the ammonium proton and ^{13}C NMR chemical shifts at 34.5 ppm (CH_3) and 43.7 ppm (CH_2) for the -CH_2-NH(CH_3)$_2$ unit. Three Smetetraz- ligands complete the square-planar co-ordination sphere of gold. The heterocyclic ligands are bonded as thiols. Thus, [Au(Hdamp-C^1)(Smetetraz)$_3$] is the first neutral gold(III) complex with a Hdamp-C^1 unit.

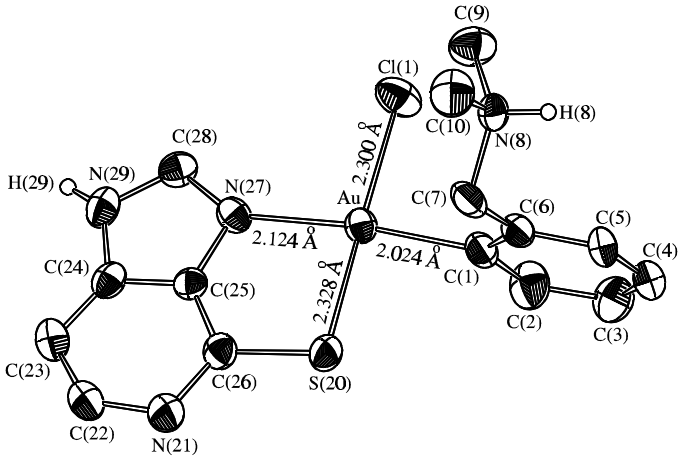

Fig. 2: Ellipsoid representation of the [Au(Hdamp-C^1)Cl(Spurine)]$^+$ complex cation. Thermal ellipsoids represent 30 per cent probability. Carbon H atoms have been omitted for clarity.

Representatively for all the described compounds with monodentate (Hdamp-C^1)$^{\pm 0}$ ligands, the structure of [Au(Hdamp-C^1)Cl(Spurine)]Cl (Fig. 2) shall shortly be discussed. This complex with the biologically important 6-mercaptopurine ligand **(6)** is formed in good yields from [Au(damp-C^1,N)Cl_2] and the HSpurine in methanol. The ligand reacts under chelate formation without adding a base. The square-planar co-ordination sphere of gold is slightly distorted with a maximum deviation of 0.08 Å for the donor atoms. Au is situated only 0.022(3) Å out of the mean plane formed by C(1), Cl(1), N(27) and S(20). The phenyl ring of the Hdamp-C^1 ligand is twisted against the co-ordination sphere by 84.07°.

Acknowledgment
This work was supported by the DEGUSSA A.G. with a generous gift of gold starting materials.

References

/1/ Mack, J., Ortner, K., Parish, R.V., Abram, U.: Gold(III)-Komplexe mit 2-(Dimethylaminomethyl)phenyl (damp-), Darstellung und Kristallstrukturen von [Au(damp-C,N)Cl_2], [Au(damp-C,N)($OOCCH_3$)$_2$] und [Au(damp-C,N)(mnt)]. Z. anorg. allg. Chem. **623**, 873 (1997).

/2/ Parish, R.V., Mack, J., Hargreaves, L., Wright, J.P., Buckley, R.G., Elsome, A.M., Fricker, S.P., Theobald, B.R.C.: Chemical and biological reactions of diacetato[2-(dimethylaminomethyl)phenyl]gold(III). J. Chem. Soc. Dalton Trans. 69 (1996).

SYNTHESIS, CHARACTERIZATION AND STRUCTURE OF BIS{2-[1-(THIOSEMICARBAZONO)ETHYL]PYRIDINE}HEXANITRATOTHORATE(IV) @ 4 MEOH

U. Abram
Forschungszentrum Rossendorf e.V., Institute of Radiochemistry

Pale yellow crystals of ($C_8H_{11}N_4S$)$_2$[Th(NO_3)$_6$] x 4 MeOH are formed when thorium nitrate and acetylpyridine thiosemicarbazone are refluxed in methanol. Thorium is 12-coordinate. The almost planar 2-[1-(thiosemicarbazono)ethyl]pyridinium cations show bond lengths which indicate a considerable delocalization of electron density.

Heterocyclic thiosemicarbazones, as well as their metal complexes, are currently under discussion because of their biological activity /1/. Although there exists a number of studies dealing with complex formation properties, comparatively few structural reports are published. Studies on reactions of heterocyclic thiosemicarbazones with actinides have not yet been reported.

Heating of Th(NO_3)$_4$ x 4 H_2O with excess of HAPTSC in methanol results in the formation of (H_2ATPSC)$_2$[Th(NO_3)$_6$] which crystallizes upon concentration of the reaction mixture. In this compound, thorium does not form any bonds to the thiosemicarbazone. In the remaining filtrate, however, a thorium thiosemicarbazonato complex of the tentative composition [Th(APTSC)(OH_2)(NO_3)$_2$]$^-$ could be detected by a FAB$^-$ mass spectrometry peak of reasonable intensity at m/z = 583. All attempts to isolate and crystallize this complex failed up to now.

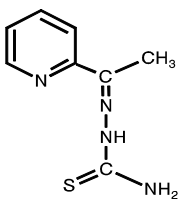

HAPTSC

The structure of (H_2APTSC)$_2$[Th(NO_3)$_6$] is given in Fig. 1. The metal is 12-coordinate with a coordination sphere which can be described as a distorted icosahedron with

twelve isosceles and eight equilateral triangles forming the surface of the coordination polyhe dron (Fig. 2). The metal is located at a centre of inversion. With this, the structure of the anion comes close to the $[Th(NO_3)_6]^{2-}$ anion in tris-2,2'-bipyridinium nitrate hexanitratothorate(IV) /2/ and is in contrast to the asymmetric complex anions in $[Mg(H_2O)_6][Th(NO_3)_6]$ x 2 H_2O /3/ and $[Th(NO_3)_3(tdpo)_4]_2[Th(NO_3)_6]$ (tdpo = tris(dimethylamido)-phosphine oxide) /4/.

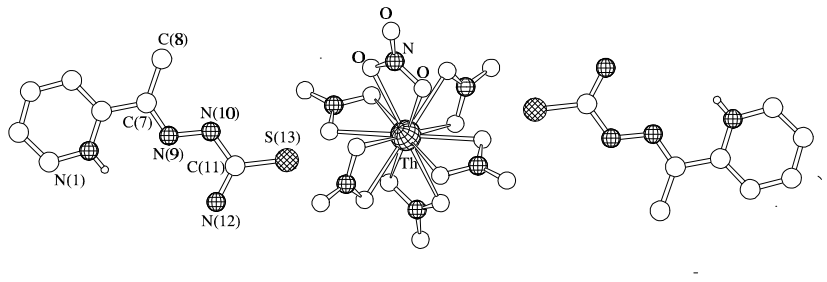

Fig. 1: Molecular structure of $(H_2APTSC)_2[Th(NO_3)_6]$

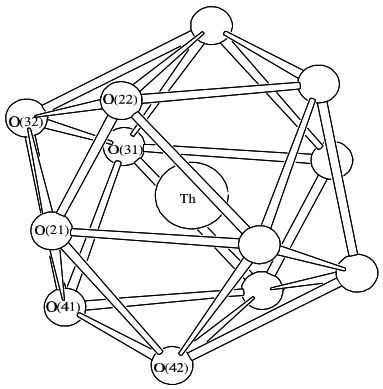

Fig. 2: ThO_{12} polyhedron

The distortions in the ThO_{12} icosahedron are mainly established by the O-Th-O angles which significantly deviate from the situation in a regular icosahedron where one could expect O-Th-O angles of 63.5E (five such), 116.5 (five such) and 180E (one such) for each specific oxygen atom. The experimental results show O-Th-O angles in the ranges of 49.5-49.8E (one such), 67.1-68.3E (4 such), 111.7-112.9E (4 such), 130.1-130.5E (one such) and (by symmetry) 180E(one such) for any individual oxygen atom. All Th-O bond lengths lie randomly in the range 2.555 (3) Å - 2.579(3) Å. The second coordination sphere of thorium is an almost regular octahedron with Th-N distances between 2.996(5) and 3.007(5) Å and a maximum deviation of the N-Th-N angles from 90E of 1.58E.

The H_2APTSC counterion is protonated at the nitrogen atom of the pyridine ring as could be derived from the structure determination. The molecule is almost planar with a maximum deviation from a least-squares plane including all non-hydrogen atoms of 0.03 Å. The C(11)-S(13) distance of 1.679(4) Å is intermediate between typical C-S single and double bond lengths. This agrees well with the C(11)-N(10) and C(11)-N(12) bond lengths of 1.359(5) and 1.320(5) Å which indicate partial double bond character. The C(7)-N(9) bond (1.284(5) Å) is significantly shorter than a C-N single bond as can be expected for a thiosemicarbazone.

References

/1/ Abram, S., Maichle-Mössmer, C., Abram, U.: Synthesis and characterization of indium(III) complexes with tri- and pentadentate thiosemicarbazones. Polyhedron **17,** 131 (1998).

/2/ Khan, M.A., Kumar, N., Tuck, D.G.: The crystal structure of tris-2,2'-bipyridinium nitrate hexanitratothorate(IV). Can. J. Chem. **62**, 850 (1984).

/3/ Scavnicar, S., Prodic, B.: The crystal structure of Double Nitrate Octahydrates of Thorium and Bivalent Metals. Acta Cryst. **18**, 698 (1965).

/4/ English, R.P., du Preez, J.G.H., Nassimbeni, L.R., van Vuuren, C.P.J.: The structure of bis(trinitratotetrakis(hexamethylphosphoramide-thorium)hexanitratothorium. S.-Afr. J. Chem. **32**, 119 (1979).

EPR SPECTROSCOPY ON $[RENX_{4/5}]^{-\,/\,2-}$ COMPLEXES (X = CL, BR, NCS)

U. Abram, R. Kirmse[1], A. Voigt[1]
Forschungszentrum Rossendorf e.V., Institute of Radiochemistry
[1]University of Leipzig, Institute of Inorganic Chemistry

Rhenium(VI) compounds of the general formulae $[ReNX_{4(5)}]^{-,\,2-}$ (X = Cl, Br, NCS) have been studied by EPR spectroscopy showing an almost linear dependence of the experimental spectral parameters on the composition of the equatorial coordination sphere.

Rhenium (VI) compounds are favored for EPR studies because of their $5d^1$ (S = 1/2) configuration. As found for the halide compounds $[ReNX_{4(5)}]^{-,\,2-}$ (X = Cl, Br) the $[ReN(NCS)_5]^{2-}$ species gives a well-resolved room-temperature X-band EPR spectrum consisting of six $^{185,\,187}$Re hyperfine structure (hfs) lines. This Re hfs sextet arises from the interaction of the unpaired electron with the nuclear spin of both rhenium isotopes ^{185}Re and ^{187}Re (I^{Re} = 5/2, natural abundance ^{185}Re 37.4 % and ^{187}Re 62.6 %). The frozen-solution EPR-spectrum of $(Bu_4N)_2[ReN$

$(NCS)_5$] is reproduced in Fig. 1. This spectrum shows a typical axially-symmetric pattern with six $^{185, 187}$Re hfs lines in the parallel and the perpendicular part. For the EPR-spectrum at T = 130 K as well as for the room-temperature spectrum ligand hfs splittings were not resolved, because of the comparatively large linewidth of $)B_{pp}$ = 9 - 19 mT. Due to the magnitude of the $^{185, 187}$Re hfs coupling constants and the nuclear quadrupole moments in both cases the equidistance of the hfs lines is disturbed.

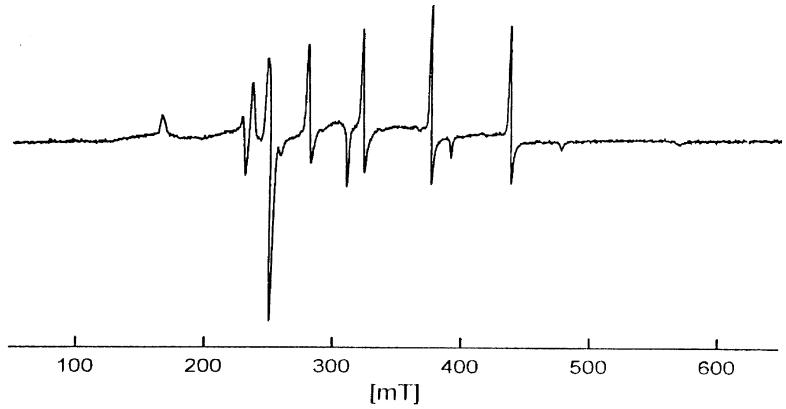

Fig. 1: Experimental EPR spectrum of $(Bu_4N)_2[ReN(NCS)_5]$

The spectra can be described by the spin-HAMILTONIAN (1) :

$$\boldsymbol{H}_{sp} = \boldsymbol{g} \cdot \mu_B \cdot \boldsymbol{S} \cdot \boldsymbol{B}_0 + \boldsymbol{S} \cdot \boldsymbol{A}^{Re} \cdot \boldsymbol{I}^{Re} + \boldsymbol{I}^{Re} \cdot \boldsymbol{Q}^{Re} \cdot \boldsymbol{I}^{Re} \qquad (1)$$

All symbols have their usual meaning. The obtained principal values of $\boldsymbol{g}$-tensors and the $^{185, 187}$Re hfs tensors $\boldsymbol{A}^{Re}$ for $(AsPh_4)_2[ReN(NCS)_5)]$ are g_5 = 1.817, g_z = 1.958, g_{av} = 1.911, A_5^{Re} = 681.6 x 10^{-4}cm^{-1}, A_z^{Re} = 379.1 x 10^{-4} cm^{-1} and A_{av}^{Re} = 479.9 x 10^{4} cm^{-1}. The values for $(NBu_4)[ReNCl_4]$ and $(NBu_4)[ReNBr_4]$ are summarized in Tab. 1.

	g_0 (Exp.)	g_o (Calc.)	a_0^{Re} (Exp.)	a_0^{Re} (Calc.)	g_5 (Exp.)	g_5 (Calc.)	A_5^{Re} (Exp.)	A_5^{Re} (Calc.)
$[ReNBr_4]^-$	2.005	2.005	447	447	2.069	2.069	665	665
$[ReNBr_3Cl]$	1.984	1.984	461	464	2.034	2.029	695	694
$[ReNBr_2Cl_2$	1.962	1.964	483	480	1.994	1.988	721	720
$[ReNBrCl_3]$	1.944	1.944	494	497	1.944	1.988	744	745
$[ReNCl_4]^-$	1.924	1.924	513	513	1.908	1.908	768	768

Tab. 1: Experimentally obtained[a)] and calculated[b)] EPR parameters for $[ReNBr_{4-p}Cl_p]^-$ mixed-ligand complexes (Hfs couplings in 10^{-4} cm^{-1}) [a)] experimental errors: g values ± 0.003, coupling constants ±3; [b)] estimated according to y = ($[ReNBr_{4-p}Cl_p]^-$) = 1/4{(4-p)y($[ReNBr_4]^-$) + py($[ReNCl_4]^-$)} with y = g_0, g_5, a_0^{Re}, A_5^{Re}.

In the spectra of the $[ReNCl_4]^-$/$[ReNBr_4]^-$ mixtures, in addition to the signals of the parent compounds, there are several new signals which indicate the formation of mixed-ligand complexes of the type $[ReNBr_{4-p}Cl_p]^-$ with p = 1 - 3. A spectrum detecting the formation of the Re(VI)N mixed-ligand complexes is shown in Fig. 2. In contrast to the EPR-investigation of the ligand-exchange reaction on the related nitridotechnetium compounds $[TcNX_4]^-$ (X = Cl, Br) /1/ only the high-field line (m_I^{Re} = 5/2) is clearly splitted. The spectral parameters of the individual compounds are listed in Tab. 1 together with the values of their parent compounds. A similar pattern with the occurrence of EPR signals of $[ReNBr_{4-p}Cl_p]^-$ (p = 1 - 3) mixed-ligand complexes can be observed in the frozen solution spectra of $[ReNCl_4]^-$/ $[ReNBr_4]^-$ mixtures.

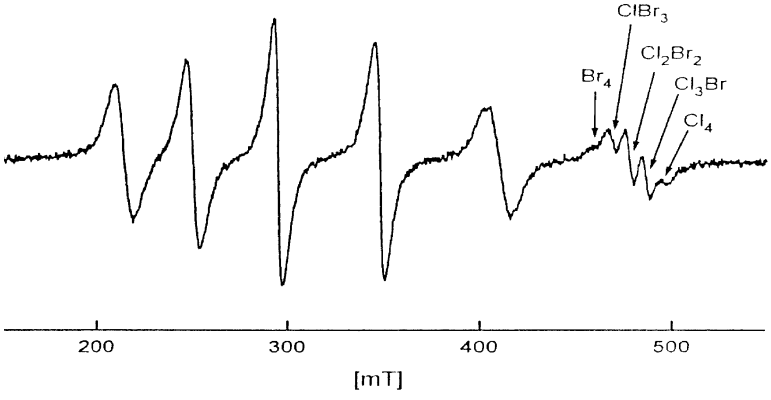

Fig. 2: Experimental EPR spectrum of $[ReNBr_{4-p}Cl_p]^-$ (p = 0 - 4) complexes in CH_2Cl_2, T = 295 K. The well-resolved high-field line (m_I^{Re} = + 5/2) shows the presence of all three possible mixed-ligand species and the parent compounds

The investigation of ligand-exchange reactions by means of EPR requires knowledge about the dependence of the EPR parameters on the type (composition, symmetry) of the coordination sphere. According to

extensive investigations for the d^1 systems CrO^{3+}, MoO^{3+}, WO^{3+}, VO^{2+} and TcN^{2+} /2,3/ a nearly linear dependence of the EPR spectral quantities g_0, g_s, a_0^{Re} and A_s^{Re} on the "heaviness" of the first coordination sphere is expected. This can be defined for the $[ReNBr_{4-p}Cl_p]^-$ complexes with p = 0 - 4 under study as given in equ. (2)

$$g_0,\ g_s,\ a_0^{Re},\ A_s^{Re}\ .\ \delta_L/\delta_{Re} = (1/4)\ [p\delta_{Cl} + (4\text{-}p)\delta_{Br}] / \delta_{Re} \qquad (2)$$

where δ_{Cl}, δ_{Br} and δ_{Re} are the spin-orbit coupling constants of chlorine, bromine and rhenium, respectively.
The proportionality (equ. (2)) holds true if there are no significant differences concerning the structure and bonding properties of the complexes considered. Thus, if the *g* values and the hfs coupling parameters A^{Re} of the parent complexes are known, the g_0, g_s, a_0^{Re} and A_s^{Re} values of the mixed-ligand complexes can be estimated simply using the "additivity rule" given in footnote b) of Tab. 1. The estimated values for g_0, g_s, a_0^{Re} and A_s^{Re} are compared with the experimentally derived ones. The experimental values are well reproduced and a nearly linear dependence of the observed EPR quantities of the $[ReNBr_{4-p}Cl_p]^-$ complexes with p = 0 - 4 on the composition of the first coordination sphere is detected.

Acknowledgment
We acknowledge grants from the Deutsche Forschungsgemeinschaft (contract AB 67/4-1) and the Fonds of the Chemical Industry.

References
/1/ Abram, U., Kirmse, R.: EPR on technetium complexes. Radiochimica Acta **63**, 139 (1993)
/2/ Kirmse, R., Stach, J., Abram, U.: Nitridotechnetate(VI) complexes. An EPR study. Inorg. Chim. Acta **117**, 117 (1988)
/3/ Marov, I.N., Kostromina, N.A.: *EPR and NMR in the Chemistry of Coordination Compounds*, Nauka, Moscow, 1979 (in Russian)

$(NBu_4)[ReNCl_4]$ - A FACILE SYNTHESIS, STRUCTURE AND REACTIONS

U. Abram, M. Braun[1]
Forschungszentrum Rossendorf e.V., Institute of Radiochemistry
[1]University of Tübingen, Institute of Inorganic Chemistry

$(NBu_4)[ReNCl_4]$ has been prepared from perrhenate, sodium azide and HCl in a simple single-pot synthesis and its structure has been elucidated by X-ray crystallography. The compound is an excellent precursor for the synthesis of new rhenium nitrido complexes.

Chemical studies on the element rhenium in the past mainly focussed on catalytic properties of numerous coordination and metallorganic compounds. In the recent years, fundamental chemical properties of this third row transition element became interesting for other communities of chemists due to potential applications of rhenium compounds in therapeutic medicinal chemistry and the use of rhenium as model for radiochemical studies on the element no. 107.
The tetrachloronitridorhenate anion, $[ReNCl_4]^-$, has firstly been prepared about 20 years ago by the reaction of the neutral rhenium(VII) nitride chloride $ReNCl_4$ with tetraphenylarsonium chloride /1/. For a large scale synthesis, however, the approach via the neutral rhenium nitride chlorides $ReNCl_3$ or $ReNCl_4$ seems to be less appropriate with regard to their syntheses from $ReCl_5$ and nitrogen trichloride and chlorine azide, respectively. Here, we describe a facile synthesis of $(NBu_4)[ReNCl_4]$ from perrhenate, sodium azide and demonstrate, that $[ReNCl_4]^-$ is a suitable starting material for the synthesis of new rhenium nitrido complexes.
Tetrachloronitridorhenate(VI) can be prepared in good yields in a single-pot synthesis from tetrabutylammonium perrhenate, HCl gas and sodium azide. The synthesis follows a general route for the preparation of tetrahalide nitrido metallates /2/ and has also been applied for the lighter homologue of rhenium. When the same protocol is applied to rhenium, a mixture of mainly rhenium(IV) and rhenium(V) compounds is obtained and $[ReNCl_4]^-$ is only formed as a minor side-product. To increase the amount of the nitrido complex it is necessary to keep the temperature of the reaction mixture low and to add several small portions of azide rather than one big amount. When the reaction is interrupted after addition of the first portion of azide, considerable amounts of ReO_4^- and $[ReOCl_4]^-$ are observed. Usually, three additions of sodium azide are sufficient to obtain $(NBu_4)[ReNCl_4]$ in good yields and high purity. The absence of the

possible impurities $(NBu_4)(ReO_4)$ and $(NBu_4)[ReOCl_4]$ can easily be checked by IR spectroscopy. The <(Re/N) vibration at 1103 cm^{-1} is well separated from the regions where the Re=O frequencies of $[ReOCl_4]^-$ (1033 cm^{-1}) and ReO_4^- (913 cm^{-1}) can be detected.

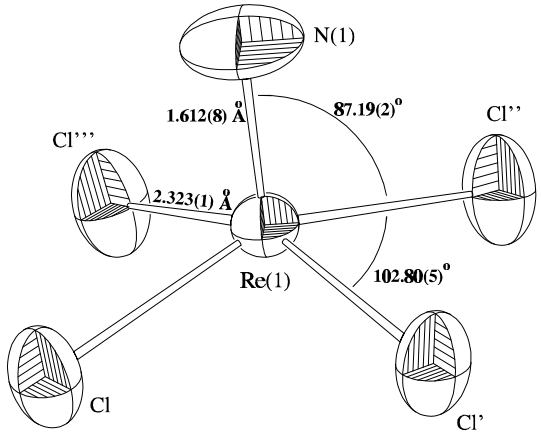

Fig. 1: Molecular structure of the $[ReNCl_4]^-$ anion

$(NBu_4)[ReNCl_4]$ is airstable and does not hydrolyze at ambient conditions. In water, however, the rapid formation of a black-brown, insoluble solid proceeds. The complex crystallizes in the tetragonal space group P4/n and the anion (see Fig. 1) shows the expected C_{4v} symmetry. The Re-N distance is in good agreement with a rhenium-nitrogen triple bond. No exceptional bonding features can be discussed for the tetrabutylammonium cation.

$[ReNCl_4]^-$ is a suitable starting material for the synthesis of rhenium nitrido complexes. The oxidation state "+6" is maintained during the reaction with halides and NCS^-. With excess organic ligands reduction to rhenium(V) complexes can be observed. Fig. 2 gives a summary of products obtained from these reactions. The previously reported formation of the Re(VI) species with coordinated Ph_3P, bipyridine (bipy) and pyridine (py) /3/ obviously results from the very mild conditions applied and is in good agreement with our observations that Re(VI) species with coordinated organic ligands can also be detected EPR spectroscopically when an only small excess of ligand is used.

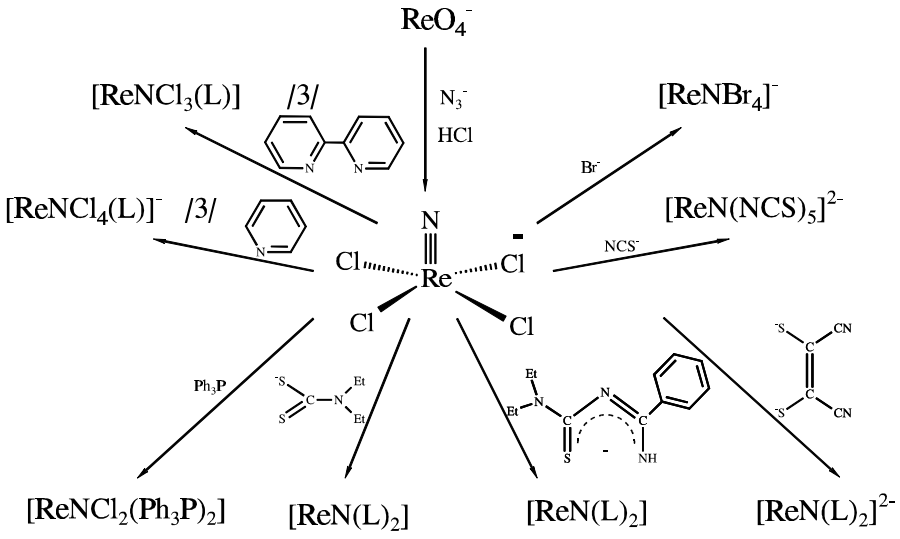

Fig. 2: Summary of reactions starting from $[ReNCl_4]^-$

Besides of reactions of $(NBu_4)[ReNCl_4]$ with Ph_3P, Me_2PhP and diethyldithiocarbamate (Et_2dtc^-) which gave the previously reported rhenium(V) complexes $[ReNCl_2(Ph_3P)_2]$, $[ReNCl_2(Me_2PhP)_3]$ and $[ReN(Et_2dtc)_2]$, we attempted reactions with N,N-diethylthiocarbamoylbenzamidine (HEt_2tcb) and sodium 1,2-dicyanoethene-1,2-dithiolate (Na_2mnt). Our recent attempts to isolate crystalline samples of $[ReN(Het_2tcb)_2]$ and $[ReN(mnt)_2]^{2-}$ from reactions of $[ReNCl_2(Ph_3P)_2]$ or $[ReNCl_2(Me_2PhP)_3]$ failed.
With $(NBu_4)[ReNCl_4]$, however, $[ReN(HEt_2tcb)_2]$ and $(NBu_4)_2[ReN(mnt)_2]$ could be easily isolated and structurally characterized /4/. Reactions with multidentate ligands are currently being investigated.

Acknowledgments
We gratefully acknowledge grants from the Deutsche Forschungsgemeinschaft (contract AB 67/4-1) and the Fonds of the Chemical Industry.

References

/1/ Liese, W., Dehnicke, K., Walker, I., Strähle, J.: Z. Naturforsch. **34**b, 693 (1978)
/2/ Dehnicke, K., Strähle, J.: Nitridokomplexe. Angew. Chem. **104**, 978 (1992)
/3/ Dehnicke, K., Prinz, H., Kafitz, W., Kujanek, R.: Liebigs Ann. Chem. 20 (1981)
/4/ Abram, U., Braun, M., Abram, S., Kirmse, R., Voigt, A.: (Nbu4)[ReNCl4] - A Facile Synthesis, Structure, EPR Spectroscopy and Reactions. J. Chem. Soc. Dalton Trans., in press

THERMAL ANALYSIS OF IRON AND URANYL COMPLEXES WITH NATURAL AND SYNTHETIC HUMIC ACIDS

G. Schuster, M. Bubner, R. Jander, S. Pompe, K.H. Heise, H. Nitsche
Forschungszentrum Rossendorf e.V., Institute of Radiochemistry

TG/DTA measurements showed that the thermal stability of the U(VI), Fe(II) and Fe(III) complexes of the natural humic acid A2 and the synthetic HA M1 is decreased compared to pure humic acids. The decrease of the oxidation temperature is reciprocally proportional to the complexation constants. It increases with the amount of bound metal and is bigger for synthetic humic acid compounds. From the inorganic oxidation residues, U_3O_8 and Fe_2O_3, the amount of bound metal and the metal ion saturation of the carboxylic groups of the humic acids were determined.

Experimental

The aim of this work was to determine thermoanalytical characteristics for the kind and the amount of metal bound in humic acid complexes. We used a synthetic humic acid prepared from phenylalanin, xylose and glycine (M1) /1/ and a purified natural HA from Aldrich (A2) /2/. Samples of about 5 mg were heated in a Setaram TG/DTA thermoanalyzer STA 92 up to 800 °C with a rate of 10 °C/min under a constant flow of oxygen of 3 L/h and were held for 10 min. During this procedure TG and DTA curves were recorded.

Results and discussion

U(VI) and Fe(III) complexes of the natural humic acid A2

Fig. 1 shows the DTA curves of the humic acid A2 and its U(VI) complexes.
The DTA diagrams of the U(VI) and Fe(III) complexes have similar shapes with one endothermic and three exothermic steps of the oxidative degradation reaction:

1. Water is released in a weak endothermic reaction up to 110 °C.
2. Up to 350 °C, the oxygen- and hydrogen-rich groups are exothermically degraded.
3. Up to 500 °C, in this exothermic step carbon rich groups are oxidized.
4. Above 500 °C, the residual carbon is oxidized in a final slightly exothermic step.

Up to 500 °C more than 90 % of the organic matter are oxidized. The final inorganic reaction products of the complexes at 800 °C under oxygen are U_3O_8 or Fe_2O_3. In comparison to the pure HA A2, the completion of the oxidation of the organic matter of the complexes (final temperature T_f of step 3) is shifted to lower temperatures. The thermal stability of the macro molecule is decreased in the complexes. The binding of the polyvalent cations to differently located carboxylic groups of the HA incorporates stress into the macromolecule which results in a lower decomposition temperature. This effect depends on the nature and amount of the bound metal. Tab. 1 lists the amounts of the uranyl ions and Fe(III) ions in the starting suspensions and the part of it, which was found again in the oxidizing residue of the complexes together with the T_f of reaction step 3 and the metal ion saturation of the carboxylic groups of the humic acids. For the A2 - U(VI) complexes with up to a 50 % COOH-group-saturation with U(VI), the thermal stability decreases proportionally to the amount of the U(VI) in the complex. At U(VI) contents of 4.49 meq/g which is near the saturation of the 4.8 meals carboxylic groups of HA A2, this effect stops and the DTA curve of the unchanged humic acid is registered. We conclude from this, that the complex formation did not take place and the two components humic acid and uranium perchlorate remain unchanged. This will be verified by other methods such as EXAFS or IR spectrometry.

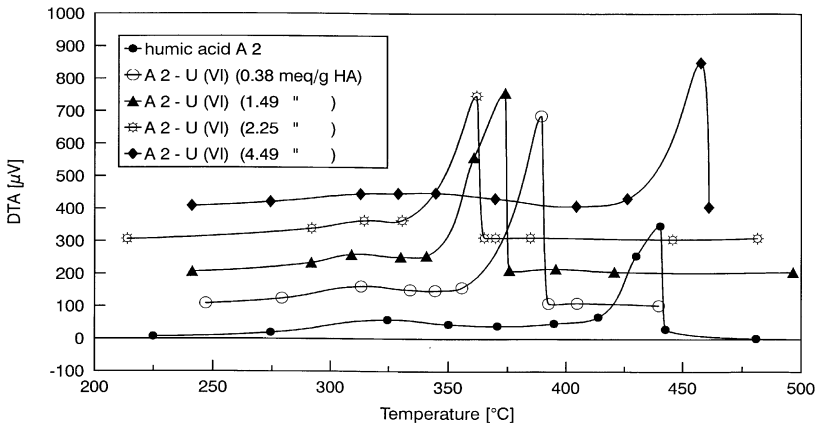

Fig. 1: Comparison of the DTA diagrams of the natural humic acid A2 and its U(VI) complexes with different uranium contents.
(y axis is displaced for clarity by 100 µV from sample to sample)

U(VI) in the starting susp. [meq]	inorganic residue U_3O_8 [%]	U(VI) in the complex [meq/g HA]	saturation of the COOH in the HA [%]	final temp. of reaction step 3 [°C]
0.48	5.26	0.38	8.2	394.8
2.4	17.45	1.49	31.1	374.8
4.8	24.25	2.25	50.0	368.4
13.2	39.76	4.59	95.6	476.2
Fe(III) in the starting susp. [meq]	inorganic residue Fe_2O_3 [%]	Fe(III) in the complex [meq/g HA]	saturation of the COOH in the HA [%]	final temp. of reaction step 3 [°C]
0.48	1.78	0.68	14.2	379.8
2.4	4.91	1.91	39.8	377.4
4.8	6.64	2.62	54.6	374.4
13.2	9.21	3.7	77.1	365.3

Tab.1: Results for the amount of bound U(VI) and Fe(III) and the thermal stability of a series of U(VI) - A2 and A2 - Fe(III) complexes with increasing metal content.
(T_f of reaction step 3 of the pure HA A2 = 440 °C)

For the iron complexes of the humic acid A2, the molar uptake of Fe (III) by HA A2 is higher and the thermal stability is lower than for the U(VI) complexes. A test was made with a Fe(II) complex prepared from a $FeSO_4$ starting solution and A2 humic acid. The amount of bound iron and the decrease of the T_f value does not reach the level of the Fe(III) complex. Compared with the complex formation constants of this three cations Fe(III), Fe(II) and U(VI), the thermal stability decreases in a reciprocal relation to the complex constants. The stronger the complex, the lower its thermal stability.

Fe(III) complex of the synthetic humic acid M1

A similar concentration series as for the A2 complexes were prepared for the Fe(III) complexes of the synthetic humic acid M1. In Fig. 2 and Tab. 2, the results of this series are shown. The humic acid M1 with only 1 meq/g carboxylic groups has a much lower capacity for the Fe(III) binding than the A2 HA. Additionally, a higher excess of iron in the preparation suspension is neccessary to reach saturation degrees similar for the A2. But according to Tab. 2, the thermal destabilization of the M1 by the Fe(III) ions is the most effective of all complexes which we have investigated and reaches a ΔT of - 145°C. Fig. 2 shows that only a very small iron contents in the macro molecule cause essential changes of the shape of the diagram to the typical DTA outfit of the complexes. We conclude that the thermal stability of humic acid is substantially lower when it is bound to uranium or iron. This enables us to differentiate between a metal compound humic acid mixture and a humic acid metal complex by comparison of the DTA curves. Additional information about the nature and the concentration of the bound metal can be derived from the end temperature of the oxidative degradation.

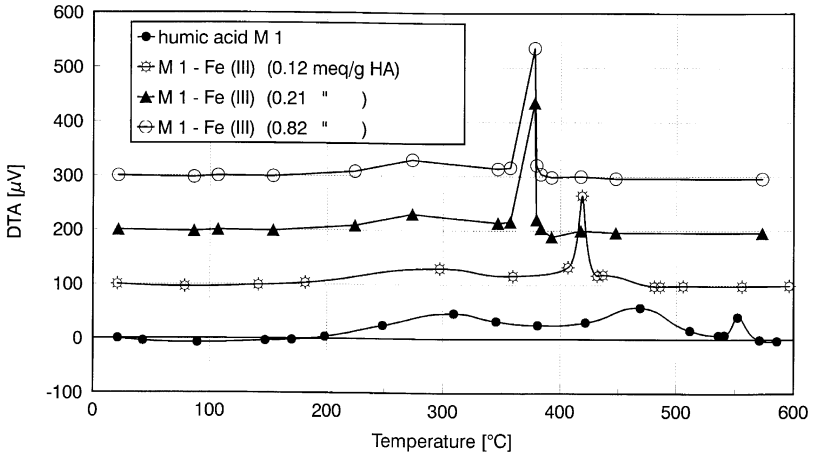

Fig. 2: Comparison of the DTA diagrams of the synthetic humic acid M1 and its Fe(III) complexes with different iron contents.
(y axis is displaced for clarity by 100 µV from sample to sample)

Fe(III) in the starting susp. [meq]	inorganic residue Fe_2O_3 [%]	Fe(III) in the complex [meq/g HA]	saturation of the COOH [%]	final temp. of reaction step 3 [°C]
0.1	0.34	0.12	12.9	469.6
1.0	0.54	0.21	20.4	394.2
5.0	2.14	0.82	81.8	384.4

Tab. 2: Results for the amount of bound Fe(III) and the thermal stability of a series of Fe(III) - M1 complexes with increasing Fe(III) content.
(T_f of reaction step 3 of the pure HA M1 = 525.8 °C)

References

/1/ Bubner, M., Pompe, S., Meyer, M., Jander, R., Schuster, G., Heise, K.H.: Synthesis of Uranium (VI) and Calcium Complexes with Carboxylic and Humic Acids. In: Report FZR-180, Institute of Radiochemistry, Annual Report 1996 (1997) p.22

/2/ Kim, J., Buckau, G.: Characterization of Reference and Site Specific Humic Acids. Report RCM 02188, TU München

Interaction of Microorganism with Radionuclides

MOLECULAR CLASSIFICATION AND URANIUM BINDING CAPABILITY OF *THIOBACILLUS FERROOXIDANS* ATCC 33020 RECOVERED FROM AN URANIUM MINE

S. Selenska-Pobell, A. Otto, S. Kutschke, P. Panak, G. Bernhard, H. Nitsche
Forschungszentrum Rossendorf e.V., Institute of Radiochemistry

A Thiobacillus isolate recovered from an uranium waste heap and described in the literature as Thiobacillus ferrooxidans ATCC 33020 is taxonomically neither closely related to the type strain of the species Thiobacillus ferrooxidans ATCC23270^T nor to any other strain of this species analyzed. This strain has a higher ability to accumulate U (VI) when compared to the type strain T. ferrooxidans 23270^T.

Thiobacilli (especially *T. ferrooxidans*) represent the main part of bacteria which have been cultured from uranium mine tailing piles /1, 2, 3/. *T. ferrooxidans* has been assumed to be the most important microorganism in biological leaching of Cu, U, Au, and Ag /1, 2, 3/. In addition, it was demonstrated that *T. ferrooxidans* is capable to accumulate U and other heavy metals in acidic liquors /2/. This may be important for uranium stabilization or even decontamination of uranium mine and mill tailings. Due to the development of new techniques for molecular microbial ecology studies, many new *Thiobacillus*-related and unrelated bacteria from U waste piles were recently characterized /1/. Some of these ”new” isolates may be even more important for finding solution to the problems of uranium pollution. The prospective for an application of such newly recovered natural *Thiobacillus* isolates requires their identification and their fast and reliable taxonomical categorization.
In this work, a highly reliable procedure for fast identification and classification of thiobacilli is presented. The procedure includes RFLP analysis of PCR-amplified 16S rDNA, 23S rDNA, and intergenic spacer rDNA between the 16S and the 23S rRNA-genes (amplified ribosomal DNA restriction enzyme analysis - **ARDREA**), as well as genomic PCR-fingerprinting using random primers (Random Amplified Polymorphic DNA - **RAPD**) and repetitive primers (Repetitive primer Amplified Polymorphic DNA - **Rep-APD**).

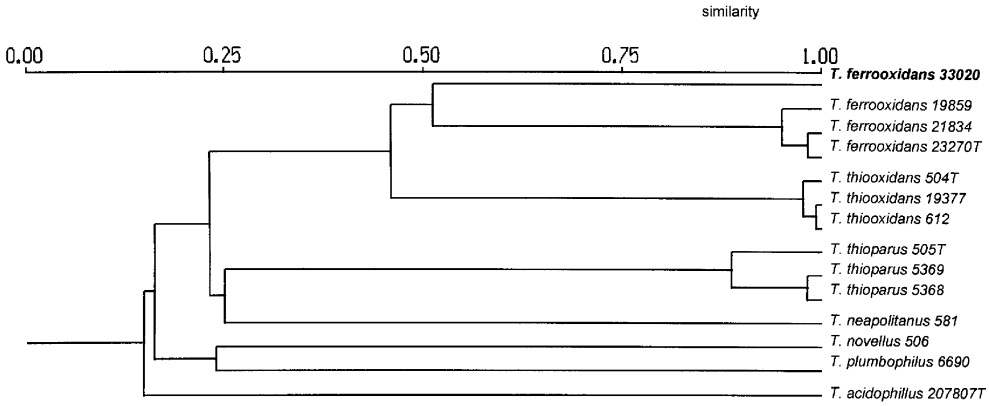

Fig.1: UPGMA dendrogram showing relationships between the strains studied as determined by ARDREA, Rep-APD, and RAPD.

The relation between the strains representing seven *Thiobacillus* species, was evaluated according to Selenska-Pobell et al. /4/ by deriving UPGMA dendrograms from the data of the ARDREA, RAPD and Rep-APD patterns. A dendrogram summarizing all results obtained by our procedure is presented in the Fig.1. The *T. ferrooxidans* type strain ATCC 23270^T and two other *T. ferrooxidans* strains (21834 and 19859) are grouped in a very tight cluster with over 90 % of similarity. The strain *T. ferrooxidans* ATCC 33020 is also related to this cluster. However, its similarity to the other three strains is only about 50 %. Interestingly, these four *T. ferrooxidans* strains are isolated from environments with different mineral content. The strain 33020 is an isolate from an uranium mine, *T. ferrooxidans* 23270^T and 21834 are recovered from two different coal mines, and the strain 19859 is an isolate from copper mine leachate. Our analysis indicates that the strain recovered from the uranium mine, *T. ferrooxidans* ATCC 33020, represents a particular branch of the species *T. ferrooxidans*, most probably a subspecies, which is neither closely related to the type strain *T. ferrooxidans* 23270^T nor to the other *T. ferrooxidans* strains studied.

The capability of the strains T*. ferrooxidans* 33020, 19859 and 23270^T to accumulate U(VI) was measured at pH 1.5. Fig. 2 (left) shows that the uranium mine isolate 33020 possesses a higher capability to accumulate uranium than the type *T. ferrooxidans* strain 23270^T and the strain *T. ferrooxidans* 19859 which originates from a cooper mine. Also shown in Fig. 2 (left) are the results for the strain *Thiomonas cuprinus* DSM 5495^T. It does not belong to the genus *Thiobacillus*, but was also recovered from an uranium mine as *T. ferrooxidans* ATCC 33020 and accumulates amounts of U(VI) which are even higher than those accumulated by the strain 33020.
Fig. 2 (right) shows the amounts of U(VI) which were released from the bacterial cells by EDTA treatment. These results demonstrate that a significant part of the U(VI) is strongly fixed by the bacterial cells and can not be re-extracted. Most probably it is bound on the cell walls. However, it is also possible that a part of the fixed U(VI) is incorporated in the bacterial cells (uptake).

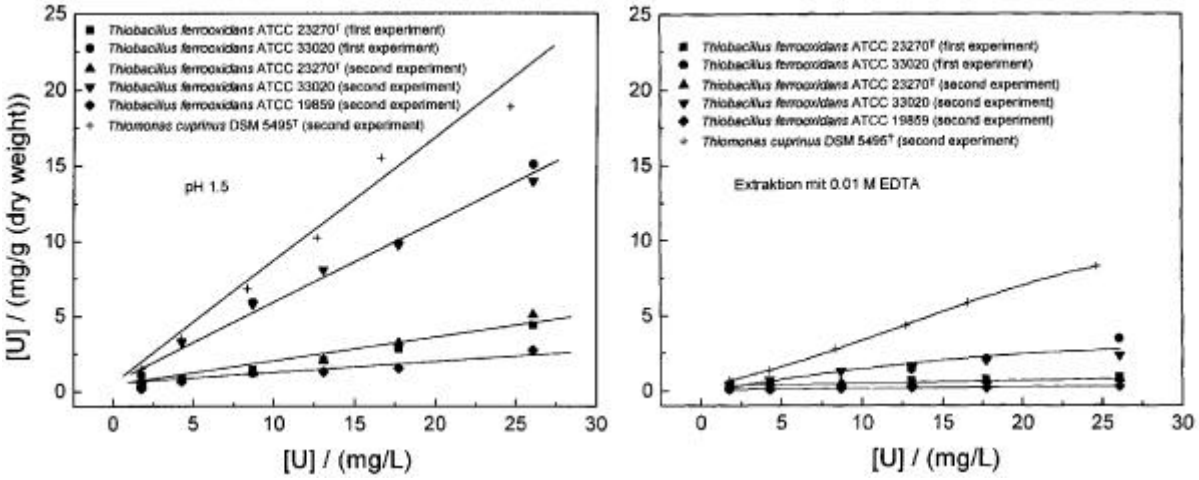

Fig. 2: Total uranium accumulation (left) and uranium concentration re-extracted with 0.01 M EDTA (right) of *Thiobacillus ferrooxidans* ATCC 23270^T, 33020, 19859 and of *Thiomonas cuprinus* DSM 5495^T.

The higher ability of the strain 33020 to accumulate uranium in comparison to the other *T. ferrooxidans* strains cannot be explained exclusively with its different geological origin. Our genetic analyses (see Fig. 1) demonstrate that this strain represents a different phylogenetic group which was not discriminated from the other *T. ferrooxidans* until now. Our preliminary results on the whole genome analysis of the four strains 19859, 21834, 23270^T and 33020 obtained by pulsed field gel electrophoresis (PFGE) show that the genomic organization of the strain 33020 significantly differs from those of the other *T. ferrooxidans* strains. The final classification of the strain 33020 will be performed by 16S rRNA gene sequence analysis. Studies on the nature of the higher uranium accumulation by the strain 33020 are in progress.
We conclude from our findings that one should use bacterial strains which originate from polluted environments for development of technologies for bioremediation of environments contaminated with uranium and other heavy metals.

Acknowledgments
This study was supported by grant 7531.50-03-FZR/607 from the Sächsisches Staatministerium für Wissenschaft und Kunst.
We thank Dr. W. Wiesner for ICP-MS measurements.

References
/1/ DiSpirito, A.A., Talnagy, J.W., Tuovinen, O.H.: Accumulation and cellular distribution of uranium in *Thiobacillus ferrooxidans*. Archives in Microbiology **135**, 250 (1983)
/2/ Goebel, B.M., Stackebrandt, E.: Cultural and phylogenetic analysis of mixed microbial populations found in natural and commercial bioleaching environments. Applied and Environmental Microbiology **60**, 1614 (1994)
/3/ Schippers, A., Hallmann, R., Wentzien, S., Sand, W.: Microbial diversity in uranium mine waste heaps. Applied and Environmental Microbiology **61**, 2930 (1995)
/4/ Selenska-Pobell, S., Evguenieva-Hackenberg, E., Radeva, G., Squartini, A.: Characterization of *Rhizobium "hedysari*" by RFLP analysis of PCR amplified rDNA and by genomic PCR fingerprinting. Journal of Applied Bacteriology **80**, 517 (1996)

STUDIES OF THE VARIABILITY OF NATURAL BACTERIAL COMMUNITIES IN URANIUM-CONTAMINATED SOILS AND DRAIN WATERS

G. Kampf, S. Selenska-Pobell
Forschungszentrum Rossendorf e.V., Institute of Radiochemistry

Results on molecular analysis of natural bacterial communities in two different uranium-contaminated environments in Saxony (the mill tailing in Coschütz/Gittersee and the uranium waste pile "Haberland") are presented. These results were obtained by PCR amplification of the ribosomal RNA intergenic spacer in DNA recovered by a direct lysis from water and soil samples.

Analysis of the indigenous bacteria in uranium- and other toxic metal-contaminated environments is of basic importance for the development of bioremediation procedures, because such bacteria are well adapted to the extremely complex geological, chemical, and biological composition of these environments. However, at present only a few percent of the bacteria living in soil and water can be cultured and analyzed in laboratory conditions /1/. For this reason, the best approach to obtain a survey of the contents and distribution of bacteria in nature is to extract their DNA by direct lysis (without cultivation) and to analyze it using molecular techniques /1, 2/. This approach was used in the work presented here.

DNA was recovered by direct lysis from 5 water and 5 soil samples from the remainders of the uranium mill tailing in Coschütz/Gittersee near Dresden as well as from 22 soil samples from the uranium waste pile "Haberland" near Johanngeorgenstadt. Before the isolation of DNA, water samples (500 ml) were filtered through a glassfibre prefilter and a 0.2 Fm membrane filter. Both filters, retaining microorganisms, were shaken for 1 hour at 37EC in 10 ml of a lysis medium containing: 50 mM EDTA, 50 mM Tris-HCl, 0.5% Tween 20, 0.5% Triton X100, 4 mg/ml lysozyme, 500 Fg/ml Proteinase K and 200 Fg/ml RN-ase A, pH 8.0, as recommended by Macherey-Nagel. After centrifugation for 20 min at 8000 rpm and 10EC, the clear lysate was further purified using Nucleobond AXG columns (Macherey-Nagel).

The DNA extraction from the soil samples of both wastes met some difficulties. Initially the method of Selenska and Klingmüller /2/ was used. However, because of the very low DNA yield from the pile samples, it was necessary to perform the lysis procedure with at least 50 g of soil instead of 2 g, used in the original method applied to an agricultural soil. As a result, the DNA extracted from uranium waste samples contained much higher amounts of humic acids in comparison to the DNA recovered from agricultural soils. In order to reduce the amount of the humic acids in the DNA fraction, which have inhibitory effects on the further DNA analysis, the following modifications of the method published in /2/ were performed: the lysis of bacteria in the soil samples was performed not as in /2/ (at 70EC with a phosphate buffer containing 1% SDS), but at 37EC with the above mentioned lysis medium. The further purification of the lysate was performed by centrifugation in CsCl density gradients or by anion exchange using the Nucleobond AXG columns. The second procedure was faster and more effective. In the case of the water samples, for example, which contained very small amounts of DNA, only the Nucleobond procedure was effective.

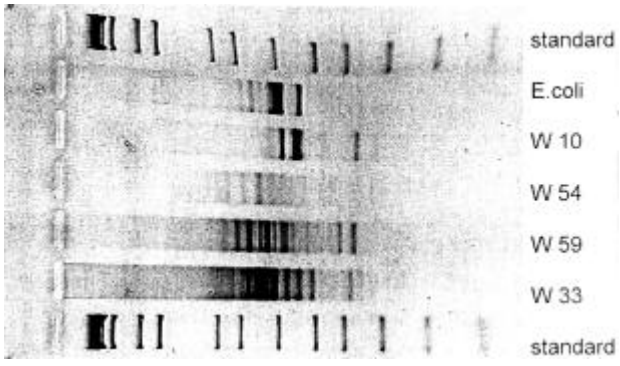

Fig. 1: RISA of the DNA recovered from four water samples (w) from the Coschütz/Gittersee mill tailings and *E. coli* (control). The standard is 1kb ladder Gibco-BRL.

The analysis of the isolated DNA was performed by PCR amplification of the bacterial intergenic spacer (IGS) between the 16S and 23S rDNA. This region of the bacterial genomes is flanked by highly conservative sequences of the 16S and 23S rRNA genes, but it possesses a high length and sequence variability. For these reasons, the **R**ibosomal RNA **I**ntergenic **S**pacer **A**nalysis (RISA) is an excellent method for fast evaluation of bacterial diversity /1, 3/. The RISA PCR primers and the amplification conditions were as those described in /1, 3/.

Both methods (gradient and Nucleobond) applied to the same sample provide DNA, the RISA-amplification of which yields almost the same patterns.

The RISA patterns varied in dependence on the place and on the depths from which the soil samples were taken. With increasing depths, up to 4-5 m, the bacterial diversity did not decrease, in some cases it was even higher. This result differs from the results of Shippers et al. /4/ who performed studies on another East German uranium waste pile, but by analysis of the culturable bacteria. These authors found a decrease of the bacterial content in the waste samples taken from depths below 2 m compared to the samples taken from the surface.
As mentioned above it was possible to extract very small amounts of DNA from the water samples (in some cases the DNA was even unvisible without PCR). The RISA analysis of these samples, however, was successfully performed and demonstrated that each sample possesses its highly characteristic IGS pattern (see Fig. 1).
The identification of the bacterial species represented by their IGS patterns will be possible by cloning and sequencing of the DNA fragments from the individual IGS bands obtained.

Acknowledgments
This work was partly supported by grant 7531.50-03-FZR/607 from the Sächsisches Staatsministerium für Wissenschaft und Kunst. We thank Dr. C. Puers and Mrs. C. Helling (TU Freiberg) for providing the water and soil samples.

References
/1/ Borneman, J., Triplett, E.W.: Molecular microbial diversity in soils from eastern Amazonia: Evidence for unusual microorganisms and microbial population shifts associated with deforestation. Appl. Environ. Microbiol. **63**, 2647 (1997)
/2/ Selenska, S., Klingmüller, W.: DNA recovery and direct detection of Tn*5* sequences from soil. Lett. Appl. Microbiol. **13**, 21 (1991)
/3/ Gürtler, V., Stanisich, V. A.: New approaches to typing and identification of bacteria using 16S-23S rDNA spacer region. Microbiology **142**, 3 (1996)
/4/ Schippers, A., Hallmann, R., Wentzien, S., Sand, W.: Microbial Diversity in Uranium Mine Waste Heaps. Appl. Environ. Microbiol. **61,** 2930 (1995)

ANALYSES OF BACTERIAL 16S rDNA IN SOIL OF A DECOMMISSIONED SAXONIAN URANIUM MINE

C. Puers, G. Kampf, S. Selenska-Pobell
Forschungszentrum Rossendorf e.V., Institute of Radiochemistry

The construction of a bacterial 16S rDNA library for soil samples of a defunct uranium mine near Johanngeorgenstadt, Saxony, Germany, was begun. Therefore, techniques were established in our laboratory for direct recovery of total DNA from soil bacteria communities, 16S rDNA polymerase chain reaction (PCR) amplification, 16S rDNA amplicon cloning, restriction fragment length polymorphism (RFLP) clone analyses. So far, the experiments led to 17 clones carrying a plasmid with an individual 16S rDNA fragment and will have to be optimized to gain more clones.

Bacterial soil compositions can be examined utilizing intrinsic 16S rDNA sequences /1, 2, 3/. The following methodology will be and partly has already been applied in order to obtain data on the bacterial community in soil samples from a former uranium mine of Johanngeorgenstadt, Saxony, Germany. One of objectives is to identify bacteria that are well adapted to radionuclide-containing environments. Intensive characterizations of identified bacteria might lead to the development of biotechnological procedures for treatment of radionuclide- and/or heavy metal-contaminated wastes, presuming that it will be possible to culture them.
In depths of 0 to 5 m soil samples were taken in a pseudo sterile manner from three sites of the „mine“ showing elevated uranium concentrations. To conserve the bacterial constitution, the samples were immediately frozen on dry ice. The bacterial DNA was isolated by a modified standard method /4/. Bacterial 16S rDNA fragments were amplified with a modified PCR technique /3/. In order to be able to sequence the 16S rDNA amplicons individually, the obtained mixture of diverse DNA fragments was ligated into the pCR®II vector (Invitrogen) and consecutively cloned using an Escherichia coli K12 derived strain (Invitrogen). RFLP analyses, employing the enzyme Hae III, permit preselection of clones for DNA sequencing. Preliminary experiments resulted in 17 clones. Refinement of the used methods is under way to obtain several hundreds instead of a few clones. Comparison of obtained 16S rDNA sequences with data in the genome database GenBank /5/ will allow approximate classification and limited

quantification of the associated bacteria. This analysis strategy can generally be used for samples from radionuclide-contaminated environments.

Acknowledgments
This work was partly supported by grant 7531.50-03-FZR/607 of the Sächsisches Staatsministerium für Wissenschaft und Kunst.

References

/1/ Stackebrandt, E., Liesack W., Goebel, B.M.: Bacterial diversity in a soil sample from a subtropical Australian environment by 16S rDNA analysis. FASEB Journal **7**, 232-236 (1993)
/2/ Borneman, J., Skroch, P.W., O'Sullivan, K.M., Palus, J.A., Rumjanek, N.G., Jansen, J.L., Nienhuis, J., Triplett, E.W.: Molecular microbial diversity of an agricultural soil in Wisconsin. Appl. Environ. Microbiol. **62**, 1935-1943 (1996)
/3/ Chandler, D.P., Fredrickson, J.K., Brockman F.J.: Effect of PCR templated concentration and distribution of total community 16S rDNA clone libraries. Molecular Ecology **6**, 475-482 (1997)
/4/ Selenska, S., Klingmüller, W.: Direct detection of *nif*-gene sequences of Enterobacter agglomerans in soil. FEMS Microbiol. Letters 80, 243-246 (1991)
/5/ Benson, D.A., Boguski, M.S., Lipman, D.J., Ostell J., Ouellette, B.F.: GenBank. Nucleic Acids Res. **26**, 1-7 (1998)

CHARACTERIZATION OF BACILLI RECOVERED FROM AN URANIUM MINE TAILING PILE

V. Miteva, I. Boudakov[1], S. Selenska-Pobell
Forschungszentrum Rossendorf e.V., Institute of Radiochemistry
[1] Institute of Microbiology, Bulgarian Academy of Sciences, Sofia, Bulgaria

For the first time Bacillus-species from an uranium mine tailing pile were taxonomically characterized. For this purpose more than hundred gram-positive sporulating bacterial isolates were cultured from the uranium mine tailing pile near Johanngeorgenstadt. One of them is classified as B. cereus and two as B. megaterium. Additional 57 isolates are preliminary categorized in 16S-ARDREA-Bacillus types which are related to the reference Bacillus species. Six of the natural isolates are not closely related and three of them are not at all related to the studied reference Bacillus strains.

In addition to the main group of bacteria (thiobacilli) which occur naturally in the wastes of uranium mining, presence of bacilli was also noticed /1/. However, no information was available on the different kinds of *Bacillus* and their distribution in uranium and toxic metal-contaminated environments. Characterization of the indigenous *Bacillus* strains of the wastes is very important because such strains may be excellent candidates for the development of bacteria-based bioremediation procedures.

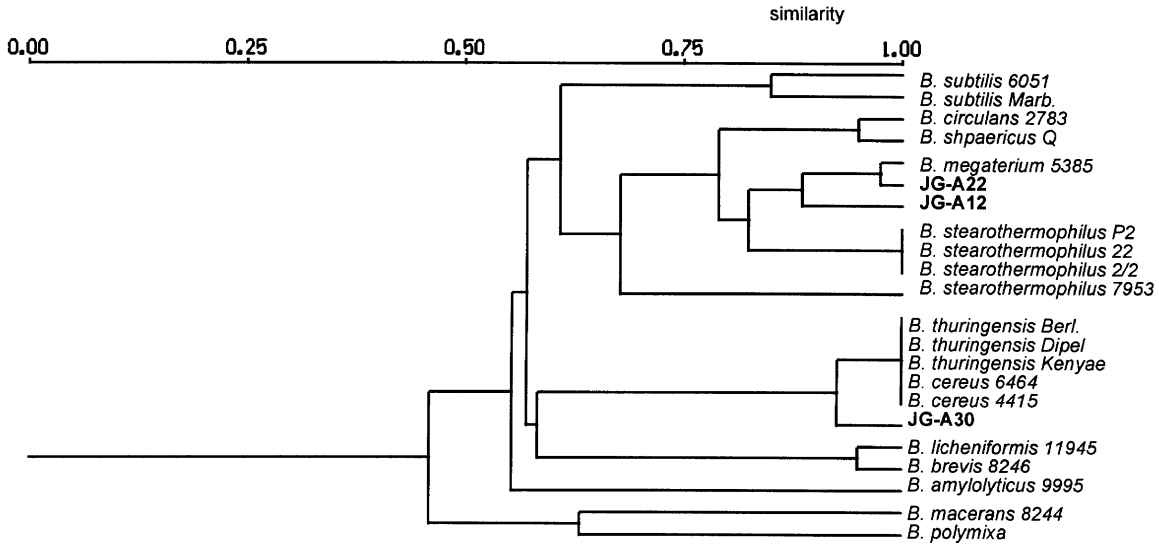

Fig.1: UPGMA dendrogram showing relationships between the natural *Bacillus* isolates JG-A12, JG-A22 and JG-A30, and the reference *Bacillus* strains as determined by 16S-ARDREA.

From the uranium mine tailing pile near Johanngeorgenstadt, 120 gram-positive sporulating bacterial strains were isolated. 75 of them were morphologically categorized as *Bacillus*. The exact classification of 60 of these isolates was begun by PCR amplification of their 16S rDNA followed by restriction fragment length polymorphism (RFLP) analysis of the resulting amplificates. The method is also known as 16S amplified ribosomal DNA restriction enzyme analysis (16S-ARDREA). Three of the natural Bacillus isolates were preliminarily classified. Two of them - JG-A22 and JG-A30 - belong to the species *B. cereus* and *B. megaterium,* respectively (Fig. 1). Interestingly, the third isolate - JG-A12 - which formes spherical spores typical for the representatives of the *species B. sphaericus*, seems to be phylogenetically more closely related to the species *B. megaterium*. The exact classification of this strain is in progress.

Enzyme	RFLP-Types	Species	Number of isolates	Unknown RFLP-Types
*Alu*I	11	*B.cereus* *B.licheniformis* *B.brevis/subtilis* *B. amyloliticus* *B.sphaericus/circulans* *B. megaterium* *B. macerans*	20 12 7 6 5 5 1	JG-A18 JG-B11 JG-B56 JG-B1T
*Hae*III	21	*B.cereus* *B.sphaericus/circulans* *B. subtilis* *B. megaterium* *B. amyloliticus* *B. macerans* *B. polymixa*	26 9 6 6 1 1 1	JG-A18 JG-A19 JG-B11 JG-B26, B56, B69 JG-B1T
*Msp*I	11	*B. cereus* *B.sphaericus/circulans* *B.licheniformis* *B.brevis/subtilis* *B. amyloliticus* *B. megaterium* *B. macerans*	15 15 13 2 1 1 1	JG-B11 JG-B26, B49, B51, B55, B69 JG-B1T JG-B5T

Tab. 1: 16S-ARDREA Grouping of the JG-Bacillus Isolates

Until now we analyzed the rest of the JG-isolates with only three of the commonly used 10 restriction endonucleases. The isolates are grouped in different RFLP types listed in Tab. 1.
From the results follows that six of the JG-isolates (JG-A18, JG-A19, JG-B26, JG-B49, JG-B51, and JG-B69) are weakly related to the studied *Bacillus* reference strains while three of them (JG-B11, JG-B56, and JG-B1T) are not at all related to these reference strains.
Our results are in agreement with the opinion expressed in Ref. 2 that the genus *Bacillus* is genetically extremely heterogenous. For a more precise classification of the JG-isolates, we are intend to involve extensive ARDREA analysis of the whole *rrn* operon, as well as genomic fingerprinting and possibly DNA sequence analyses of the isolated Bacillus strains.

Acknowledgments
This study was supported by grant 7531.50-03-FZR/607 from the Sächsisches Ministerium für Wissenschaft und Kunst. The participation of I. Boudakov was financed by the BMFT, grant WTZ-Bul-014-97, Bonn. We thank Dr. Puers for providing soil samples from the uranium wastemine tailing pile near Johanngeorgenstadt.

References
/1/ Cerdá, J., Gonzalez, S., Rios, J.M., Quintana, T.: Uranium concentrates biosorption in Spain: A case study. FEMS Microbiology Reviews **11**, 235 (1993)
/2/ Ash, C., Farrow, J.A.E., Wallbanks, S., Collins M.D.: Phylogenetic heterogenity of the genus Bacillus revealed by comparative analysis of small-ribosomal RNA. Letters in Applied Microbiology **13**, 202 (1991)

URANIUM REDUCTION BY A NATURAL *DESULFOVIBRIO* ISOLATE JG 1

P. Panak, B.C. Hard [1], K. Pietzsch [1], S. Selenska-Pobell, G. Bernhard, H. Nitsche
Forschungszentrum Rossendorf e.V., Institute of Radiochemistry
[1] UFZ-Umweltforschungszentrum Leipzig-Halle GmbH

We examined the reduction of U(VI) by a Desulfovibrio isolate (JG 1) from a uranium mining waste pile and compared the results to the reduction of uranium by a sulfate-reducing bacterial reference strain (Desulfovibrio desulfuricans DSM 642^T). Quantitative and kinetic studies showed that the reduction capacity of JG 1 is much higher and less pH dependent.

The reduction of U(VI) was studied by sulfate-reducing bacteria, *Desulfovibrio desulfuricans* DSM 642^T, recovered from a soil near a gas main, and a natural *Desulfovibrio* isolate (JG 1) recovered from an uranium mining waste pile (Haberlandhalde, Johanngeorgenstadt, Saxony, Germany). The representatives of the genus *Desulfovibrio* can use U(VI) as a terminal electron acceptor to obtain energy for growth while the reduced U(IV) precipitates /1-3/. We compared the reduction capacity of the natural isolate with that of the reference strain by studying the uptake and its kinetics under various conditions.

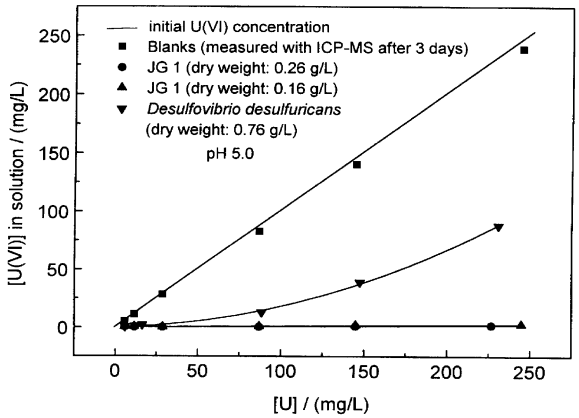

Fig. 1: Decrease of U(VI) concentration in solution after 3 days in presence of the strain *Desulfovibrio desulfuricans* DSM 642^T, the isolate (JG 1) from a uranium mining waste pile, and in absence of biomass (blanks).

Fig. 1 shows the amount of U(VI) removed from the reaction solution by bacterial reduction as a function of the initial U(VI) concentration for the strain *Desulfovibrio desulfuricans* and the JG 1 culture. JG 1 with a biomass of 0.16 g/L reduced U(VI) quantitatively up to at least 245 mg/L, which was the highest amount investigated. The reference strain *Desulfovibrio desulfuricans*, however, could only reduce about 60 % of this amount at comparable U(VI) concentrations, although an almost five times larger biomass was used. Hence, the reduction capability of the two bacterial strains differs by at least a factor of 8 (per biomass) at the investigated uranium concentration. The U(VI) concentrations of the blanks measured by ICP-MS after 3 days did not differ significantly from the initially added concentrations. This indicates that no formation of insoluble hydrolysis species and sorption on the surface of the reaction tubes occured that may have disturbed the experiments.

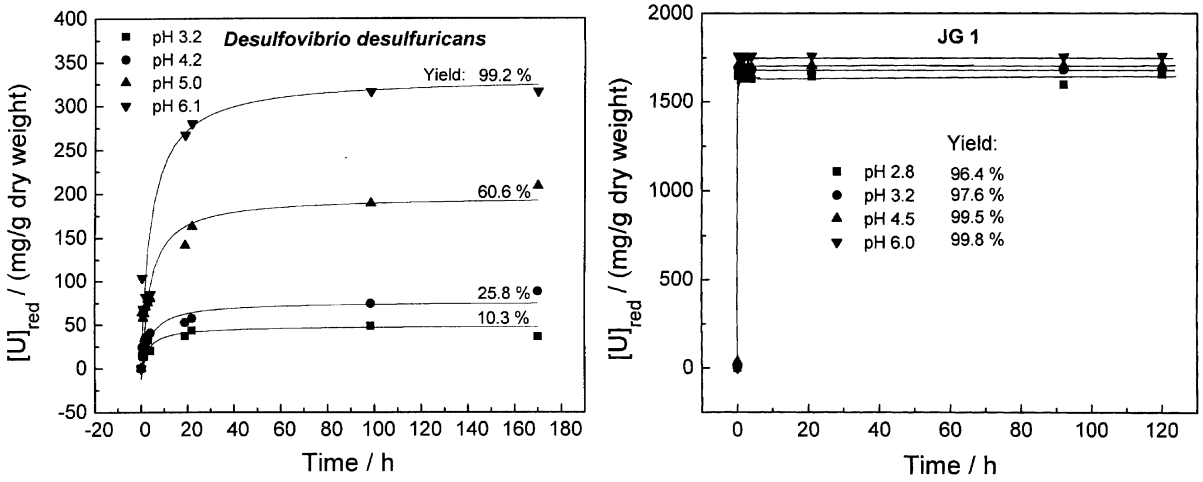

Fig. 2: Amount of U(VI) converted to insoluble U(IV) by *Desulfovibrio desulfuricans* (left) and JG 1 as a function of time at different pH-values (right). The results are normalized to the dry weight of the bacteria.

Fig. 2 a and b present the amount of U(VI) converted to insoluble U(IV) as a function of time for different pH values. The results are normalized to the dry weight of the bacteria. As demonstrated by the time dependencies of the bacterial reduction, for *Desulfovibrio desulfuricans* the

main transformation of U(VI) occured during the first 24 hours which agrees with /4/. From 24 to 100 hours, only a slight increase of the U(IV) amount was observed. After 100 hours, the following limiting values were reached:

pH 3.2:	41.2 ± 5.0 $mg/g_{dry\ weight}$
pH 4.2:	81.1 ± 6.9 $mg/g_{dry\ weight}$
pH 5.0:	198.5 ± 9.9 $mg/g_{dry\ weight}$
pH 6.1:	316.2 ± 0.1 $mg/g_{dry\ weight}$

An yield increase from 10.3 to 99.2 % was observed when the pH was changed from 3.2 to 6.1. The rate and yield increase with increasing pH corresponds well to the neutral pH-optimum for survival of this reference strain. In contrast to the results of the reference strain, a quantitative reduction was observed for JG 1 within 15 minutes at all pH-values (Fig. 2 b). These results show that microbial reduction is very effective and quite pH independent for the natural isolate. The reduction capacity of *D. desulfuricans* already decreased significantly at pH 4.2 and a nearly complete uptake was only reached at pH 6.1. For JG 1 nearly complete uptake occurred already at pH 2.8. JG 1 seems to be more inert to chemical changes of the surrounding environment and uses U(VI) instead of sulfate as energy source more efficiently than the reference strain. These results indicate that natural isolates from uranium mining waste piles are of particular importance for bioremediation purpose because they are more adaptable to environmental pH changes. A preliminary characterization of the precipitate produced by another sulfate-reducing bacterial strain by X-ray absorption near-edge spectroscopy (XANES) has confirmed the formation of U(IV). Further oxidation state analyses by XANES on JG 1 and other natural isolates from uranium waste piles are in progress.

Acknowledgments

This work was supported by a grant 7531.50-03-FZR/607 from the Sächsisches Staatsministerium für Wissenschaft und Kunst. We thank Dr. W. Wiesener for ICP-MS-measurements.

References

/1/ Lovley, D.R., Widman, P.K., Woodward, J.C., Phillips, E.J.P.: Reduction of Uranium by Cytochrome c_3 of Desulfovibrio vulgaris. Appl. Environ. Microbiol. **59/11**, 3572-3576 (1993)

/2/ Lovley, D.R.: Dissimilatory Metal Reduction. Ann. Rev. Microbiol. **47**, 263-290 (1993)

/3/ Lovley, D.R., Phillips, E.J.P.: Reduction of Uranium by Desulfovibrio desulfuricans. Appl. Environ. Microbiol. **58**, 850-856 (1992)

/4/ Gorby, Y.A., Lovley, D.R.: Enzymatic Uranium Precipitation. Environ. Sci. Technol. **26**, 205-207 (1992)

Application of X-Ray Absorption Spectroscopy

DETERMINATION OF U(VI) REDUCTION AFTER BACTERIAL METABOLIZATION BY URANIUM L_{III}-EDGE XANES SPECTROSCOPY

T. Reich, P. Panak, B. Mack, M.A. Denecke, C. Hennig, A. Roßberg, L. Baraniak, S. Selenska-Pobell, G. Bernhard, H. Nitsche
Forschungszentrum Rossendorf e.V., Institute of Radiochemistry

A sulfate-reducing bacterial strain of the species Desulfomicrobium baculatum metabolizes U(VI). The uranium oxidation state after metabolization was determined by x-ray absorption near-edge fine structure (XANES) spectroscopy.

Certain microorganisms can reduce uranium(VI) to uranium(IV) under anaerobic conditions and thus reduce the mobility of uranium in the environment /1, 2/. Therefore, the study of uranium interaction with heterotrophic anaerobic bacteria is important for the development of efficient and cost-effective remediation processes of uranium contaminated sites.
We applied uranium L_{III}-edge XANES spectroscopy to determine the uranium oxidation state after metabolization of uranium(VI) by a sulfate-reducing bacterial strain of the species *Desulfomicrobium baculatum*. After culturing the bacterial strain in 600 mL growth medium, the bacterial cells were obtained by centrifugation. Then they were suspended in 0.9% NaCl solution and the sample was incubated with 50 mL 10^{-4} M U(VI) solution at pH 5.0. After shaking the sample for two days under nitrogen atmosphere, the biomass was separated by centrifugation, washed with 5 mL 0.9% NaCl solution, and sealed in a polyethylene cuvette for XANES measurements. Two 0.04 M U(IV) and U(VI) solutions in 1 M $HClO_4$ served as reference samples for the uranium oxidation states. The U(VI) stock solution was obtained by dissolving $Na_2U_2O_7 \cdot 6H_2O$ in 7 M $HClO_4$. Part of this solution was reduced electrochemically to U(IV) at a mercury pool cathode. In addition, two samples with molar ratios of U(IV) to U(VI) of 3.0 and 0.33 were prepared by mixing U(IV) and U(VI) solutions under nitrogen atmosphere. Four mL of each solution was transferred into air-tight polyethylene cuvettes of 13 mm diameter. Uranium L_{III}-edge spectra were measured at ambient temperature at HASYLAB at the experimental station RÖMO II, beamline X1.1, using the Si(311) double-crystal monochromator detuned 50% of the maximum incident flux. The bacteria sample was measured in fluorescence mode; all solution samples in transmission mode. The energy scale was calibrated against the first inflection point (defined as 17165 eV) of a 0.04 M U(VI) solution sample, which was measured simultaneously. After background removal, the spectra were normalized to equal intensity at 17250 eV. The U(IV)/U(VI) ratio of the aqueous mixtures was determined by fitting their XANES features as a linear combination of the experimental XANES of the single-component solutions. The same approach has been success-fully applied to the determination of the As(III)/As(V) ratio in arsenic containing water samples /3/.

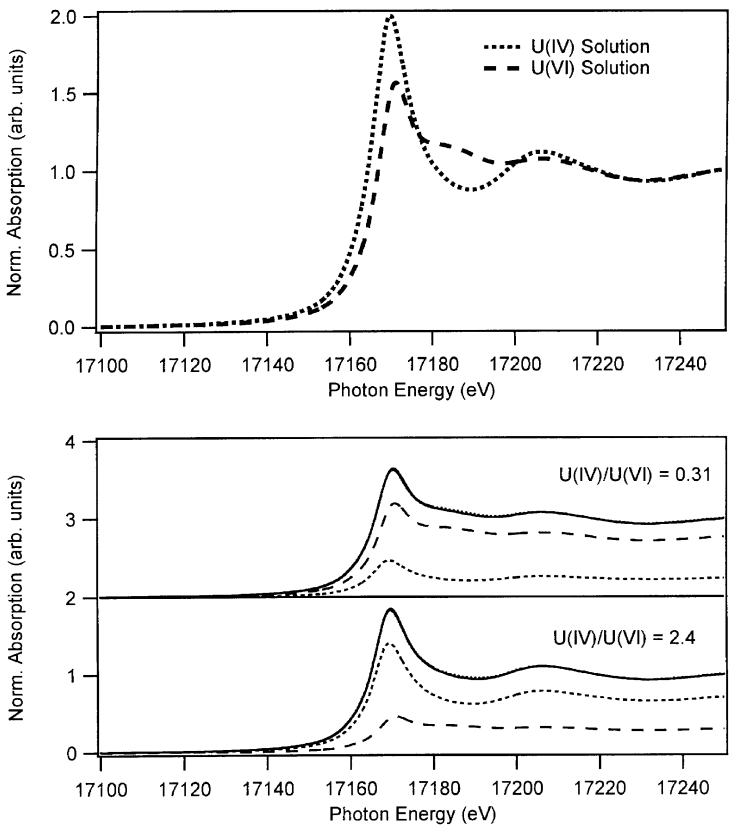

Fig. 1: Top: Experimental U L_{III}-edge XANES spectra of U(IV) and U(VI) reference solutions containing 0.04 M uranium in 1 M $HClO_4$. Bottom: Experimental U L_{III}-edge XANES spectra of two 0.04 M uranium solution mixtures (dots) and the U(IV) (short-dashed curve) and U(VI) (long-dashed curve) constituents of the fit (solid curve).

Fig. 1 shows the uranium L_{III}-edge XANES spectra of the aqueous reference solutions and the

mixtures containing both U(IV) and U(VI). Compared to U(VI), the white line (WL) intensity of the U(IV) XANES spectrum is increased and its energy is reduced. Additional changes occur also in the XANES above the WL. These observations agree with previous uranium L_{III}-edge XANES measurements of UO_2 and $UO_2(NO_3)_2 \cdot 6H_2O$ /4/. The observed spectral changes allow to distinguish between U(IV) and U(VI) oxidation states and to determine their relative concentration as illustrated in Fig. 1. The fitted XANES of the mixtures coincide with the experimental spectra. The U(IV)/U(VI) ratios of 2.4 and 0.31 obtained are close to the corresponding values of 3.0 and 0.33 used for preparing these mixtures.

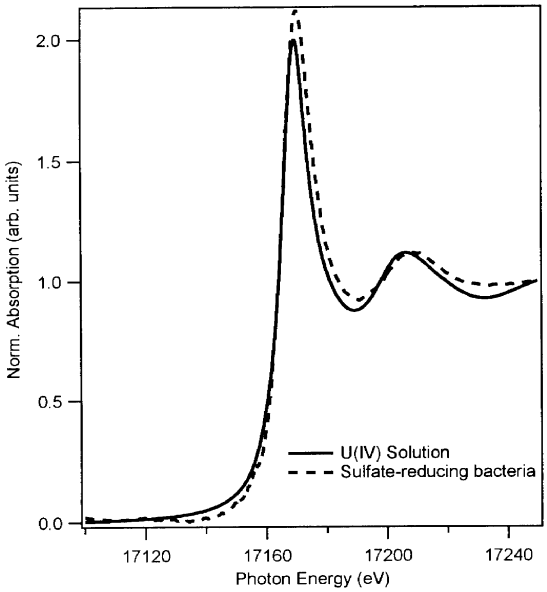

Fig. 2: Experimental U L_{III}-edge XANES spectra of 0.04 M U(IV) solution and uranium after bacterial metabolization of U(VI).

Fig. 2 shows a comparison of the uranium L_{III}-edge XANES spectra of the bacterial sample with the U(IV) reference solution. After metabolization of hexavalent uranium by sulfate-reducing bacteria, uranium XANES shows almost identical spectral features as the U(IV) solution. Small deviations can indicate different uranium near-neighbor surroundings between the bacterial sample and the reference solution. As in the case of the U(IV) reference solution, the energy of the WL maximum is shifted by 1.7 eV to lower energy relative to the U(VI) reference. It can be concluded that the bacteria sample contained only reduced tetravalent uranium.

Our measurements clearly demonstrate the analytical potential of uranium L_{III}-edge XAFS spectroscopy for the investigation of bacteria-uranium interactions. It can be applied for the determination of U(IV) and U(VI) oxidation states and structural parameters of uranium near-neighbor surroundings.

References

/1/ Lovley, D.R., Phillips, E.J.P., Gorby, Y.A., Landa, E.R.: Microbal reduction of uranium. Nature **350**, 413 (1991)

/2/ Lovley, D. R.: Dissimilatory metal reduction. Ann. Rev. Microbiol. **47**, 263 (1993)

/3/ Denecke, M.A., Friedrich, H., Reich, T., Bernhard, G., Knieß, T., Rettig, D., Zorn, T., Nitsche, H.: Determination of relative arsenite and arsenate concentrations in aqueous mixtures by XANES. HASYLAB Annual Report 1996 **1**, 751 (1997)

/4/ Petiau, J., Calas, G., Petitmaire, D.: Delocalization versus localized unoccupied 5f states and the uranium site structure in uranium oxides and glasses probed by x-ray-absorption near-edge structure. Phys. Rev. B **34**, 7350 (1986)

STRUCTURAL INVESTIGATIONS OF THE SYSTEM $Ca^{2+}/UO_2^{2+}/CO_3^{2-}$ BY EXAFS

T. Reich, G. Geipel, M.A. Denecke, P.G. Allen [1], J.J. Bucher [1], N.M. Edelstein [1], D.K. Shuh [1], G. Bernhard, H. Nitsche

Forschungszentrum Rossendorf e.V., Institute of Radiochemistry

[1] Chemical Sciences Division, Lawrence Berkeley National Laboratory, Berkeley, USA

The structure of a recently discovered aqueous species, $Ca_2UO_2(CO_3)_{3(aq.)}$, /1/ was studied by EXAFS and compared to two model systems, i.e., $[UO_2(CO_3)_3]^{4-}_{(aq.)}$ and $Ca_2UO_2(CO_3)_3 \cdot 11H_2O$.

During recent studies of calcium-rich waters related to uranium mining, the existence of a neutral complex $Ca_2UO_2(CO_3)_{3(aq.)}$ was established /1/. We performed extended x-ray absorption fine structure (EXAFS) measurements to validate the new species and to study its structure. EXAFS measurements were carried out on two solution samples. Solution **1** consisted of 0.5 mM UO_2^{2+}, 2 mM Ca^{2+}, and 5 mM CO_3^{2-} at pH of 8.0. Solution **2** was calcium-free and contained 1 mM UO_2^{2+} and 20 mM CO_3^{2-} at pH 8.0. According to speciation calculations using the software package EQ3/6, the complex stability constant for the new complex, and the NEA data base, solutions **1** and **2** should contain nearly 82% of the $Ca_2UO_2(CO_3)_{3(aq.)}$ - complex and 99% of the $[UO_2(CO_3)_3]^{4-}_{(aq.)}$ species, respectively. For comparison, we measured two solid

samples **3** and **4**, which have the same stoichiometric composition as solution complex **1**. Sample **3** was a natural Liebigite, $Ca_2UO_2(CO_3)_3 \cdot 11H_2O$, obtained from the Mineralogical Collection of Technische Universität Bergakademie Freiberg, Germany. Sample **4** was a synthetic Liebigite prepared according to /2/.

EXAFS measurements of samples **1**-**4** were performed on beam line 4-1 at the Stanford Synchrotron Radiation Laboratory (SSRL) using a Si(220) double-crystal monochromator. The uranium L_{II}-edge EXAFS spectra of samples **1** and **2** were measured in fluorescence mode. Due to higher concentrations, the uranium L_{III}-edge EXAFS spectra of samples **3** and **4** could be measured in transmission mode. For energy calibration, a UO_2 foil was used as a reference and measured simultaneously. The ionization potentials of the uranium L_{II} and L_{III} edges were defined as 20965 and 17185 eV, respectively. The EXAFS spectra were analyzed according to standard procedures using the suite of programs EXAFSPAK and theoretical scattering phases and amplitudes calculated with the scattering code FEFF7.

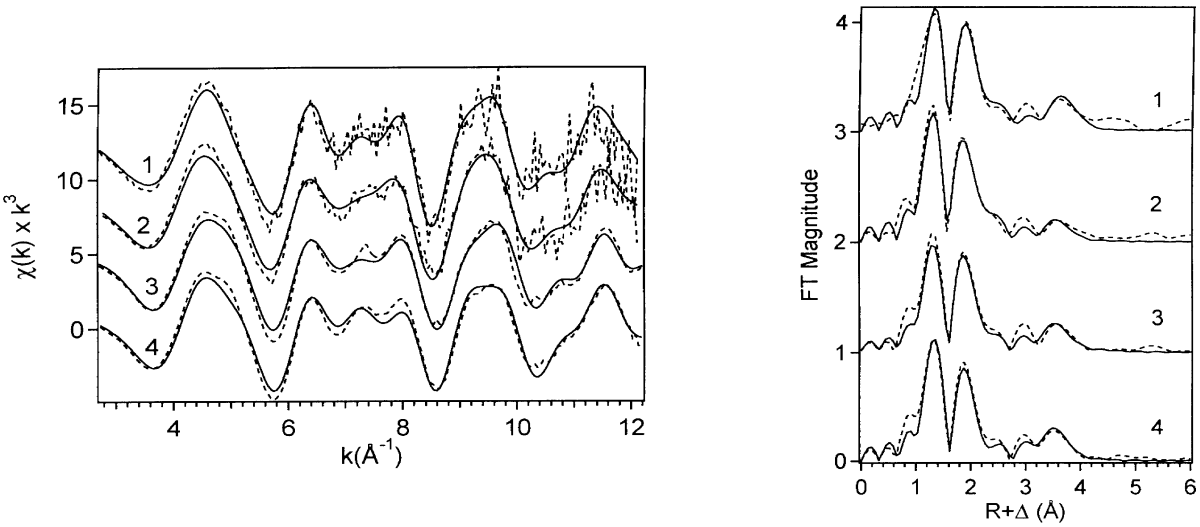

Fig. 1: Left: k^3-weighted EXAFS spectra of (1) $Ca_2UO_2(CO_3)_{3(aq.)}$, (2) $[UO_2(CO_3)_3]^{4-}_{(aq.)}$, (3) natural liebigite, and (4) synthetic liebigite, $Ca_2UO_2(CO_3)_3 \sim 11H_2O$. Right: Corresponding Fourier transforms without phase corrections. The dotted lines are the experimental data, and the solid line is the theoretical fit.

The k^3-weighted uranium L_{II} and L_{III} edge EXAFS spectra of samples **1** - **4** together with the best fits to the data are shown in Fig. 1. Natural and synthetic liebigite samples show very similar EXAFS pattern up to k equal 12 $Å^{-1}$. Due to the much lower uranium concentration in solutions **1** and **2**, the noise level of their EXAFS is higher than for samples **3** and **4**. Nevertheless, the solution samples show similar EXAFS oscillations as the liebigite mineral samples indicating nearly identical uranium near-neighbor surrounding in all samples. This is also reflected by the observed similarities of the corresponding Fourier transforms (see Fig. 1).

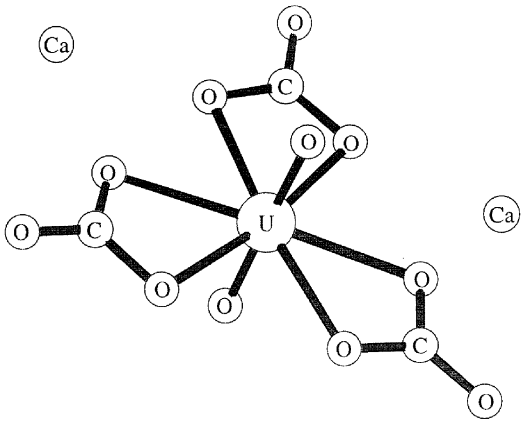

Fig. 2: Ball-and-stick drawing illustrating the structural model used for fitting the EXAFS spectra.

Based on the crystal structure of $Ca_2UO_2(CO_3)_3 \cdot 11H_2O$ /3/, a fit to the experimental spectra of samples **3** and **4** was performed using the structural model given in Fig. 2.

The model consisted of four uranium coordination shells belonging to the $UO_2(CO_3)_3$ unit, i.e., U-O_{ax}, U-O_{eq}, U-C, and U-O_{dis}. The U-O_{dis} coordination shell was modeled by the three-legged multiple-scattering interaction along the linear U-C-O_{dis} path. Since the $UO_2(CO_3)_3$ units are linked by several types of calcium polyhedra, an additional U-Ca shell was included in the fit. According to the crystal structure, the closest calcium atoms are located at 4.07 Å between neighboring CO_3 units in the equatorial plane (see Fig. 2). As can be seen from Tab. 1, the interatomic distances obtained by EXAFS are in good agreement with the crystallographic values. In spite of this agreement, it is difficult, if not impossible, to detect the presence

of two calcium atoms at 4.07 Å unambiguously. The fit did not deteriorate significantly if the U-Ca shell was excluded from the fit since the missing U-Ca amplitude contribution was compensated by a small increase of the U-O_{dis} amplitude.

Sample	Description	2x(U-O_{ax})		6x(U-O_{eq})		3x(U-C)		3x(U-O_{dis})		2x(U-Ca)	
		R(Å)	F^2(Å^2)	R(Å)	F^2(Å^2)	R(Å)	F^2(Å^2)	R(Å)	F^2(Å^2)	R(Å)	F^2(Å^2)
1	$Ca_2UO_2(CO_3)_{3(aq.)}$	1.81	0.001	2.44	0.005	2.90	0.004	4.22	0.002	3.94	0.008
2	$[UO_2(CO_3)_3]^{4-}{}_{(aq.)}$	1.80	0.001	2.44	0.005	2.89	0.002	4.20	0.004	-	-
3	Liebigite (nat.)	1.80	0.002	2.43	0.006	2.88	0.003	4.17	0.002	4.04	0.014
4	Liebigite (synth.)	1.81	0.0009	2.43	0.006	2.89	0.004	4.18	0.007	4.00	0.005
XRD*	Liebigite (nat.)	1.78		2.43		2.86		4.12		4.07	

*) Distances measured by XRD /3/

Tab. 1: EXAFS structural parameters for samples **1** - **4** and comparison with XRD. The uncertainty of R is ±0.02 Å.

The EXAFS spectra of samples **1** and **2** were fitted with the $UO_2(CO_3)_3$ unit as a structural model. As can be seen from the obtained structural parameters given in Tab. 1, the $Ca_2UO_2(CO_3)_{3(aq.)}$ - complex consists of the same $UO_2(CO_3)_3$ unit as in $[UO_2(CO_3)_3]^{4-}{}_{(aq.)}$ and solid liebigite. Although a somewhat better fit for sample **1** was obtained by including the U-Ca shell than without, the location of the two calcium atoms in the aqueous complex cannot be derived from such small differences in the fit. However, the EXAFS results do not contradict the possibility that the calcium atoms in $Ca_2UO_2(CO_3)_{3(aq.)}$ assume similar positions as in the liebigite mineral (see Fig. 2).

Acknowledgment
EXAFS measurements were made at SSRL, which is operated by the US Department of Energy.

References

/1/ Bernhard, G., Geipel, G., Brendler, V., Nitsche, H.: Speciation of uranium in seepage waters of a mine tailing pile studied by time-resolved laser-induced fluorescence spectroscopy (TRLFS). Radiochim. Acta **74**, 87 (1996)
/2/ Meyrowitz, R., Ross, D.R., Weeks, A.D.: Synthesis of liebigite. U.S. Geol. Survey Prof. Paper **475-B**, B 162 (1963)
/3/ Mereiter, K.: The crystal structure of liebigite, $Ca_2UO_2(CO_3)_3$~$11H_2O$. TMPM Tschermaks Min. Petr. Mitt. **30**, 277 (1982)

POLARIZED XAFS INVESTIGATIONS ON THE U L_{III}-EDGE OF BARIUM URANYL PHOSPHATE HYDRATE

C. Hennig, G. Zahn[1], M. A. Denecke, A. Roßberg, T. Reich, G. Bernhard, H. Nitsche
Forschungszentrum Rossendorf e.V., Institute of Radiochemistry
[1] TU Dresden, Institute of Crystallography and Solid State Physics

X-ray absorption spectroscopy (XANES and EXAFS) was used to investigate orientation-dependent polarization effects on the uranyl unit in crystalline barium uranyl phosphate hydrate.

Results and discussion

EXAFS and XANES on oriented samples such as single crystals is dependent on the polarization vector g. This dependence can be used as a unique indicator for the linear uranyl ion orientation /1/. For example, the orientation and specific binding sites of sorbed uranyl ions onto mineral surfaces of known orientation can be determined.

We investigated the U L_{III}-edge XANES and EXAFS of a single-crystal barium uranyl phosphate hydrate ($Ba[UO_2PO_4]_2 \cdot 8H_2O$) which contains layers of $[UO_2]^{2+}$ coordinated with $[PO_4]^{3-}$ tetrahedra. These layers are bridged by Ba^{2+}, H^+ and H_3O^+ cations, giving an overall near-tetragonal symmetry. The orientation of the crystal was determined by x-ray diffraction. A sample was obtained by cleaving a larger crystal along {001} and {100}.

Based on a reference compound with similar lattice constants, we assume that the crystal linear uranyl units are aligned parallel to [001]. Uranium L_{III}-edge XANES spectra are shown in Fig. 1. The measurements were performed with the polarization vector g oriented 90°, 45°, and 30° angles to [001] in the (010) zone. From a 90° angle between the polarization vector and the

axial U-O bonds, the first and the third absorption maxima dominate; at smaller angles the relative intensity of the second absorption maximum increases.

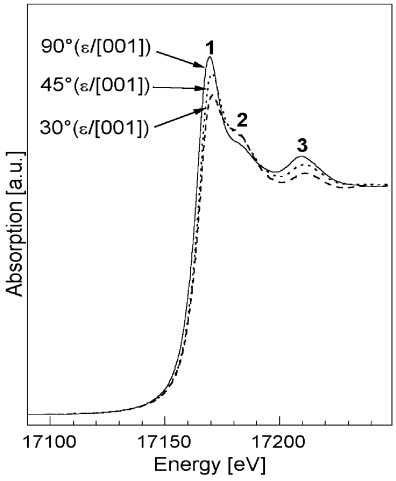

Fig. 1: U L_{III}-edge XANES. The polarization vector g is oriented at 90°, 45°, and 30° angles to [001]. Spectra have been normalized to equal intensity at 17250 eV.

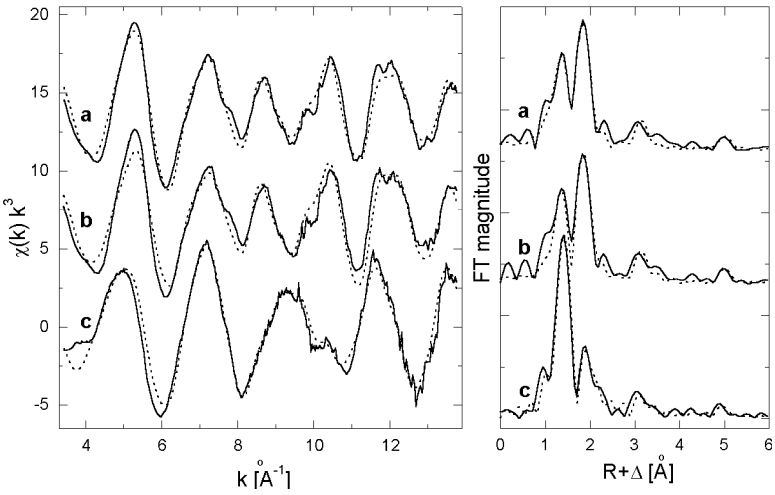

Fig. 2: U L_{III}-edge EXAFS. The polarization vector g is oriented parallel to [100] (**a**) and [110] (**b**) and with a 30° angle to [001] in the (010) zone (**c**). At left **P**(k)k^3, at right the corresponding Fourier transforms. Continuous lines are experimental spectra, dotted lines are theoretical fit curves.

Two different explanations for the second absorption maximum, the resonance at about 15 eV above the L_{III}-edge white-line maximum, have been discussed in the literature. One explanation is based on pressure dependent measurements of UO_3 and attributed this feature to shake-up processes /2/. Another interpretation identified this feature as a multiple-scattering resonance associated with the axial U-O bonds in various uranium compounds /1,3/. This interpretation stemmed from polarization dependent measurements and ab initio multiple-scattering calculations using the FEFF code /4/. Our experiments show that the relative intensity of this resonance increases if the polarization vector is aligned nearly along the axial U-O bonds. This observation confirms the multiple-scattering assignment of this feature and is supported by our own theoretical FEFF calculations (not shown here).
The U L_{III}-edge EXAFS shows a significant polarization dependence as demonstrated in Fig. 2. The amplitudes of the Fourier transformed shells are strongly affected by the orientation of the polarization vector relative to [001].
The largest dependence is evident in the Fourier transforms at distances corresponding to uranyl axial oxygen atoms and equatorial oxygen atoms. From fits to the spectrum recorded when the polarization vector g is oriented 90° to [001] in the direction [100], the effective bond distance for the axial and equatorial U-O calculated using scattering parameters from FEFF6 are 1.75 Å and 2.29 Å, respectively. The U-P bond distance is 3.59 Å, and the U-U distance is 5.2 Å. The linear polarization strongly influences the effective coordination numbers, N_i. Note that the spectra **a** and **b** are essentially the same. Changing the orientation of g from [100] to [110] does not significantly influence the amplitudes of the second coordination shells. This effect may be due to the tetrahedral distortion of the U-O bonds with regard both to [100] and [110] direction.

Acknowledgments
EXAFS and XANES measurements were performed at beamline RÖMO II at DORIS, Hamburg.

References

/1/ Hudson, E.A., Allen, P.G., Terminello, L.J., Denecke, M.A., Reich, T.: Polarized x-ray-absorption spectroscopy of the uranyl ion: Comparison of experiment and theory. Phys. Rev. B **54**, 156 (1996)
/2/ Bertram, S., Kaindl, G., Jové, J., Pagès, M., Gal, J.: Electronic Structure of Actinide Compounds from L_{III} -Edge X-Ray Absorption. Phys. Rev. Lett. **63**, 2680 (1989)
/3/ Hudson, E.A., Rehr, J.J., Buchner, J.J.: Multiple-scattering calculations of the uranium L_{III} edge x-ray-absorption near edge structure. Phys. Rev. B **52**, 13815 (1995)
/4/ Zabinsky, S.I., Rehr, J.J., Ankudinov, A., Albers, R.C., Eller, M.J.: Multiple-scattering calculations of x-ray-absorption spectra. Phys. Rev. B **52** 2995 (1995)

INVESTIGATION OF AQUO AND CHLORO COMPLEXES OF UO_2^{2+}, NpO_2^{+}, Np^{4+}, AND Pu^{3+} BY X-RAY ABSORPTION FINE STRUCTURE SPECTROSCOPY*

P.G. Allen [1], J.J. Bucher [1], D.K. Shuh [1], N.M. Edelstein [1], T. Reich
Forschungszentrum Rossendorf e.V., Institute of Radiochemistry
[1] Chemical Sciences Division, Lawrence Berkeley National Laboratory, Berkeley, USA

U, Np, and Pu $L_{II,III}$-edge X-ray absorption fine structure (XAFS) spectra were collected for the UO_2^{2+}, NpO_2^{+}, Np^{4+}, and Pu^{3+} ions as a function of chloride concentration in aqueous solution. At low chloride concentration, the hydration numbers and corresponding bond lengths for the different ions are as follows: UO_2^{2+}, N = 5.3, R = 2.41 Å; NpO_2^{+}, N = 5.0, R = 2.50 Å; Np^{4+}, N = 11.2, R = 2.40 Å; Pu^{3+}, N = 10.2, R = 2.51 Å. As the Cl^- concentration increases, inner-sphere Cl^- complexation occurs, resulting in a decrease in the hydration numbers and an expansion of the actinide-oxygen (water) bond lengths (for NpO_2^{+} see Fig. 1).

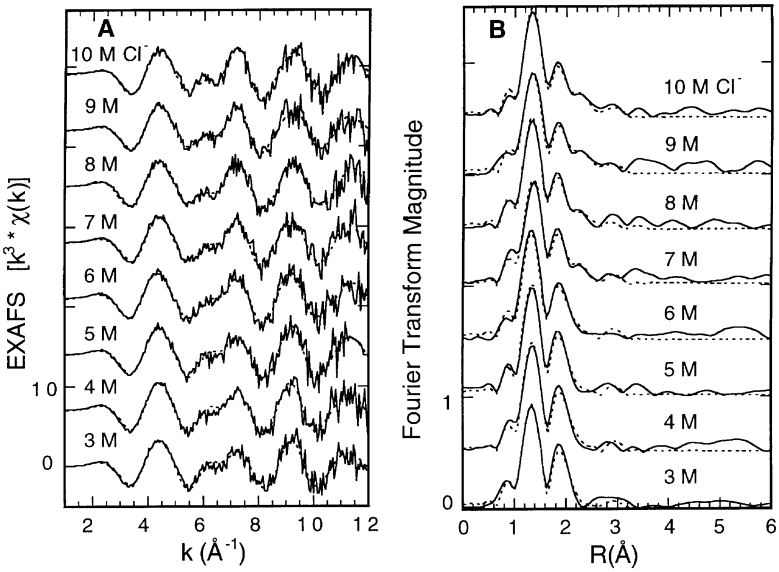

Fig. 1: Raw Np L_{III}-edge k^3-weighted EXAFS data (A) and corresponding Fourier transforms (B) taken over k=1–12 Å^{-1} for NpO_2^{+} as a function of [Cl^-]: experimental data (—), theoretical fit (▒▒▒).

The Pu^{3+} ion shows only a decrease in hydration number (40%) and no inner-sphere Cl^- complexation for [Cl^-] < 14 M. For concentrations up to 10-14 M Cl^-, the average Cl^- coordination numbers and bond lengths are as follows: UO_2^{2+}, N = 2.6, R = 2.73 Å; NpO_2^{+}, N = 1.0, R = 2.84 Å; Np^{4+}, N = 2.0, R = 2.61 Å. Structural changes are observed in the near-edge spectral region as shown by significant changes in the white line intensities upon Cl^- com-plexation. For ions with similar structures, i.e. Pu^{3+} and Np^{4+} or the actinyl ions NpO_2^{+} and UO_2^{2+}, positive energy shifts are observed with increasing oxidation state. The ability to use XAFS speciation results to calculate equilibrium constants and the relationship of these results to previous studies are discussed.

* abstract; article published in: Inorg. Chem. **36**, 4676 (1997)

SUBSHELL PHOTOIONIZATION CROSS SECTION CALCULATIONS FOR URANIUM 4f AND 5f ELECTRONS

V.G. Yarzhemsky [1], T. Reich, M.B. Trzhaskovskaya [2], V.I. Nefedov [1]
Forschungszentrum Rossendorf e.V., Institute of Radiochemistry
[1] Kurnakov-Institute of General and Inorganic Chemistry, Russian Academy of Sciences, Moscow, Russia
[2] St. Petersburg Institute of Nuclear Physics, Russian Academy of Sciences, Gatchina, Russia

The subshell photoionization cross sections of uranium 4f and 5f photoelectrons have been calculated with relativistic self-consistent Dirac-Slater potentials. At low photon energies, strong deviations of the branching ratio of the 4f photoionization cross sections from the statistical value occur due to relativistic effects.

Accurate experimental or theoretical values for photoionization cross sections are essential for the quantitative surface analysis by x-ray photoelectron spectroscopy (XPS) /1/. Photoionization cross section values are needed to calculate the atomic ratios from the measured relative photoelectron intensities of the elements of interest. For quantitative XPS analysis of uranium samples, e.g., complexes of uranium with humic acids or on mineral surfaces, the intense U $4f_{7/2}$ photoelectron line is measured /2/. In addition, U 4f and 5f photoelectron lines contain important information on the electronic structure of uranium compounds /3/. The surface sensitivity of

XPS measurements can be tuned by changing the energy of the exciting x-rays using synchrotron radiation. Therefore, the knowledge of the photoionization cross sections as a function of photon energy is also important.

We calculated the photoionization cross sections for the uranium $4f_{5/2}$, $4f_{7/2}$, and $5f_{5/2}$ subshells in the energy range from near threshold to 1.5 keV. The relativistic calculations were based on the relativistic self-consistent Dirac-Slater potential of the neutral atom with the configuration $[Rn]5f_{5/2}^{3}6d_{3/2}^{1}7s_{1/2}^{2}$ and included all multipoles of the radiation field. To simulate the influence of the chemical surrounding of uranium on the photoionization cross section, a second calculation was performed for an excited neutral state of the uranium where one $5f_{5/2}$ electron was promoted to the $7p_{1/2}$ shell. In both calculations we used the same experimental values for the electron binding energies. The coefficient *C* in the exchange term of the Dirac-Slater potential was equal to 0.667. The calculations were performed using the program RIANE /4/. Details of the calculation method can be found in Ref. 4 and references therein.

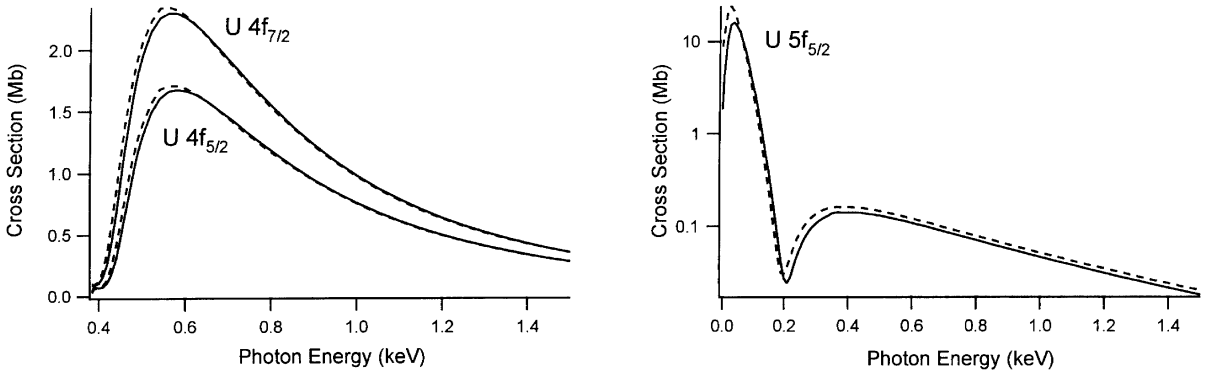

Fig. 1: Atomic subshell photoionization cross sections for uranium 4f (left) and 5f (right) electrons. Solid line, ground state; dashed line, excited state of uranium (see text). The cross sections are given for completely filled shells.

Fig. 1 shows the calculated photoionization cross sections for the uranium 4f and 5f subshells. Note that the subshell photoionization cross sections are given for completely filled *j*-subshells. For the U $5f_{5/2}$ photoionization cross section, a deep minimum near 200 eV is observed which may be due to an interference between the *j*+1, *j*-1, and *j* channels. The calculations for the exited state show an increase in the photoionization cross section of the U $5f_{5/2}$ shell (completely filled) of about 10% compared to the ground state. For the 4f subshell photoionization cross sections, no significant difference between ground and excited states are observed (see Fig. 1).

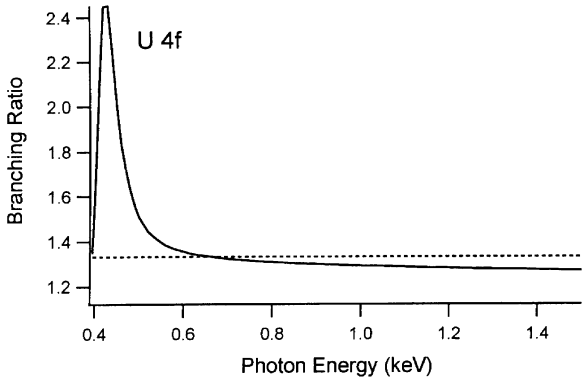

Fig. 2: Branching ratio $F_{7/2}/F_{5/2}$ for uranium 4f shell. The horizontal dashed line indicates the statistical value.

Fig. 2 shows the branching ratio of the 4f shells. At high photon energies, the calculated branching ration is close to the statistical value of $(l + 1)/(l) = 1.33$. As can be seen from Fig. 2, relativistic effects become important at low photon energies and lead to a strong devia-tion of the branching ratio from the statistical value. However, at low photon energies, the calculation of photoionization cross sections and branching ratios depends strongly on the approximation for taking into account the electron hole. To obtain more accurate values for the branching ratios, the relativistic calculations could be performed, for example, in the random phase approximation with exchange.

Acknowledgment

One of us, V.G.Y., thanks for financial support by the Sächsische Staatskanzlei.

References

/1/ Nefedov, V.I.: *X-ray Photoelectron Spectroscopy of Solid Surfaces.* VSP, Utrecht, 1988

/2/ Teterin, Yu.A., Nefedov, V.I., Ivanov, K.E., Baev, A.S., Geipel, G., Reich, T., Nitsche, H.: X-ray photoelectron spectroscopy investigation of the interaction of $UO_2(ClO_4)_2$ with calcite and diabase minerals. Zh. Neorg. Khim. **41**, 1884 (1996) (in Russian)

Nefedov, V.I., Teterin, Yu.A., Lebedev, A.M., Teterin, A.Yu., Dementjev, A.P., Bubner, M., Reich, T., Pompe, S., Heise, K.H., Nitsche, H.: ESCA investigation of the interaction of uranyl and calcium ions with humic acids. Inorg. Chim. Acta, in press

/3/ Teterin, Yu.A., Gagarin, S.G.: Inner valence molecular orbitals and the structure of X-ray photoelectron spectra. Russ. Chem. Rev. **65**, 825 (1996)

/4/ Band, I.M., Kharitonov, Yu.I., Trzhaskovskaya, M.B.: Photoionization cross sections and photoelectron angular distributions for x-ray line energies in the range 0.132-4.509 keV. Atom. Data Nucl. Data Tab. **23**, 443 (1979)

EXAFS INVESTIGATIONS OF THE COMPLEXATION BEHAVIOR OF UO_2^{2+} WITH MODEL COMPOUNDS OF PHENOLIC WOOD DEGRADATION PRODUCTS

A. Roßberg, T. Reich, C. Hennig, M.A. Denecke, L. Baraniak, H. Nitsche
Forschungszentrum Rossendorf e.V., Institute of Radiochemistry

EXAFS were studied on the U L_{III}-edge of uranyl complexes with 3,4-dihydroxybenzoic acid (protocatechuic acid - PCS) and 2-hydroxyphenol (catechol - BCT) in water. From speciation calculations (concentration of complex as a function of pH) it was expected, that both ligands form 1:1 and 1:3 complexes at pH 5 and pH 10, respectively and that PCS forms a 1:2 complex at pH 6.8.
Lignin formation by wood degradation and its interaction with UO_2^{2+} are currently being studied at the institute. In preparation for UO_2^{2+} lignin EXAFS, we used PCS and BCT as model substances.

Experimental

Baraniak et al. /1/ determined the complex formation constants of uranium(VI) with PCS. The speciation of the complexes in absence of CO_2 was calculated with the computer-program RAMESES at 0.1M ionic strength ($NaClO_4$) and at 25 °C. The metal concentration was 1 mM $UO_2(ClO_4)_2$ and the ligand concentrations for PCS and BCT were 50 mM. UO_2^{2+} hydrolysis was considered in the calculations. The complexation equilibria for PCS (eq. 1-3) /1/ and for BCT (eq. 4-6) /2/ are:

UO_2^{2+}	+	PCS^{3-}	=	$UO_2(PCS)^-$			log$ = 14.8	(1)
UO_2^{2+}	+	$2PCS^{3-}$	=	$UO_2(PCS)_2^{4-}$			log$ = 25.9	(2)
UO_2^{2+}	+	$3PCS^{3-}$	=	$UO_2(PCS)_3^{7-}$			log$ = 32.7	(3)
$UO_2$2+	+	H_2BCT	=	$UO_2(BCT)$	+	$2H^+$	log$ = -7.14	(4)
$UO_2(BCT)$	+	H_2BCT	=	$UO_2(H(BCT)_2)^-$	+	H^+	log$ = -4.38	(5)
$UO_2(H(BCT)_2)^-$	+	H_2BCT	=	$UO_2(H_2(BCT)_3)^{2-}$	+	H^+	log$ = -5.6	(6)

The results of the speciation calculations are shown in Fig. 1. For PCS and BCT the $UO_2(PCS)^-$ complex (1) and the $UO_2(BCT)$ complex (4) form at pH 5, respectively. The $UO_2(PCS)_2^{4-}$ complex (2) forms at pH 6.8. At pH 10, the $UO_2(PCS)_3^{7-}$ complex (3) , and for BCT, the $UO_2(H_2(BCT)_3)^{2-}$ complex (6) are prevalent. The U L_{III}- edge spectra of the five complexes were measured at the HASYLAB beam line RÖMO II and at the SSRL beam line 4-1. The fluorescence signal was measured with a 4-pixel-germanium detector, because of the low UO_2^{2+} concentration.

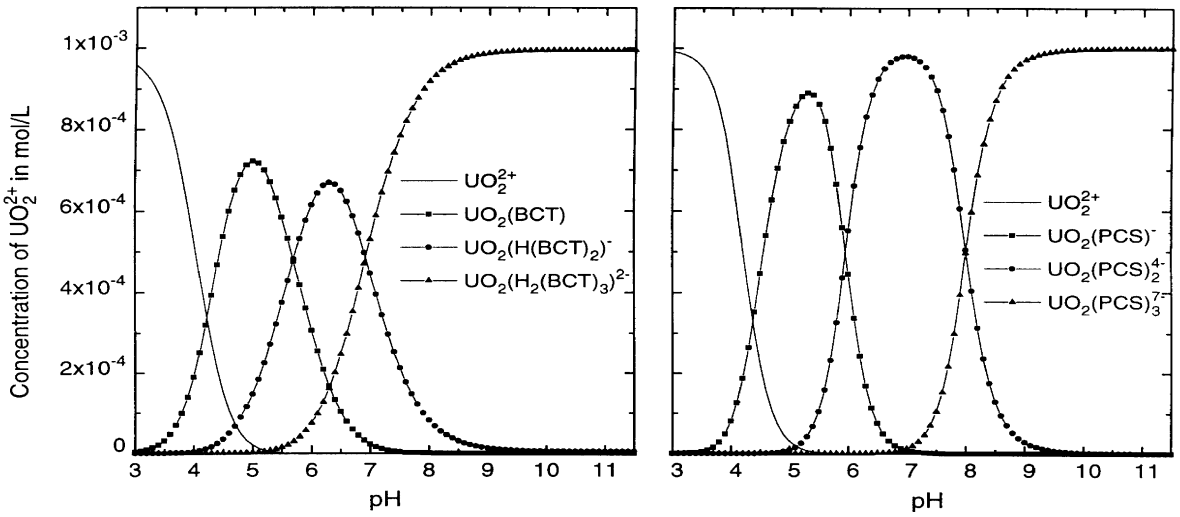

Fig. 1: Calculated speciation of UO_2^{2+} complexes with BCT (left) and PCS (right); complex formation constants for PCS and BCT are from /1/ and /2/, respectively.

Results and Discussion

It is supposed that PCS coordinates to the UO_2^{2+}- ion as a 5- membered chelate ring and that the carboxylic group is not involved in the complexation /3/. For BCT at pH 10, a 1:3 complex is expected. Our goal was to examine if the 1:3 complex with PCS also exists and to determine the role of the carboxylic group in the complexation behavior of PCS.

To evaluate the EXAFS spectra, theoretical phases and amplitudes were calculated using the single scattering interface from OPT (FEFF7).

System	pH	MS	U-O axial			U-O equatorial			[a]E*
			R	F^2*10^{-3}	N*	R	F^2*10^{-3}	N	
PCS,UO_2^{2+}	5	H	1.80	1.1	2	2.42	10	5.7(4)	-13.8
PCS,UO_2^{2+}	5	S	1.79	2.0	2	2.44	8	4.9(4)	-13.0
BCT,UO_2^{2+}	5	H	1.78	2.4	2	2.39	8	5.6(2)	-15.7
PCS,UO_2^{2+}	6.8	S	1.81	2.4	2	2.37	9	5.5(4)	-13.0
PCS,UO_2^{2+}	10	S	1.81	1.5	2	2.38	6	5.4(3)	-13.0
BCT,UO_2^{2+}	10	H	1.81	1.5	2	2.37	6	5.7(3)	-15.7

*) - constant during the fit procedure

Tab. 1: Fit results for the first and second coordination shells. ( ) E - energy shift, N - coordination number, R - radial distance in Å, F^2 - Debye Waller factor in $Å^2$, MS - measuring station: S= SSRL, H= HASYLAB)

Tab. 1 shows the results of the EXAFS fits. The average of the radial distance is 1.80 ± 0.02 Å between uranium and axial oxygen. This distance increased with increasing pH. The number of the oxygen atoms in the equatorial plane averages 5.5 ± 20%. At pH 10, the spectra of the PCS and BCT comple-xes are identical (Fig. 2, spectra a and b). That means that at pH 10 no differences arise from the additional carboxylic group. These complexes appear to coordinate UO_2^{2+} identically. The short U-O_{eq} distance of 2.37 Å is characteristic for complexation of UO_2^{2+} with two neighboring phenolic OH groups. The 1:2 PCS complex at pH 6.8 shows similar bonding. In contrast, differences in the radial distance of the equatorial oxygen atoms appear between PCS and BCT complexes (Tab. 1).

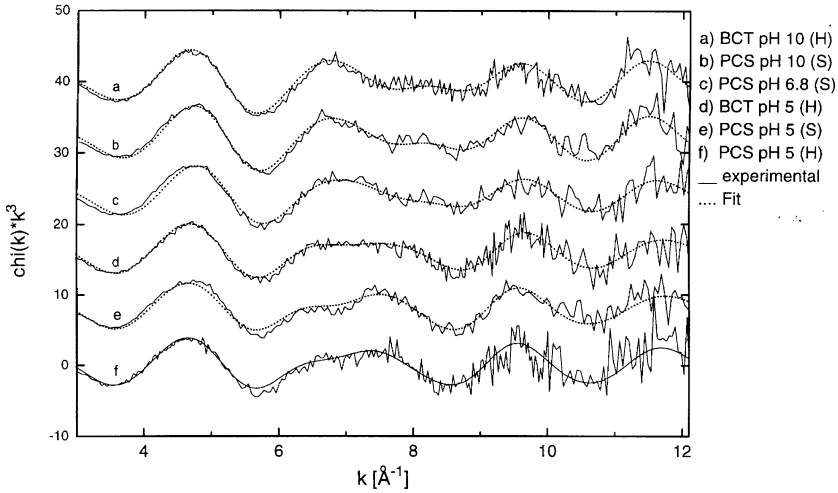

Fig. 2: Raw k^3-weighted EXAFS spectra from PCS and BCT complexes, measuring station: S= SSRL, H= HASYLAB

Also, the EXAFS spectra d, e, and f in Fig. 2 show differences. The EXAFS spectra e and f in Fig. 2 (PCS complexes, pH 5) are comparable with the EXAFS spectrum of uranyl triacetate /4/. In this compound Three carboxylate goups, with a radial U-O_{eq} distance of 2.46 Å, coordinate the UO_2^{2+} ion in a bidentate fashion.

The average radial U-O_{eq} distance of 2.43 Å from the PCS complexes at pH 5 is significantly longer than the radial U-O_{eq} distance of 2.39 Å from the BCT complex at pH 5 (see Tab. 1). At pH 5, the PCS complexes the uranium through the carboxylic group.

Conclusions

The spectrum of the 1:3 complex from BCT - $UO_2(H_2(BCT)_3)^{2-}$ - is comparable to the EXAFS spectrum of the postulated PCS complex at pH 10, (Fig. 2, spectra a and b). This shows that the coordination structure of the UO_2^{2+} - PCS and PCT complexes at pH 10 is identical. At pH # 5, the EXAFS spectra of the PCS and the BCT complex are different. The average radial U-O_{eq} distance from the PCS complex is greater then the radial U-O_{eq} distance from the BCT complex (Tab. 1). We are currently using IR and UV/Vis spectroscopy to evaluate the bonding states.

References

/1/ Baraniak, L., Schmidt, M., Bernhard, G., Nitsche, H.: Complex formation of hexavalent uranium with lignin degradation products. In: Report FZR-180, Institute of Radiochemistry, Annual Report 1996, p. 28 (1997)

/2/ Martell, A.E., Smith, R.M., Motekaitis, R.J.: *Critically Selected Stability Constants Of Metall Complexes. Database Version 2.0.* Texas A & M University (1995)
/3/ Jayadevadappa, E.S., Renukarani, S., Hukkeri, P.B.: Studies of chelate formation of 4-Carboxycatechol with some metal ions. J. Karnatak Univ., Science **14**, 64-71 (1969)
/4/ Denecke, M.A., Reich, T., Pompe, S., Bubner, M., Heise, K.H., Nitsche, H., Allen, P.G., Bucher, J.J., Edelstein, N.M., Shuh, D.K.: Differentiating Between Monodentate and Bidentate Carboxylate Ligands Coordinated to Uranyl Ions Using EXAFS. J. Phys. IV France **7**, C2-637 (1997)

Behavior of Colloids and Aerosols

PARTICLE GROWTH PHENOMENA IN FILTERED BOG WATER

H. Zänker, W. Richter, G. Hüttig, H. Nitsche
Forschungszentrum Rossendorf e.V., Institute of Radiochemistry

Humic-rich water from a mountain bog was filtered through small pore size Nuclepore filters and observed by PCS during an aging period of 11 days. Significant particle growth could be detected. It is due to physico-chemical coagulation or to biological growth.

Water from the Kranichsee mountain bog, which is situated in the uranium mining area near Johanngeorgenstadt (Saxony), was investigated by colloid measuring techniques. The total organic carbon concentration of this water was 65 mg/L, the pH value was 3.7, and the concentration of inorganic species was about 10 mg/L. Humic acid and fulvic acid were the prevailing organic constituents. The inorganics were primarily Na, K, Mg, Al, Si, Ca, Fe, SO_4^{2-}, HCO_3^-, and Cl^-. The original bog water was filtered through a 100 nm pore size Nuclepore filter. Only a minor fraction of the organic matter (< 30 %) was removed from the sample by this filtration; most of the humic material passed through the filter. However, the scattered light intensity emitted by the solution when illuminated by a laser beam decreased significantly due to this filtration step (by a factor of five). This is attributable to the fact that the light intensity is governed by the relatively few larger (i.e. filtrable) particles whereas the many small particles (humic acid molecules) provide only a minor contribution to light scattering. The filtrate was stored at 25 °C and observed during an aging period of 11 days. It remained unchanged to the human eye for several days. Then thread-like or web-like small white objects appeared that preferentially grew in the lower part of the cuvettes (far below the laser beam).

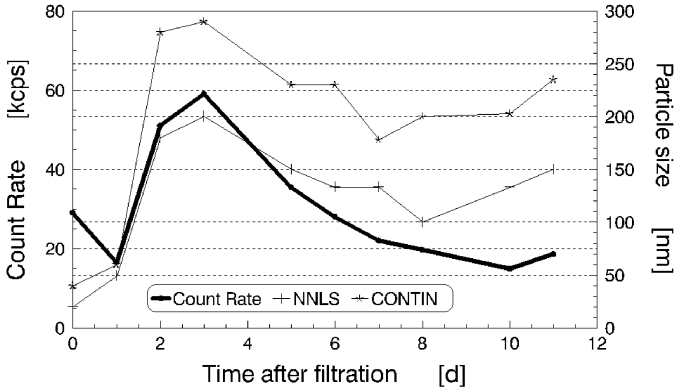

Fig. 1: Time dependence of the photomultiplier count rate and the particle size (thin lines) evaluated by two different methods of deconvolution after filtration through a 100 nm Nuclepore filter.

Fig. 1 shows the course of the scattered light intensity and the particle size results (CONTIN and NNLS deconvolutions, cf. /1,2/) as determined by a fixed-angle BI-90 type photon correlation spectroscope (Brookhaven Instruments Corp. Holtsville, USA) during this aging period. The figure shows that the scattered light intensity (photomultiplier count rate) does not remain constant but increases. This is accompanied by a pronounced increase of the calculated particle size. We attribute this behavior to the growth of particles after the filtration. The further course of the count rate and the particle size is remarkable. After the short and relatively steep increase these values gradually decrease again, i. e., they show a maximum.

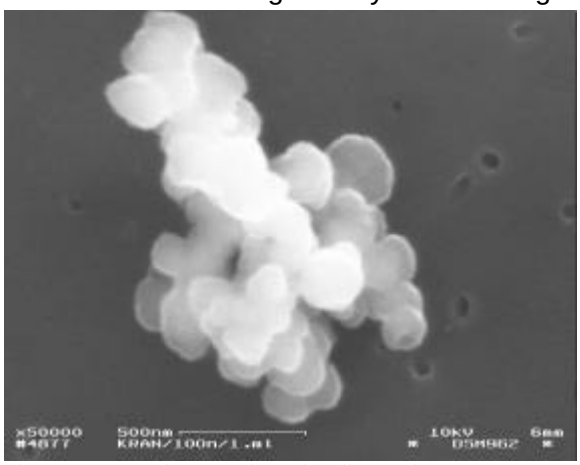

Fig. 2: SEM micrograph of the filter cake on a 100 nm Nuclepore filter. Prefiltration through a 100 nm filter. Aging time after prefiltration: 11 days. Length of the bar: 500 nm

After 11 days of aging the filtrate was again filtered through a 100 nm Nuclepore filter. The filter was coated with carbon and investigated by scanning electron microscopy (Zeiss DSM 962, Oberkochen, Germany). Fig. 2 gives an example of a SEM micrograph.

A relatively compact agglomerate is to be seen that consists of 'building units' of about 200 nm. A very good agreement between the size of the 'building units' and the PCS results exists (Fig. 1). Obviously, the 'building units' move freely in the water sample and the agglomerates are formed on the filter membrane during filtration.

Both physico-chemical coagulation and biological growth may cause particle growth in the humic acid filtrate. One should take into consider-

ation that the solution was, as in the nature in a mountain bog, exposed to air during aging. The occurrence of a maximum in the count rate and PCS particle size curves suggests that opposing (competing) processes played a role. Thus, an explanation of Fig. 1 could be the competition between particle growth and sedimentation of particles that have reached a certain limiting particle size. The shape of the particles in our SEM micrograph does not indicate a biological nature of the newly-grown particles (no strictly regular or 'anatomical' structure). This, however, cannot be decided from the SEM scans alone. The particle growth phenomena need further investigation. The presence of relatively large submicron particles in a humic rich water can take influence on the transport of contaminants like heavy metals in the nature in case these particles act as carriers of the contaminants. The transport behavior of the larger particles differs from that of the unagglomerated humic or fulvic acid molecules.

References

/1/ Schurtenberger, P., Newman, M.E.: Characterization of Biological and Environmental Particles Using Static and Dynamic Light Scattering. In: *Environmental Particles*. IUPAC Series on Environmental Analytical and Physical Chemistry. Buffle, J., van Leeuwen, H.P. (eds.), Vol. 2, Lewis Publishers 1993, p.37-116

/2/ Stock, R.S., Ray, W.H.: J. Polym. Sci. Polym. Phys. Ed. **23**, 1393 (1985)

LIGNIN COLLOIDS IN AQUEOUS SOLUTION

W. Richter, H. Zänker, H. Nitsche
Forschungszentrum Rossendorf e.V., Institute of Radiochemistry

Colloid particles of lignin in aqueous solution were measured as a function of pH by filtration and photon correlation spectroscopy. The particle size and the number of particles increased with decreasing pH.

The shafts of uranium mines in Saxony and Thuringia, Germany, were been forced with wood which degrades upon flooding of the decommissioned mines with ground and surface waters. Organic wood degradation probes like lignin are being produced by this process can influence the chemical properties and thus the migration behavior of radionuclides and heavy metals. Lignin is one of the major degradation products. Because lignin solutions can form colloids, knowledge on their size and concentration is important.

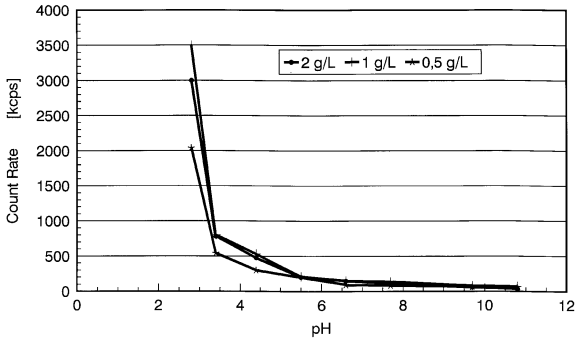

Fig. 1: Dependence of scattered light intensities on the pH value in organosolv lignin solutions

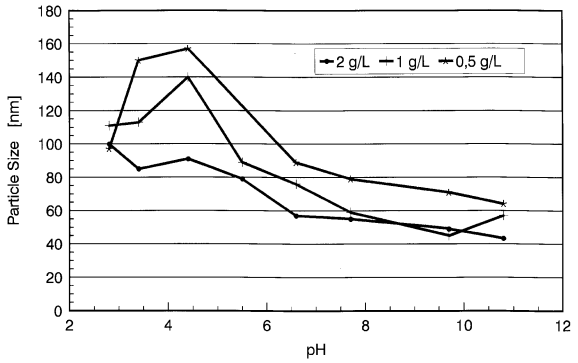

Fig. 2: Particle size as a function of pH of the lignin solution

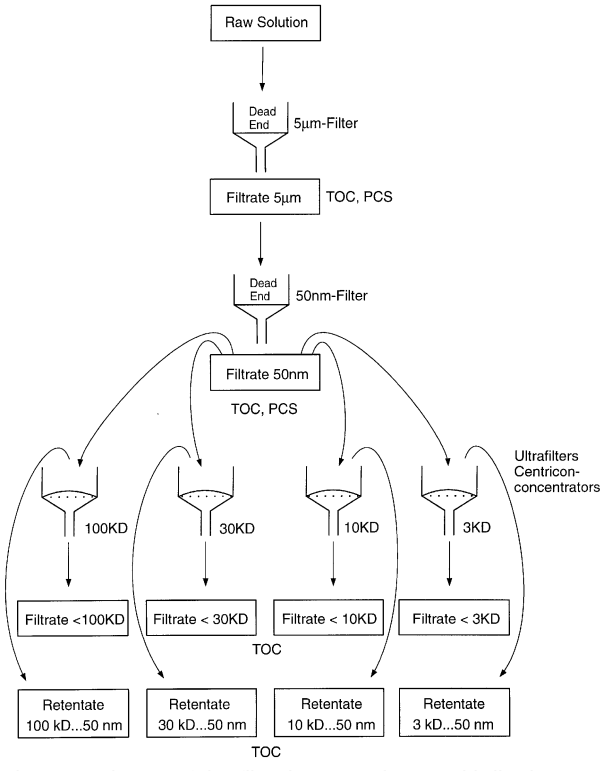

Fig. 3: Scheme of the filtration experiment with lignin at pH 7.3

Organosolv lignin was used to study the size and the size distribution of colloidal particles in aqueous solution as a function at the pH. The lignin was dissolved in Milli-Q-water (2 g/L) and the pH was adjusted to 10.8 with 0.1 M NaOH. The pH was changed stepwise by the dropwise addition of 1 M HCl. The colloidal particles that formed were measured with a photon correlation spectroscope (BI-90 from Brookhaven Instruments Corp). Measurements were carried out immediately after the pH was adjusted and staged constant. The following measuring parameters were used: 400 mW laser power, 514.5 nm scattering wavelength, 90° scattering angel, and 25°C. The results of the PCS-measurements are given in Fig. 1 and Fig. 2.
Both count rate and particle size increase with decreasing pH. The colloidal-suspended particles in the lignin solution grow from 40 nm at pH 10 to 150 nm at pH 3. This is in good accordance with the dissociation constants (pK_{diss}) of the carboxylic and phenolic hydroxyl groups. These are 4.4 and 9.3, respectively /1/. Macromolecules are dissociated in alkaline medium and the repulsive forces due to the negative loaded carriers prevent agglomeration. At pH < 4.4 all functional groups are protonated. Attractive forces prevail over the repulsive forces under these conditions and the formation of hydrogen bonds makes the small particles agglomerate to larger ones.

The measurement of the particle size distribution is intricate for a given particle system because of the complicated relation between the scattered light intensity and the particle size (r^6 dependence of the scattered light intensity on the particle radius) /2/. Due to this relation, large particles mask smaller ones. After removing large particles by filtration, one is, however, able to measure smaller particles. To determine the size distribution of the colloidal particles, we filtered the pH-7.3-solution according to the scheme shown in Fig. 3.
The PCS measurements of the raw solution and the 5 µm filtrates provided a particle size between 50 and 65 nm. After filtration through a 50 nm filter, the particles were measured as only a few nanometers in size. In this size region PCS measurements are not very reliable because the count rate is low and the count statistics are poor.

In order to better characterize the lignin particles in the small size range, the fractions of organic material in the filtrates (Fig. 3) was determined by total organic carbon (TOC) analysis. Tab. 1 lists the colloid size distribution in the lignin solution after size fractionation by filtration and ultrafiltration.
These results show that about 70% of the lignin is in the size range between 30 kD (approximately 2 nm) and 50 nm. This corresponds well with the results of size exclusion chromatography (SEC) measured on lignin and humic acids /3/. By static light scattering (multi-angle light scattering), weight-average molecular weights, M_W, of 2,000 to 146,000 Daltons were found for lignin samples /4/. This suggests that the particles of 65 nm found with the PCS measurements are agglomerates and the smaller particles of the nm range are the real primary particles in lignin solutions.

Particle Size	Content
> 5 µm	4 %
50 nm - 5 µm	7 %
100 kD - 50 nm	46 %
30 kD -100 kD	23 %
10 kD - 30 kD	2 %
3 kD - 10 kD	5 %
< 3 kD	13 %

Tab. 1: Particle size distribution in the lignin solution at pH 7.3 as determined by filtration and TOC analysis.

Acknowledgment
We thank N. Zier and R. Schiene, Institute of Plant and Wood Chemistry, Tharandt, TU Dresden, for promising us with the lignin.

References
/1/ Schmidt, M., Baraniak, L., Bernhard, G., Nitsche, H.: Interaction of U(VI) with Wood Degradation Products. A potentiometric Study. In: Report FZR-180, Institute of Radiochemistry, Annual Report 1996, (1997) p. 30
/2/ Schurtenberger, P., Newman, M.E.: Characterization of biological and environmental particles using static and dynamic light scattering. In: *Environmental Particles*. Lewis Publishers, 1993, p. 37
/3/ Schmidt, M., Baraniak, L., Bernhard, G., Nitsche, H.: Size Exclusion Chromatography (SEC) of Lignin and Humic Acids. In: Report FZR-123, Institute of Radiochemistry, Annual Report 1995, (1996) p. 71
/4/ Pla, F.: Determination of Molecular Weight, Size, and Size Distribution. In: S.Y. Lin, C.W. Dence (eds.): *Methods in Lignin Chemistry*. Springer Verlag Berlin, 1992

PHOTON CORRELATION SPECTROSCOPY AND SCANNING FORCE MICROSCOPY ON HUMIC ACID

H. Zänker, M. Mertig [1], M. Böttger, G. Hüttig, S. Pompe, W. Pompe [1], H. Nitsche
Forschungszentrum Rossendorf e.V., Institute of Radiochemistry
[1] Technische Universität Dresden, Institute of Material Science

Natural peat humic acid was studied by photon correlation spectroscopy (PCS) in aqueous solution and scanning force microscopy (SFM) after deposition on a mica substrate. Two of the various particle types found on the mica surface are representative of the aqueous solution (and not only of the deposition process on the mica). One of these representative particle types is obviously the humic acid macromolecule itself.

Natural peat humic acid (Aldrich Chemical Co.) was purified by three precipitation-dissolution steps according to the procedure described by Kim and Buckau /1/. It was studied in aqueous solution by photon correlation spectroscopy (PCS) /2/ and scanning force microscopy (SFM) after deposition (spin-coating) on freshly cleaved mica /3/. The concentration of the humic acid was varied between 20 and 1000 ppm, the pH value between 2.7 and 11.3 and the relative air humidity during spin coating between 10 and 90%. PCS indicated the presence of particles of about 130 nm in diameter (Fig. 1) which was independent of the pH and the humic acid concentration.

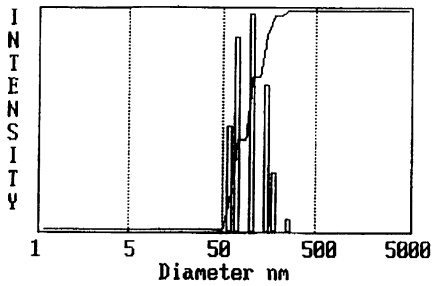

Fig. 1: Typical PCS particle size distribution of a humic acid solution. Prefiltration through a 1000 nm Nucle-pore filter. Concentration 200 ppm; pH 6.2. Particles were found in the size range from 50 to 300 nm with the light intensity weighted peak being at 130 nm. Similar particle size distributions were obtained for the other pH values and humic acid concentrations studied.

Four particle classes were found on the mica substrate by SFM:

Class (1) Relatively large 'submicron chunks' of several hundreds of nm in diameter and up to 50 nm in height (the equivalent spherical diameter lies between 100 and 150 nm),
Class (2) 'Elongated agglomerates' of several hundred nm in length and only few nm in height,
Class (3) 'Disk-like agglomerates' of about 50 nm in diameter and only few nm in height,
Class (4) 'Subunits' of only few nm in diameter and height (the equivalent spherical diameter is 5 to 10 nm).

Fig. 2

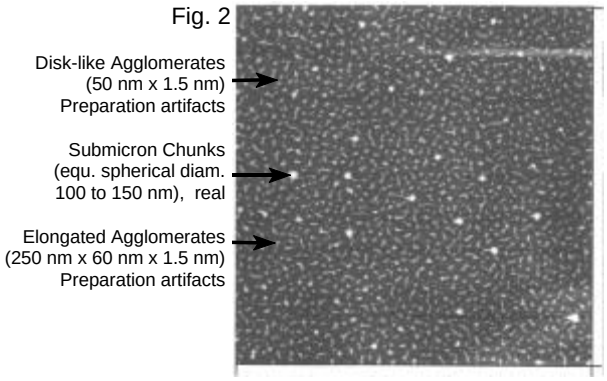

Fig. 3

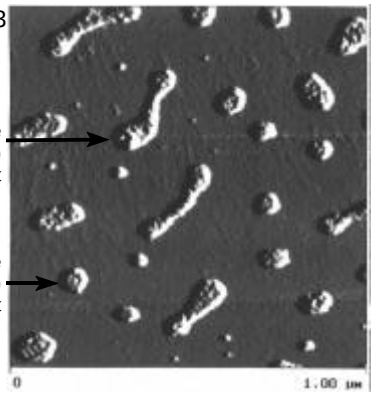

SFM images of humic acid deposited on mica by means of spin-coating. Prefiltration with 1000 nm Nuclepore filter. Concentration 200 ppm; relative air humidity during spin-coating # 40 %.
Fig. 2: 10 µm scan. pH 11.3; 'Submicron chunks', 'elongated agglomerates' and 'disk-like agglometates' can be discerned. The 'submicron chunks' are real, the agglomerates are preparation artifacts.
Fig. 3: 1 µm scan. pH 11.3; 'Elongated agglomerates' and 'disk-like agglomerates' with a characteristic substructure are visible. Height of the deposits: 1.5 to 2 nm. Periodicity of the substructure: 12 to 14 nm. The agglomerates are preparation artifacts, the substructure is real.

Fig. 4

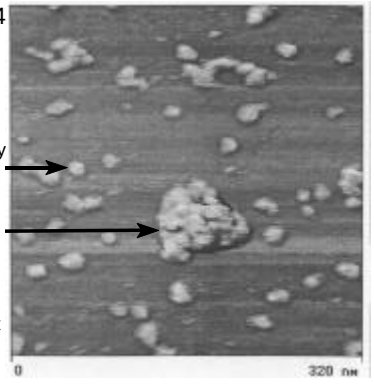

Fig. 4: 320 nm scan. pH 4.2; Individual 'subunits' (real) and a larger agglomerate (preparation artifact) with a characteristic substructure are visible. Height of the fully disintegrated 'subunits': 3.5 nm. Height of agglomerate in the center: 12 nm ('subunits' are obviously laying on top of each other in this type of 'disk-like agglomerates' which was only found at low pH values). Periodicity of the substructure: about 12 nm.

The first three particle classes can be discerned in the SFM micrograph in Fig. 2. Classes (2) and (3) can better be seen in Fig. 3 and Fig. 4 which are SFM scans of higher magnification. Fig. 3 and Fig. 4 also reveal that the particles of Classes (2) and (3) consist of a substructure: 'subunits' of a diameter of 10 to 15 nm are discernible (Class 4).
Dilution experiments (Fig. 5) confirmed the nature of the fourth particle class. Fully disintegrated 'subunits' are found at a humic acid concentration of 20 ppm, i. e., the 'subunits' forming the objects in Fig. 3 and Fig. 4 and the fine spots in Fig. 5 (c) are identical.

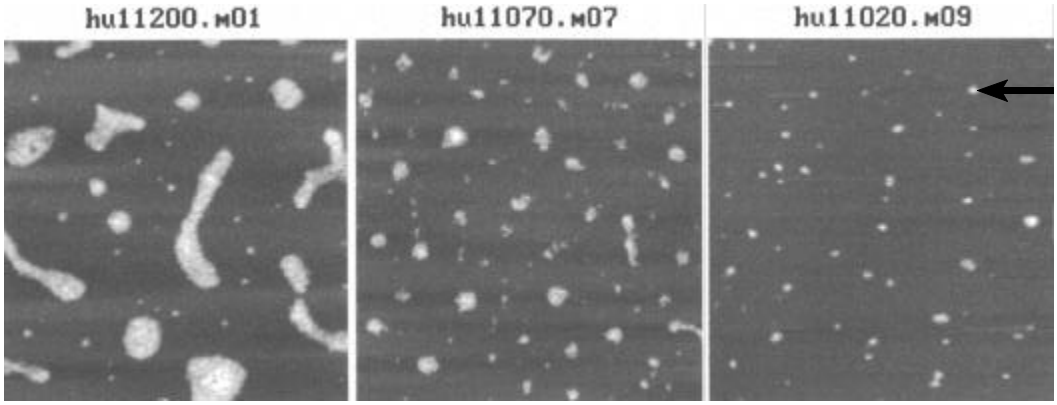

Fig. 5: Comparison of SFM images of humic acid at three humic acid concentrations. 1 µm scans. pH 11.3; relative air humidity during spin coating $\leq$ 40 %. Concentrations (a) 200 ppm, (b) 70 ppm, (c).20 ppm. Dilution of the solution results in the appearance of fully disintegrated 'subunits' on the mica surface. The 'subunits' are real.

Much effort was made to assess which of these particle classes were representative of states in the aqueous humic acid solution and which resulted only from processes during sample deposition on the mica. The comparison of the results gained by the two complementary experimental methods proved very helpful in this assessment. We found that two of the four particle classes detected by SFM exist also in the aqueous solution.
The first of these 'representative' classes is the class of the 'subunits' (Class 4) that occur as isolated spots on the mica surface if the spin-coated humic acid solution was diluted. They are able to form loose and easily changeable agglomerates on the substrate if the humic acid concentration is sufficiently high. To extrapolate the SFM results to the possible conformation of the humic acid in solution, the equivalent spherical diameter of these 'subunits' is calculated from their height and their diameter on the mica surface. It is about 5 to 10 nm, approximately the size range where humic acid molecule sizes are expected. We regard them as the molecules. As a comparison between Fig. 3 and Fig. 4 (note the different magnifications of the two images) demonstrates, not only dilution but also lowering the pH value at a constant concentration increases the tendency of the individual 'subunits' to appear in their fully disintegrated form on the mica surface.
The second particle class on the mica that is representative of the aqueous solution are the 'submicron chunks' (Class 1). These particles are rather rigid and behave entirely inert when concentration and pH value are changed. The fraction of the humic acid existing in the form of the 'submicron chunks' is only less than 10 mass % even though the particles of this class are responsible for most of the scattered light. The 'submicron chunks' are the particles detected by PCS (the 'subunits' are below the PCS particle size detection limit under the measuring conditions given).
The remaining two particle types in the SFM images, Classes (2) and (3), are not representative of the aqueous solution but are formed on the mica surface during spin-coating.

pH Value	Height of the 'Subunits' [nm]
2.7	3.5
4.2	3.5
6.2	2.5
11.3	1.5 to 2

Tab.1: Height of the 'subunits' in dependence on the pH value; error of SFM height measurement: < 5%.

Tab. 1 gives the heights of the 'subunits' on the mica surface as determined by SFM as a function of the pH of the spin-coated solution. From the flatness of these units (heights < 4 nm compared to the diameter of 10 to 15 nm), we conclude that the humic acid structures possess a high flexibility (deformability). This high flexibility is in accordance with the random coil model for organic macromolecules.
It is , however, striking that this flexibility decreases if the

pH value is lowered. In the more acidic region the individual 'subunits' are significantly higher than in the alkaline region. This 'response' of the SFM images to the pH value provides direct experimental evidence that the random coil hypothesis of polyelectrolyte molecules (see e. g. /4/) is correct for humic acid. In alkaline and neutral solutions the humic acid molecules are obviously 'expanded' (deprotonated form), whereas they are 'contracted' in the more acidic pH region (protonated form).
Not much is known about the strikingly inert 'submicron chunks' yet. They seem to be an inherent constituent of the investigated peat humic acid that can not even be removed by the relatively thorough purification according to the method by Kim and Buckau /1/.

References

/1/ Kim, J.I., Buckau, G.: *Preparation of a Reference of Humic Acids.* Report RCM 0288, Technische Universität München, Institut für Radiochemie, 1988
/2/ Schmitz, K.S.: *An Introduction to Dynamic Light Scattering by Macromolecules.* Academic Press, Boston 1990
/3/ Mertig, M., Thiele, U., Bradt, J. Leibiger, G., Pompe, W., Wendrock, W.: Scanning Force Microscopy and Geometrical Analysis of Two-Dimensional Collagen Network Formation. Surface and Interface Analysis **25**, 514-521 (1997)
/4/ Swift, R. S.: In: *Humic Substances II. In Search of Structure.* Hayes, M.H.B., MacCarthy, P., Malcolm, R., Swift, R.S. (Eds.), John Wiley & Sons, Chichester 1989, p. 449-465

PARTICLE EMISSION FROM UV-IRRADIATED SILICA SURFACES

D. Rettig, P. Merker, H. Nitsche
Forschungszentrum Rossendorf e. V., Institute of Radiochemistry

The release of small particles (diameter 8 to 200 nm) was observed from UV-irradiated quartz glass vessels passed by wet air. The effect is supposed to result from the photoexcitation of water or silicon hydroxide groups in the amorphous and micro porous hydrated silica layer at the quartz glass surface.

The resuspension and emission of small particles from surfaces into a surrounding gas plays an important role in natural phenomena and many engineering processes. Particle resuspension can interfere in semiconductor manufacturing and clean room technologies. In nature, for example, radioactivity deposited in soils may be intimately associated with the soil particles, but can be resuspended by eolian weathering. The resuspension generally occurs only under turbulent flow conditions for particles greater than a few micrometers.
Recently, however, Yablokov and Andronova /1/ observed the take-off of micron-sized aerosol particles from desert soil in Kalmykia under windless and sunny weather conditions. The authors assumed that after soil water evaporates during the daytime heating, the take-off of particles is a result of electrostatic repulsion forces.
To verify the reported resuspension effect under laboratory scale conditions, we attempted to use the quartz glass vessel technique developed for electrostatic particle deposition experiments /2/. However, any charged particles could not escape from the vessel because of the electrostatic self-charging of the quartz glass. Surprisingly, we noticed a strong particle emission from the vessel without any pre-deposited particles during irradiation with a mercury UV lamp emitting the 185 and 254 nm lines. In contrast to this, heating up to 220 °C and irradiation with wave lengths larger than 254 nm did not cause any emission of particles.

These experiments are carried out as follows:
Clean filtered air with defined water contents was flowed through an empty quartz glass vessel which was made from freshly blown glass just before the experiments. For several experiments, the vessel was rinsed with high purity water and then dried at 220 °C. During irradiation with a low-pressure mercury UV lamp (8 W), the particles escaping from the quartz vessel were counted in a condensation particle counter. The steady-state particle concentration in the air flowing from the vessel was measured as a function of air humidity and distance between the lamp and the vessel's surface (Fig. 1). The aerosol was characterized on-line by SMPS measurements and, after sampling, on micro porous polyester membrane filters by SEM (Fig. 2), EDX and XRF analysis. Only silica particles were found on the filters.
Fig. 1 shows that the humidity in the air promotes the particle generation. The water molecules are sorbed on the surface or in the internal structures of a silica gel layer, forming silanol,

/Si-OH, silanediol, $=Si=(OH)_2$, and possibly silanetriol, $-Si/(OH)_3$, groups by breaking the siloxane bonds, /Si-O-Si/ /3/.

Two photochemical reactions can be postulated:

(1) photolysis decomposes the internal silanols and causes water to leave the silica network under disruption, thereby ejecting fragments into the gas, or
(2) photo synthesis may form orthosilicic acid, $Si(OH)_4$, which is supposed to be volatile with water /4/.

The orthosilicic acid molecules condense in the gas phase to form aerosol nuclei. Fig. 1 also shows the fate of the aerosol. At low irradiance (distance > 50 cm), the small particles cannot be measured because they deposit on the vessel's walls and/or on the tubing. At higher irradiance, the particles grow and their concentrations is limited by coagulation. The spheric particles, shown in Fig. 2, have a bimodal distribution in the SMPS spectra with modal diameters of 15 and 100 nm.

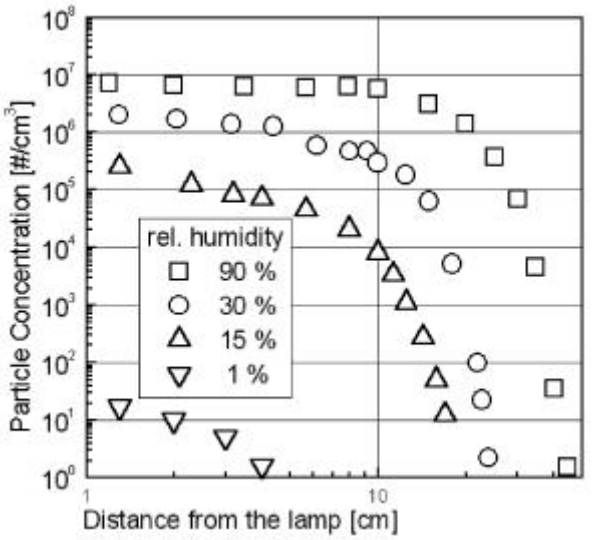

Fig. 1: Concentration of neutral particles escaping from the quartz glass vessel in dependance of the distance between the lamp and the quartz glass surface (decreasing irradiance) and of the humidity of the air at 23°C.

Conclusions

This paper describes for the first time particle emission for neutral silica in moist air from quartz glass surfaces that were irradiated with a low-pressure mercury lamp. The experimental parameters are discussed in detail. No conclusions can be drawn about the role of charged particles in a remobilization process.

The photochemical process can be used to generate pure silica aerosols and highly dispersed silicic acid powders. The results also show that mercury lamps may produce aerosols when they are used to sterilize clean rooms. We are currently investigating the effect of the radiation wavelength on the photochemical aerosol generation. Only then will we be able to fully assess the importance of this phenomenon in natural processes, such as weathering.

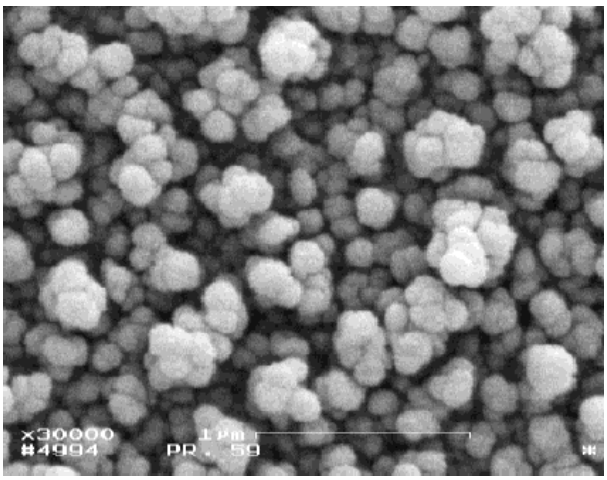

Fig. 2: SEM image of particles sampled at relative air humidities of 90% at 23 °C with 2 cm irradiation distance from the lamp during 60 h.

Acknowledgments

The authors would like to thank Mrs. E. Christalle, Institute of Ion-Beam Physics and Materials Research of the FZR, for the SEM micrographs and EDX analysis, Mr. M. Saupe, VKTA Rossendorf, for the EDXRF analysis, and Dr. E. Förster for advice with the irradiation experiments.

References

/1/ Yablokov, M.Yu., Andronova, A.V.: J. Aerosol Sci. **28**(1), 563-564 (1997)
/2/ Rettig, D., Merker, P., Nitsche, H.: J. Aerosol Sci. **28**(1), 139-140 (1997)
/3/ *Ullmann´s Encyclopedia of Industrial Chemistry.* VCH, Weinheim, Vol. A23, p.583 (1993)
/4/ *Ullmanns Encyklopädie der technischen Chemie*. München, Vol. 15, p.702 (1964)

Chemistry of the Heaviest Elements

DWELL TIME BEHAVIOR OF KRYPTON IN QUARTZ CAPILLARIES

M. Grantz
Forschungszentrum Rossendorf e.V., Institute of Radiochemistry

The dependency of the dwell time from the probability to collide with the tube wall is set out. This probability is given for components of the carrier gas and for trace amount components (tac) with an inner clock and leads to different dependencies of the dwell time from the tube radius. The fission products of the reaction ^{235}U (n, sf) ^{91}Kr, produced by an induced reaction ^{8}Be (d, n) ^{9}B at the U-120 cyclotron Rossendorf, were used to evalulate the dwell time in quartz tubes with different diameters at liquid nitrogen temperature. The slope of dwell time versus tube radius assures the postulated different behavior of tac with an inner clock. The fitted data are close to theoretical predictions.

The dwell time (t_{dwell}) is given by the time spent in the gas phase and the sum of time of all individual adsorptions (t_{ads}). When the number of adsorptions is large, one can evaluate average values for both of the terms without great error.

$$t_{dwell} \approx \frac{l}{\eta \cdot v_0} \cdot q \cdot t_{ads} \approx \frac{B \cdot r^2 \cdot l \cdot T_{st}}{2 \cdot M \cdot T_{exp}} \left[1 + \frac{6 \cdot v_M \cdot t_{ads}}{8} \right] \qquad (1)$$

q is the average number of adsorptions, v_0 the maximum laminar flow velocity, and $0 < \eta < 1$ is a factor for average flow velocity of the component in the gas phase. For a component of the carrier gas in a laminar flow this value is given by basic kinetic gas theory ($\eta = 1/2$). The column has the radius r and length l and a volume flow M measured at room temperature (T_{st}) passes through it at the temperature T_{exp}. The time between two collisions in the gas phase is given by the fraction of the mean free path (8) and Maxwell velocity (v_M). 6 gives the ratio of collisions which will take place with the column wall instead with another molecule. *For components of the carrier gas the calculation of 6 is easy ($6_{cg} = 8/2r$).* For the evaluation of 6 for trace amount components (tac) with an inner clock three times are important:

- the time between two collisions: $t_c = 8/v_M$
- the radial relaxation time: $t_r = 3Br^2/8v_M$ /1/
- the longitudinal relaxation time: $t_l = v_0/(j_m + \frac{3}{4})$; with $(j_m + \frac{1}{2})\,8 = r$ and $r \gg 8$.

The radial relaxation time is the time needed for tac to spread over the cross section of the tube. The longitudinal relaxation time is the time needed for tac close to the wall to pass through the tube. If the half-life of tac with an inner clock is smaller or of the same order of magnitude as the longitudinal relaxation time, the tac in regions close to the wall cannot pass the tube to the detection system. The detector will only count tac which will pass the tube mostly in the center regions. *For tac with an inner clock 6 is given by: $6_{tac} = 2(j_m + \frac{3}{4})/j_m^2(j_m - 1)$* /2/. This value is related to the radial relaxation time but a factor 3B/ 2.

The different values for 6_{cg} and 6_{tac} put into equation (1) lead to different radial dependency of t_{dwell}. An experiment with simple adsorption/ desorption processes and an adsorption time long enough to give an significant contribution to the 1 in the bracket term, can help to decide whether the adsorption probability of free tac with an inner clock is different from that of carrier gas.

The adsorption of noble gases on a quartz surface is a simple adsorption/ desorption process. The parameters J_0 and E_{ads} of the Frenkel equation [$t_{ads} = J_0 \exp(E_{ads}/RT)$] are given for Argon /3,4/ and lead for a temperature of 78 K to a individual adsorption time of 77 µs on glass and 9.0 ms on quartz. This is a lower limit for the adsorption time of Kr and Xe. At the U-120 cyclotron the noble gases Kr and Xe were produced in an $^{8}Be(d,n)^{9}B$; $^{235}U(n,sf)$ products reaction at deuteron energies of 28 MeV and lead through quartz tubes with diameters of 1, 2 or 4 mm, each of length of 1006 mm. For investigation the nuclide ^{91}Kr with half life of 8,6 s was used. The tubes were cooled over a length of 1000 mm with liquid nitrogen.

	cg- model	tac- model
η	1/2	0.1688 (± 4.03%)
t_{ads} [s]	$9.463 \cdot 10^{-5}$ (± 2.83%)	0.2197 (± 9.65%)
J_0 [10^{-14} s]	1.7 : 20	1.7 : 20
E_{ads} [kJ/ mole]	12.57 : 14.16	17.98 : 19.58

Tab. 1: Results of Dwell Time Behavior.

The dwell time is evaluated from relative activities. The dependency of the dwell time from the tube radius is shown in Fig. 1. The fitted data for η and t_{ads} are listed in

Tab. 1. The adsorption energy is calculated from the individual adsorption time t_{ads}.

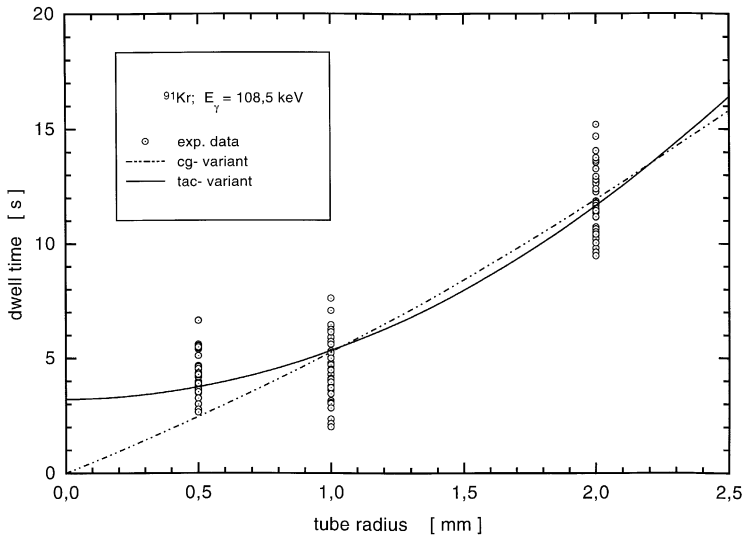

Fig. 1: Dwell Time of ^{91}Kr in Quartz Capillaries.

There are two indices for a different collision behavior of tac with an inner clock compared with components of the carrier gas.
- The slope of fitted data is within all experimental errors only for 6_{tac}.
- The experimental data give reasonable results for 6_{tac} .
The lower limit for the desorption energy is 15.91 kJ/ mole for argon /3/! The energy for the carrier gas model is below this limit even when one would use the lower J_0 for glass! The tac model gives for Kr an adsorption energy a little higher than for Ar. The difference between Kr and Ar in adsorption energy is a factor 1.2 to 3 smaller than the difference of the enthalpy of vaporization which is reasonable.

$,_{tac}$ is given by:
Ratio of average laminar flow velocity divided by the maximum flow velocity multiplied with the probability to become a free particle. This yields $, = \mathbf{b} * 0{,}25335$. This is in perfect agreement with the theoretical value of $\mathbf{b} * G_{i=1}^{4} (\mathbf{c} + 1/4B)^{i}$ for the probability of a spherical particle to change the radial position. The factor **b** is from the average laminar flow velocity for *free* particles distributed over a paraboloid /2/.

Acknowledgment
The support of the BMBF of the Federal Republic of Germany under contract 06 DR 666 I (4)/1 is gratefully acknowledged.

References
/1/ Schmutzger, E.: *Lehrbuch der theoretischen Physik.* VEB Deutscher Verlag der Wissenschaften, Berlin (1989) 1806
/2/ Grantz, M.: Calculation of Rate Constants of the Basic Reactions of Reaction Gas Chromatography - Trace Amount Components in Laminar Gas Flow. In: Report FZR-180, Institute of Radiochemistry, Annual Report 1996, p.61 (1997)
/3/ de Boer, W.: *Principles of Adsorption Chromatography.* 2nd ed., Clarendon Press, Oxford (1968) p.30
/4/ Vahle, A.: *Hochtemperaturgaschromatographie mit Spurenmengen der Homologen des Elementes 106 im O_2- $H_2O_{(g)}$ / $SiO_{2(s)}$- System.* TU Dresden, Thesis (1996) 15

THERMOCHROMATOGRAPHIC DETERMINATION OF EINSTEINIUM ADSORPTION ENTROPIES ON TANTALUM, TITANIUM, AND NIOBIUM

S. Taut, S. Hübener , B. Eichler [1], K. Eberhardt [2], N. Trautmann [2], J.R. Peterson [3]
Forschungszentrum Rossendorf e.V., Institute of Radiochemistry
[1] PSI Villigen; [2] Universität Mainz; [3] University of Tennessee, Knoxville

For the first time the adsorption entropies of elemental einsteinium on titanium, niobium, and tantalum were studied by thermochromatography.

Recently, we have carried out extensive thermochromatographic adsorption studies of metallic divalent heavy actinides in their elemental state up to nobelium /1, 2, 3/. The results can be used to estimate other metallic properties of these elements. One possible application is the calculation of sublimation enthalpies, which we determined for einsteinium in /2/. In this case, an experimentally well-established linear correlation exists between adsorption and sublimation enthalpies. Thus, it was sufficient to use values of adsorption heat *differences* of similar metals to einsteinium.
To obtain an insight in other metallic properties of the adsorbed actinides, accurate values of

the *absolute* adsorption heats are necessary. To accurately determine the adsorption heat from the adsorption temperature one has to know the corresponding adsorption entropy. In previous calculations, we only estimated this property /4/.

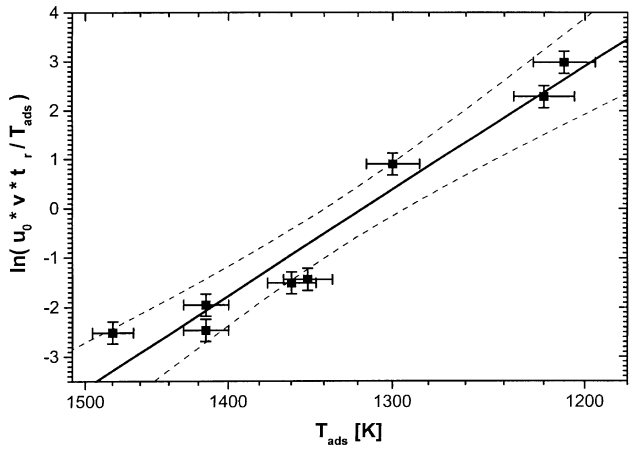

Fig. 1: Arrhenius Plot of Einsteinium on Tantalum.

In this work, we determined the adsorption entropy more exactly through thermochromatography. As shown in /4/, it can be obtained by measuring the adsorption temperatures as a function of both chromatography time and carrier gas flow.
We chose einsteinium for the adsorption experiments because this is the first clearly metallic divalent actinide. It should, therefore, serve as an appropriate model substance for the heavier actinides up to nobelium. Tantalum, titanium, and niobium were used as adsorbent metals.
The experimental setup and procedure are described in detail elsewhere /2, 3/.
Fig. 1 shows the Arrhenius plot of the adsorption on tantalum. The adsorption heat can be derived from the slope of this graph, whereas the intercept gives the adsorption entropy.

Tab. 1 lists the results of our measurements.

Adsorbent metal	Adsorption Entropy	Adsorption Enthalpy
Titanium	-144 J/(mol K)	-199 kJ/mol
Niobium	-160 J/(mol K)	-276 kJ/mol
Tantalum	-183 J/(mol K)	-327 kJ/mol

Tab. 1: Adsorption Enthalpies and Entropies of Einsteinium.

The small entropy values support both the experimentally found strong adsorbate bonding and the adsorption in the atomic state.

Acknowledgments
This work was funded by DFG. The authors are indebted for the use of ^{254}Es to the Office of Basic Energy Sciences, U.S. Department of Energy, through the transplutonium element production facilities at the Oak Ridge National Laboratory, managed by Lockheed Martin Energy Research Corporation.

References
/1/ Hübener, S., et. al.: Thermochromatographic studies of heavy actinides in metal columns. J. Alloys Comp. **213/214**, 429 (1994)
/2/ Taut, S., et. al.: Thermochromatography of Heavy Actinides - Determination of the Sublimation Enthalpy of Es. Radiochimica Acta **78**, 33 (1997)
/3/ Taut, S., et. al.: Thermochromatography of Heavy Actinides - Adsorption of No-259 on Ti, V, Nb, Ta, and Mo. accepted by J. Alloys Comp.
/4/ Eichler, B., et. al.: Evaluation of the Enthalpy of Adsorption from Thermochromatographical Data. Radiochimica Acta **30**, 233 (1982)

ON-LINE GAS CHROMATOGRAPHY OF SHORT-LIVED MO AND W ISOTOPES IN THE O_2-$H_2O_{(g)}$/$SiO_{2(s)}$-SYSTEM - EXPERIMENT AND SIMULATION

A. Vahle, M. Grantz, S. Hübener, D.T. Jost [1], A. Türler [1]
Forschungszentrum Rossendorf e.V., Institute of Radiochemistry
[1] Paul Scherrer Institut Villigen, Laboratory of Radio- and Environmental Chemistry

In preparation for an experiment to study the chemical properties of element 106 (seaborgium, Sg), model studies were performed with short-lived isotopes of its homologues Mo and W. Thermodynamic state functions of the studied surface reactions as well as retention times were determined.

To characterize Sg and to look for general trends at the end of the periodic table, Sg has to be studied in comparison to other elements; first of all to its lighter homologues Mo and W. The experimental set-up has to be tested by model experiments with trace amounts of short-lived isotopes of these elements. Thermodynamic state functions have to be determined to find

optimum conditions for the chemical characterization of Sg and to predict and interpret the behavior of Sg in real experiments.
The behavior of trace amounts of the Sg homologues in the O_2-$H_2O_{(g)}$/$SiO_{2(s)}$-system has been already studied earlier by off-line thermochromatography with long-lived nuclides /1/. It was found that all group 6 elements are transported via reaction gas chromatography $MO_2(OH)_{2\,(g)}$ W $MO_{3\,(ads)} + H_2O_{(g)}$ characterized by relatively slow kinetics. Reaction gas chromatography as a special case of gas chromatography can be simulated by means of a Monte Carlo model described in /2/.
In this work several experimental arrangements for on-line isothermal high temperature gas chromatography were tested studying short-lived isotopes of Mo and W. Mo isotopes were produced in the ^{235}U (n, f) reaction at the FZR U-120 cyclotron using neutrons from the reaction ^{9}Be (d, n) ^{10}B. To obtain short-lived W isotopes, an enriched ^{152}Gd target was bombarded with ^{20}Ne at the PSI PHILIPS cyclotron. The He/MoO_3-jet used to transport the reaction products to the chromatography apparatus was operated with a He-flow rate of 1.0 L/min. A newly developed five section chromatography furnace was used which provides a high temperature reaction zone of 1350 K and an isothermal zone. The temperature of the isothermal zone may be varied between 800 K and 1350 K. For details see /4/. Moist oxygen was added as reactive gas at the column entrance. The partial pressure of water vapor was about 2.5 kPa.

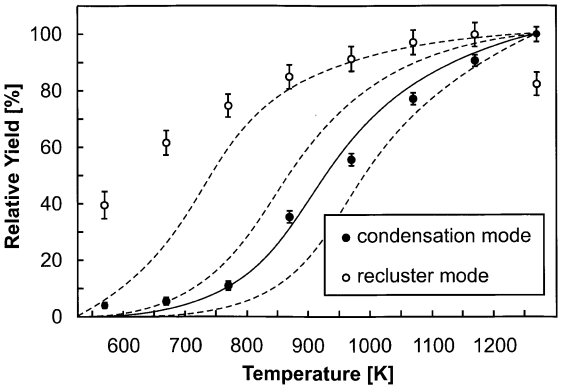

Fig. 1: Relative yield of ^{104}Mo ($t_{1/2}$ = 59.4 s) as a function of the isothermal temperature, solid: MC simulation, $)H^{E}_{diss.ads}$ = - 54 kJ/mol, dotted: $)H^{E}_{diss.ads}$ = - 50 ± 9 kJ/mol.

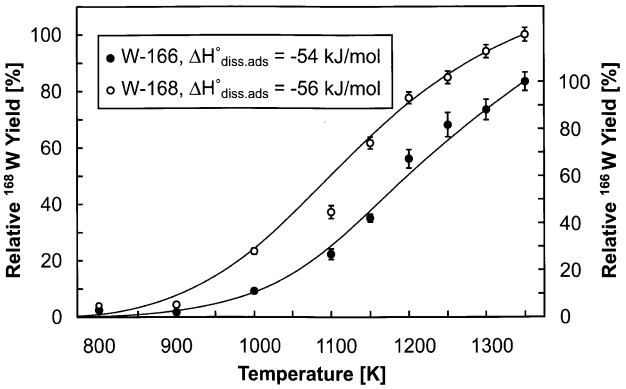

Fig. 2: Relative yields of ^{166}W ($t_{1/2}$ = 18.8 s) and ^{168}W ($t_{1/2}$ = 51 s) as a function of the isothermal temperature.

In a first experimental series, the volatile Mo species leaving the column with the carrier gas were injected into a recluster chamber where they were attached to KCl aerosol particles injected with 1.5 L/min Ar. The total gas, containing the products under study attached to the KCl particles, was then transported through a capillary to the counting device. It consisted of a glass fibre filter station mounted on top of a HPGe detector. Fig. 1 shows the relative yields of ^{104}Mo as a function of the isothermal temperature. The extremely flat yield curve results from the tendency of increasing chemical yield and decreasing recluster yield at increasing temperature. The experimental data are difficult to evaluate. In former thermochromatography experiments a dissociative adsorption enthalpy $)H^{E}_{diss.ads}$ = -50 ± 9 kJ/mol was derived. Yield curves which were calculated with this enthalpy value are shown as dotted lines in the figure. As can be seen, these curves do not fit the experimental data. A maximum yield of 27 ± 3 % compared to a direct catch on a glass fibre filter without passing the experimental arrangement was obtained for ^{104}Mo at 1170 K. A dwell time of about one minute was determined for the recluster chamber.
In a second series, the volatile Mo species leaving the chromatography column were directly deposited on thin Al foils mounted on the wheel of the GSI rotating wheel multidetector analyzer ROMA to reduce the time passing between chromatography and detection of the species. The wheel was operated with a collection/detection time of 60 s. Results of these experiments are also shown in Fig. 1.
The solid line was obtained by Monte Carlo simulation with an enthalpy value of $)H^{E}_{diss.ads}$ = -54 kJ/mol, which best fits the experimental data. The experimental data correspond well with the $)H^{E}_{diss.ads}$ = -50 ± 9 kJ/mol from the earlier thermochromatography experiments /1/. A retention time of 7 seconds was determined for the chromatographic column at its highest

operation temperature by the Monte Carlo method. About 10 seconds result from the $T_{50\%}$-value /3/.
W as the heaviest homologue of Sg was studied by a further improved experimental arrangement. A separate condensation chamber was placed between the column and the rotating wheel to establish optimum pressures for direct condensation (80 mbar) and detection (< 5 mbar) and to cool the wheel. Detailed experimental conditions are described in /4/.
Fig. 2 shows the relative yields (maximum value = 100 %) of ^{166}W and ^{168}W as a function of the isothermal temperature together with yield curves calculated by Monte Carlo simulation. The best fit of the experimental data was obtained with enthalpy values of $-\Delta H^{E}_{diss.ads}$ = -54 and -56 kJ/mol for ^{166}W and ^{168}W, respectively. These values correspond well with the value of $-\Delta H^{E}_{diss.ads}$ = -62 ± 13 kJ/mol derived from earlier thermochromatography experiments /1/. The retention time spent by the W species during their travel from the column entrance to the Al foil as determined by Monte Carlo simulation was about 20 s. From the nuclide yield ratio at 1350 K, a retention time of 8 s was calculated /4/ which seems to be a more reliable value since a few assumptions without proven correctness were used to simulate the chromatographic process.

Acknowledgments
This work was supported by the BMBF, contract 06 DR 666 I (4)/1, and was performed in cooperation with the GSI Darmstadt.

References
/1/ Vahle, A., PhD Thesis, TU Dresden 1996
/2/ Vahle, A., Hübener, S., Dressler, R., Eichler, B., Türler, A.: Radiochim. Acta **78**, 53 (1997)
/3/ Gäggeler, H., Dornhöfer, H., Schmidt-Ott, W.D., Greulich, N., Eichler, B.: Radiochim. Acta **38**, 103 (1980)
/4/ Hübener, S., Grantz, M., Salamatin, L., Vahle, A., Jost, D.T., Türler, A.: this report

ON-LINE HIGH TEMPERATURE GAS CHROMATOGRAPHY OF SHORT-LIVED TUNGSTEN NUCLIDES IN MOIST OXYGEN

S. Hübener, M. Grantz, L. Salamatin, A. Vahle, D.T. Jost[1], A. Türler[1]
Forschungszentrum Rossendorf e.V., Institute of Radiochemistry
[1] PSI Villigen

The reaction gas chromatography of tungsten oxidehydroxide was studied in quartz glass columns. The short-lived isotopes ^{166}W and ^{168}W were used in combination with a new high temperature gas chromatography furnace that was directly coupled with the detection unit ROMA. At a column temperature of 1350 K, a retention time of 8 s and a chemical yield of 53 % were measured for ^{166}W .

Gas chromatography of the group 6 elements Mo, W, and Sg in the O_2-$H_2O_{(g)}$/$SiO_{2(s)}$-system can be classified as reaction gas chromatography characterized by relatively slow kinetics that are often collision-controlled. In test experiments with the OLGA II apparatus, about one minute retention times were measured for tungsten species /1/; far too long for studying the seaborgium nuclides ^{265}Sg or ^{266}Sg.
An improved experimental arrangement was tested by studying the short-lived tungsten isotopes ^{166}W and ^{168}W which were produced in the ^{20}Ne on ^{152}Gd reaction at the PSI PHILIPS cyclotron. A He/MoO_3-jet was used to rapidly transport the reaction products to the chromatography apparatus. A newly developed five-section chromatography furnace was tested which allows to operate differently shaped chromatography columns with outer diameters up to 18 mm at isothermal temperatures up to 1375 K. The columns were straight open tubular quartz glass columns with the following specifications: (a) inner diameter 3.5 mm, (b) 6 cm long preheating section, (c) constriction for positioning quartz wool as a high temperature reaction zone, (d) 38 cm long isothermal zone, and (e) capillary outlet. To replace the time consuming reclustering step between chromatography and detection, the volatile tungsten species leaving the chromatography column were directly deposited on aluminium foils mounted on the circumference of the rotating wheel of the GSI **ro**tating wheel **m**ultidetector **a**nalyzer ROMA. To establish an optimum pressure for the direct deposition of about 80 mbar and at the same time a pressure below 5 mbar in the detection positions of the ROMA chamber, a separate deposition chamber was placed between column and rotating wheel. Furthermore, the deposition chamber was

connected to a cooling thermostat and cooled the wheel.

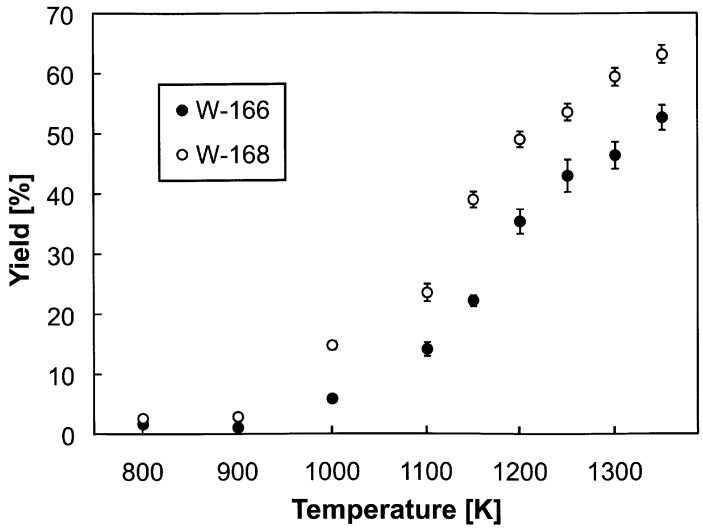

Fig. 1: Yields of ^{166}W and ^{168}W as a function of the isothermal temperature

The gas-jet was operated with a He-flow rate of 1.0 l/min. At the column entrance, 0.5 l/min O_2 gas, moistened with H_2O at 323 K, were added to form volatile oxidehydroxides. The temperature of the reaction zone was 1350 K, the isothermal column temperature was varied between 800 and 1350 K, whereas the temperature of the outlet was held above 950 K. The rotating wheel was operated with a cycle-time for collection and detection of 20 s. At a coolant temperature of 283 K the temperature of the rotating wheel in the first detection position did not exceed 298 K. The activity of the foils was measured either by "- or (- spectrometry.

Fig. 1 shows the yields of ^{166}W and ^{168}W as function of the temperature of the isothermal zone as measured by gamma spectrometry relative to the activity of the gas-jet. To measure the activity of the gas-jet, the aerosol particles passing through an open unheated column were collected on glass fibre filters.

From the yield ratio at 1350 K, a retention time t_r = 8 s was calculated spent by the tungsten species during their travel from the column entrance to the aluminium foil. The retention time was calculated by using the following equation which was adapted from /2/:

$$t_r = 1/(8_1-8_2)\ \ln y_2/y_1 \qquad (1)$$

(8 = decay constant, y = nuclide yield)

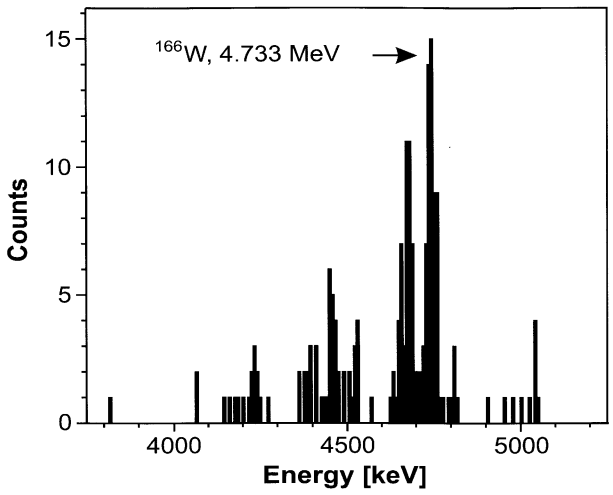

Fig. 2: Alpha-spectrum measured in detection position 1

The alpha spectrometric measurements were carried out in 2B geometry with a resolution of 30 keV (FWHM). Fig. 2 shows a typical "-spectrum measured in the first detection position next to the deposition chamber. The main peak was assigned to ^{166}W (4.739 MeV). Nuclides like ^{152}Ho (4.52 MeV) and ^{151}Dy (4.07 MeV), produced in transfer reactions of the target nuclide, were detected only in negligible quantities which shows that they were retained nearly quantitatively on the column.

The results are promising with regard to future studies of seaborgium. However, as a pre-requisite for the unequivocal detection of seaborgium, alpha spectroscopy in 4B geometry needs to be established.

Acknowledgments

The support of the BMBF under contracts 06 DR 666 I (4)/1 and 06 DR 824 2 is gratefully acknowledged.

References

/1/ Hübener, S., et al.: Report FZR-94, Institute of Radiochemistry, Annual Report 1994, p.92 (1995)
/2/ Dressler, R., et al.: PSI Annual Report 1994, Annex IIIA, p.45 (1995)

II. PUBLICATIONS, PATENTS, LECTURES AND POSTERS

PUBLICATIONS

Abram, U., Schulz-Lang, E., Abram, S., Wegmann, J., Dilworth, J.R., Kirmse, R., Woolins, J.D.
Technetium(V) and Rhenium(V) Nitrido Complexes with Tetraphenylimidodithiodiphosphinate, $[(Ph_2PS)_2N]^-$
J. Chem. Soc. Dalton Trans. 623 (1997)

Abram, U., Schulz-Lang, E., Dilworth, J.R.
Structure of Chlorobis(dimethylphenylphosphine)bis(imidotetraphenyldithiophosphinatoS,S') nitridorhenium(V)
Acta Cryst. **C53,** 289 (1997)

Abram, S., Maichle-Mössmer, C., Abram, U.
Indium(III) Complexes with Tridentate Nitrogen Donor Ligands. Synthesis, Characterization and Crystal Structures of Complexes with 2,6-Bis(acetyloxime)pyridine and 2,6-Bis(1-phenylimino ethyl)pyridine
Polyhedron **16**, 2183 (1997)

Abram, S., Maichle-Mössmer, C., Abram, U.
Mixed-Ligand Complexes of Indium (III). Reactions of $[InCl_3(L^1)(MeOH)]$ with bidentate Ligands. Synthesis, Characterization and Crystal Structures of $[In(L^1)Cl(ox)(OH_2)] \cdot 2\ H_2O$, $[In(L^1)Cl(mnt)] \cdot MeOH$ and $[In(pythio)_3]$ (L^1 = Pyridine-2,6-bis(acetyloxime), ox^{2-} = oxalate, mnt^{2-} = l,2-dicyano ethene-1,2-dithiolate, pythio = pyridine-2-thiolate)
Polyhedron **16**, 2291 (1997)

Abram, S., Abram, U.
2-[1-(Thiosemicarbazono)ethyl]pyridinium Chloride
Acta Cryst. **C53**, 360 (1997)

Abram, S., Maichle-Mössmer, C., Abram, U.
Synthesis and Characterization of Indium(III) Complexes with Tri- and Pentadentate Thiosemicarbazones. Crystal and Molecular Structures of $[InCl_2(HDAPTSC)] \cdot 2$ DMSO, $[InCl_2(APTSC)(MeOH)]$, $[In(APTSC)_2]PF_6$, and $[InCl(APTSC)(mnt)] \cdot (H_2APTSC)$ ($H_2DAPTSC$ = 2,6-diacetylpyridine-bisthiosemicarbazone, HAPTSC = 2-acetylpyridinethiosemicarbazone, mnt^{2-} = 1,2-dicyanoethene-1,2-dithiolate)
Polyhedron **17**, 131 (1997)

Allen, P.G., Bucher, J.J., Shuh, D.K., Edelstein, N.M., Reich, T.
Investigation of Aquo and Chloro Complexes of UO_2^{2+}, NpO_2^+, Np^{4+}, and Pu^{3+} by X-ray Absorption Fine Structure Spectroscopy
lnorganic Chemistry **36,** 4676 (1997)

Allen, P.G., Shuh, D.K., Bucher, J.J., Edelstein, N.M., Reich, T., Denecke, M.A., Nitsche, H.
Chemical Speciation Studies of Radionuclides by XAFS
J. Phys. IV France **7**, C2-789 (1997)

Allen, P.G., Siemering, G.S., Shuh, D.K., Bucher, J.J., Edelstein, N.M., Langton, C.A., Clark, S.B., Reich, T., Denecke, M.A.
Technetium Speciation in Cement Waste Forms Determined by X-ray Absorption Fine Structure Spectroscopy
Radiochimica Acta **76**, 77 (1997)

Allen, P.G., Booth, C.H., Bucher, J.J., Denecke, M.A., Edelstein, N.M., Nitsche, H., Reich, T., Shuh, D.K., Marasinghe, G.K., Karabulut, M., Ray, C.S., Day, D.E., Shumsky, M.G.
Studies of Actinides by X-ray Absorption Spectroscopy
Stanford Synchrotron Radiation Laboratory 1996 Activity Report, p. A-206 (1997)

Allen, P.G., Bucher, J.J., Denecke, M.A., Durbin, P., Edelstein, N.M., Kullgren, B., Reich, T., Shuh, D.K.
XAFS of Neptunium Incorporated in Mammals
Stanford Synchrotron Radiation Laboratory 1996 Activity Report, p. A-232 (1997)

Allen, P.G., Bucher, J.J., Clark, S.B., Denecke, M.A., Edelstein, N.M., Langton, C.A., Nitsche,

H., Reich, T., Shuh, D.K., Siemering, G.S.
Technetium and Neptunium Speciation in Cement Waste Forms
Stanford Synchrotron Radiation Laboratory 1996 Activity Report, p. A-276 (1997)

Baraniak, L., Thieme, M., Funke, H., Bernhard, G., Nitsche, H.
Verhalten des Radiums im Flutungsprozeß des Uranbergwerks Königstein
Wiss. Z. Techn. Univers. Dresden **46**, 90-94 (1997)

Baraniak, L., Thieme, M., Funke, H., Bernhard, G., Nitsche, H., Nindel, K., Schreyer, J.
Über das Verhalten des Radiums im Flutungsprozeß des Uranbergwerks Königstein
Jahresbericht 1996 des Forschungszentrums Rossendorf e.V., S.21-27 (1997)

Baraniak, L., Schmidt, M., Schiene, R., Jelen, K., Koch, H., Nitsche, H.
Untersuchung des Grubenholzabbaus und Speziation der löslichen Abbauprodukte während der Flutung des Schlema-Alberodaer Grubensystems und Untersuchung der Einflußnahme der organischen Stoffe auf den chemischen Zustand sowie das Migrationsverhalten von Radionukliden und Schwermetallen
Abschlußbericht SMWK-Förderprojekt 4-7541.83-FZR/4O2, Mai 1997

Bonsdorf, G., Denecke, M.A., Schäfer, K., Christen, S., Langbein, H., Gunßer, W.
X-Ray Absorption Spectroscopic and Mössbauer Studies of Redox and Cation-Ordering Processes in Manganese Ferrite
HASYLAB-Annual Report 1996 **I**, 834 (1997)

Bubner, M., Matucha, M., Sasek, V., Heise, K.H., Nitsche, H., Veleminsky, J., Spizek, J.
Investigations of microbial degradation of PCB congeners using isotopically modified tracers
Ekolog. Khim. (russ.) **6**(3), 204-211(1997)

Denecke, M.A., Friedrich, H., Reich, T., Bernhard, G., Knieß, T., Rettig, D., Zorn, T., Nitsche, H.
Determination of Relative Arsenite and Arsenate Concentrations in Aqueous Mixtures by XANES
HASYLAB-Annual Report 1996 **I**, 751(1997)

Denecke, M.A., Reich, T., Pompe, S., Bubner, M., Heise, K.H., Nitsche, H., Allen, P.G., Bucher, J.J., Edelstein, N.M., Shuh, D.K.
Differentiating between Monodentate and Bidentate Carboxylate Ligands Coordinated to Uranyl Ions Using EXAFS
J. Phys. IV France **7**, C2-637 (1997)

Dilworth, J.R., Hübener, R., Abram, U.
Synthesis and Characterization of Bis(tetrabutylammonium)bis(isotrithionedithiolato-S,S')-nitrido technetate(V), $(Bu_4N)_2[TcN(dmit)_2]$
Z. anorg. allg. Chem. **623**, 880 (1997)

Dressler, R., Schumann, D., Taut, S., Fischer, S., Binder, R.,Yakushev, A.B.,Buklanov, G., Dinh Thi Lien, Domanov, V.P., Szeglowski, Z., Kubica, B., Guseva, L.I., Tikhomirova, G.S., Gäggeler, H.W., Bruchertseifer, H.
First Observation of (-Ray Emission Assigned to the Decay of ^{164}W
Radiochimica Acta **77**, 241-244 (1997)

Egli, A., Hedinger, R., Hegetschweiler, K., Kissner, R., Alberto, R., Schibli, R., Abram, U., Gramlich, V., Baumgärtner, F., Schubiger, P.A., Herrmann, W.A.
Hydrolysis of the Organometallic Aquaion *fac*-$[Re(CO)_3(H_2O)_3]^+$. Mechanism, Determination of the pK_A and the Stability Constants of the Hydrolytic Products
Organometallics **16**, 1833 (1997)

Eichler, B., Hübener, S., Erdmann, N., Eberhardt, K., Funk, H., Herrmann, G., Köhler, S., Trautmann, N., Passler, G., Urban, F.-J.
An Atomic Beam Source for Actinide Elements: Concept and Realization
Radiochimica Acta **79**, 221-233 (1997)

Gärtner, M., Böttger, M., Eichler, B., Gäggeler, H.W., Grantz, M., Hübener, S., Jost, D.T., Piguet, D., Dressler, R., Türler, A., Yakushev, A.B.
On-line Gas Chromatography of Mo, W and U (Oxy)chlorides

Radiochimica Acta **78**, 59-68 (1997)

Geipel, G., Brachmann, A., Brendler, V., Bernhard, G., Nitsche, H.
Uranium(VI) Sulfate Complexation Studies by Time-Resolved Laser-Induced Fluorescence Spectroscopy
Radiochimica Acta **75**,199-204 (1996)

Geipel, G., Reich, T., Brendler, V., Bernhard, G., Nitsche, H.
Laser and X-ray Spectroscopic Studies of Uranium-Calcite Interface Phenomena
J. NucI. Mat. **248**, 408 (1997)

Johannsen, B., Jankowsky, R., Noll, B., Spies, H., Reich, T., Nitsche, H., Dinkelborg, L.M., Hilger, C.S., Semmler, W.
Technetium Coordination Ability of Cysteine-containing Peptides: X-ray Absorption Spectroscopy of a ^{99}Tc Labeled Endothelin Derivate
Appl. Radiat. Isot. **48**,1045 (1997)

Kuhn, N., Abram, U., Maichle-Mössmer, C., Wiethoff, J.
$[Li_{12}O_2Cl_2(ImN)_8(THF)_4]$ x 8 THF: ein Peroxokomplex des Lithiums mit neuartiger Käfigstruktur
Z. anorg. allg. Chem. **623**, 1121 (1997)

Mack, J., Ortner, K., Abram, U., Parish, R.V.
Gold(III)-Komplexe mit 2-(N,N-Dimethylaminomethyl)phenyl ($damp^-$). Darstellung und Kristallstrukturen von $[Au(damp\text{-}C,N)Cl_2]$, $[Au(damp\text{-}C,N)(OOCCH_3)_2]$ und [Au(damp-C,N)(mnt)] (mnt^{2-} = 1,2-Dicyanoethene-1,2-dithiolat)
Z. anorg. allg. Chem. **623**, 873 (1997)

Nebelung, C., Nitsche, H., Bernhard, G.
Methode zur schnellen Bestimmung von Actiniden in Bauschutt zur Freigabeentscheidung
V. Stillegungskolloquium Hannover, 24.-25.06.1997
IV. Statusbericht Stillegung und Rückbau kerntechnischer Anlagen
Tagungsband S.293-301

Nitsche, H., Baraniak, L.
Radioecological Aspects on the Interaction of Radionuclides and Heavy Metals with Biomass: Methods for Speciation and Structural Information
in: C. Ronneau, O. Bitchaeva (eds.) *Biotechnology for Waste Management and Site Restoration.* Kluwer Academic Publishers (1997), pp. 55-59

Radeva, G., Selenska-Pobell, S.
Alteration of the symbiotic properties of Rhizobium melilot by plasmid manipulations
Microbious **89**,187-196 (1997)

Reich, T., Hudson, E.A., Denecke, M.A., Allen, P.G., Nitsche, H.
Structural Analysis of Uranium(VI) Complexes by X-ray Absorption Spectroscopy
Poverkhnost **4-5**,149 (1997)

Reich, T., Brendler, V., Denecke, M.A., Allen, P.G., Bucher, J.J., Edelstein, N.M., Shuh, D.K., Nitsche, H.
Structural Analysis of Uranium(VI) Complexes with Simple Carboxylic Acids in Aqueous Solution Using EXAFS
Stanford Synchrotron Radiation Laboratory 1996 Activity Report, p. A-299 (1997)

Rettig, D., Merker, P., Nitsche, H.
Detection of Aerosol Losses in Glass Vessels
J. Aerosol Sci. **28**, pp. 139-140 (1997)

Selenska-Pobell, S., Döring, H., Evguenieva-Hackenberg, E.
Unusual organization of the 23S rRNA genes in Rhizobiaceae
Soil Biology and Biochemistry **29**, 905-909 (1997)

Schädel, M., Brüchle, W., Dressler, R., Eichler, B., Gäggeler, H.W., Günther, R., Gregorich, K.E, Hoffman, D.C., Hübener, S., Jost, D.T., Kratz, J.V., Paulus, W., Schuhmann, D., Timokhin,

S., Trautmann, N., Türler, A., Wirth, G., Yakushev, A.
Chemical properties of element 106 (seaborgium)
Nature **388,** 55-57 (1997)

Schröder, U., Richter, R., Hartung, J., Abram, U., Beyer, L.
Substituierte 1,2,4-Thiadiazolium-dichloroaurate(I) und -tetrachloroaurate(III) als Reaktionsprodukte von N-Thiocarbamoylbenzamidinen mit Tetrachlorogold(III)-Verbindungen.
Z. Naturforsch. **52b**, 620 (1997)

Schulz-Lang, E., Abram, U., Strähle, R.
Synthese, Eigenschaften und Struktur von $LiAuI_4$ und $KAuI_4$ mit einer Diskussion der kristallchemischen Verwandtschaft zwischen den Halogenoauraten $RbAuCl_4$, $AgAuCl_4$, $RbAuBr_4$ und $LiAuI_4$
Z. anorg. allg. Chem. **163**, 1791 (1997)

Schumann, D., Andrassy, M., Nitsche, H., Novgorodov, A.F., Bruchertseifer, H.
Sorption Behaviour of Uranium on Cation and Anion Exchange Resins from HCl/HF-Containing Aqueous Solutions: Model Experiments for the Determination of Chemical Properties of Element 106 (Seaborgium)
Radiochimica Acta **79**, 217-220 (1997)

Taut, S., Hübener, S., Eichler, B., Gäggeler, H.W., Schädel, M., Zvara, I.
Thermochromatography of Heavy Actinides - Determination of the Sublimation Enthalpy of Es
Radiochimica Acta **78**, 33-38 (1997)

Teterin, Yu.A., Ivanov, K.E., Baev, A.S., Nefedov, V.I., Geipel, G., Reich, T., Nitsche, H.
X-ray Photoelectron Study of the Interaction of $UO_2(ClO_4)_2$ with Calcite and Diabase Minerals in Water Solutions
Poverkhnost **4-5**, 202 (1997)

Vahle, A., Hübener, S., Dressler, R., Eichler, B., Türler, A.
Reaction Gas Chromatography of Oxide and Hydroxide Species of Molybdenum - Simulation and Experiment
Radiochimica Acta **78**, 53-57 (1997)

Wittern, U., Strähle, J., Abram, U.
Synthese von Nitrenkomplexen mit N-Trimethylsilylanilin. III. Charakterisierung und Kristallstruktur von $[Re(NPh)(OsiMe_3)Cl(NH_2Ph)(py)_2][ReO]$ und *trans*-$[Re_2O_3(py)_4]$
Z. anorg. allg. Chem. **623**, 218 (1997)

PH.D. THESES

Brachmann, A.
Zeitaufgelöste laser-induzierte Floureszenzspektroskopie zur Charakteristik der Wechselwirkung des Uranylions mit Huminsäuren und Carboxylatliganden
TU Dresden, Germany, 1997

Moll, H.
Zur Wechselwirkung von Uran mit Silicat in wäßrigen Systemen
TU Dresden, Germany, 1997

Pompe, S.
Entwicklung huminsäureähnlicher Melanoidine als Funktionalitätsmodelle tür Huminsäuren und ihr Vergleich mit Fluka-Huminsäure hinsichtlich ihres Komplexbildungsverhaltens gegenüber Uran(VI)
TU Dresden, Germany, 1997

LECTURES

Abram, U., Mack, J., Ortner, K.
Gold(III)-Komplexe mit 2-(N,N-Dimethylaminomethyl)phenyl - Darstellungen, Strukturen und Reaktionen
Chemiedozententagung 1996
Berlin, Germany, 16.-19.03.1997

Abram, U.
Technetium- und Rheniumkomplexe mit Thioharnstoffen und ihren Derivaten
Leipziger Treffen für Koordinationschemie
Leipzig, Germany, 20.-21.05.1997

Abram, U.
Nitridoliganden als Lewis-Säuren in der Koordinationschemie
Universität Oldenburg, Fachbereich Chemie
Oldenburg, Germany, 08.07.1997

Abram, U.
Nitridobrücken zwischen Rhenium und Elementen der 3. Hauptgruppe
Technische Universität Dresden, Institut für Analytische Chemie
Dresden, Germany, 10.07.1997

Abram, U.
Technetium - a Man-made Element Conquers the Hospital
Federal University of Brasilia, Department of Chemistry
Brasilia, Brazil, 18.09.1997

Abram, U.
Technetium - a Man-made Element Conquers the Hospital
Federal University of Santa Maria, Department of Chemistry
Santa Maria, Brazil, 23.09.1997

Abram, U.
Coordinated Nitrido Ligands - Lewis Bases for the Coordination Chemist
University of Montevideo
Montevideo, Uruguay, 29.09.1997

Abram, U.
Metallkomplexe in der Medizin
Workshop für Bioanorganische Chemie, Technische Universität Dresden
Dresden, Germany, 22.10.1997

Abram, U.
Koordinierte Nitridoliganden - Lewis-Säuren für den Komplexchemiker
Universität Potsdam, Institut für Anorganische Chemie
Potsdam, Germany, 06.11.1997

Abram, U.
Technetium - ein künstliches Element erobert das Krankenhaus
Johannes-Gutenberg-Universität Mainz, Institut für Kernchemie
Mainz, Germany, 26.11.1997

Abram, U.
Nitrido Ligands as Bridges between Main Group and Transition Metals
St. Annes Conference 1997 Oxford
Oxford, England, 17.12.1997

Allen, P.G., Shuh, D.K., Bucher, J.J., Edelstein, N.M., Reich, T.
An XAFS Investigation of the Formation of Actinide Aquo and Chloro Complexes
214th American Chemical Society National Meeting
Las Vegas, NV, USA, 07.-11.9.1997

Arnold, T.
Identification of an uranium surface species sorbed onto ferrihydrite by TRLFS (Time-resolved Laser-induced Fluorescence Spectroscopy)
Workshop: ”The Münster workshop on Mineral Surface Science"
Münster, Germany, 02.-04.04.1997

Arnold, T
Sorption von U(VI) auf Ferrihydrit
Workshop: “Geochemische Modellierung”
Karlsruhe, Germany, 23.-24.04.1997

Arnold, T.
Uranium Sorption on Phyllite
NEA International Meeting on Chemical Modeling of Sorption in the Field of Radioactive Waste Management
Oxford, Great Britain, 06-08.05.1997

Bernhard, G., Geipel, G., Brendler, V., Nitsche, H.
Uranium Speciation in Waters of Different Uranium Mining Areas
Actinides'97
Baden-Baden, Germany, 21.-26.09.1997

Brendler, V.
Einbindung geochemischer Speziationsmodule in Risk-Assessment Software
Workshop: “Geochemische Modellierung”
Karlsruhe, Germany, 22.-24.04.1997

Bubner, M., Pompe, S., Heise, K.H., Nitsche, H.
Vergleichende Untersuchungen der Funktionalität von synthetischen Huminsäuren und Aldrich-Huminsäure
Arbeitstagung der Deutschen Gesellschaft für Moor- und Torfkunde e.V.
Bad Elster, Germany, 04.-05.09.1997

Denecke, M.A.
EXAFS Investigations on Uranium(VI) Complexed with Carboxylates or Humates and Sorbed onto Silica
Argonne National Laboratory
Argonne, IL, USA, 11.03.1997

Denecke, M.A.
EXAFS Investigations on Uranium(VI) Complexed with Carboxylates or Humates and Sorbed onto Silica
Hamburger Synchrotronstrahlungslabor, HASYLAB
Hamburg, Germany, 19.03.1997

Denecke, M.A.
XAFS Investigations on Uranium(VI) Complexed with Carboxylates and Sorbed onto Silica or Minerals
European Synchrotron Radiation Facility
Grenoble, France, 15.09.1997

Denecke, M.A., Reich, T., Bubner, M., Pompe, S., Heise, K.H., Nitsche, H., Allen, P.G., Bucher, J.J., Edelstein, N.M., Shuh, D.K.
Determination of Structural Parameters of Uranyl lons Complexed with Organic Acids using EXAFS
Actinides'97
Baden-Baden, Germany, 21.-26.09.1997

Denecke, M.A.
XAFS Studies of the lnteraction of Radionuclides with Environmentally Relevant Materials
Forschungszentrum Karlsruhe, Institut für Nukleare Entsorgungstechnik
Karlsruhe, Germany, 20.11.1997

Geipel, G., Bernhard, G., Brendler, V., Nitsche, H.
Complex Formation between UO_2^{2+} and CO_3^{2-} Studied by Laser-lnduced Photoacoustic Spectroscopy
Migration'97
Sendai, Japan, 26.-31.10.1997

Geipel, G., Brachmann, A., Rutsch, M., Brendler, V., Bernhard, G., Nitsche, H.
Laser lnduced Photoacoustic Spectroscopy using Solid State Tunable Lasers (OPO)
LLNL, Glenn T. Seaborg Institute for Transactinium Science
Livermore, CA, USA, 19.11.1997

Geipel, G., Brendler, V., Bernhard, G., Nitsche, H.
Laser lnduced Spectroscopy at the Institute of Radiochemistry in Rossendorf
LANL, Actinide and Environmental Structural Chemistry
Los Alamos, New Mexico, USA, 25.11.1997

Grantz, M.
Trace Amount Components in Laminar Gas Flow - Theoretical and Experimental Studies
4. Workshop ”Physics and Chemistry of the Heaviest Elements"
Stenungsund, Sweden, 05.-08.06.1997

Heise, K.H., Pompe, S., Bubner, M., Nitsche, H.
Synthetische Huminsäuren für die Umweltforschung: Anforderungen und Realisierung
Arbeitstagung der Deutschen Gesellschaft für Moor- und Torfkunde e.V.
Bad Elster, Germany, 04-05.09.1997

Hennig, C.
XAS-Datenanalyse mit Hilfe von FEFF-Rechnungen
Institut für Physikalische und Theoretische Chemie, Universität Leipzig
Leipzig, Germany, 11.11.1997

Hübener, S.
Status of the Preparation for Seaborgium Gas Chemistry Experiments with Oxidehydroxides
4. Workshop “Physics and Chemistry of the Heaviest Elements"
Stenungsund, Sweden, 05.-08.06.1997

Hübener, S., Taut, S., Eichler, B.
Thermochromatographic Adsorption Studies - an Approach to Measure Metallic Properties of the Heaviest Actinides
Actinides' 97
Baden-Baden, Germany, 21.-26.09.1997

Mack, B., Abraham, A., Baraniak, L.
Untersuchungen zum Redoxverhalten von Huminsäure und Lignin
Workshop: “Huminsäure”
Saarbrücken, Germany, 10.7.1997

Moll, H., Geipel, G., Brendler, V., Bernhard, G., Nitsche, H.
Interaction of uranium(VI) with silicic acid in aqueous solutions studied by time-resolved laser-induced fluorescence spectroscopy (TRLFS)
Actinides'97
Baden-Baden, Germany, 21.-26.09.1997

Nebelung, C., Bernhard, G., Nitsche, H.
Fortschrittsbericht: Direktmessung " -aktiver Nuklide in Bauschutt zur Freigabeentscheidung
7. Sitzung Arbeitskreis “Freimessung von Anlagenteilen und Bauschutt aus dem Abbau kerntechnischer Anlagen des Brennstoffkreislaufes"
Köln, Germany, 12.05.1997

Nitsche, H.
Moderne interdisziplinäre Entwicklungen in der Radiochemie.
Technische Universität München, Naturwissenschaftliche Fakultät
München, Germany, January 1997, invited

Nitsche, H.
Actinides in the Environment.
The Robert A. Welch Foundation Conference on Chemical Research
XXXXI The Transactinide Elements
Houston, USA, October 1997, invited

Nitsche, H.
Basic Research for Environmental Remediation:
Speciation and Complexation of Aqueous Uranium.
LLNL, Glenn T. Seaborg Institute tor Transactinium Science
Livermore, CA, USA, January 1997, invited

Nitsche, H.
lnterdisciplinary Nuclear Chemistry: Applications to Actinide Environmental Chemistry and Studies of the Chemical Properties of the Heaviest Elements.
University of California Berkeley, Chemistry Department
Berkeley, CA, USA, January 1997, invited

Pompe, S.
Melanoidine als definierte Huminsäureanaloga für Komplexbildungsuntersuchungen.
Workshop: “Geochemische Modellierung radiotoxische und chemisch-toxische Stoffe in natürlichen aquatischen Systemen”
Forschungszentrum Karlsruhe, Institut für Nukleare Entsorgungstechnik
Karlsruhe, Germany, 23.-24.04.1997

Pompe, S.
Erste Stabilitätsuntersuchungen an synthetischen und natürlichen Huminsäuren.
Workshop zum Forschungsvorhaben “Einfluß von Huminstoffen auf das Migrationsverhalten radioaktiver und nichtradioaktiver Schadstoffe unter naturnahen Bedingungen”
Saarbrücken, Germany, 10.07.1997

Pompe, S., Heise, K.H.
Fortschrittsbericht über die Synthese von Huminsäuren und deren Komplexbildungsverhalten gegenüber Uranylionen.
Workshop zum Forschungsvorhaben “Einfluß von Huminstoffen auf das Migrationsverhalten radioaktiver und nichtradioaktiver Schadstoffe unter naturnahen Bedingungen”
Saarbrücken, Germany, 10.07.1997

Pompe, S.
Melanoidine - Chemisch modifizierbare Funktionalitätsmodelle zur Untersuchung des Komplexbildungsverhaltens von Huminsäuren.
Forschungszentrum Karlsruhe, Institutsseminar INE
Karlsruhe, Germany, 17.09.1997

Reich, T., Nitsche, H.
Actinide Chemistry at the Dedicated Rossendorf Beamline (ROBL) at the ESRF
27èmes Jounées des Actinides
Dijon, France, 26.-29.4.1997, invited

Reich, T.
EXAFS Studies of Uranium Sorption on Mineral Surfaces
2nd German-Russian Symposium on Electron and X-ray Spectroscopy
Berlin, Germany, 02.-05.11.1997, invited

Reich, T.
Anwendung von XAFS-Spektroskopie in der Radioökologie
Institut für Experimentalphysik II, Universität Würzburg
Würzburg, Germany, 21.11.1997

Rutsch, M.
Complex Formation between Uranyl and Arsenate Studied by Time-Resolved Laser-lnduced Fluorescence Spectroscopy (TRLFS)
LLNL, Glenn T. Seaborg Institute for Transactinium Science
Livermore, CA, USA, 18.11.1997, invited

Shuh, D.K., Allen, P.G., Bucher, J.J., Edelstein, N.M., Denecke, M.A., Reich, T., Nitsche, H.
X-ray Absorption Fine Structure of Actinides in Concentrated Electrolytes
Actinides'97
Baden-Baden, Germany, 21.-26.09.1997

Taut, S.
Thermochromatography of No
4. Workshop “Physics and Chemistry of the Heaviest Elements"
Stenungsund, Sweden, 05.-08.06.1997

Türler, A., Eichler, B., Gäggeler, H.W., Hübener, S., Jost, D.T., Lebedev, V., Timokhin, S.N., Yakushev, A.B., Zvara, I.
Evidence for relativistic effects in the chemistry of element 104
Actinides'97
Baden-Baden, Germany, 21.-26.09.1997

Vahle, A.
On-line Isothermal Gas Chromatography with Short-lived Mo and Tc Isotopes in the O_2-$H_2O_{(g)}$/ $SiO_{2(s)}$ System
4. Workshop “Physics and Chemistry of the Heaviest Elements"
Stenungsund, Sweden, 05.-08.06.1997

Vahle, A.
Hochtemperaturgaschromatographie mit Spurenmengen der Homologen des Elementes 106 im O_2-$H_2O_{(g)}$/$SiO_{2(s)}$ -System
on the occasion of the awarding of the “Georg-Helm-Preis"
TU Dresden, Germany, 08.10.1997

Vahle, A.
Faszination Transactinidenforschung
on the occasion of the awarding of the “Doktorandenpreis der WBL”
Köln, Germany, 30.10.1997

Zänker, H.
Colloid Chemistry of Humic Acid
First Project Meeting of the FU project “Effects of Humic Substances on the Migration of Radionuclides: Complexation and Transport of Actinides"
Forschungszentrum Karlsruhe, Institut für Nukleare Entsorgungstechnik
Karlsruhe, Germany, 03.-04.03.1997

Zänker, H., Hüttig, G., Richter, W., Nitsche, H.
Characterization of the Submicron Particles in the Kranichsee Moor Water
Second Project Meeting of the EU project “Effects of Humic Substances on the Migration of Radionuclides: Complexation and Transport of Actinides”
British Geological Survey.
Nottingham, United Kingdom, 13.-14.11.1997

POSTERS

Baraniak, L., Schmidt, M., Bernhard, G., Nitsche, H.
Complexation of Uranium(VI) with the Main Components of Mine-wood Degradation.
Part I. Complexation with Protocatechuic Acid, Vanillic Acid and Vanillin
Migration'97
Sendai, Japan, 26.-31.10.1997

Bernhard, G., Geipel, G., Brendler, V., Nitsche, H.
Laserspektroskopie zur Bestimmung der chemischen Speziation von Uranylkomplexen
GDCh Hauptversammlung 1997
Wien, Austria, September 97

Bernhard, G., Brendler, V., Geipel, G., Reich, T., Nitsche, H.
Validation of Complex Formation of Ca^{2+}, UO_2^{2+} and CO_3^{2-}
Migration'97
Sendai, Japan, 26.-31.10.1997

Brendler, V., Bernhard, G., Nitsche, H.
Coupling geochemical speciation to risk assessment codes
CIC Meeting
Zürich, Switzerland, November 1997

Bubner, M., Pompe, S., Jander, R., Heise, K.H., Schuster, G., Nitsche, H.
Model Investigation of Aqueous UO_2^{2+}/Ca^{2+} Humic Acid Complexation
Actinides‘97
Baden-Baden, Germany, 21.-26.09.1997

Czerwinski, K., Denecke, M.A., Pompe, S., Moll, H., Reich, T., Nitsche, H.
Complexation of Uranium(VI) with the Siderophore Desferrioxamine B
Migration'97
Sendai, Japan, 26.-31.10.1997

Denecke, M.A., Friedrich, H., Reich, T., Bernhard, G., Knieß, T., Rettig, D., Zorn, T., Nitsche, H.
Determination of Relative Arsenite and Arsenate Concentrations in Aqueous Mixtures by XANES
HASYLAB Nutzertreffen
Hamburg, Germany, 31.01.1997

Denecke, M.A., Reich, T., Pompe, S., Bubner, M., Heise, K.H., Nitsche, H., Allen, P.G., Bucher, J.J., Edelstein, N.M., Shuh, D.K., Czerwinski, K.R.
EXAFS Investigations of the Interaction of Humic Acids and Model Compounds with Uranyl Cations in Solid Complexes
Migration'97
Sendai, Japan, 26.-31.10.1997

Geipel, G., Bernhard, G., Brachmann, A., Brendler, V., Nitsche, H.
Untersuchungen zu Speziation von f-Elementen mittels laserinduzierter photoakustischer Spektroskopie
Anakon'97
Konstanz, Switzerland, 06.-08.04.1997

Geipel, G., Bernhard, G., Brendler, V., Nitsche, H.
Uranyl Carbonate Complexes studied by Laser-Induced Spectroscopy
Actinides'97
Baden-Baden, Germany, 21.-26.09.1997

Nebelung, C., Nitsche, H., Bernhard, G.
A fast method for low-level actinide measurement in concrete
Actinides'97
Baden-Baden, Germany, 21.-26.09.1997

Otto, A., Kutschke, S., Selenska-PobeII, S.
Identification and Discrimination of Thiobacill using ARDREA, RAPD and Rep-APD
15. DECHEMA-Jahrestagung der Biotechnologen
Münster, Germany, 04.-06.03.1997

Panak, P., Hard, B.C., Pietzsch, K., Kutschke, S., Röske, K., Selenska-PobeII, S., Bernhard, G., Nitsche, H.
Bacteria from uranium mining waste pile: Interaction with U(VI)
Actinides ‘97
Baden-Baden, Germany, 21.-26.09.1997

Pompe, S., Brachmann, A., Bubner, M., Geipel, G., Heise, K.H., Nitsche, H.
Determination and Comparison of Uranyl Complexation Constants with Natural and Model Humic Acids
Migration'97
Sendai, Japan, 26.-31.10.1997

Rettig, D., Merker, P., Nitsche, H.
Detection of Aerosol Losses in Glass Vesseis
European Aerosol Conference
Hamburg, Germany, 15.-19.09.1997

Schuster, G., Bubner, M., Pompe, S., Heise, K.H., Nitsche, H.
Thermoanalytical Investigations on the Oxidizing Degradation of Natural and Synthetic Humic Acids and their Calcium and Uranyl Complexes
12. Ulm-Freiberger Kalorimetrietage
Freiberg, Germany, 19.-21.3.1997

Taut, S., Hübener, S., Eichler, B., Türler, A., Gäggeler, H.W., Timokhin, S.N., Zvara, I.
Thermochromatography of No-259
Actinides'97
Baden-Baden, Germany, 21.-26.09.1997

Woedtke v., F., Reich, T., Denecke, M.A., Nitsche, H., Oppermann, H.
Strukturuntersuchungen an Mischkristallen $V_{1-x}Nb_xO_2$
9. Tagung Festkörperanalytik
Chemnitz, Germany, 23.-26.06.1997

III. SEMINARS

INSTITUTE SEMINARS

Dr. Jörg Hadermann
Paul Scherrer Institut, Villigen, Schweiz
Modelle zum Stofftransport in geklüfteten Medien: Probleme der Validierung
02.04.1997

Dr. Wolfgang Hummel
Paul-Scherrer-Institut, Labor für Entsorgung, Villigen, Schweiz
Chemische Modellierung: ein Zahlenlotto
30.04.1997

Dr. Andre M. Scheidegger
Plant and Soil Sciences Department, University of Delaware, Newark, USA
Anwendung der Röntgenabsorptionsspektroskopie zur Untersuchung der Sorptionskinetik an Bodenbestandteilen
15.05.1997

Prof. Dr. Yuri Vlassov
Head of Radiochemistry Department, Faculty of Chemistry, St. Petersburg University, Russia
The Radiochemistry Department of St. Petersburg: Radionuclides and Chemical Sensors
16.05.1997

Dipl.-Chem. Thorsten Klein
TU München, Institut für Wasserchemie und Chemische Balneologie
Asymmetrische Fluß-Field-Flow-Fractionation (FFF) - eine neue Trenntechnik zur Charakterisierung von Huminkolloiden und anderen Hydrokolloiden
04.06.1997

Dr. Larc Tröger
HASYLAB, DESY, Hamburg
Nahordnungsuntersuchungen während chemischer Reaktionen und an Nanoclustern
05.06.1997

Wolfgang Buermann, MSc.
Department of Physics, University of Connecticut, Storrs, CT, USA
Tight Metal Binding in Humic Acids
20.06.1997

Prof. Dr. Thomas Wolff
Professur für Grenzflächen- und Kolloidchemie, Institut für Physikalische Chemie und Elektrochemie, Technische Universität Dresden
Aus der Schnittmenge von Kolloidchemie und Photochemie
01.07.1997

Prof. Dr. David Waite
Department of Water Engineering, University of New South Wales, Sidney, Australia
Uranium Sorption to Mineral Substrate: lmplications for Transport
05.09.1997

Dr. Roy Wogelius
Department of Earth Sciences, University of Manchester, UK
How will Minerals Dissolve? In Situ Synchrotron Experiments at the Mineral-Fluid Interface
11.09.1997

Prof. Dr. Ulrik K. Kläning
Department of lnorganic Chemistry, University Aarhus, Denmark
Oxygen Atom Exchange by the Reactions $O^- + H_2O = OH^- + OH$ and $OH + H_2O = H_2O + OH$
12.09.1997

Dr. David Wruck
Lawrence Livermore National Laboratory, Livermore, CA, USA
Particle Counting by Laser-Induced Breakdown
01.10.1997

Dr. Annie Kersting
Lawrence Livermore National Laboratory, Livermore, CA, USA
Migration of Radionuclides in Groundwater at the Nevada Test Site: Evidence of Colloidal Transport through Fractured Rock
22.10.1997

Dr. Bernhard Kienzler
Forschungszentrum Karlsruhe, Institut für Nukleare Entsorgungstechnik
Modellierungen der Humin-Kolloid-Migration - Vorstellungen, Ansätze und Lösungsmöglichkeiten
25.11.1997

Dr. Vanya Mitewa
Institut für Mikrobiologie, Bulgarische Akademie der Wissenschaften Sofia, Bulgaria
Molecular Characterization of Bacillus Isolates: Demonstration of the Presence of Different Bacilli in the Uranium Waste Heap “Haberlandhalde"
17.12.1997

INTERNAL SEMINARS (open to the public)

DC A. Roßberg
Berechnung von theoretischen Parametern für die EXAFS- und XANES-Analyse mittels FEFF6
20.06.1997

Dr. M.A. Denecke
FEFF-Berechnungen zur Mehrfachstreuung in der EXAFS-Analyse am Beispiel von Uranylcarboxylaten
04.07.1997

Dr. Hans Syhre
PANALYTIK GmbH, Rossendorf
Flugzeit (TOF)-SIMS: Neue Möglichkeiten der Spuren- und Oberflächenanalytik
09.10.1997

Prof. Dr. Heinz Filthuth
E'cole Supeneure de Physique et de Chimie Industrielles de la Ville de Paris, France
Neue Technologien zum Nachweis radioaktiver Isotope im Makro- und Mikrobereich: Radio-Imaging mit höchster Ortsauflösung und Nachweisempfindlichkeit
29.10.1997

D. Vulpius
Darstellung und Charakterisierung von Uranylkarbonat
13.11.1997

WORKSHOPS

Workshop ”Huminsäuren"
Forschungszentrum Rossendorf, Institut für Radiochemie (IfR)
Universität Leipzig, Institut für Geophysik und Geologie (IfGG)
Rossendorf, 14.01.1997

H. Nitsche (IfR)
Arbeitsrichtungen des Instituts für Radiochemie

H. Kupsch (IfGG)
Die Leipziger Georadiochemie

D. Rößler (IfGG)
Die Sequentielle Chromatographie

U. Gottschalch (IfGG)
Die ionenfokussierende Elektrophorese von Huminstoffen unter Einsatz der Radiotracer Lanthan-140 und Indium-111

S. Pompe (IfR)
Darstellung und Charakterisierung von synthetischen Huminsäuren als Funktionalitätsmodelle natürlicher Huminsäuren

M. Bubner (IfR)
Synthese von Referenzsubstanzen für Uranyl-Huminsäurekomplexe

M.A. Denecke (IfR)
EXAFS-Untersuchungen der Wechselwirkung von Uran(VI) mit natürlichen und synthetischen Huminsäuren

A. Brachmann (IfR)
Bestimmung der Komplexbildungskonstanten des Urans mit Funktionalitätsmodellen und natürlichen Huminsäuren mittels Zeitaufgelöster Laserfluoreszensspektroskopie

L. Baraniak (IfR)
U(VI)-Komplexierung mit phenolischen Ligandabbauprodukten

K. Franke (IfGG)
Untersuchungen spezifischer Eigenschaften von Huminstoffen mittels yy-Winkelkorrelation (TDPAC)

H. Zänker (IfR)
Nachweis micellartiger Agglomerate in wäßrigen Lösungen von Huminsäure und Uranylhumatkomplexen

Arbeitstreffen
Forschungszentrum Rossendorf, Institut für Radiochemie (IfR)
TU Dresden (TUD), Institut für Anorganische Chemie, Arbeitskreis Koordinationschemie
Rossendorf, 16.04.1997

H. Nitsche (FZR)
Forschungsziele des Instituts für Radiochemie

K. Gloe (TUD)
Forschungsziele des Arbeitskreises Koordinationschemie

J. Trepte (TUD)
Neue Heterocalixarene - Synthese und Wirteigenschaften

M. Mackrodt (TUD)
Komplexbildungseigenschaften von Pentalenokronenethern

Ch. Chartroux (TUD)
Aromatische Käfigverbindungen als potentielle Komplexbildner für Ag(I)

T. Krueger (TUD)
Molecular Modelling - Rechnungen zu Struktur-Wirkungsbeziehungen

M. Czekalla (TUD)
Entwicklung von Aminosäurerezeptoren

T. Reich (FZR)
EXAFS-Strukturanalyse am Beispiel von Uranylkomplexen in wässeriger Lösung

H. Zänker (FZR)
Charakterisierung von Umweltkolloiden

G. Geipel (FZR)
Laserspektroskopische Verfahren zur Bestimmung der Speziation und Komplexbildungskonstanten von Uranylverbindungen

S. Pompe (FZR)
Melanoidine als Huminsäureanaloga für Komplexbildungsuntersuchungen

L. Baraniak (FZR)
Wechselwirkung des U(VI) mit Substanzen des natürlichen Holzabbaus

T. Arnold (FZR)
Zur Sorption von Uran mit Ferrihydrit

D. Rettig (FZR)
Charakterisierung und Anlagerung von Schadstoffen an Aerosole

Symposium on Spectroscopic Methods in Actinide Chemistry
Rossendorf, 29.09.1997

L. Terminello
Glenn T. Seaborg Institute, Lawrence Livermore National Laboratory, Livermore, CA, USA
An Overview of Transactinium Research at LLNL

D. Wruck
Glenn T. Seaborg lnstitute, Lawrence Livermore National Laboratory, Livermore, CA, USA
Studies of Actinide Carbonates in Aqueous Solutions at Elevated Temperatures

P.G. Allen
Chemical Sciences Division, Lawrence Berkeley National Laboratory, Berkeley, CA, USA
Characterization of Chloro and Aqueous Complexes with Actinides by EXAFS Spectroscopy

D.K. Shuh
Chemical Sciences Division, Lawrence Berkeley National Laboratory, Berkeley, CA, USA
Study of Actinide Materials by Synchrotron Radiation Techniques

Symposium Radiochemie - Mikrobiologie
Grundlagenforschung zum Verständnis der Wechselwirkungen
Rossendorf, 05.12.1997

H. Nitsche
Einführung in die Thematik

C. Puers
Direkte Analyse der bakteriellen Diversität in Uranhalden

G. Kampf
Untersuchung der bakteriellen Diversität in der Haberlandhalde mit Hilfe der Analyse des ribosomalen Intergen-Abschnittes (RISA)

S. Selenska-Pobell
Molekulare Analyse kultivierbarer Bakterien aus Uranhalden

J. Wober
Molekulare Charakterisierung von natürlich vorkommenden Desulvovibro-Isolaten, die für die Uranmediation relevant sein können

P. Panak
Wechselwirkung von Bakterien aus Uranhalden mit Uran(VI)

IV. PERSONNEL

PERSONNEL

Director

Univ.-Prof. Dr. H. Nitsche

Administrative Staff

H. Pospischil
K. Wünsche
G. Kreusel*

Scientific Staff

Prof.(appl.) Dr. U. Abram
Dr. T. Arnold*
Dr. L. Baraniak
PD Dr. G. Bernhard
Dr. V. Brendler+
Dr. M. Böttger
Dr. M. Bubner
Dr. M.A. Denecke+
Dr. H.-J. Engelmann
DBC K. Flemming*
Dr. E. Förster*
Dr. H. Funke
Dr. G. Geipel
Dr. A. Günther*
Dr. K.H. Heise
Dr. C. Hennig+
Dr. S. Hübener
Dr. G. Kampf*
Dr. P. Merker
DC C. Nebelung
Dr. P. Panak*
Dr. S. Pompe*
Dr. C. Puers+
Dr. T. Reich
Dr. D. Rettig
Dr. W. Richter
DC L. Salamatin
Dr. S. Selenska-Pobell*
Dr. K. Schmeide*
Dr. G. Schuster*
Dr. S. Taut*
Dr. A. Vahle
DBC J. Wober*
Dr. H. Zänker

Technical Staff

DI(FH) B. Barz
B. Eisold
J. Falkenberg
DI(FH) H. Friedrich
DI(FH) Ch. Fröhlich
Dl(FH) G. Grambole
G. Heinz
S. Heller*
H. Heyne
B. Hiller
DI(FH) G. Hüttig
DI(FH) R. Jander
P. Kluge
DI(FH) M. Meyer
Ch. Müller
H. Neubert
DC(FH) A. Otto
A. Rumpel
R. Ruske
DI(FH) K. Wolf*

Graduate Students

DC A. Abraham
DC S. Amayri
DM A. Brachmann
DP M. Grantz
DBT S. Kutschke
DC B. Mack
DC H. Moll
DB J. Raff
DC A. Roßberg
DC M. Rutsch
DC M. Schmidt
DC B. Schmidt-Brücken
DC T. Zorn

Trainee

M. Dauer
C. Vulpius

+ post doc
* term contract

DC: Dipl.-Chem.
DI: Dipl.-Ing.
DP: Dipl.-Phys.
DBC: Dipl.-Biochem.
DBT: Dipl.-Biotech.
DB: Dipl.-Biol.
DM: Dipl.-Mineral.

V. ACKNOWLEDGMENTS

ACKNOWLEDGMENT OF FINANCIAL SUPPORT

The Institute is part of the Forschungszentrum Rossendorf e.V., which is financed in equal parts by the Federal Republic of Germany and the Free State of Saxony.

Five projects were supported by the Bundesministerium für Bildung, Wissenschaft, Forschung und Technologie (BMBF):

- Stillegung und Rückbau: Direktmessung "-aktiver Nuklide in Bauschutt zur Freigabeentscheidung.
  Contract No. BMBF 02 S 7655 A8
- Chemie der schwersten Elemente:
  Hochtemperaturgaschromatographie des Elements 106
  Contract No. BMBF 06 DR 666 I(4)/1
- Chemie der schwersten Elemente:
  Hochtemperaturgaschromatographie der Elemente 106 und 107
  Contract No. BMBF 06 DR 824 (2)
- lnfluence of humic acids on migration behavior of radioactive and non-radioactive heavy elements under natural conditions.
  Contract No. BMBF 02 E 88150
- Biosorption of uranium by bacillus for remediation of uranium wastes
  Contract No. DRL: BUL-014-97

Four projects were supported by Commission of the European Communities:

- Restoration Strategies for Radioactive Contaminated Sites and their Close Surroundings (RESTRAT).
  In collaboration with:
  SCK-CEN Mol, Belgium; Studsvik Ecosafe AB, Sweden; Riso National Laboratory, Danmark; Westlakes Research Institutes, Great Britain
  Contract No. F14P-CT95-0021
- Cooperative Network Matching EU and FSU Activities in the Field of Nuclear Fission Safety (NETWORK/NNFS).
  In collaboration with:
  JRC lspra, ltaly; SIEVERT Moscow, Russia; UIOP Kiew, Ukraine; INTERPROJECT Minsk, Weißrußland
  Contract No. F14C-CT96-0016
- Effects of Humic Substances on the Migration of Radionuclides: Complexation and Transport of Actinides.
  Contract No. F14W-CT96-0027
- Joint European Thermodynamic Database for Environmental Modeling (JETDEM).
  In collaboration with:
  FZK Karlsruhe, Germany; RCM Environmental Ltd., United Kingdom; Kungliga Tekniska Hogskolan, Department of Chemistry, Sweden; University of Aberdeen, Department of Chemistry, United Kingdom; Quantisci, Spain; Uppsala University, Institute of Earth Sciences, Sweden
  Contract No. F14W-CT96-0029

The Sächsisches Staatsministerium für Wissenschaft und Kunst provided support for the following projects:

- Mine-water Induced Wood Decomposition and lnfluence of the Degradation Products on Radionuclide Speciation, Sorption and Migration.
  Contract No. SMWK 4.7541.83-FZR/402
- lnfluence of Natural Water-borne Organic Substances on the Valency of Radionuclides and

Toxic Heavy Metals.
Contract No. SMWK 4.7541.88-FZR/512

- Soil-Plant Transfer Factors for Uranium.
  Contract No. SMWK 4.7531.50-03-VKTA/601
- Wechselwirkung von Mikroorganismen mit Uran und ausgewählten Radionukliden: Charakterisierung der Biosorption und ihrer genetischen Grundlagen mit Hinblick auf Ausbreitungsverhalten und Bioremedation.
  Contract No. SMWK 4.7531.50-03-FZR/607
- Wechselwirkung zwischen Proteinen und Metalloberflächen. Teilvorhaben C: Wechselwirkung von bakteriellen Zellhüllenproteinen mit Metallclustern.
  Contract No. SMWK 4.7531.05-03-0370/708
- Untersuchung der Bildung von kolloidalen organischen Partikeln in Bergwerkswässern.
  Contract No. SMWK 4.7533.70-FZR/704
- Chemical conversion of ^{14}C-labeled products to [^{14}C]Barium carbonate for long-time disposal.
  Contract No. SMWK 4.7581.312/20
- Förderung von Maßnahmen und Projekten der Entwicklungshilfe für die Staaten Mittel-, Ost- und Südeuropas sowie die neuen unabhängigen Staaten (NUS):
  Reise- und Aufenthaltsbeihilfen für Gastwissenschaftler (2x).
  Regierungspräsidium Dresden

One project was supported by Deutsche Forschungsgemeinschaft (DFG):

- Experimentelle Untersuchung der Eigenschaften schwerer Actinoide im elementaren Zustand mittels chromatographischer Methoden.
  Contract No. DFG HU 642/1-2

Four projects were supported by the following sponsors:

- Development of experimental arrangements and methods for on-line high temperature gas-chromatography of the heaviest elements.
  In cooperation with GSI.
  GSI DRNIK.
- Complexation and Sorption Phenomena of Uranium in Environmentally-Relevant Systems.
  Stanford Synchrotron Radiation Laboratory SSRL; U.S. Department of Energy
  Contract No. 2362 MP
- EXAFS-Untersuchungen umweltrelevanter Uranylkomplexverbindungen und deren Sorbate.
  Hamburger Synchrotronstrahlungslabor HASYLAB am Deutschen Elektronen-Synchrotron DESY.
  Contract No. II-94-06
- INTAS: Gas-phase chemistry studies of elements 104 and 106.
  In collaboration with:
  University of Berne, Switzerland,
  Joint Institute of Nudear Research, Russia
  Contract No. INTAS 94-424.